



# A mechanical model of muscle mechanics

Lorenzo Marcucci

## ► To cite this version:

Lorenzo Marcucci. A mechanical model of muscle mechanics. Life Sciences [q-bio]. Ecole Polytechnique X, 2009. English. NNT: . pastel-00004880

**HAL Id: pastel-00004880**

**<https://pastel.hal.science/pastel-00004880>**

Submitted on 27 Mar 2009

**HAL** is a multi-disciplinary open access archive for the deposit and dissemination of scientific research documents, whether they are published or not. The documents may come from teaching and research institutions in France or abroad, or from public or private research centers.

L'archive ouverte pluridisciplinaire **HAL**, est destinée au dépôt et à la diffusion de documents scientifiques de niveau recherche, publiés ou non, émanant des établissements d'enseignement et de recherche français ou étrangers, des laboratoires publics ou privés.





# Contents

<b>1</b>	<b>Muscle physiology and early modeling</b>	<b>1</b>
1.1	Muscle physiology . . . . .	1
1.2	Mechanical experiments . . . . .	7
1.3	Mechanical modeling . . . . .	14
1.3.1	Hill 1938 model . . . . .	14
1.3.2	Huxley 1957 model . . . . .	19
1.3.3	Huxley and Simmons 1971 model . . . . .	22
<b>2</b>	<b>Power Stroke</b>	<b>29</b>
2.1	Introduction . . . . .	29
2.2	Recent Models . . . . .	30
2.3	New model of a power stroke . . . . .	38
2.3.1	General shape of the energy . . . . .	38
2.3.2	Double parabolic approximation . . . . .	41
2.4	Deterministic case: global minimum . . . . .	43
2.4.1	One cross-bridge . . . . .	43
2.4.2	$N$ cross-bridges . . . . .	45
2.5	Stochastic case: $N$ cross-bridges at finite temperature . . . . .	48
2.6	Variable power stroke size . . . . .	50
2.7	Negative slope of the $T_2(\delta)$ curve . . . . .	57
2.7.1	Inhomogeneity in a chain of sarcomeres . . . . .	62
2.7.2	Distribution of the attachment positions . . . . .	73
2.8	Rate of fast tension recovery . . . . .	76
2.9	Discussion . . . . .	85
<b>3</b>	<b>The attachment-detachment process</b>	<b>87</b>
3.1	Introduction . . . . .	87
3.2	A model of frictional motor . . . . .	89



---

3.3	Brownian ratchets . . . . .	91
3.3.1	Magnasco model . . . . .	95
3.3.2	Prost et al. model . . . . .	98
3.3.3	Cooperative and non-cooperative motors . . . . .	101
3.4	Direct simulation of a set of stochastic equations . . . . .	107
3.5	Thermal ratchet . . . . .	109
3.6	Cooperative Magnasco model . . . . .	111
3.6.1	Governing equations . . . . .	111
3.6.2	Benchmark problem: $K = 0$ . . . . .	113
3.6.3	Cooperative Magnasco model with $K \neq 0$ . . . . .	116
<b>4</b>	<b>Full cross-bridge cycle</b>	<b>123</b>
4.1	Introduction . . . . .	123
4.2	Numerical implementation of the power stroke model . . . . .	125
4.2.1	Isometric case . . . . .	125
4.2.2	Length clamp device . . . . .	127
4.3	Whole cycle models . . . . .	130
4.3.1	Extended Huxley and Simmons potential . . . . .	130
4.3.2	Chemical-Spring-Motor model (CSM) . . . . .	133
4.3.3	Spring-Chemical-Motor model (SCM) . . . . .	136
4.3.4	Spring-Chemical-Motor model with a backbone (SCM1) . . . . .	140
4.3.5	Discussion . . . . .	148
<b>5</b>	<b>Conclusions</b>	<b>151</b>
<b>A</b>	<b>Appendix</b>	<b>155</b>
A.1	Brownian motion . . . . .	155
A.2	Probability . . . . .	155
A.3	The Langevin Equation . . . . .	157
A.4	Diffusion of a particle in a fluid . . . . .	159
A.5	The Fokker-Plank equation . . . . .	161
A.6	High friction limit . . . . .	163
A.6.1	The Fokker-Plank equation in the high-friction limit . . . . .	163
A.6.2	Canonical distribution . . . . .	165
A.6.3	The First passage time . . . . .	166
A.7	Kramers' approximation . . . . .	167
A.8	Brownian motion in a periodic potential . . . . .	169

---

A.9 Gillespie method . . . . .	172
--------------------------------	-----



# Acknowledgments

This thesis was developed at the Laboratoire de Mécanique des Solides (LMS) and mainly funded by the Marie Curie Research Training Network and partially by Société Fx-Conseil. Many people have contributed in different ways to this work, I would like to thank all of them and in particular:

My advisor Prof. Lev Truskinovsky for the discussions which we have had during all these three years and for his encouraging to reach a stronger understand of the mathematical techniques used in this work.

Dr. Jean-Marc Allain for the interest expressed on the development of this work and for his helpful suggestions.

Prof. Chaouqui Misbah for accepting to be the President of my thesis committee as well as Prof. François Gallet and Prof. Vincenzo Lombardi which have found the time to read and report on my thesis document. I would also like to thank Prof. Marie-Christine Ho Ba Tho, Prof. Cécile Sykes and Prof. Pascal Martin for accepting to participate to my thesis committee and for their suggestions to improve the final version of the thesis.

All the people of the Laboratoire de Mécanique des Solides where I spent the last three years. I met many nice persons, with a high professionalism. My special thanks go to Director Bernard Halphen for his support before and after the defense of the thesis.

Prof. Grégoire Allaire, team leader at the Ecole Polytechnique of the Multi-scale modelling and characterisation for phase transformations in advanced materials (MULTIMAT) project in the Marie Curie Research Training Network.

I would like to express my gratitude to Prof. Vincenzo Lombardi and Prof. Gabriella Piazzesi for having shared with me part of their tremendous amount of knowledge on muscle mechanics from the very beginning of this work. I remember especially our first meeting and the time which they have given to my questions despite the differences in our respective approaches to the same subject. I have seen my idea of *philo sophia* in their attitude.

---

I will not mention here all the persons belonging to my private life which have supported me in different ways, but this work is dedicated to them.

# Introduction

Skeletal *muscle contraction* is a broad domain of science that covers many areas, from biophysics and chemistry to mechanics. The foundations of the theory of muscle contraction were built 50 years ago, when it was understood that it is myosin “cross-bridge”, linking adjacent myosin and actin filaments, that generates force and motion. Since that time many experimental advances have been made. These advances have not been always matched by improvements in the building of mathematical models.

Mathematical approaches to muscle contraction are mainly based on the ideas proposed in the Huxley 1957 model [4] and Huxley and Simmons 1971 model [10], that dominated the field for the past half century. Although they do not account for all observed phenomena, these models still represent the paradigm of choice. The two models of Huxley can be seen as complementary since the Huxley 1957 model describes the attachment-detachment process and the events related to the slow time scale, while the Huxley and Simmons 1971 model describes the power stroke process and the events related to the fast time scale.

In this Thesis we shall follow some recent insight and explore the possibility to bring together these two type of processes and to obtain a unified model that is able to describe the whole cross-bridge cycle. Before the unification we first modify the existing models to cast them into a fully mechanical framework. Both Huxley 1957 model [4] and Huxley and Simmons 1971 model [10], present *ad hoc* assumptions regarding the chemical rate constants that drive the processes. Similar assumptions were made in all recent models to fit the experimental data at the expense of maintaining the link with mechanics.

In Chapter 1 we describe the physiology of muscles and their mechanical behavior, as well as the corresponding experimental procedures. There we also give the details of the Huxley 1957 model and Huxley and Simmons 1971 model which are important for the original development in the subsequent pages.

In Chapter 2, we deal with the attached state and reexamine the power stroke

---

theory through the eyes of a mechanical engineer. It has been already observed in the literature [17] that the Huxley and Simmons 1971 model of power stroke encounters problems in matching the observed time scale of tension relaxation when a realistic value of the stiffness of the myosin head is taken. After a review of how the more recent models, which incorporate one or more aspects of the original Huxley and Simmons 1971 model, deal with these problems, we present our modification of the theory which places the power stroke mechanism entirely in a mechanical framework. The novelty of our approach from the perspective of mechanics is that we deal with the mechanical behavior of a multi-stable system in a Brownian domain, where the effects of thermal fluctuations are important. We obtain an analytical description of the behavior of our model at equilibrium and during the transients and show how the resulting modification of the Huxley and Simmons 1971 model helps one to avoid the intrinsic problems of this model indicated above. Finally we show that our model gives a new meaning to the power stroke step, which is in quantitative agreement with all recent experimental observations.

In Chapter 3, we turn to the attachment-detachment process and review from the new, fully mechanical point of view the Huxley 1957 model. We show that this model can be viewed as belonging to a class of models of Brownian ratchets. These models, first developed in the early '90s, have an important role in the description of molecular motors of which the myosin II is an example. We are interested in the Brownian ratchets theory because it allows one to have a completely mechanical interpretation of the muscle contraction process. We present different types of ratchets representing the process of ATP hydrolysis. We modify one of these models by including cooperative effects and adapt it to the description of the slow time phase of the contraction phenomenon. We also develop and test in this Chapter a numerical algorithm to solve the coupled system of stochastic differential equations which is later used for our numerical experiments.

In Chapter 4, we combine the power stroke model from Chapter 2 with the model of a cooperative Brownian ratchet developed for the simulation of the attachment-detachment process in Chapter 3. We present different ways of linking together the two models and study both advantages and limitations of each version of the unified model. We finally come up with a model capable of providing fully mechanical description of all four stages of the biochemical Lymn-Taylor cycle of muscle contraction. The resulting model still has drawbacks and we present some perspectives regarding how to resolve the remaining problems.

---

In the last Chapter 5 we collect the main new developments from each Chapter and present a general discussion and conclusions. In Appendix we review some mathematical results regarding stochastic differential equations which we used in the Thesis.





# Chapter 1

## Muscle physiology and early modeling

### 1.1 Muscle physiology

The movements of a muscle on a macroscopic scale appear as the result of the concerted action of millions of elemental units that work in unison. The most studied muscles are called *skeletal muscles* because these muscles are attached to the skeleton. The contraction of skeletal muscles is under voluntary control. They belong to the class of *striated muscles* which are composed of long, parallel, cylindrical fibers. Each of these fibers is a multinucleate cell, of  $1 - 100\text{ mm}$  in length and  $10 - 100\text{ }\mu\text{m}$  in diameter. Fibers contain myofibrils, also cylindrical in shape with a diameter of  $0.5 - 2\text{ }\mu\text{m}$ . Myofibrils are made of repeated segments each about  $2.5\text{ }\mu\text{m}$  in length, that are called *sarcomeres* (Fig. 1.1) [95].

Sarcomere is the smallest element of a muscle that can contract. Being placed in series, sarcomeres generate the contraction of the whole muscle. Each sarcomere is formed by an array of filaments of two different types, which interact with each other: a thinner filament, containing the protein *Actin*, and a thicker filament, containing the protein *Myosin*. The sarcomere can be divided in zones: in Fig. 1.2 we see a longitudinal and a transverse view of it. In the region where the filaments overlap, six thin filaments are located around each thick filament (Fig. 1.2b). Thin filaments are anchored to the Z-disk (from german *zwischen*, between) which connects adjacent sarcomeres. Thick filaments are anchored to M-line (Mittel, middle of the sarcomere, not showed in Fig. 1.2) and also to the Z-disk via an elastic element the giant protein *titin*. These repeating structures, (A=anisotropic at the polarizing microscope, I=isotropic, H=hell=clear) observed under the microscope,

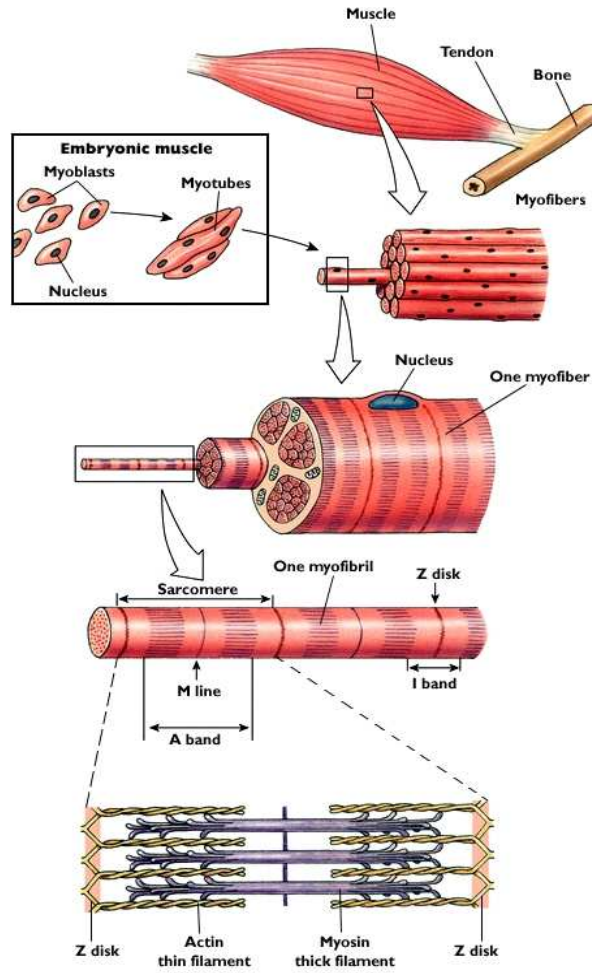


**Figure 1.1:** Muscle's anatomical microstructure

generate the typical striated structure that gives the name to this type of muscles [19]. A longitudinal view as it appears on a electron micrograph is given in Fig. 1.3.

The sliding-filament hypothesis was proposed fifty years ago. It assumes that during contraction the thin filament moves past the thick one, so that both the sarcomere, and the muscle, shorten without changing the length of the two structures. The hypothesis was based on the papers of Hugh Huxley and Jean Hanson [2] (using a phase contrast light microscopy) and of Andrew Huxley and Rolf Niedergerke [3] (using a specially developed interference light microscope) both published in 1954. Both works showed that when the muscle contracts the filaments keep a constant length, and the conclusion was made that they must slide during shortening. This hypothesis has not been immediately accepted: the then current view was that myosin was a long negatively charged polypeptide without much structure that shorten down due to the addition of  $Ca^{2+}$  [76]. Later on, it became clear that

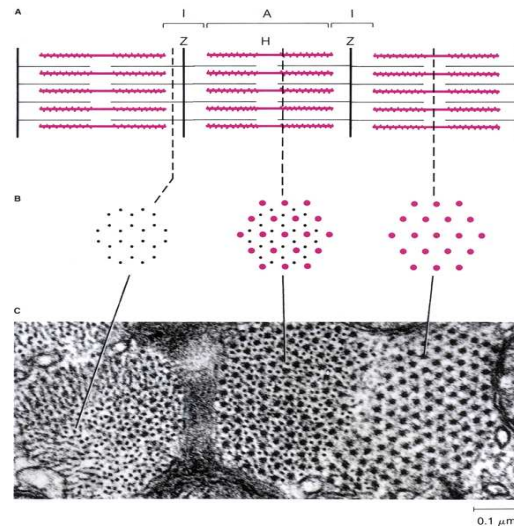


**Figure 1.2:** Longitudinal and transverse view of a sarcomere: (a) Longitudinal view of 3 sarcomeres (sketch). (b) Transverse view at 3 different section (sketch). (c) Transverse view of 3 sarcomeres (microscope). From [97]

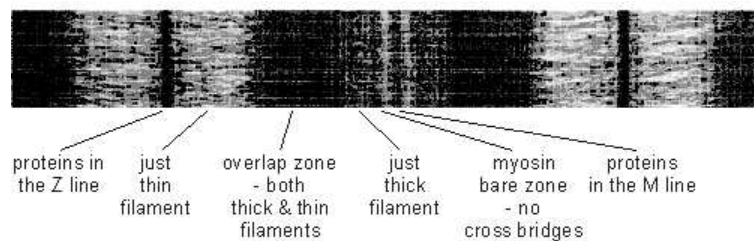


**Figure 1.3:** Longitudinal view of a sarcomere as seen in electron micrograph. From [98]

the two filaments interact through the *cross-bridges* (later we use notation Xb); these are the globular portions, or heads, that emerge in regularly repeating couples from the thick filament formed by the polymerisation of the dimeric protein myosin II (Fig. 1.4). Each head has a site with an affinity for actin, and a site with an affinity for a high energy molecule, called ATP (adenosinphosphate). The first site bounds an actin monomer while the second site an ATP molecule which acts as the fuel for the muscle motor. ATP is hydrolyzed by myosin in ADP (adenosin~~d~~iphosphate) and orthophosphate which subsequently are dissociated with release of chemical energy [9].

A simplified model of Xb cycle is shown in Fig. 1.5, where one can see four most important states in which Xb can exist. When attached to actin (state 2 in the figure), each Xb uses its potential energy to pull the actin filament through a *power stroke* (state 3) which, according to crystallographic studies, consists in a tilting of the lever arm portion of the head [33]. The relative sliding of the filaments takes

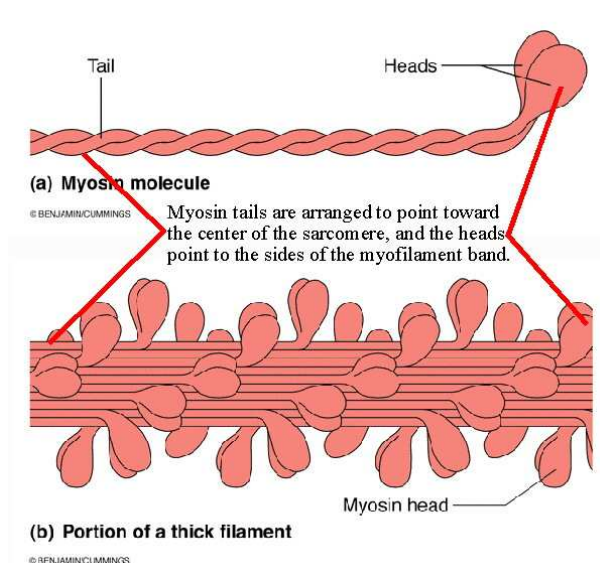


**Figure 1.4:** Myosin filament structure. (a) Myosin molecule (couple). (b) Bundle of coupled myosin molecules which generate the thick filament. From [100]

place in one direction (plus direction), but due to the antiparallel arrangement of the two halves of the sarcomere, the two Z-disks are pulled towards the center of the sarcomere, reducing its length. In this sense, the half-sarcomere, the zone between one Z-disk and the next M-line, can be seen as the smallest element that can contract. To go back to its original configuration (state 1) the Xb needs another ATP to detach from actin and start another cycle (state 4). It then binds to a new *active site* on the actin filament (state 2) and the whole process starts again [64]. This inner working is described in the bio-chemical Lymn-Taylor model of a cross-bridge cycle [9]. The cycle in Fig. 1.5 is a simplified four-states model that omits a number of intermediate states, nevertheless it describes the essential steps of the process. An important general observation is that muscle needs ATP for both the contraction and the relaxation; the unphysiological depletion of ATP below a certain concentration will prevent the detachment of the heads from the actin filament, which causes *rigor mortis* [19].

The structure of the head can be resolved with a precision of one nanometer [33], [87]. It has been proved that the relative displacement of the filaments is mainly taking place during the power stroke (state 3). It is achieved by a rotation of the distal part (C-terminal) of the head that acts like a lever arm. This mechanism gives to the whole approach the name of *swinging lever arm theory*.

Regulation of the contraction is due to the fact that Xbs can bound actin only when the concentration of calcium ions is high enough. The troponin is a protein

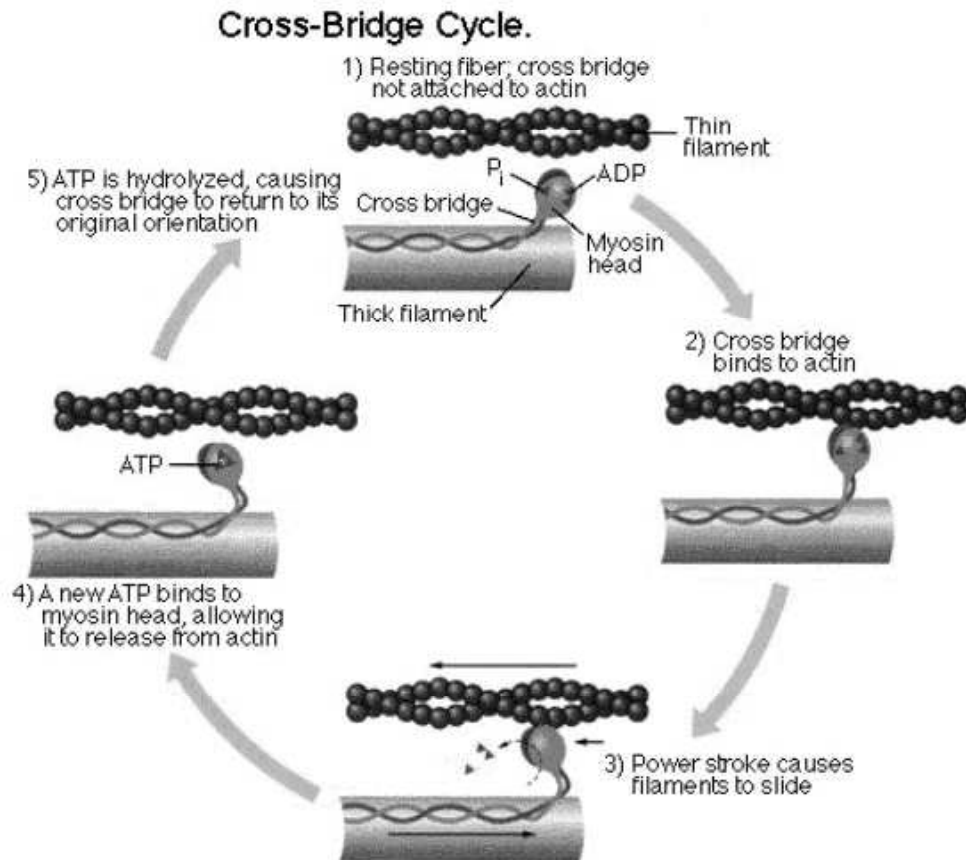


**Figure 1.5:** Simplified Cross Bridge (Xb) cycle (see text). From [44]

that is attached to the protein tropomyosin and lies within the groove between the two strands of the actin filament in muscle tissue. In a relaxed muscle, tropomyosin prevents the interaction of myosin with the attachment site on actin, thus preventing contraction. When the muscle cell is stimulated, calcium channels open in the sarcoplasmic reticulum and release calcium into the sarcoplasm. Some of this calcium ions attach to troponin, causing a conformational change that moves tropomyosin out of the way so that the Xbs can attach to actin and produce muscle contraction. The ions  $Ca^{2+}$  are stored in the sarcoplasmic reticulum (SR) surrounding the myofilaments. The action potential originated at the neuromuscular junction triggers the release of calcium from the SR almost synchronously everywhere by inducing an increase in  $Ca^{2+}$  permeability of the SR membrane. The contraction is maintained until the nerve continues to fire; when the train of action potentials stops, the  $Ca^{2+}$  permeability falls, while the  $Ca^{2+}$  pump brings back the calcium into the SR. The decrease of calcium concentration below the threshold inactivates the thin filament and induces relaxation of muscle [19] (Fig. 1.6).

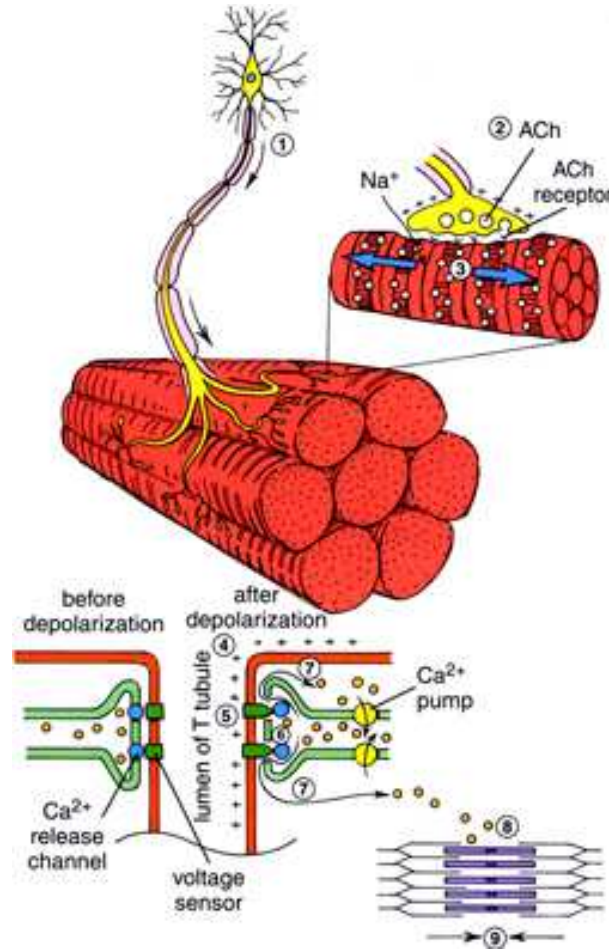


**Figure 1.6:** Excitation contraction coupling: schematic description. From [97]

We have given here a brief overview of the complex events that lead to the contraction of skeletal muscles. A complete description should take into consideration how the electrical signal generates the biochemical processes, with all their complexity, which finally leads to the mechanical force or displacement in sarcomeres. We would like to emphasize that in this work we shall consider only the mechanical aspects of the contraction, avoiding the description of proteins interaction through chemical rate constants. Despite some limitations in the physical interpretation of the final model, discussed at the end of the thesis, this approach allows one to produce a fully mechanical model of the contraction in the sarcomere, opening the way to the construction of artificial muscle type machines. Moreover, as we shall show the new approach improves, in some aspects, the predictive power of the model respect to the chemical approach.

## 1.2 Mechanical experiments

There exist different experimental approaches to the study of the mechanics of muscle contraction (see [76], [75], [78] and references therein). The technology used in these experiments has been often highly innovative, leading to technological spin-off. We have already mentioned different microscopy techniques. Another technique is the *in vitro* motility assay, where single myosin molecules attached to a bead trapped by a laser beam are used to measure the generated force. Differently, the IVMA measures the speed of sliding of actin filaments, attached to a bead, gliding on a bed of myosins. Then the synchrotron radiation (an intense X-ray source) was developed to study the Xb movements *in situ* in whole muscle or single fibres. Finally protein crystallography was applied to investigate the power stroke in the myosin molecule at atomic resolution (see Fig. 1.7) [76].

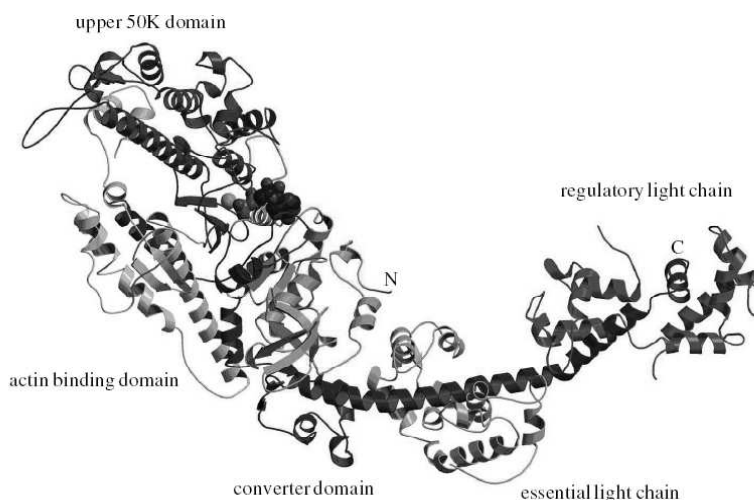


**Figure 1.7:** Structure of myosin S1 from chicken skeletal muscle. From [33]

In this Thesis we approach the modeling of skeletal muscles contraction from a mechanical point of view. Therefore, we shall be mainly interested in a particular set of experiments performed on the muscle fibers or myofibrils. These experiments have common aspects with the usual mechanical measurements aimed at testing the behavior of passive materials [19].

A muscle responds to a single stimulus with a single transient rise in tension, called twitch. Two stimuli, generated after a suitable interval of time, produce identical force transients. When the second twitch starts before the first one is over, the second one develops a larger peak tension. With a train of stimulations the force reaches a steady state value, called unfused tetanus, and characterized by the oscillating behavior with the stimulation frequency (Fig. 1.8). At a higher



frequency the mean force rises to an almost constant value: this situation is called tetanus. The required frequency depends on the type of muscles and on the temperature (50-60 Hz in mammalian muscles at body temperature, not used in the figure) [19]. An experiments in which we are interested have been made in the state of tetanus, that can be viewed as a steady state condition.

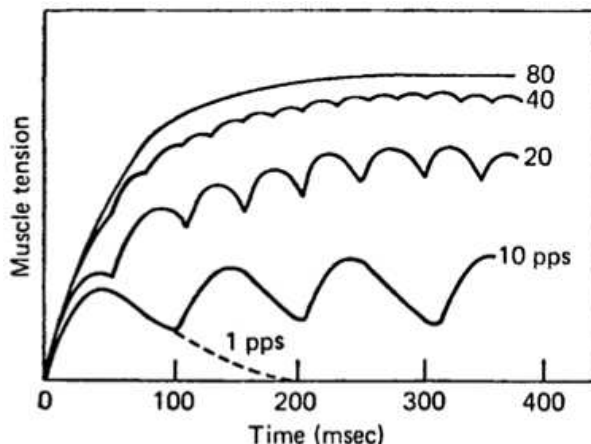


**Figure 1.8:** Force generated at different stimulation frequency. 1 pps correspond to the single twitch, at 80 pps is reached the tetanus. From [97]

The mechanical experiments, either on a fiber or on a myofibril, are usually performed with one end of the specimen fixed and the other linked to a lever with a catch mechanism and a transducer of force (Fig. 1.9). In this Section we shall explain in detail the three major protocols used in these type of experiments and present their main results.

### Force-length curves

When the catch mechanism is fixed, the muscle undergoes an *isometric* contraction. By imposing tetanization with the ends fixed one can register the tension generated by the muscle. By varying the initial length of the muscle before the tetanization, a *force-length* curve can be constructed [95].

In Fig. 1.10 we show the schematic force length curve for the total force and for its two components: active force and passive force. Passive force is the resistance generated by elastic components in parallel to the contractile element, it becomes relevant when the sarcomeres are overstretched. The passive resistance is almost zero until a certain critical elongation of the sarcomere, and then increases fast showing nonlinear elasticity. Subtracting the passive force from the total isometric force, we obtain the component of the force that a muscle can generate actively.

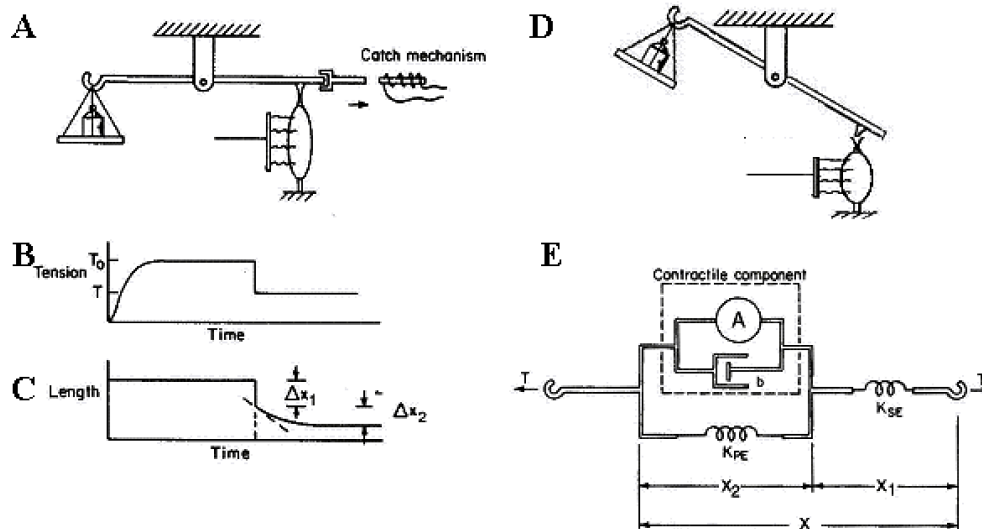


**Figure 1.9:** Experimental devices (a,d), experimental curves(b,c) and one version of the Hill's model (e) (see Section 1.3.1). (a) When the catch mechanism is acting the muscle can be tetanized at a constant length, left part of (c), reaching the tetanus at  $T_0$  in (b). When the system is released (d), the isotonic contraction against a constant load,  $T$  in (b), generates the length-time curve in the right part of (c). From [19]

Different types of muscles have different passive responses and so different total forces, but the active force-length curve, for most of them, shows the same non-monotone behavior [7]. This behavior (Fig. 1.11) is in agreement, with the fact that the two filaments must overlap to generate force. In fact, the maximum active force is generated when the overlap between the two filaments is optimal, i.e. when all the Xbs see an actin site where they can bound and, at the same time, there is no interference between the two half parts of a sarcomere. When the initial length in the passive state is such that some Xbs, the ones near the M-line, do not have any active site to attach, the active force starts to decrease linearly with the total number of Xbs available to interact with actin. For shorter initial lengths than those corresponding to the plateau of the force-length curve, two opposite actin filaments start to interfere with each other, that again contributes to a decrease of force [7].

An important thing to note is that the force-length (T-l) curve is created point by point: first we fix a length in the passive state, then we tetanize the muscle and register the force which develops in isometric contraction. The T-l curve represents therefore a series of isometric activations at different initial passive lengths. In particular this curve does not represent the response of the muscle to quasi-static stretching.

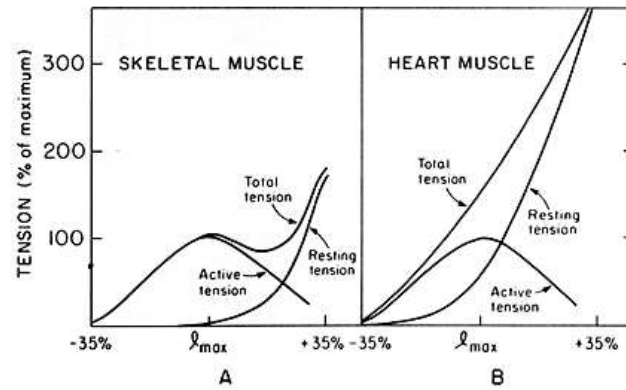


**Figure 1.10:** Total, passive and active force as a function of the length for two different types of muscles. The passive force is analyzed stretching the muscle in the passive state. The total force is analyzed tetanizing the muscle from a constant passive length. The active force is derived by subtraction. From [19]

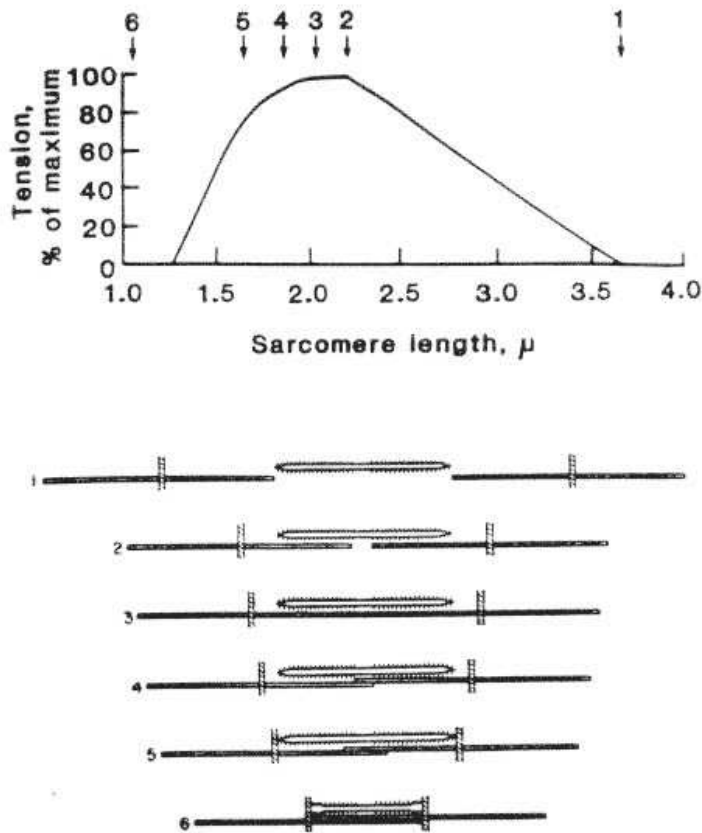


**Figure 1.11:** Upper figure: Active tension generated by isometric tetanization from different passive lengths of the sarcomere. Lower figure: relative positions of the thin filament (black line) and of the thick filament (white body) at the points indicated in the upper figure. From [19]

### Force-velocity experiments

The dynamical behavior of skeletal muscles is usually studied in a different type of experiments [1], [67], [66], [93] aimed at constructing the *force-velocity* curve. This curve relates the load imposed to a contracting muscle to the velocity at which the muscle shortens. It can be obtained, still point by point, within the experimental setup discussed before [5]: a muscle is tetanized at a fixed passive length, then the lever is released, while a constant load is applied. The length of the muscle is plotted against time (Fig. 1.12). As soon as tension is reduced, the muscle length decreases: this typically fast response shows the presence of an elastic element whose shortening takes place before a slower time scale dynamics of the Xb cycle gets activated. After this fast transient, the muscle starts to shorten at constant velocity. Repeating the experiment with different loads, one can construct the curve plotted in Fig. 1.13.

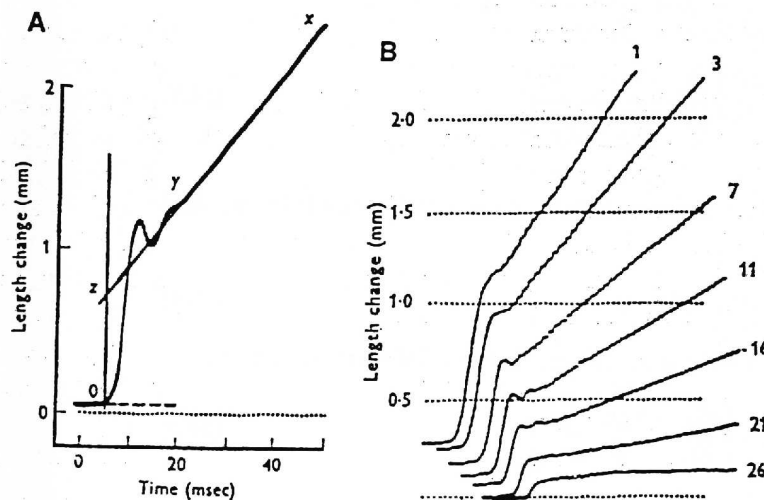


**Figure 1.12:** Shortening vs. time curves, for one load (A) and for different loads (B). Length change axes refers to shortening. The oscillating regime is due to the mechanical apparatus. From [5]

As we can see, there is a maximum velocity  $v_0$  that the muscle contraction can reach under free (unloaded) shortening; this velocity is independent of the length of the muscle in the passive state. There is also a load against which the muscle undergoes an isometric contraction at  $v = 0$ , this value is provided by the T-l curve. Applying a constant load greater than this value gives the force velocity curve in lengthening (or eccentric) portion. This latter range is much less known than the shortening range because of the higher dispersion of the experimental points. A general feature is that above a certain threshold, about  $1.8 F_{v=0}$ , the velocity goes

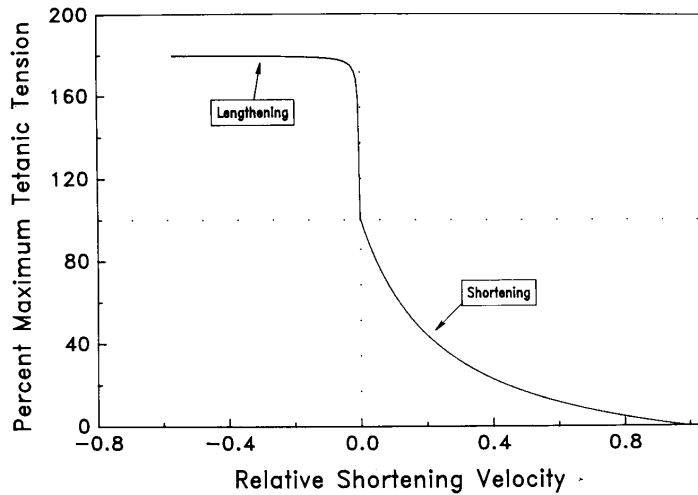


**Figure 1.13:** Force-velocity curve. In shortening the behavior can be described by an hyperbola which intersects the abscissa at the maximum unloaded speed (normalized) and the ordinate at the isometric tetanic tension. The slope has a discontinuity in the isometric point  $v = 0$ . A plateau is observed at high lengthening velocities. From [99]

to infinity. Moreover there is a discontinuity in the derivative of the  $F - v$  curve at the isometric point  $v = 0$ : in the eccentric portion the derivative of the curve is six time greater than in the shortening portion. In order to construct the force-velocity curve the steady shortening state must be reached, which happens in a typical time scale of tens of milliseconds [93]. The transient that precedes this state takes place in a typical time scale of some milliseconds and can be analyzed also in a slightly different mechanism, which we introduce in the next Section.

### Experiments on fast force recovery

There is a third type of experiments with which we shall mainly occupy ourselves in this Thesis. Imposing on a tetanized muscle a small increment, say negative, of length  $\delta$  generates a change in tension as shown in Fig. 1.14(a) (see [10] and references below). There is an instantaneous (hundreds of microseconds) decrease in tension to a new value called  $T_1$ , just as it would be if the thin and thick filaments were attached to each other by elastic springs. Almost immediately after this elastic stress drop, the tension rises and then for some time (milliseconds time scale) remains close to a plateau level (called  $T_2$ ) before finally recovering fully the value it had had before the length change (tens of milliseconds time scale). The changes in length in these experiments are very small, about 4-10 nm per half sarcomere, and the time scales involved for  $T_2$  recovery (milliseconds) are

such that it is realistic to assume that the number of attached Xbs remains fixed. Imposing different length increments, one obtains the relationship between the imposed length increments and the tensions  $T_1$  and  $T_2$  shown in Fig. 1.14(b).

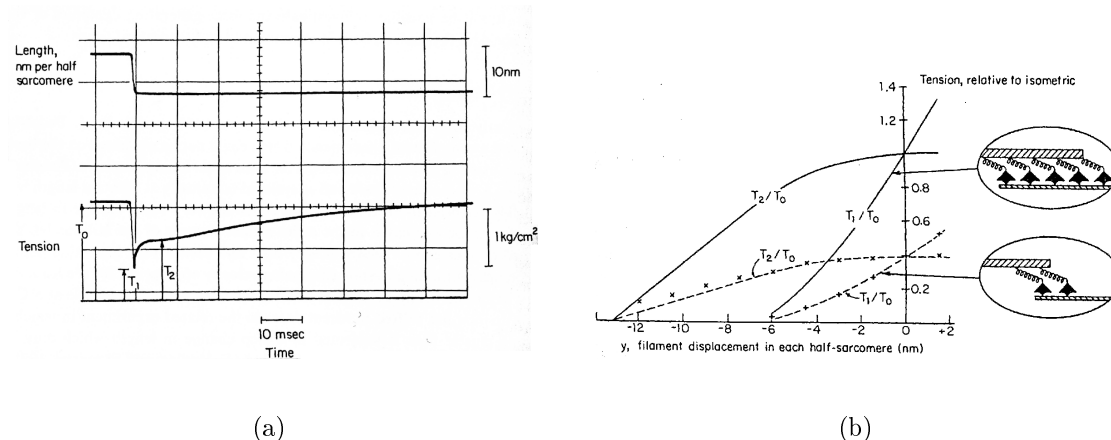


**Figure 1.14:** Fast recovery experiments. (a) A rapid small shortening is applied to the muscle (upper trace) and the resulting tension history is measured (lower trace). (b) The curves  $T_1$  and  $T_2$  vs. the imposed length increment for two different values of initial length, normalized with respect to the higher isometric tension  $T_0$ . Symbols are defined in the text. From [19]

An important understanding that derives from this experiment is that the values of  $T_1$  at various shortenings lay practically on a straight line. Another important result is that the rate of recovery of tension changes with the step imposed in a highly non linear manner (see Fig. 1.15). It tends to increase in an exponential way from positive length steps to higher negative steps.

The behavior exhibited by a muscle in this set of experiments is an important source of information about muscle mechanics, because at least the fast time response producing the functions  $T_1(\delta)$  and  $T_2(\delta)$  appears to be independent of the attachment-detachment process. Since the pioneering paper of Huxley and Simmons [10] these experiments have been repeated by many groups [14] [41] [43] [67].

The force-length, the force-velocity and the  $T_1$  and  $T_2$  vs. step-length curves are the most important experimental results that deal directly with the mechanisms of muscle contraction. We have given references to some recent experiments revealing for instance the history dependence in the mechanical response when muscle is stretched after tetanization [52]. Nevertheless, in what follows, we shall focus on the explanation of only the main experimental facts that are considered to be well established.

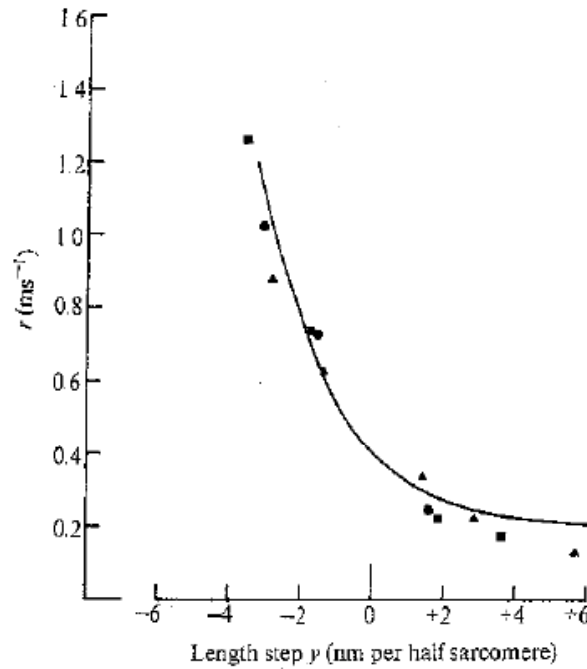


**Figure 1.15:** Rate constant  $r$  of quick tension recovery following a length increment of magnitude  $y$ . Estimated as  $\ln(3)/t_{1/3}$  where  $t_{1/3}$  is the time for recovery from  $T_1$  to  $(2T_2 + T_1)/3$ . From [10]

## 1.3 Mechanical modeling

In this Section we introduce several basic models aimed at explaining the mechanical behavior of muscles. They are: the Hill 1938 model, the Huxley 1957 model and the Huxley and Simmons 1971 model. These models represent the basis on which the majority of more recent models are based. Some of this more recent models are reviewed later in the Thesis.

### 1.3.1 Hill 1938 model

An analytical expression for the concentric part of the force-velocity curve was obtained by Hill in 1938 [1]. He used his own experiments focused on the energetics of muscle contraction against a constant force. First he observed that when the muscle is allowed to shorten, it liberates more energy (thermal and mechanical) than during isometric contraction. He divided the total energy rate  $E$  into three terms: the *maintenance heat rate* ( $A$ ) liberated by a muscle in isometric contraction, the *shortening heat rate* ( $H$ ), that is the total heat liberated during the contraction minus  $A$ , and the rate of work done ( $W$ ) equal to  $F \cdot v$  where  $F$  is the constant applied force and  $v$  is the velocity uniquely related to it, as we have seen in our

discussion of the force velocity curve. Hill wrote the energy balance in the form:

$$E = A + H + W \Rightarrow E - A = H + W. \quad (1.1)$$

By a very precise measurement of the first term  $A$  and of the total energy rate  $E$ , Hill observed empirically the relation:

$$H + W = b(F_0 - F). \quad (1.2)$$

In the right hand side of (1.2) we see the difference between the force  $F$  applied to the muscle and the maximal force  $F_0$  exerted by it in an isometric contraction when  $v = 0$ . Independently Hill observed that  $H$  depends linearly on the velocity of contraction,  $H = av$ . In this way we have:

$$H + W = av + Fv = b(F_0 - F). \quad (1.3)$$

By rearranging terms in (1.3), Hill obtained:

$$(a + F)(v + b) = b(a + F_0). \quad (1.4)$$

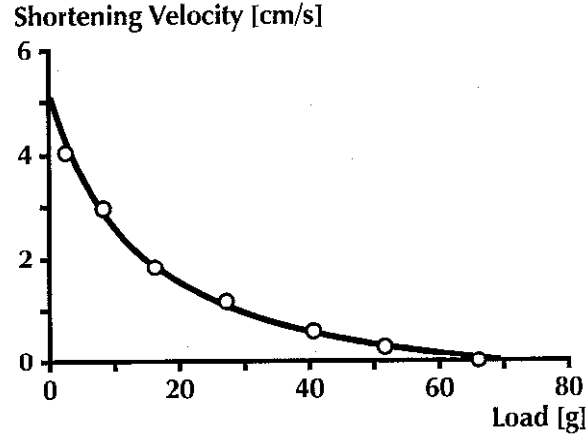


**Figure 1.16:** Force velocity relation. The circles represent the experimental observation (frog muscle), the line corresponds to the curve (1.4). From [52]

In the  $F-v$  space equation (1.4) describes a hyperbola with asymptotes  $-a$  and  $-b$  (see Fig. 1.16) [46]. It fits the experimental points very well (using appropriate values of  $a$  and  $b$ ) for a large variety of muscles. In the free contraction  $F = 0$ , the velocity becomes maximal  $v_{max}$  and it has been observed that for many type of muscles across species and temperatures [52]:

$$\frac{a}{F_0} = \frac{b}{v_{max}} = 0.25. \quad (1.5)$$



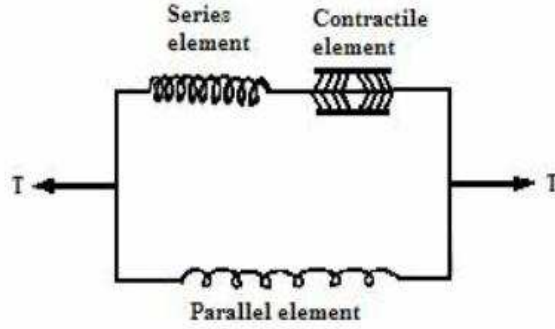


**Figure 1.17:** Hill 1938 model with a series of a passive spring and a contractile element, both in parallel with a second passive spring. From [19]

With these results, Hill proposed a model (see Fig. 1.17) where the active muscle is represented by an elastic element SE in series with a contractile element CE whose function is to link the applied force to the velocity, in a *black box* manner. Successively, to account for passive elasticity, an elastic element PE was added in parallel with the CE and the SE (Fig. 1.17).

In the passive state the CE can be stretched without any resistance. During the contraction, the total force generated by the system is  $F = k_p u + k_s(u - w)$ . Here  $k_s(u - w) = f_{CE}[w', l_0]$ ,  $k_s$  is the stiffness of the SE and  $k_p$  of the PE,  $u$  the total displacement,  $w$  the displacement of the CE,  $f_{CE}$  is the force in the contractile element which depends on the rate of change of the displacement  $w' = v$ . According to observations made by Hill, the CE exerts a force of the type

$$f_{CE} = \begin{cases} 0 & \dot{w} \leq -F(l_0)\frac{b}{a} \\ \frac{F(l_0)b + a\dot{w}}{-\dot{w} + b} & -F(l_0)\frac{b}{a} \leq \dot{w} \leq 0 \\ 1.5F(l_0) - 0.5\frac{F(l_0)b' - a'\dot{w}}{\dot{w} + b} & 0 \leq \dot{w} \leq F(l_0)\frac{b'}{a'} \\ 1.5F(l_0) & F(l_0)\frac{b'}{a'} \leq \dot{w} \end{cases}$$

that accounts also for the eccentric contraction. The isometric force  $F_0$  has a dependence on the initial length of the muscle  $l_0$ , as shown by the force length curve. The force is equal to zero for large negative values of  $w'$  (shortening), while it can be directly obtained from (1.4) for smaller contraction velocities. In the eccentric region,  $w' > 0$ , the values are taken to match the behavior observed experimentally (see Fig. 1.13).

The model leads to a differential equation that can be solved to obtain the

time dependence of the force for different given protocols of stretches. Thus if we introduce a parameter  $\beta$  to account for the concentration of calcium, as in the first and third part of Fig. 1.18, we obtain:

$$F(l_0, t) - k_p u = \beta f_{CE} \left[ \left( 1 + \frac{k_p}{k_s} \right) \dot{u} - \frac{F(l_0, t)}{k_s}, l_0 \right] \quad (1.6)$$

where  $0 < \beta < 1$  modulates the force in the contractile element  $f_{CE}$ . Two examples of loading programs are presented in Fig. 1.18. The elongation, equal for both experiments, is given by a ramp that increases the length of the muscle, maintains it constant and then shortens it to the initial state. The activation parameters were different. The experimental observations obtained for the given elongation history is shown in Fig. 1.19. The predictions of the model are in Fig. 1.20: the two responses are rather similar.

For 50 years Hill 1938 model dominated the field. In this period many ideas have been added to the model in order to accommodate newly discovered facts [52]. Originally quite simple the model became more and more complicated and lost its appeal; however the simplest version is still today used to simulate the mechanical behavior of muscles.

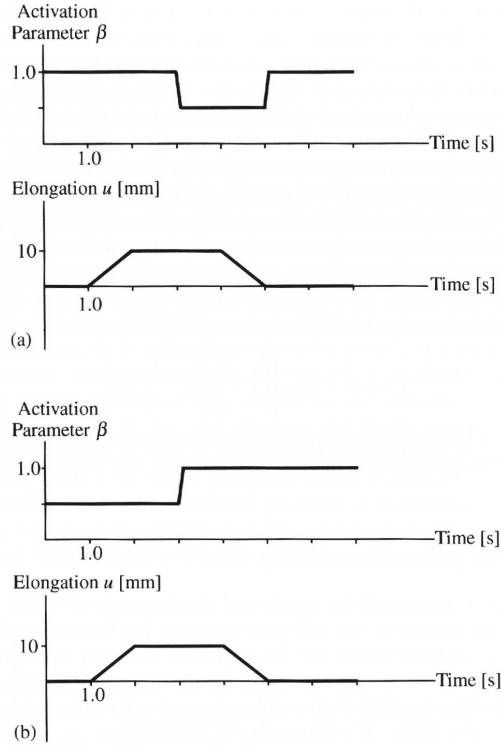


**Figure 1.18:** Two different experimental procedures for Hill's 1938 model. The response is illustrated in Fig. 1.20. From [52]

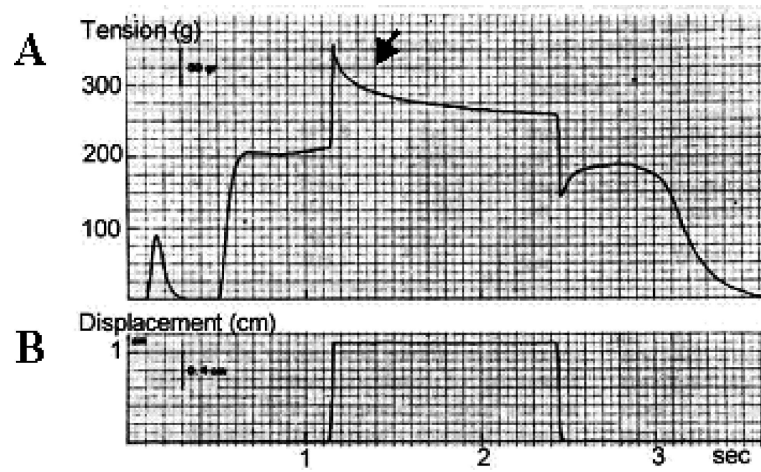


**Figure 1.19:** Experimental results for the elongation history shown in Fig. 1.18. From [13]

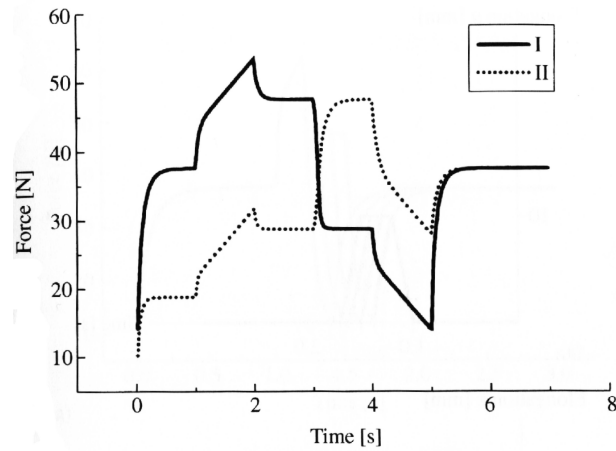


**Figure 4.10** Force response.

**Figure 1.20:** Response of the Hill's 1938 model for two different procedures I (upper part of Fig. 1.18) and II (bottom part). From [52]

The main reason for the search of different concepts in muscle modeling was the following: Hill's model does not provide insights into the mechanism of the production of force. Its *black box* nature is sufficient to give a good fit to the experimental curves, but it does not provide a tool for the understanding of the mechanisms that operates at the micro-scales which are not visible in the standard mechanical experiments.

### 1.3.2 Huxley 1957 model

Before 1954, most theories of muscle contraction were based on the idea that shortening and force production were the result of some kind of folding or coiling of large protein molecules. In 1954, HE Huxley and J Hansen [2] as well as AF Huxley and RM Niedergerke [3] demonstrated that muscle contraction is not associated with any change of length inside the microstructure. These authors postulated that the force is generated through the interaction of actin and myosin filaments.

Based on this understanding, AF Huxley developed in 1957 a new theory of muscle contraction [4]. The thick myosin filament is assumed to be fixed in space while the thin filament is assumed to slide parallel to myosin with constant velocity  $v$ . The movement is generated by a mechanical structure (that is now known to be the Xb) that can occupy different positions along the backbone of actin, and whose movement is limited by an elastic element (Fig. 1.21(a)). The model postulates that the number of active Xbs is constant and considers only the full activation of the muscle (tetanic response).

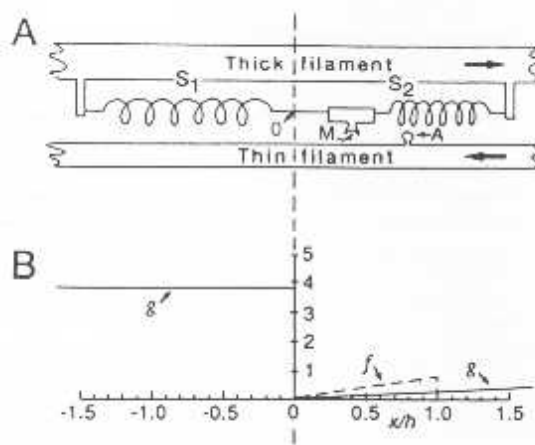


**Figure 1.21:** Huxley 1957 model. (a) The myosin head M is elastically coupled to the backbone. The interaction between the filaments can be established when M reach the attachment site A on the actin filament. (b) hypotheses on the attachment and detachment functions. From [4]

The structure in question can attach itself only to specific sites on the actin filament. When it is attached, then there is a force between actin and myosin, which depends on the position of Xb. To calculate the total force generated by the muscle one needs to know the total number of attached Xbs at each position  $x$  relative to the reference position of the structure, at every time  $t$ .

As a result of thermal fluctuations Xbs attach to the actin in a range of axial position. They exert a force if they reach the attached position where the elastic element is stretched; notice that a source of asymmetry is needed to generate a net force in one particular direction [4]. It is assumed that the probability  $f$  that a detached Xb can attach and the probability  $g$  that an attached Xb can detach, are functions of the variable  $x$ , as showed in Fig. 1.21(b). The attachment probability  $f(x)$  is assumed to be linear in  $x$  and is zero both beyond a maximum distance  $h$ , and for  $x < 0$  (the Xb can not attach to an active site when the elastic element is compressed). The detachment probability function  $g(x)$  is also linear for positive  $x$ , the probability increases even beyond  $h$ , and is large and constant for negative  $x$ . If  $n(x, t)$  is the fraction of the total population of attached Xbs whose distance from the active site is  $x$  at time  $t$ , then its time evolution can be found from a first order kinetic equation [4]:

$$\frac{\partial n(x, t)}{\partial t} - v \frac{\partial n(x, t)}{\partial x} = (1 - n(x, t))f(x) - n(x, t)g(x). \quad (1.7)$$

Huxley limited the analysis to steady state case, when the solution is constant in time, so the first term in the left is zero. The equation (1.7) allows the computation of  $n(x)$  at different  $v$ : at zero velocity  $n(x)$  reaches the constant value  $f/(f + g)$ . At higher values of velocity there are two factors that reduce its value: first there is less time for the Xbs to attach, second the Xbs are brought faster towards negative values of  $x$ . The predictions of the model (1.7) are illustrated in Fig. 1.22. The analytical solution is given by:

$$n(x, v) = \begin{cases} \frac{f_1}{f_1 + g_1} [1 - \exp(-\phi/v)] \exp(\frac{xg_2}{v}) & x \leq 0 \\ \frac{f_1}{f_1 + g_1} \left\{ 1 - \exp \left[ \left( \frac{x^2}{h^2} - 1 \right) \frac{\phi}{v} \right] \right\} & 0 \leq x \leq h \\ 0 & x \geq h \end{cases} \quad (1.8)$$

where

$$\phi = \frac{f_1 + g_1}{2} h.$$

Using this solution one can write an explicit expression for the force velocity dependence. Indeed, assume that each Xb acts like a linear spring with elastic modulus

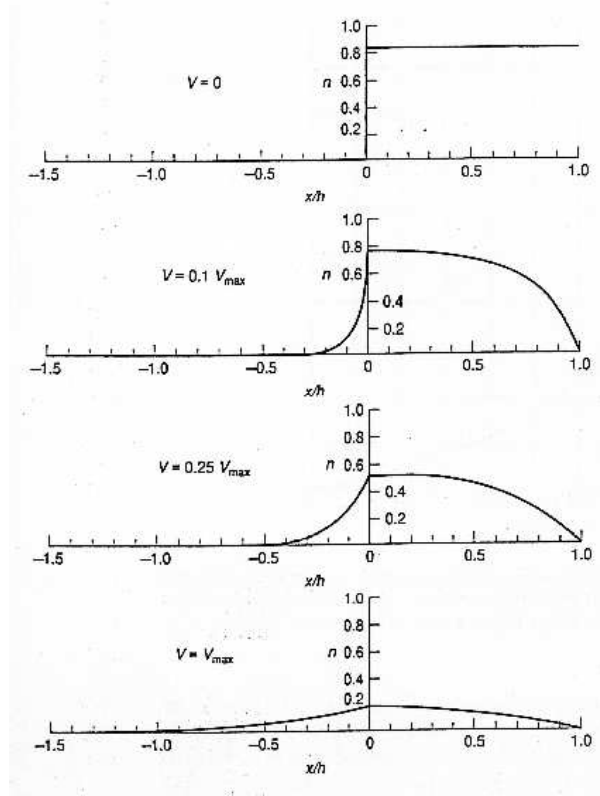


**Figure 1.22:** Relative distribution of Xbs at various velocities according to Huxley 1957 model. From [4]

$k$ , generating a force proportional to its displacement  $kx$ . Then the total tension can be written as:

$$T(v) = \rho \int_{-\infty}^{\infty} kxn(x, v)dx = \rho k \frac{f_1 + g_1}{2} \frac{h^2}{2} \left\{ 1 - \frac{v}{\phi} (1 - e^{-\phi/v}) \left[ 1 + \frac{1}{2} \left( \frac{f_1 + g_1}{g_2} \right) \frac{v}{\phi} \right] \right\} \quad (1.9)$$

where  $\rho$  stands for the density of Xbs per unit volume. Optimizing the parameters to fit the Hill's data, Huxley obtained an excellent fit as in Fig. 1.23. The isometric tension becomes  $C(f/(f + g))$ , where  $C$  depends on the number of Xbs present in the segment of muscle under consideration and on the other parameters of the model, for instance the elastic constant.

In addition to the concentric part of the force velocity curve the model predicts also other features of the muscle response, even if only qualitatively. For instance, the model predicts the eccentric part of the force velocity curve, showing both a different slope of the curve at the isometric point and an asymptotic behavior of the force at high velocities. Both values however are highly overestimated. The model also overestimates the rate of heat release during lengthening, however this problem, as pointed out in [4], can be eliminated through the assumption that

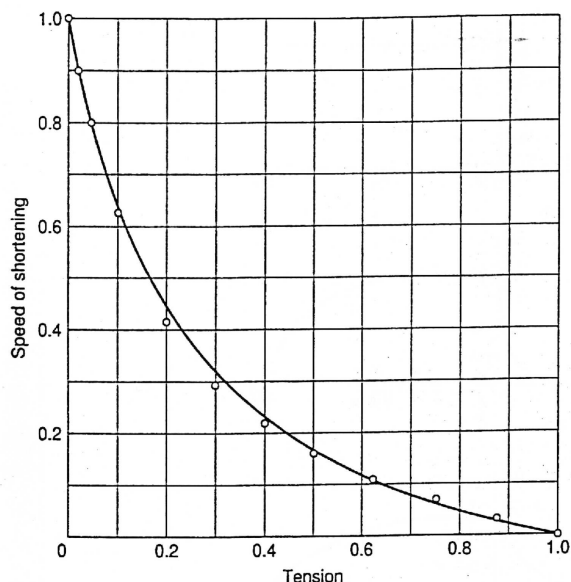


**Figure 1.23:** Huxley's prediction for the force velocity curve (line) and experimental data (points). From 1.23

during lengthening there is a mechanical breakdown of the Xbs, which detach without ATP release. Many more recent developments have been done along these lines, see for instance [21], [22], [27], [58], [64]. Overall, the Huxley 1957 model represents an improvement over the Hill 1938 model because it gives a precise mathematical description of the microscopic events behind the *black box* behavior postulated by Hill.

### 1.3.3 Huxley and Simmons 1971 model

The experimental response of muscles to rapid length increments, described in Section 1.2, cannot be easily explained by the 1957 Huxley's model. The pioneering experiments of this type, made in [10], have lead to the development of another important mathematical model: Huxley and Simmons' model of 1971. This model is not an expansion of the Huxley 1957 model, but is a quite different model which deals only with force generated by the attached Xbs. In particular it does not take into account the detachment process. What brings the necessity of a new model is the fact that the rapid recovery of force takes place in the milliseconds time scale, which is difficult to explain in the framework of the slower attachment-detachment process, related to the time scale of tenth of a second. The approach used by Huxley and Simmons, which we shall describe below, is the predominant idea even in the most recent models. This approach has recently received further

confirmation from the measurements of the axial motions of the myosin heads at angstrom resolution by X-ray interference technique [66].

The particular mechanism suggested by Huxley and Simmons for the structure of the Xbs is shown in Fig. 1.24. First of all, they assumed that the Xb contains a linear elastic spring linked to the head of the myosin. When attached to the actin filament, the head of the myosin can be in two states, and can switch from one state to another in a jump fashion. The ratio of the rates of jumps are controlled by the relative energy of the two states. The energy  $U_h$  of the head is a double well function of configuration coordinate  $x$ , it is plotted in Fig. 1.25 together with the parabolic energy of an elastic element. The switching can stretch or relax the elastic element, so we can refer to the states as a “low” force generating state and a “high” force generating state. The total potential energy  $U_{tot}$ , given by the sum of the potential energy of the elastic element  $U_s$  and the potential energy of the chemical state  $U_h$ , is plotted in Fig. 1.26.

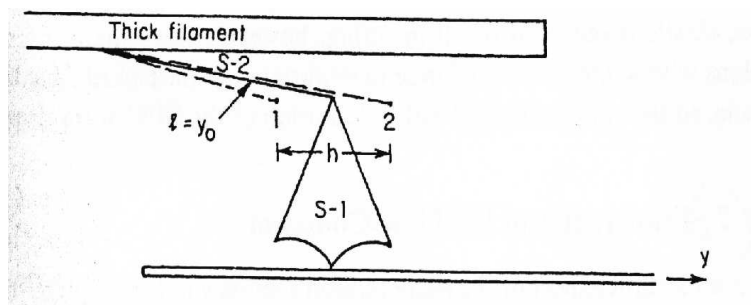


**Figure 1.24:** Huxley and Simmons 1971 model. The myosin head S-1 is linked to the thick filament through an elastic element S-2 and has two stable positions. From [19]

The model analyzes the distribution of Xbs in each of the energy well in order to obtain the total force generated by the muscle. Because in each half sarcomere the Xbs are arranged in parallel between an actin filament and the relative myosin filament, the total generated force is the sum of the forces generated by each Xb. It is assumed that when the muscle is isometrically tetanized, the two states have the same total energy.

Due to the linearity of the elastic element:

$$U_s = \frac{1}{2}Kl^2 = \frac{K}{2}\left(y_0 \pm \frac{h}{2} + y\right)^2 \quad (1.10)$$

where  $l$  is the stretch which can be written as the sum of  $y_0 \pm h/2$  (where  $y_0$  is a point located at equal distance from both wells,  $h$  is the distance between the wells) and  $y$ , the increment of length imposed on the muscle. We recall that  $U_h$  has



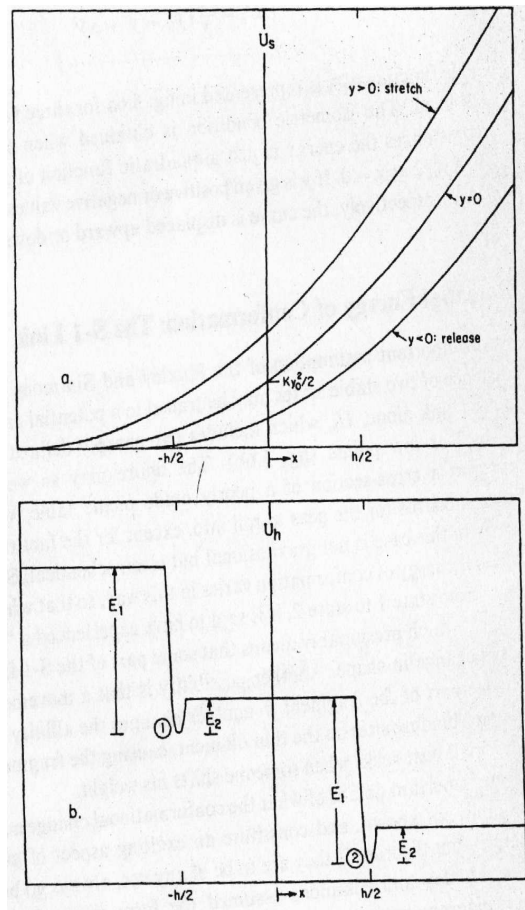


**Figure 1.25:** The potential energies in Huxley and Simmons 1971 model. (a) Elastic energy in isometric contraction ( $y = 0$ ), after stretch ( $y > 0$ ) and after release of the muscle ( $y < 0$ ). (b) Configurational energy of the head, two stable states 1 and 2 are present. From [19]

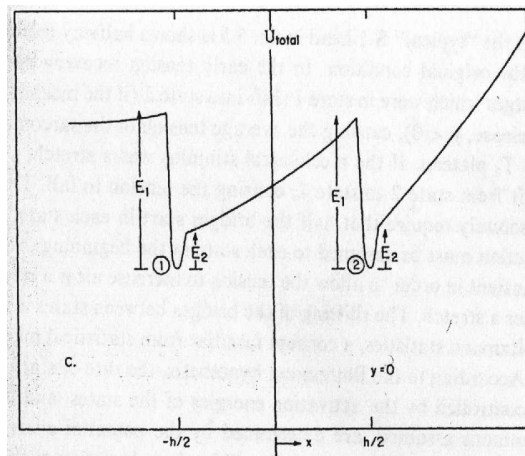


**Figure 1.26:** The total energy  $U_{tot} = U_h + U_s$  in Huxley and Simmons 1971 model as a function of the configuration of a Xb in the isometric case ( $y = 0$ ). From [19]

two potential energy wells, corresponding to the two states 1 and 2. The heights of the potential energy barriers  $E_1$  and  $E_2$  in Fig. 1.25, are assumed to be the same for both wells. Since in the state of isometric contraction the two minima of the total potential energy have the same level when  $y = 0$ , the total number of Xbs in the two configurations is the same. When a length increment is imposed,  $y \neq 0$ , there is a change in  $U_s$  (upper part of Fig. 1.25) and therefore in the total energy  $U_{tot} = U_s + U_h$ , as shown in Fig. 1.27.

Before giving the mathematical details, we describe briefly how the model works. The change in the total length  $y$  first affects the tension in the linear spring, and is therefore responsible for the  $T_1$  force observed in the experiments. After the step, the levels of the energy in the two minima become different, and a change in the total number of Xbs in each state is generated. This adjustment process follows kinetics postulated for the jump process, and takes place in a slower time scale than the time scale responsible for the  $T_1$  response. The final steady state is responsible for the value of force  $T_2$ .

To compute the forces  $T_1$  and  $T_2$ , we need to know the relative number of Xb,  $n_1$  and  $n_2$  in each well,  $n_1 + n_2 = 1$ . Under the assumption that the state of detailed balance is reached, the rate constants  $k_+$ , describing transitions from position 1 to position 2, and  $k_-$ , describing transition from 2 to 1, are related through:

$$\frac{k_+}{k_-} = C \exp \left[ \frac{(B_{12} - B_{21})}{k_B T} \right], \quad (1.11)$$

where  $T$  is the absolute temperature,  $k_B$  the Boltzmann constant,  $C$  a constant to be determined and  $B_{12}$  and  $B_{21}$  the activation energies for passing from state 1 to state 2 and vice versa. In Fig. 1.27, we also see that  $k_-$  is constant since  $B_{21}$  is a fixed quantity independent of the tension in the elastic element. Therefore we can write  $B_{21} = E_1$  and  $B_{12} = E_1 + \Delta U_{tot}$ , where  $\Delta U_{tot}$  is given by

$$\Delta U_{tot} = (E_2 - E_1) + \frac{1}{2}K \left[ \left( y_0 + y + \frac{h}{2} \right)^2 - \left( y_0 + y - \frac{h}{2} \right)^2 \right] = \quad (1.12)$$

$$Kh(y_0 + y) + (E_2 - E_1)$$

Since in isometric contraction the two states have the same energy:

$$\Delta U_{tot} |_{y=0} = 0 \Rightarrow -Kh y_0 = (E_2 - E_1), \quad (1.13)$$

the relation (1.11) becomes:

$$\frac{k_+}{k_-} = \exp \left( \frac{-Kh y}{k_B T} \right). \quad (1.14)$$

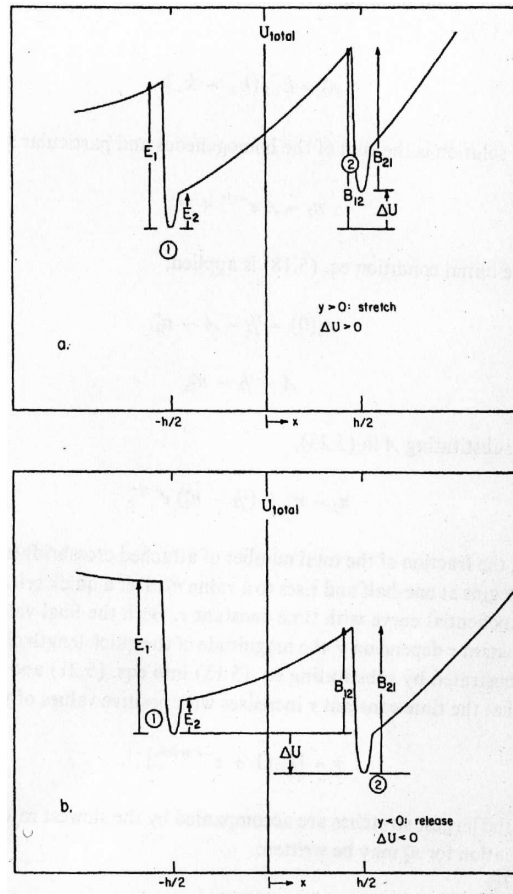


**Figure 1.27:** The different behavior of Huxley and Simmons 1971 model: total energy in stretch ( $y > 0$ , where the configuration 1 is energetically preferred) and in release ( $y < 0$ , where the configuration 2 is energetically preferred) modes. From [10]

The differential equation describing the number of Xbs in the state 2 during transients is:

$$\frac{dn_2(t)}{dt} = k_+ n_1(t) - k_- n_2(t) = -(k_+ + k_-) n_2(t) + k_+. \quad (1.15)$$

Due to the hypothesis of equal energies of the states during isometric contraction we obtain that  $n_2(0) = 1/2$ . We can now solve (1.15) and write:

$$n_2(t) = n_2^\infty + (0.5 - n_2^\infty) \exp[-t(k_+ + k_-)] \quad (1.16)$$

where:

$$n_2^\infty = \frac{k_+}{k_+ + k_-}.$$

One can see that the fraction of Xbs in state 2, starts at one-half and rises to the value  $n_2^\infty$  exponentially with rate  $k_+ + k_-$ . To compute the steady state tension, only the ratio of the rates constants (1.14) is needed. The transient of tension can

be written as:

$$\begin{aligned} T(y, t) &= n_1(t)K \left( y_0 + y - \frac{h}{2} \right) + n_2(t)K \left( y_0 + y + \frac{h}{2} \right) \\ &= K[y_0 + y + (n_2(t) - 0.5)h]. \end{aligned}$$

The characteristic values of tension predicted by this model are  $T_1(y) = T(y, 0) = K(y_0 + y)$  and  $T_2(y) = T(y, \infty) = K[y - 0 + y + (n_2^\infty - 0.5)h]$ .

In order to compute these functions, one needs the elastic constant  $K$ . As it was not known at that time, Huxley and Simmons used the data on the rate of recovery  $r(y)$  (Fig. 1.15). They obtained a fit:

$$r(y) = r_0(1 + e^{-\alpha y})$$

with  $r_0 = 0.2 \text{ ms}^{-1}$  and  $\alpha = 0.5 \text{ nm}^{-1}$ . As we have seen, the same curve can be predicted from the model:

$$r(y) = k_+ + k_- = k_-(1 + e^{-Kh/k_B T y}). \quad (1.17)$$

Huxley and Simmons used this formula to obtain the values of both  $k_-$  and  $Kh = \alpha k_B T$ . Then they could compute the equilibrium force:

$$T_2(y) = \frac{\alpha k_B T}{h} \left( y_0 + y - \frac{h}{2} \tanh \frac{\alpha y}{2} \right) \quad (1.18)$$

which is shown in Fig. 1.28. The resulting curves  $T_1(y)$  and  $T_2(y)$  exhibit the same

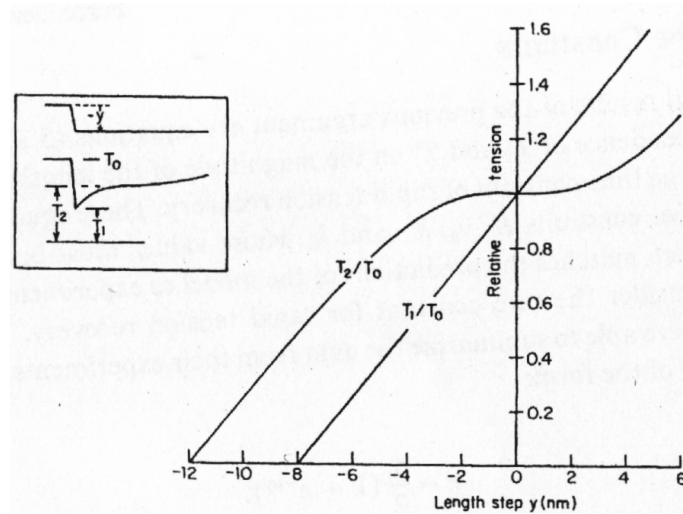


**Figure 1.28:** Prediction of the Huxley and Simmons 1971 model. From [10]

general features as the experimental curves shown in Fig. 1.14(b). The resulting

value for the stiffness becomes  $K \simeq 0.2 \text{ pN/nm}$ , however a value of one order of magnitude greater [35] [38] [36] [80] [92] was proven later. We shall come back on the importance of this value extensively in Chapter 2, however we mention here that the more realistic value  $K = 2 \text{ pN/nm}$  affects dramatically the prediction of the model. First, we see immediately from (1.17) that the  $r(\delta)$  dependence will be highly overestimated, because it depends on  $K$  exponentially. Second, the  $T_2(\delta)$  curve is more inflected with the higher value of the parameter  $K$ , thus it shows a negative slope at  $\delta = 0$  which is in contrast with the experimental result.

There were several recent attempts to improve the quantitative predictions of the theory [18] [43] [48] [59] [73] [96], however nothing fundamentally new has been added to the model. The most attractive feature of the Huxley and Simmons 1971 model is that it attempts to link biochemistry to mechanics. Not only in the more recent models this link was not improved, but, on the contrary, it was almost lost. In the next Chapter we shall give a brief review of some of these models and propose a new one where the link is improved and further quantified.

# Chapter 2

## Power Stroke

### 2.1 Introduction

The special character of the mechanical response of skeletal muscles described in Chapter 1, allows one to classify them as *active* materials, because they can adapt to external stimuli. The advances in technology are often linked to the development of such materials that can provide active functioning, like sensing and actuation. In the past, active response was achieved through organizing elements, with passive response at the micro-level, into complex structures with multiple equilibrium states. However modern technologies require that such mechanisms function at micrometer and even nanometer scales, so traditional solutions become unacceptable, and there is a demand for materials where the complex behavior is realized already at the molecular level. An example of such materials is given by shape memory alloys, where the multi-stability of the system at the molecular level is due to phase transformation which does not require diffusion, and can be induced by stress, temperature or electro-magnetic field. The analysis and modeling of such active materials has reached a level of precision that one would want to achieve in the description of skeletal muscles, given some similarity of the behavior of the two types of systems. The similarity is based on the idea of multi-stability of the microscopic elements of the system.

As we have seen in Chapter 1 the model of Huxley and Simmons (HS71) can describe fast response of skeletal muscles assuming the presence of bi-stable elements with double well energy. In this model the energy landscape is degenerate because the wells are infinitely narrow. This leads to a description in terms of a jump process, which requires the knowledge of chemical rate constants. In the HS71 model, the definition of the energy for the states *between* the minima is

not needed: the Xb switches between the states instead of continuously moving between them. This makes the precise analytical comparison of this model with mechanical models of shape memory alloys difficult. Despite these apparent distinctions, the main ingredients in both types of models are similar which leaves a possibility to link the Huxley and Simmons model to the continuum theory of martensitic transformations in active materials.

We recall that, the main difference between the multi-stable and conventional linear elastic elements is that the energy of the former is non-convex. As it was shown in the pioneering work of Ericksen [11], this non convexity is of fundamental importance for the interpretation of the behavior experimentally exhibited by shape memory alloys, which is related to the presence of multiple stable micro-configurations. Ericksen considered the behavior of a continuum 1-D problem for a material with a non-convex energy under slowly varying load showing that a mathematical model based on bi-stability can explain hysteresis. After that, a thorough study of the problem was performed, in particular a precise description of the microscopic events was obtained by discretizing the 1-D continuum problem and viewing it as a chain of bi-stable elements [11], [16], [29], [62].

In this Chapter we reformulate the original Huxley and Simmons 1971 model in this precise mathematical framework. We show that this reformulation can produce a picture which avoids some drawbacks of the original HS71 model. We start by briefly describing the way in which other recent models have dealt with these drawbacks. Then we introduce our new mechanical model aimed first at modeling the power stroke only and present a quantitative analysis of this model including the comparison with experimental curves.

## 2.2 Recent Models

Already in 1978 [17] it was realized that the Huxley and Simmons 1971 model can not predict correct time scale of tension relaxation, if a realistic value of the stiffness of the elastic element is used. The quantitative resolution of this and other problems of the HS71 model, already mentioned in Section 1.3.3, will be given later in this Chapter, while now we would like to briefly review the main approaches used to circumvent these problems. In particular we show that the way chosen by the authors of the recent models to deal with the drawbacks of the HS71 model, leads to almost complete loss of coupling between the two aspects of the problem: mechanical and biochemical. The goal of these models was not only to resolve the

uncorrect time scale predicted by the HS71, however here we shall focus only on this aspect of the problem.

### Eisenberg and Hill model

An early modification of the original HS71 model was proposed in 1978 by Eisenberg and Hill [17]. The model was extended in 1980 on a more quantitative basis [18]. It is based on the observation that by assuming two very narrow energy wells, Huxley and Simmons made implicitly the hypothesis that the transition between the states takes place only after a Xb had collected the total amount of energy needed to overcome the barrier.

Eisenberg and Hill proposed to make the wells wider in order to allow the transition to start at lower energy. They also linked the force generated by the Xb in each state with the first derivative of the free energy, instead of the stretch of the elastic element, that has now been formally eliminated. Without the elastic element, the coordinate  $x$  of the Xb is controlled by the imposed length of the sarcomere, actually the coordinate  $x$  has become a measure of axial position of the particular actin site at which the Xb is attached. The origin  $x = 0$  was chosen in such a way that the Xb in the pre-power stroke state is in its resting position. At every value of  $x$  the Xbs can be in four different states whose free energies were postulated to have an  $x$ -dependence shown in Fig. 2.1. Here  $AM^\ddagger DD$  is the actin-myosin complex in the pre-power stroke state and  $AMD$  is the actin-myosin complex in the post-power stroke state, (phases 2 and 3 in Fig. 1.5). Similarly  $M^{**}D$  and  $M^\ddagger D$  are two detached states, the refractory state and the non-refractory state, respectively (phases 4 and 1 in Fig. 1.5). The different angles of the lever arm in the two attached states are reflected by the different positions of the minima in the relative energies. The change of state is assumed to be a jump process, allowing the Xb to follow the entire Xb-cycle as shown by the arrows in Fig. 2.1.

In defining the rate constants of the individual jump processes, Eisenberg and Hill used the hypothesis of detailed balance which imposes one condition for the ratio of each pair of rate constants. In the most general form this condition can be written as:

$$k_{jm}(x)/k_{mj}(x) = \exp\left(\frac{G_j(x) - G_m(x)}{k_B T}\right) \quad (2.1)$$

The elastic element is present in this model through the  $x$ -dependence of the energies  $G_i(x)$ . What is important to note is that nothing in this setting is said about



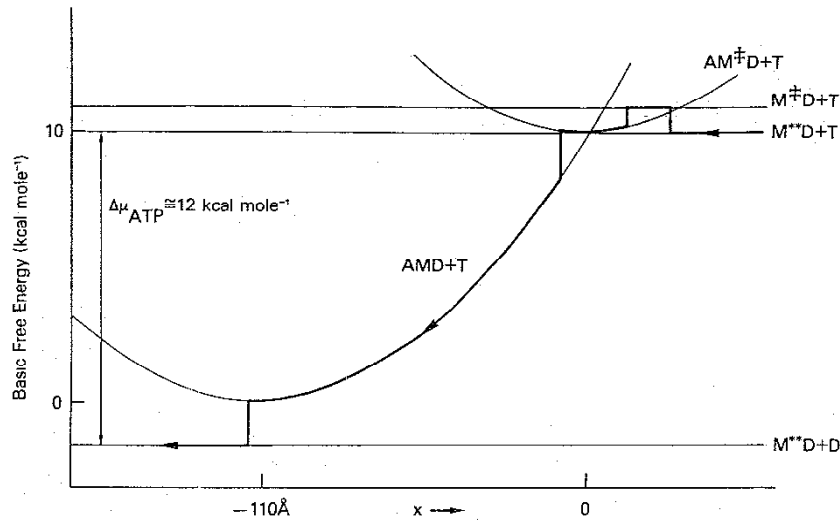


**Figure 2.1:** Free energies for two attached states and two detached states in the Eisenberg and Hill model. The state  $M^{**}D + D$  is shifted with respect to  $M^{**}D + T$  by an amount of energy given by the ATP hydrolyzation. The arrows show a possible Xb cycle. From [17]

the shape of the energy barrier *between* the states at a given  $x$ . That leaves for each transition one of the rate constants  $k_{ij}$  as a free parameter. In the Huxley and Simmons 1971 model the dependencies of both rate constants on the step  $x$  were completely defined by the shape of the total energy. Instead in Eisenberg and Hill model these constants retain some freedom (used in Fig. 2.2), since only one condition, equations (2.1), is imposed. To our knowledge, the EH78 model was first to abandon the mechanical transparency of the HS71 model even though some features of the HS71 model were preserved. In a sense the biochemical interpretation of dynamics has overcome the mechanical basis of the HS71 model. The freedom left by the EH78 model was used to choose the  $k(x)$  dependencies phenomenologically in order to fit the experimental observations almost perfectly.

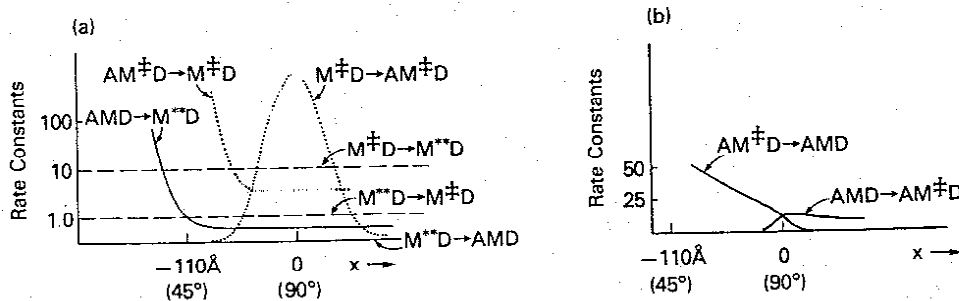


**Figure 2.2:** Hypothesis on the constants for the EH78 model. From [17]

### Piazzesi and Lombardi model

The model of Piazzesi and Lombardi developed in 1995 [43], deals with the entire cycle of the Xb, and is able to predict both the force velocity curve and the behavior of the muscle subjected to rapid increments in the total length as well as the flux of energy and the efficiency of the contraction. There are two detached states, D1 and D2, and three attached states, A1, A2 and A3 in Fig. 2.3 A. Moreover there are two distinct paths in which Xbs can split ATP to generate force. Two active states, A1 and A2, are common for the two paths, as shown in Fig. 2.3(a). From A2 there is a *long* path, which contains a second active state A3 before the detachment of the head D1. This path can compete with the *short* one, where the head detaches immediately after A2 into D2. The long path generates larger force but it has a lower reaction rate, about 20/second. The reaction rate for the short path is about 100/second. The corresponding rate constants satisfy the detailed balance equation (2.1). As in the Eisenberg and Hill model, the functions  $k_{jm}(x)$  and  $k_{mj}(x)$  depend on the imposed step, and this dependence can be chosen to fit the experimental data. The specific choice of the authors is shown in Fig. 2.3(b-e). The system of differential equations governing the distribution of the number of Xbs in various states,  $a_1$ ,  $a_2$ ,  $a_3$  and  $d_1$ ,  $d_2$ , generalizes the equation proposed by Huxley in 1957. Without going in all details we just mention that the system consists of the equations of the type:

$$\begin{aligned} \frac{\partial a_1(x, t)}{\partial t} = & k_1(x)d_1(x) + k_{-2}(x)a_2(x) + k_6(x)d_2(x) - \\ & (k_{-1}(x) + k_2(x) + k_{-6}(x))a_1(x, t) - v \frac{\partial a_1(x, t)}{\partial x} \end{aligned} \quad (2.2)$$

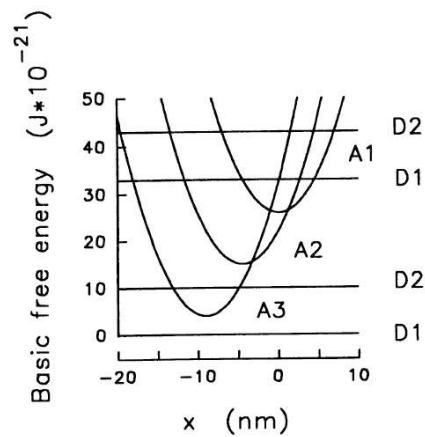
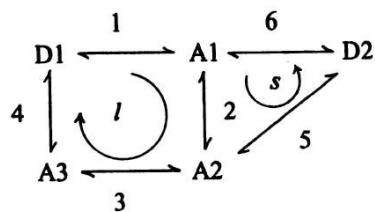
for each of the five possible states and is solved numerically.

Small length increments bring the Xb in the region where the short cycle is favored and, being rapid, it can explain the behavior observed experimentally at moderate shortening velocities. For higher length step the long cycle is preferred, leading to the possibility to fit the 11 *nm* power stroke. In this way the model is able to predict both *force-velocity* curve (computed considering the constant curvature of the free energy  $G_i(x)$  as in the EH78 model and shown in Fig. 2.4(a)) and “step in length” type experiments (Fig. 2.4(b)).

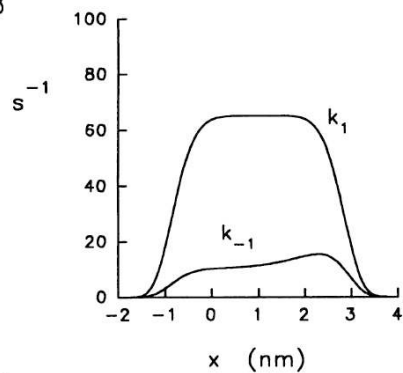
### Huxley and Tideswell model

Huxley and Tideswell proposed in 1996 a model which was explicitly developed to overcome the drawbacks of the original HS71 model [48]. This new model is based

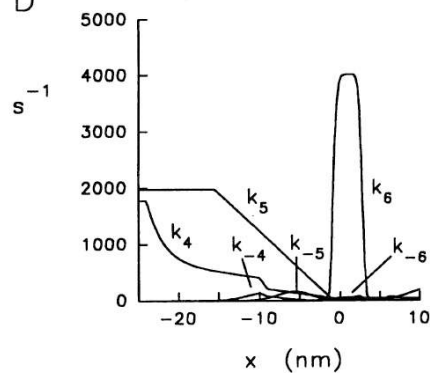
A



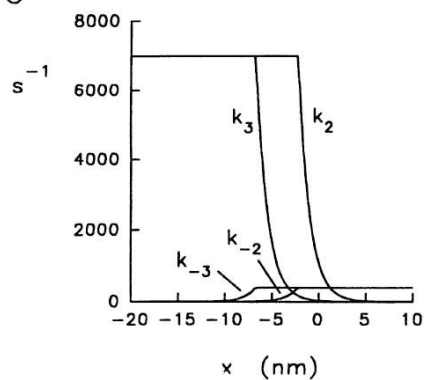
B



D



C



E

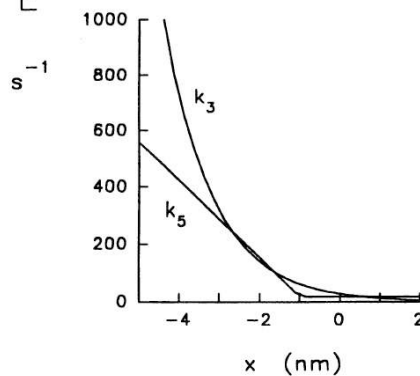


**Figure 2.3:** General scheme and rate constants for the Piazzesi and Lombardi model. A: (Left) Scheme of the PL95 model, A=attached, D=detached. (Right) Basic free energy of each state. B-E: Functions expressing the dependence of the rate constants on  $x$ . From [43]

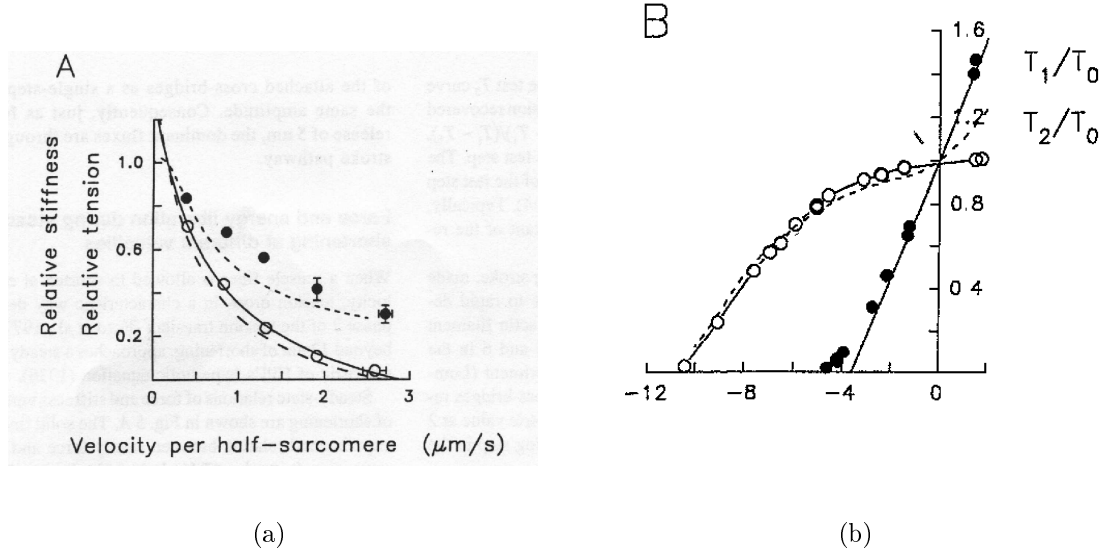


**Figure 2.4:** Comparison between simulations (lines) and experimental results (points) of the PL95 model. (a) Force-velocity curve. (b) Modeling of T1 and T2. From [43]

on the same idea as the HS71 model, however new features were added. Among them, the most important for our approach are that, first, three attached states  $A_1$ ,  $A_2$ , and  $A_3$  are considered, with two constant power strokes between them of  $5.4 \text{ nm}$  and  $4.5 \text{ nm}$ . Second, the rate coefficients for each of the four possible reactions  $A_1 \rightarrow A_2$ ,  $A_2 \rightarrow A_1$ ,  $A_2 \rightarrow A_3$ , and  $A_3 \rightarrow A_2$ , are given by the expression

$$A/(1 + \exp[B(x - C)])$$

where  $x$  is related to the stretch of the elastic element and  $A$ ,  $B$  and  $C$  are different for each transition, so that 12 parameter have to be specified. Observe that as in the previous models, there is an  $x$ -dependence of the rate constants. In order to respect the condition (2.1) some constraints are added, however, no explicit shape of the free energy was prescribed, which means weaker mechanochemical coupling than in HS71 model. Finally, to mimic the incommensurability of the spacing of the active sites on the actin filament with respect to the spacing of the heads along the myosin filament, five populations of Xbs were equally spaced relative to the active sites. The authors observed that with the last assumption the tension  $T_2(\delta)$  ends up averaged over the range of spacing of the active sites (see also Section 2.7.2). Under the assumption that this spacing is equal to  $5.5 \text{ nm}$ , the diameter of the actin monomer, the computed  $T_2(\delta)$  curve contains a flat region around  $\delta = 0$  even with  $K = 2 \text{ pN/nm}$ . This solves the first incoherence of the HS71 model (Section 1.3.3).

Despite this success the single stroke size of  $5.5 \text{ nm}$  was too small to justify other experimental observations, and for this reason the authors were forced to add a second active state in the model. The behavior of the model was analyzed numerically, and a rather good fit of the experimental data regarding the rate of recovery was reached. The results are shown in Fig. 2.5, together with unsatisfactory predictions of HS71 model. This solved even the second problem of the original 1971 model.

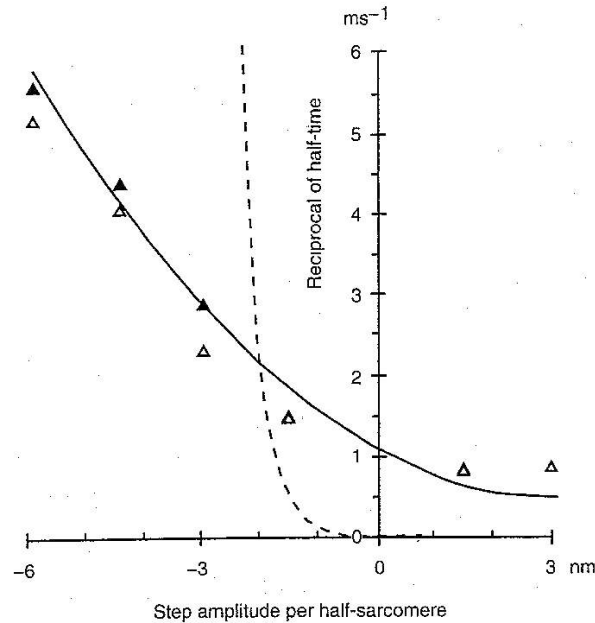


**Figure 2.5:** Reciprocal of half-time of tension recovery vs. imposed length step. Solid line: experimental values from [14]. Points: Huxley and Tideswell model prediction. Dotted line: Huxley and Simmons model prediction

We emphasize, however, that the price of a larger number of possible states was a larger number of free parameters, and that the precise relation between the rate constants and the shape of the total energy used in HS71 model has been partially lost. We should mention though that, the hypothesis that the rate constants vary exponentially with the work done in stretching of the elastic element, was preserved (see [39]). As the authors have observed, this represents a difference between their model and the Eisenberg and Hill model, where the authors used, as a typical reaction rate, “*an arbitrary function adjusted to obtain agreement*”.

### Smith et al. model

As a last example, we discuss a very recent and the most complete model of muscle contraction, published in August 2008 [96]. This model is able to reproduce almost

all known experimental observations related to isotonic and isometric contractions of skeletal muscles. In fact it is the first attempt to produce a comprehensive theory, and its key features are shown in Fig. 2.6. The entire Xb cycle is modeled including an intermediate state between the pre-power stroke state (5 in the figure) and the post-power stroke state (8 in the figure). Two paths are available to complete the cycle (through 6 or 7 in the figure). Again, the rate “constants” for the attachment and detachment processes depend on the pre-power stroke strain  $x$  in a phenomenological semi-empirical way. Although the model is able to predict a large number of fine features observed in experiments, its mechanochemical coupling is rather poor and is surely weaker than in the Huxley and Simmons model. Here resides the interest of a new model with a detailed mechanochemical coupling.

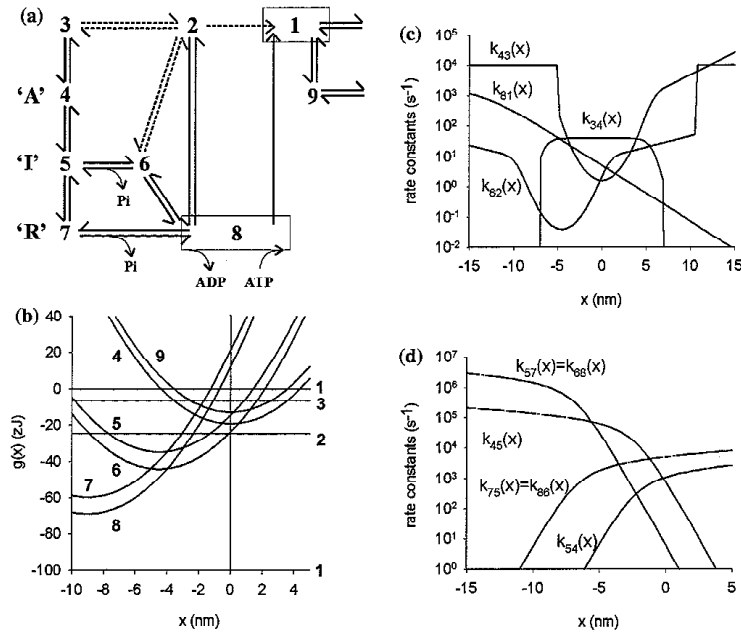


**Figure 2.6:** Key features of the model of Smith et al. : a) The cycle of the Xb, b) Free energy of the states c) e d) dependencies of the rate constants on the pre-power stroke position. From [96]

## Conclusions

In the rest of this Chapter we shall explore how far a rather simple mechanical model of the attached Xbs can describe the experimental facts without invoking *ad hoc* assumptions concerning the stretch dependence of the constants of chemical reactions. Instead, we turn to the micro-scale and introduce explicitly a feature which is very important for the mechanics of muscles but is usually dealt with only implicitly in the bio-chemical framework: the mechanical interaction of the

system with random forces (Brownian motion). The presence of a thermal reservoir allows each mechanical unit to explore the whole energy landscape much beyond the global or local minima. Our approach is not completely new in mechanics, for instance, it has been used for the description of rubber type elasticity of shape memory alloys in [81]. The introduction of random forces influences dramatically the behavior of the multi-stable mechanical system and because of this, our model is interesting also from a purely mechanical point of view.

## 2.3 New model of a power stroke

The half-sarcomere is formed by a number of identical Xb arranged in parallel between the two filaments. If all Xbs are synchronized, we may assume that the force producing behavior of a half-sarcomere is simply that of each Xb times the total number of attached Xbs. We represent each single Xb as a linear spring in series with a bi-stable contractile element (Fig: 2.7). The energy of the contractile element will be non convex with two asymmetric energy wells. As an extension of the Huxley and Simmons 1971 model, here we include into the model the elasticity inside each well which allows a direct use of the mechanical theory of bi-stable elastic elements. The limiting case of the new model, when the elastic moduli tend infinity, should produce the same results as the Huxley and Simmons model. A

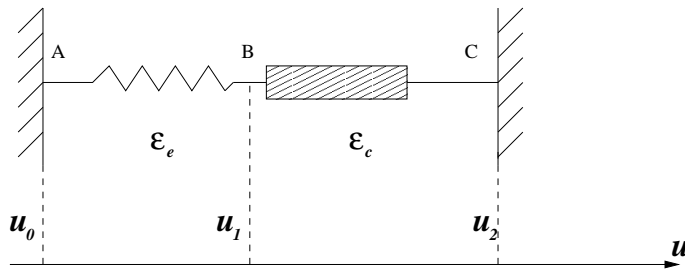


**Figure 2.7:** The model of an attached Xb: an elastic element in series with a bi-stable element

point that has to be made clear is that at this stage of the analysis, and throughout all this Chapter, the attachment-detachment will be suppressed, and only the Xbs that are attached to the actin filament will be considered.

### 2.3.1 General shape of the energy

The fact that the energy of the *contractile element* has two wells means that the Xb can be in two states which we shall be calling “long” and “short” phase. The

force generated by a single Xb will depend on the phase: at a given total length, the long phase will keep the elastic element in the low stress state while the short phase will necessarily generate higher force (Fig. 2.8). Because all the Xbs are supposed to be equal and act in parallel, the total force generated by the half sarcomere will depend on the relative number of Xbs in each of the two states.

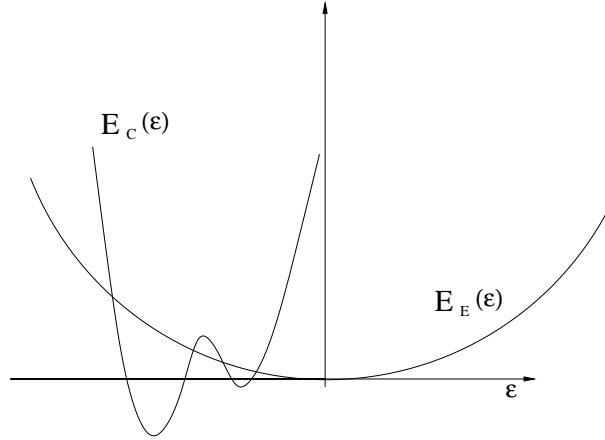


**Figure 2.8:** Elastic and contractile energy

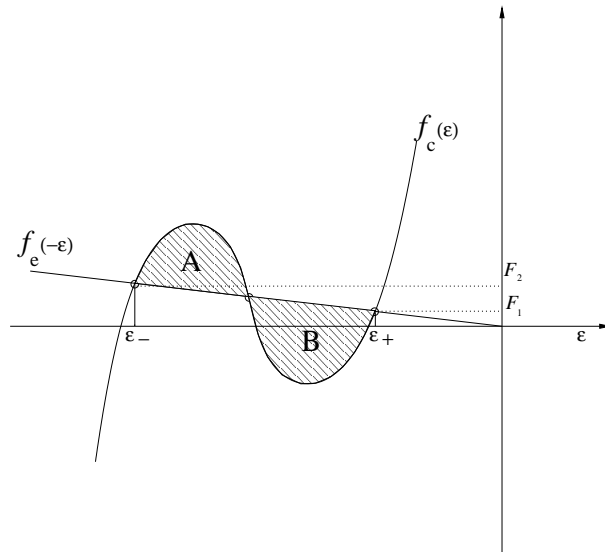


**Figure 2.9:** First derivatives of the elastic and of the contractile energies and the graphical solution of the equilibrium equations

Let us introduce  $u_0, u_1, u_2$ , the displacements of the points A, B, and C in Fig. 2.7:  $u_0$  can be assumed equal to zero and  $u_2$  is equal to the imposed total displacement. The symbols with an apex zero refer to the reference state. We can define  $\varepsilon_e = (u_1 - u_1^0)$  and  $\varepsilon_c = (u_2 - u_1 - u_2^0 + u_1^0)$  the elongations of the elastic element and of the contractile element, respectively. The total energy of a Xb will



be the sum of the energy of the contractile element and the energy of the elastic element:

$$E_T(\varepsilon_c, \varepsilon_e) = E_c(\varepsilon_c) + E_e(\varepsilon_e). \quad (2.3)$$

The total elongation of the half sarcomere is  $\delta = (u_2 - u_2^0)$ . In the experiments that we shall be considering  $\delta$  will be the control parameter (length clamp device). In this situation, the strains of the two elements are related:

$$\varepsilon_e + \varepsilon_c = \delta. \quad (2.4)$$

Consider first an isometric experiment where the total length of the muscle  $u_2^0$  is imposed in the passive state and then maintained constant after tetanization ( $\delta = 0$ ). The strain of the spring will be equal to the inverse of the strain of the contractile element  $\varepsilon_e = -\varepsilon_c = -x$ . In this case the total energy  $E_T(x) = E_c(x) + E_e(-x)$  will be a function of  $x$  only, which can then be viewed as the only internal coordinate. The minima of the total energy can be computed from the equilibrium equation

$$\frac{dE_T(x)}{dx} = 0,$$

which can be rewritten as:

$$f_c(x) = f_e(-x). \quad (2.5)$$

Here  $f = \partial E / \partial x$  is the tension which must be equal in both elements. We can illustrate the solution of the equilibrium equation (2.5) graphically. Due to the linearity of the elastic element, we can represent the solution as an intersection of a curve  $f_c(x)$  and a straight line shown in Fig. 2.9, where the points  $\varepsilon_-$  and  $\varepsilon_+$  correspond to the two minima of the total energy  $E_T(x)$ . As in the Huxley and Simmons model, we assume that in the state of isometric contraction the minima have the same value of the total energy. This condition can be written as:

$$\Delta E_{tot} = (E_c(\varepsilon_-) + E_e(-\varepsilon_-)) - (E_c(\varepsilon_+) + E_e(-\varepsilon_+)) = 0$$

or

$$\int_{\varepsilon_+}^{\varepsilon_-} f_c dx = \int_{\varepsilon_+}^{\varepsilon_-} f_e dx. \quad (2.6)$$

We therefore obtained the “equal area construction” saying that at  $\delta = 0$  the two signed areas  $A$  and  $B$ , in figure 2.9, must be equal.

Consider how solution of equilibrium equation (2.5) is changing in response to the increment  $\delta$ . In this case  $\varepsilon_e + \varepsilon_c = \delta$  and we can write  $\varepsilon_c = x$ ,  $\varepsilon_e = -x + \delta$ . The  $f_e$  in Fig. 2.9 line will be shifted by  $\delta$  in such a way that it will intersect the

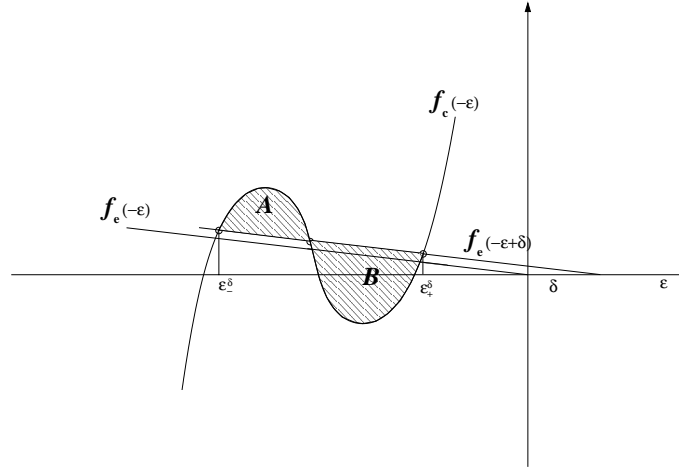


**Figure 2.10:** The effect of a length step  $\delta$  on the elastic energy:  $f_e$  is shifted on the left changing the ratio of the areas  $A$  and  $B$

abscissa in  $x = +\delta$ ; we recall that  $\delta$  in Fig. 2.10, is chosen to be positive. The area  $B$  become larger than the area  $A$ , and so the energy in the local minimum  $\varepsilon_-(\delta)$  is larger than the one in the global minimum  $\varepsilon_+(\delta)$ .

### 2.3.2 Double parabolic approximation

To proceed analytically consider a special case when the energy of the contractile element can be represented by two parabolas with a minima in the points  $0$  and  $a$ . In these points the energy has the values  $0$  and  $d$ , respectively (see Fig. 2.11(a)). The highly simplified double parabolic approximation for the energy is not necessary, but will be convenient for two reasons. First the bi-quadratic form of the energy will allow some analytical transparency of the results. Second, the piecewise quadratic approximation will give us certain advantages in the quantitative fitting of the experimental data, because it makes possible an analytical treatment of the model. We remark that the general predictions of the model do not depend on the exact shape of the energy.

At this point it is not so important to specify the value of  $x$  where the intersection between the two parabola takes place: we temporally assume that the transition from one parabola to the other takes place exactly between the minima, say at  $a/2$ . If the parabolas have different moduli, this will bring a discontinuity into the energy function, however at this stage it does not create any problem. In fact, a third parabola will be added to reproduce the maximum of the energy, however for the moment we can stay with bi-quadratic approximation. We can

write:

$$E_c(x) = \begin{cases} \frac{1}{2}k_2(x-a)^2 + d & x \leq \frac{a}{2} \\ \frac{1}{2}k_1(x)^2 & x > \frac{a}{2} \end{cases} \quad (2.7)$$

where the curvatures of the wells  $k_1$  and  $k_2$  can be different. The elastic energy of the series spring with stiffness  $K$  is:

$$E_e(x, \delta) = \frac{1}{2}K(x - l_0 - \delta)^2. \quad (2.8)$$

As we see, its relaxed state is reached in  $x = l_0$ .

We can now compute the location of the minima of the total energy at  $\delta = 0$ :

$$\begin{cases} a_1 = \frac{Kl_0}{k_1 + K} \\ a_2 = \frac{Kl_0 + k_2a}{k_2 + K} \end{cases} \quad (2.9)$$

Graphically, Fig. 2.9 now becomes Fig. 2.11(b). Obviously, the values of the

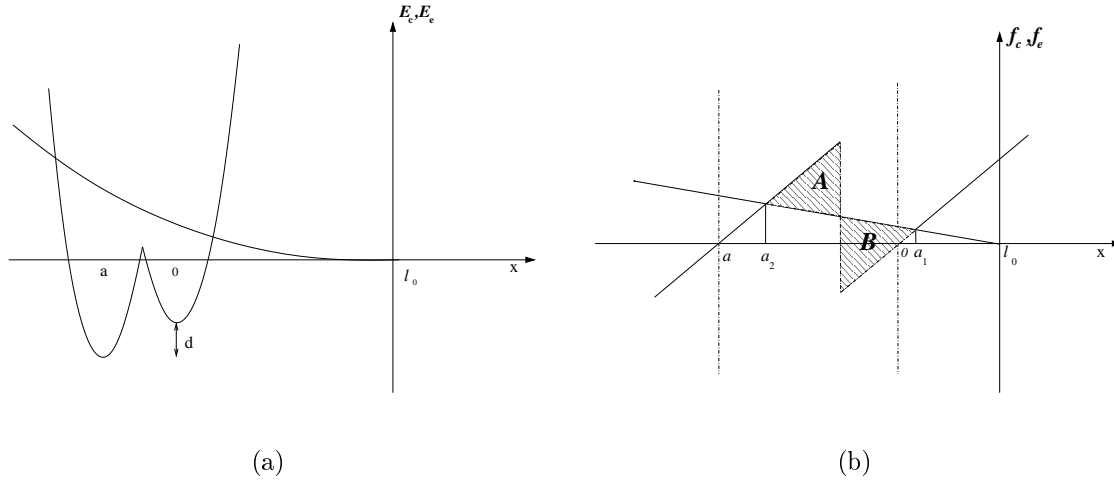


**Figure 2.11:** Schematic description of the energy and tension for the double parabola approximation. (a) Bi-quadratic energy. (b) Minima in the bi-linear case

parameters have to be such that  $a_2 < a/2 < a_1$ . We can see that in the Huxley and Simmons model, where  $k_2 = k_1 = \infty$ , the minima are  $a$  and  $0$ , no matter what  $K$  and  $\delta$  are, as in Fig. 2.11(b). The condition (2.6) ensuring the same value of energy in the minima, gives the expression for  $d$ :

$$d = -\frac{1}{2} \frac{k_2 K}{k_2 + K} (l_0 - a)^2 + \frac{1}{2} \frac{k_1 K}{k_1 + K} l_0^2. \quad (2.10)$$

## 2.4 Deterministic case: global minimum

As we have already explained the contraction of muscles takes place in a Brownian domain where the temperature  $T \neq 0$  and effect of the stochastic external force is not negligible. However to understand the working of the model it is instructive to start with the deterministic case when  $T = 0$ . In this case we assume that the observed value of  $x$  must correspond to the global minimum of the total energy. When  $\delta = 0$  the energies of the two states corresponding to the global minimum are equal and the two states (2.9) are equally probable.

### 2.4.1 One cross-bridge

We begin by analyzing the behavior of a single Xb assuming that an increment is imposed on its length. In the mechanical experiments described in Chapter 1, the observable is typically the force generated at one end of the specimen. Since, in the proposed model, the force at equilibrium is equal in both contractile and elastic elements, it can be computed as the product of the elastic constant  $K$  and the strain of the elastic element. The force generated by the single Xb can have either the “low” value:

$$F_1 = -K(a_1 - l_0), \quad (2.11)$$

or the “high” value:

$$F_2 = -K(a_2 - l_0), \quad (2.12)$$

as we show in Fig. 2.9. Those values can be linked to the low force generating state (pre-power stroke) and the high force generating state (post-power stroke) expected in the Xb cycle (see Chapter 1).

When a change in length is imposed ( $\delta \neq 0$ ), the minima of the total energy shift to:

$$\begin{cases} a_1 = \frac{K(l_0 + \delta)}{k_1 + K} \\ a_2 = \frac{K(l_0 + \delta) + k_2 a}{k_2 + K}. \end{cases} \quad (2.13)$$

When the elastic moduli in the wells are infinite as in the HS71 model, the minima remain always at  $a_1 = 0$  and  $a_2 = a$  no matter what the value of  $\delta$  is. In this case we can see graphically from Fig. 2.12, that the difference of the energy in the two minima after the step  $\delta$  is  $E_T(a_1) - E_T(a_2) = K\delta a$ . Since we have chosen  $a < 0$ , we see that  $\delta < 0$  shift the global minimum into the second well.

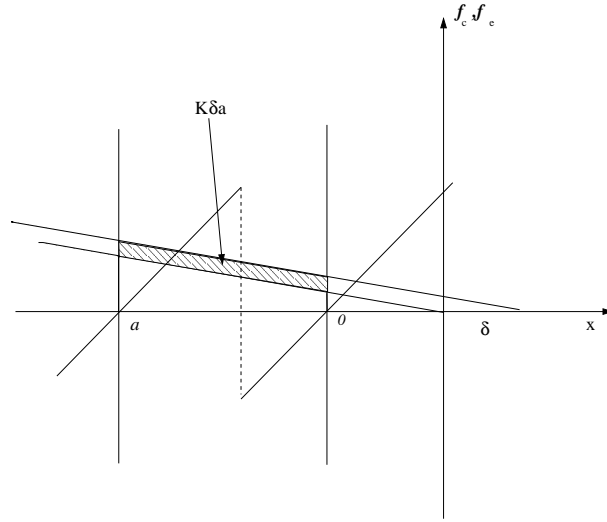


**Figure 2.12:** Lengthening in the piecewise linear case. The vertical lines represent the Huxley and Simmons model. In this last case, the dashed area is equivalent to  $E_T(0) - E_T(a)$

In our case, by inserting (2.13) into  $E_T$ , we obtain:

$$E_T(a_1) = \frac{1}{2} \frac{k_1 K}{k_1 + K} (l_0 + \delta)^2, \quad (2.14)$$

and, analogously,

$$E_T(a_2) = \frac{1}{2} \frac{k_2 K}{k_2 + K} (l_0 + \delta - a)^2 + d. \quad (2.15)$$

Comparing the two values we can write:

$$\Delta E_T(\delta) = E_T(a_1) - E_T(a_2) = \quad (2.16)$$

$$\frac{1}{2} \delta^2 \left( \frac{k_1 K}{k_1 + K} - \frac{k_2 K}{k_2 + K} \right) + \frac{k_1 K}{k_1 + K} \delta l_0 - \frac{k_2 K}{k_2 + K} \delta (l_0 - a).$$

In the  $\Delta E_T - \delta$  plane, equation (2.16) gives a parabola and as expected  $\Delta E_T(0) = 0$ . Using the numerical values obtained later in the Thesis by means of quantitative fitting of the experimental curves (Tab. 2.1), we obtain  $k_1 > k_2$  and

$$\frac{d\Delta E_T(\delta)}{d\delta} \Big|_{\delta=0} = \left( \frac{k_1 K}{k_1 + K} - \frac{k_2 K}{k_2 + K} \right) l_0 + \frac{k_2 K}{k_2 + K} a < 0. \quad (2.17)$$

Therefore the sign of  $E_T(a_1) - E_T(a_2)$  is the opposite of the sign of  $\delta$  and, exactly as in the HS71 model, shortening makes preferable the global minimum in  $a_2$  while stretching makes preferable the minimum in  $a_1$ . When  $\delta \neq 0$  the tension generated by the Xb is given by the formulas:

$$\begin{cases} F_1(\delta) = -K \left( \frac{K(l_0 + \delta)}{k_1 + K} - l_0 - \delta \right) & \delta > 0 \\ F_2(\delta) = -K \left( \frac{K(l_0 + \delta) + k_2 a}{k_2 + K} - l_0 - \delta \right) & \delta < 0. \end{cases} \quad (2.18)$$

These equations take into account both the displacement of the reference position for the elastic element and the shift of the minima. The tension given by (2.18) is the zero-temperature analog of the tension  $T_2$  generated by the muscle in the steady state after an increment in length. We obtain that, since  $\Delta E_T(0) = 0$ , the definitions of the tetanized tension  $T_0$  and of tension  $T_1$ , are ambiguous in the case of one Xb. Therefore we need to take into account many Xb.

### 2.4.2 $N$ cross-bridges

In order to establish a complete relation to experiments, we consider now one half-sarcomere composed by  $N_{Xb}$  heads, that work in parallel, as in Fig. 2.13. If one

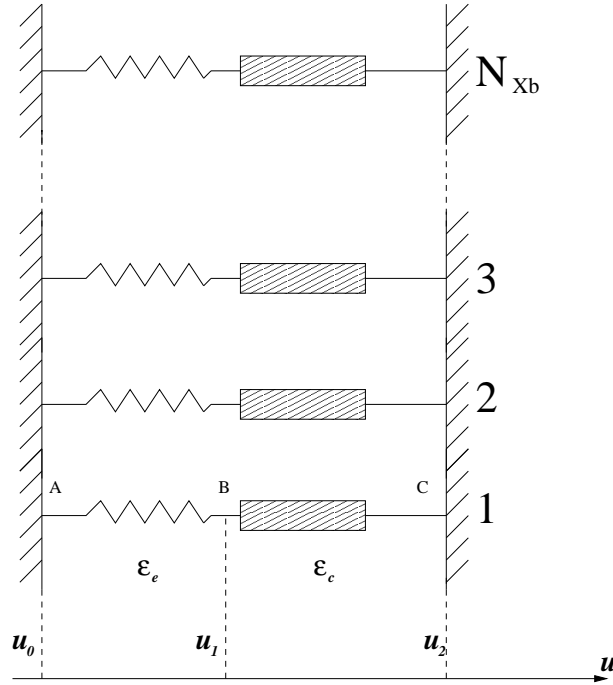


**Figure 2.13:** The model of  $N_{Xb}$  attached Xbs

knows the number of attached Xbs in each state, one can compute the total force as:

$$T(\delta) = N_1(\delta)F_1(\delta) + N_2(\delta)F_2(\delta) = N_{Xb}(n_1(\delta)F_1(\delta) + n_2(\delta)F_2(\delta)) \quad (2.19)$$

where  $N_1(\delta)$  and  $N_2(\delta)$  are the number of elements in each state, and

$$\begin{cases} n_1^\delta = N_1(\delta)/N_{Xb} \\ n_2^\delta = N_2(\delta)/N_{Xb} \end{cases} \quad (2.20)$$

are the corresponding fractions.

When the muscle is tetanized at  $\delta = 0$  the two minima are at the same level and the position of each Xb depends on the initial conditions imposed on the system. The isometric tension can be computed as:

$$T_0 = -KN_{Xb}(n_1^0 a_1(0) + n_2^0 a_2(0) - l_0) \quad (2.21)$$

where the apex zero, in the relative number of Xbs in each minima  $n_i$ , indicates that they are calculated at  $\delta = 0$ .

The function  $T_1(\delta)$  describes the instantaneous response. One may think that  $T_1(\delta)$  can be computed supposing that during the fast response the elastic element undergoes deformation  $\delta$  while the myosin head, embedded in a viscous fluid, maintains its position occupied before the step. In this case, if we call  $x_1$  and  $x_2$  the positions of the Xbs just after the step, we should impose  $x_1 = a_1(0)$  and  $x_2 = a_2(0)$ , obtaining

$$T_1(\delta) = -KN_{Xb}(n_1^0 x_1 + n_2^0 x_2 - l_0 - \delta), \quad (2.22)$$

or, in other word:

$$T_1(\delta) = T_0 + KN_{Xb}\delta. \quad (2.23)$$

Actually, this may not be the case in the real experiments. Indeed a realistic value of the drag coefficient  $\eta$  for the myosin head, is  $60 - 90 \text{ pN ns/nm}$ , and the magnitude of the elastic constant is about  $1 \text{ pN/nm}$ . Therefore the characteristic time for the head to relax inside its well after the imposed step is of the order of  $0.1 \mu\text{s}$  [64], while the time scale of the observations is typically one order of magnitude larger [67]. In view of this estimates, a more realistic approximation for  $T_1$  is given by the formula:

$$T_1(\delta) = -KN_{Xb}(n_1^0 a_1(\delta) + n_2^0 a_2(\delta) - l_0) + KN_{Xb}\delta. \quad (2.24)$$

We see that its value is determined not only by the change in length of the elastic element, but also by the shift of the minima of the total energy.

The relative change in tension  $T_1/T_0$  can now be written as:

$$\frac{T_1(\delta)}{T_0} = 1 + \left( \frac{n_1^0 k_1 / (k_1 + K) + n_2^0 k_2 / (k_2 + K)}{n_1^0 l_0 k_1 / (k_1 + K) + n_2^0 k_2 (l_0 - a) / (k_2 + K)} \right) \delta. \quad (2.25)$$

The tension  $T_1$  does not represent equilibrium. Suppose now that instead the system follows global minimum of the total energy. When even a small increment is imposed, a global minimum becomes non-degenerate, and all the Xbs jump into one energy well. Because of (2.16), the relative numbers of Xbs in the two minima

will switch from  $n_1^0, n_2^0$  to  $n_1 = 0, n_2 = 1$  (or  $n_1 = 1, n_2 = 0$ ) and the final tension  $T_2$  will be:

$$T_2(\delta) = -KN_{Xb}(a_2(\delta) - l_0 - \delta) \quad (2.26)$$

for  $\delta < 0$ , and:

$$T_2(\delta) = -KN_{Xb}(a_1(\delta) - l_0 - \delta) \quad (2.27)$$

for  $\delta > 0$ . The relative tension in the equilibrium state is:

$$\frac{T_2(\delta)}{T_0} = \frac{(k_2/(k_2 + K))\delta + k_2(l_0 - a)/(k_2 + K)}{n_1^0 l_0 k_1/(k_1 + K) + n_2^0 k_2(l_0 - a)/(k_2 + K)} \quad (2.28)$$

for  $\delta < 0$ , and:

$$\frac{T_2(\delta)}{T_0} = \frac{k_1(l_0 + \delta)/(k_1 + K)}{n_1^0 l_0 k_1/(k_1 + K) + n_2^0 k_2(l_0 - a)/(k_2 + K)} \quad (2.29)$$

for  $\delta > 0$ .

The predicted curves  $T_1/T_0$  and  $T_2/T_0$  vs.  $\delta$  are linear in  $\delta$ , with different slopes if  $k_1 \neq k_2$ . Figure 2.14 represents typical shape of tension-displacement for representative values of the parameters. The system after the instantaneous elastic response  $T_1$  reaches the steady state tension  $T_2$ . The bold line, which represents the global minimum in the steady state, shows a jump which is not observed in experiments. To avoid this pathological behavior and to produce a smoother curve, we can follow the idea of the Huxley and Simmons and introduce a probability distribution of the Xbs in different phases. This approach is pertinent since the thermal diffusion is important at such scales.

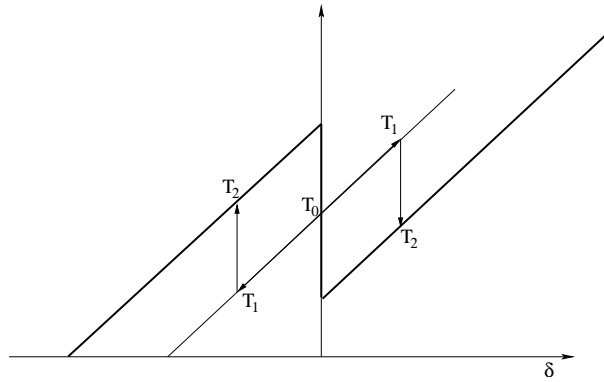


**Figure 2.14:**  $T_2/T_0$  and  $T_1/T_0$  vs.  $\delta$  curves (arbitrary units) in the elastic-global minimum response ( $k_1 = k_2$ )



## 2.5 Stochastic case: $N$ cross-bridges at finite temperature

In order to make the curve  $T_2(\delta)$  smoother, Huxley and Simmons made an additional assumption regarding the distribution of the Xbs. Instead of considering the deterministic behavior in which all the Xbs are in the global minimum, they assumed that their positions can be described by steady state solution of the equation describing a stochastic process. This assumption comes from the understanding that thermal fluctuations can not be neglected at this scale. Taking thermal motion into consideration is crucial for cellular mechanics because the chemical reactions that drive biological processes have the energetic barriers that are only a little higher than the thermal energy, given by the Boltzmann constant times the temperature  $k_B T$  [64]. Since thermal forces are randomly directed and uncorrelated, the resulting motion can be modeled by diffusion. Huxley and Simmons approached the problem from the point of view of a jump process, because the curvatures of their energy wells were infinite and as a result their diffusion process was degenerate. It is worthwhile to note that every jump process can be viewed as an approximation of the diffusion process, even if the contrary is not always true (see Section A.7). In their description, Huxley and Simmons have defined the kinetic constants of reaction that describes the passage between the two states for each Xb. In both, the jump process and the diffusion process, the rate constants must satisfy the detailed balance condition in order to correctly describe the equilibrium state.

The condition of detailed balance can be understood in terms of a canonical distribution (see Section A.6.2):

$$p_s = \frac{e^{-E/k_B T}}{\sum e^{-E/k_B T}}. \quad (2.30)$$

The subscript  $s$  indicates equilibrium steady state and  $E$  is the energy of the state.

Suppose that the relative number of Xb in two sharp wells,  $n_1$  and  $n_2$ , satisfy the canonical distribution. Then:

$$\frac{n_2}{n_1} = e^{-\frac{E_2 - E_1}{k_B T}}. \quad (2.31)$$

The same expression for the steady state probability distribution is derived in Section A.6.1 in a different way; we briefly sketch here the derivation because it introduces the diffusion process which will be important from now on. The

equation of motion of a particle, subjected to a potential  $E_T(x)$  and to a thermal noise can be written in the over-dumped case as (Langevin equation):

$$\eta \dot{x}(t) + E'_T(x) = \Gamma(t), \quad (2.32)$$

where  $\Gamma(t)$  is a white noise. Since this is a stochastic differential equation, the path of the particle is different in every realization, even under the same initial conditions. A way to study the behavior of such a system is through the associated differential equation for the evolution of probability distribution  $p(x, t)$ . This function gives the probability to find a particle in the position  $x$  at time  $t$ . The equation for  $p(x, t)$  is called Fokker-Plank equation (see Section A.5). For the case (2.32) it can be written as:

$$\frac{\partial p(x, t)}{\partial t} + \frac{\partial S(x, t)}{\partial x} = 0 \quad (2.33)$$

where we introduced the probability current  $S$ :

$$S = -\frac{E'_T(x)}{\eta} p - \frac{k_B T}{\eta} \frac{\partial p}{\partial x} \quad (2.34)$$

The steady state is defined as  $S = \text{const}$ , and if  $E_T(x)$  goes to infinity for  $|x| \rightarrow \infty$ , the boundary conditions require that  $S = 0$ . In this case, equation (2.33) has the following solution:

$$p_s(x, \delta) = \frac{e^{-E_T(x, \delta)/k_B T}}{\int_{-\infty}^{\infty} e^{-E_T(x, \delta)/k_B T} dx} = \mathcal{N}^{-1} e^{-E_T(x, \delta)/k_B T} \quad (2.35)$$

where  $\mathcal{N}$  is a normalization constant and the dependence on  $\delta$  was inserted to remind that in our case the total energy depends on the step length imposed. We can now define the quantities  $n_1$  and  $n_2$  as:

$$\begin{aligned} n_1^\delta &= \int_{a/2}^{\infty} p_s(x, \delta) dx \\ n_2^\delta &= \int_{-\infty}^{a/2} p_s(x, \delta) dx. \end{aligned} \quad (2.36)$$

Here we use the same symbols as in (2.20) because even with these new definitions  $N_{Xb} n_1^\delta$  represents the mean number of Xbs in the first state. We recover (2.30) from (2.35) in the limit when the curvatures of the energy wells go to infinity. Then  $p_s(x, t)$  approaches two  $\delta$ -functions and the rate  $n_2^\delta/n_1^\delta$  assumes the value as in equation (2.31).

The rest of this Chapter is devoted to the discussion of our attempts to use the framework in order to fix the drawbacks of the Huxley and Simmons 1971

model. In particular we show how the introduction of the elasticities of the wells, integrated into the diffusion theory, allow one to avoid some of the problems while preserving strong relation between the mechanical and the chemical aspect of the phenomenon.

## 2.6 Variable power stroke size

The Huxley and Simmons 1971 model suggests the mechanism behind the fast recovery of tension, and forms the basis on which almost all more recent models have been constructed. Despite this fact, the model has some difficulties with the reproduction of the experimental behavior. As discussed in Section 1.3.3, almost all of these problems come from the value used for the stiffness of the elastic element  $K$ . It was not known at the time of the creation of the Huxley and Simmons' model and they used an indirectly estimated value of  $K = 0.2 \text{ pN/nm}$ . Unfortunately, according to modern data [36], [55] the value of  $K$  should be at least one order of magnitude higher. In what follows we shall show how the introduction of the elasticity effects into the structure of the energy wells removes the inconsistency. The question was first raised by Eisenberg and Hill in the 1978, however, to the author's knowledge, this is the first time that the incoherency is resolved in a quantitative way with the use of elasticity in the wells.

After the pioneering work of Huxley and Simmons, the experiments showing fast recovery of tension, were redone several times (see e.g. [14], [20], [41]). Moreover, one can say that it is still today the major protocol used in the study of the mechanics of muscles (e.g. [43], [67]). The reason is that this type of experiments give important information about the behavior of the Xbs in the attached state. The new, more precise experiments become possible because of the huge improvement in the measurement and loading techniques. For example, Huxley and Simmons imposed an increment of the total length because they “*were not able to impose a change in tension sharply enough to distinguish the component of length change that is truly synchronous with the tension change from that which lags behind the tension change*”. Today, such tension change can be made in tens of microseconds and the time resolution can be of 1 microsecond [67]. It was shown that in the length clamp experiments [43] and in the load clamp experiments [67], the corresponding tension vs. deformation curves are almost identical, as shown in Fig. 2.15. What became clear with the improvement of the techniques, is that the curve  $T_2(\delta)$  at large values of  $\delta$  has a slope different from the one of the curve

$T_1(\delta)$  (see Fig. 2.15): the former is more shallow than the latter.

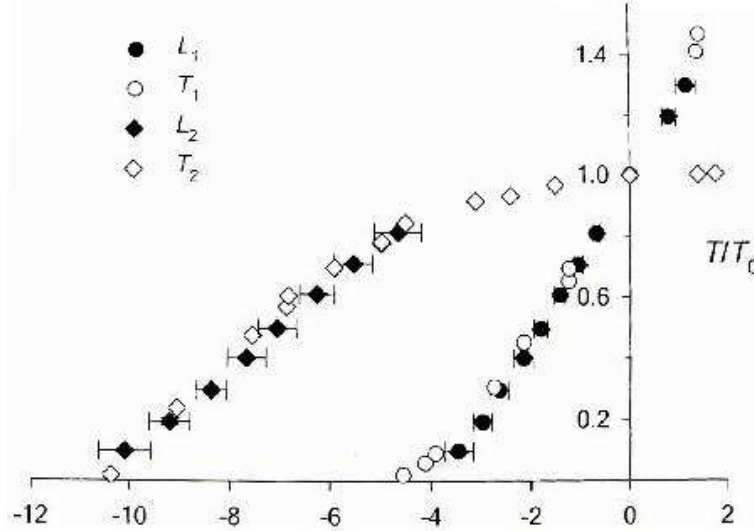


**Figure 2.15:** Experimental behavior of the  $T_1/T_0$  and  $T_2/T_0$  curves: length clamp device (T, open symbols), tension clamp device (L, filled symbols). From [67]

We recall that the linear part of the decreasing  $T_2 - \delta$  curve corresponds to the situation when all the Xbs are in the second well. In this situation further shortenings only decrease the tension generated by the elastic element since further jumps of Xbs are impossible. We also recall that because the location of the minima is fixed in Huxley and Simmons model, the slope of the  $T_2 - \delta$  and  $T_1 - \delta$  curves will be the same. Indeed, in this situation the subsequent decrease in tension relaxes the elastic element, but does not create additional jumps of Xbs. The model will predict the same slope for both  $T_1 - \delta$  and  $T_2 - \delta$  curves at large  $\delta$ , which is uniquely related to the elasticity modulus  $K$ . We can therefore conclude that the difference in slopes originates from the features of the Xbs which are not described by the Huxley and Simmons 1971 model. To generate a different size of the power stroke at different loads (which is what was experimentally observed in [67]), the model must be changed. Since the size of the power stroke is prescribed by the distance between the energy minima, it does not depend on  $\delta$ , if the wells are infinitely narrow. Therefore the wells should be delocalized.

In the model with quadratic wells, the probability distribution in the steady state, given by equation (2.35), is almost Gaussian inside the wells. If the energy barrier is higher than the thermal energy, in our case if for the second well

$$E_T(a/2) - E_T(a_2) \gg k_B T \quad (2.37)$$

then  $p_s(x, \delta)$  goes to zero quite fast away from the energy minima. In this case we

can make some simplifications in (2.35) and other similar relation, which will be later confirmed by our numerical test. For instance, considering the second well, we can define:

$$E_{T, 2}(x, \delta) = \left( \frac{1}{2}k_2(x - a)^2 + d + \frac{1}{2}K(x - l_0 - \delta)^2 \right), \quad (2.38)$$

and write

$$\begin{aligned} \int_{-\infty}^{a/2} x p_s(x, \delta) dx &= \mathcal{N}^{-1} \int_{-\infty}^{a/2} x e^{-E_{T, 2}(x, \delta)/k_B T} dx \simeq \\ &\mathcal{N}^{-1} \int_{-\infty}^{\infty} x e^{-E_{T, 2}(x, \delta)/k_B T} dx. \end{aligned} \quad (2.39)$$

Now, multiplying the right hand side by

$$\frac{\int_{-\infty}^{a/2} e^{-E_{T, 2}(x, \delta)/k_B T} dx}{\int_{-\infty}^{\infty} e^{-E_{T, 2}(x, \delta)/k_B T} dx} \simeq 1, \quad (2.40)$$

we can write:

$$\int_{-\infty}^{a/2} x p_s(x, \delta) dx = n_2^\delta a_2. \quad (2.41)$$

The analogous results can be obtained for the first well. In this computation we made an assumption that the integral of  $f(x)p_s(x)$  from  $x = -\infty$  to  $x = a/2$ , can be replaced by the integral extended to an infinite interval. Within this approximation, the power stroke is again determined by the distance between the minima. This distance controls the shift between the linear segments of the curves  $T_1(\delta)/T_0$  and  $T_2(\delta)/T_0$  and is constant if and only if the derivatives  $T'_1(\delta)$  and  $T'_2(\delta)$  are equal.

To show analytically how the curvatures of the wells affect the slopes of the curves  $T_1(\delta)$  and  $T_2(\delta)$  we first notice that all equations obtained for the case when the temperature  $T = 0$ , are still valid at temperatures  $T \neq 0$  because of the assumption (2.37). For instance, we can write:

$$T_0 = N_{Xb} \int_{-\infty}^{\infty} -K(x p_s(x, 0) - l_0) dx \simeq -N_{Xb} K(n_1^0 a_1(0) + n_2^0 a_2(0) - l_0) \quad (2.42)$$

and similarly:

$$T_2(\delta) = N_{Xb} \int_{-\infty}^{\infty} (-K(x p_s(x, \delta) - l_0 - \delta)) dx \simeq -N_{Xb} K(n_1^\delta a_1(\delta) + n_2^\delta a_2(\delta) - l_0 - \delta) \quad (2.43)$$

Now, recall that by using considerations from Section 2.4.2 we can write the tension  $T_1(\delta)$ :

$$T_1(\delta) \simeq -N_{Xb} K(n_1^0 a_1(\delta) + n_2^0 a_2(\delta) - l_0 - \delta). \quad (2.44)$$

Here the relative number of Xbs in each well is taken to be the same as before the step. Equation (2.44) can be obtained rigorously from the Kramers' theory whose fundamental hypothesis is that relaxation *within* each well is much faster than the equilibration *between* the wells (see Section A.7). We shall be using this approximation extensively later in this Chapter.

We can make use of the obtained formulas for  $T_1(\delta)$  and  $T_2(\delta)$  to compute the slopes of the corresponding curves at large negative  $\delta$ . We recall that at large  $\delta$  all Xbs are in the second minimum. We can then use the following linear approximation:

$$T_2^*(\delta) = -N_{Xb}K(a_2(\delta) - l_0 - \delta). \quad (2.45)$$

From this relation and from relations (2.36) and (2.13) we obtain:

$$\frac{d}{d\delta} \frac{T_1(\delta)}{T_0} = \frac{n_1^0 k_1 / (k_1 + K) + n_2^0 k_2 / (k_2 + K)}{n_1^0 l_0 k_1 / (k_1 + K) + n_2^0 k_2 (l_0 - a) / (k_2 + K)} \quad (2.46)$$

and

$$\frac{d}{d\delta} \frac{T_2^*(\delta)}{T_0} = \frac{k_2 / (k_2 + K)}{n_1^0 l_0 k_1 / (k_1 + K) + n_2^0 k_2 (l_0 - a) / (k_2 + K)}. \quad (2.47)$$

The value of the shortening at which  $T_2^*(\delta) = 0$  can be calculated from equation (2.45). We obtain

$$\delta_{(T_2^*=0)} = a - l_0. \quad (2.48)$$

At this value of  $\delta$ , all Xbs are symmetrically distributed around  $x = a$ , the relaxed position of the elastic element. To specify the numerical value of  $\delta_{(T_2^*=0)}$ , we can use the experimental data obtained in the length clamp experiment shown in Fig. 2.15 (open symbols). More specifically, we shall perform a linear fitting of the points that represent the  $T_1(\delta)/T_0$  curve and of those points that represent the linear decreasing part of the  $T_2(\delta)/T_0$  curve. The values of parameters are reported in Table (2.1). In particular, we obtain the value  $\delta_{(T_2^*=0)} = -10.8 \text{ nm}$ . The curve  $T_1(\delta)/T_0$  crosses the abscissa at  $\delta_{(T_1=0)} = -3.87 \text{ nm}$ . This gives  $d(T_1(\delta)/T_0)/d(\delta) = 0.258 \text{ nm}^{-1}$ . The linear fitting of the  $T_2^*(\delta)$  curve, gives the slope  $0.138 \text{ nm}^{-1}$ , so the ratio of the slopes is 1.87. These are the values that we would like to fit. From equation (2.48) we can set

$$a = -10.8 + l_0 \text{ nm}. \quad (2.49)$$

The value of  $l_0$  will be found from other data.

Comparing equations (2.46) and (2.47), we see that if  $k_1 = k_2$  the two slopes  $\frac{d}{d\delta} T_2^*(\delta)$  and  $\frac{d}{d\delta} T_1(\delta)$ , are the same. This is the reason why the Huxley and Simmons model predicts the same slope for both curves. We can also see that

the slope of  $T_2^*(\delta)$  will be smaller than the slope of  $T_1(\delta)$  if  $k_1 > k_2$ . One might think that the difference will increase when  $k_1 \gg k_2$ , but we have to remember that an increase in  $k_1$  will also decrease  $n_1^0$ , reducing this effect.

Now, we make again use of the hypothesis (2.37). We observe that in this approximation the integral  $\int_{-\infty}^{a/2} \exp[-E_T(x, \delta)/k_B T] dx$  can be approximated by  $\int_{-\infty}^{\infty} \exp[-E_{T, 2}(x, \delta)/k_B T] dx$ . This allows a simplification of the expression for the functions  $n_1(\delta)$  and  $n_2(\delta)$  given by equation (2.36). For instance, at  $\delta = 0$  we obtain

$$\begin{aligned} n_2^0 &\simeq \mathcal{N}^{-1} \int_{-\infty}^{\infty} \exp[-E_{T, 2}(x, 0)/k_B T] dx = \\ &= \frac{\sqrt{2\pi}}{\mathcal{N}} \frac{\exp\left[-\frac{2d + (Kk_2(a - l_0)^2)/(K + k_2)}{2k_B T}\right]}{\sqrt{\frac{K + k_2}{k_B T}}}. \end{aligned} \quad (2.50)$$

Similarly,

$$n_1^0 \simeq \frac{\sqrt{2\pi}}{\mathcal{N}} \frac{\exp\left[-\frac{Kk_1 l_0^2}{2(K + k_1)k_B T}\right]}{\sqrt{\frac{K + k_1}{k_B T}}}. \quad (2.51)$$

For the particular value of  $d$  from (2.10), the nominators in both (2.50) and (2.51) are the same and we can write:

$$\begin{cases} n_1^0 \simeq \frac{\sqrt{k_2 + K}}{\sqrt{k_2 + K} + \sqrt{k_1 + K}} \\ n_2^0 \simeq \frac{\sqrt{k_1 + K}}{\sqrt{k_2 + K} + \sqrt{k_1 + K}}, \end{cases} \quad (2.52)$$

here the normalization constant  $\mathcal{N}$  is eliminated imposing  $n_1^0 + n_2^0 = 1$ .

We can now use the condition that the derivative of  $T_1(\delta)/T_0$  must be 1.87 times the derivative of  $T_2^*(\delta)/T_0$ . Using equations (2.46) and (2.47), we obtain the condition:

$$\begin{aligned} \frac{dT_1(\delta)/d\delta}{dT_2^*(\delta)/d\delta} &= \frac{\sqrt{k_2/K + 1}}{\sqrt{k_1/K + 1} + \sqrt{k_2/K + 1}} \frac{k_1/K(k_2/K + 1)}{k_2/K(k_1/K + 1)} + \\ &\frac{\sqrt{k_1/K + 1}}{\sqrt{k_1/K + 1} + \sqrt{k_2/K + 1}} = d_{slope} = 1.87. \end{aligned} \quad (2.53)$$

One can see that this ratio does not depend on either  $a$  or  $l_0$ , but only on the elasticities  $k_1$ ,  $k_2$  and  $K$ . Moreover, the three moduli enter in only two dimensionless combinations:  $k_1/K$  and  $k_2/K$ . The contours  $d_{slope} = \text{const}$  in the  $(k_1/K, k_2/K)$  plane are shown in Fig. 2.16. By increasing the ratio of  $k_1$  to  $k_2$  we obtain a higher

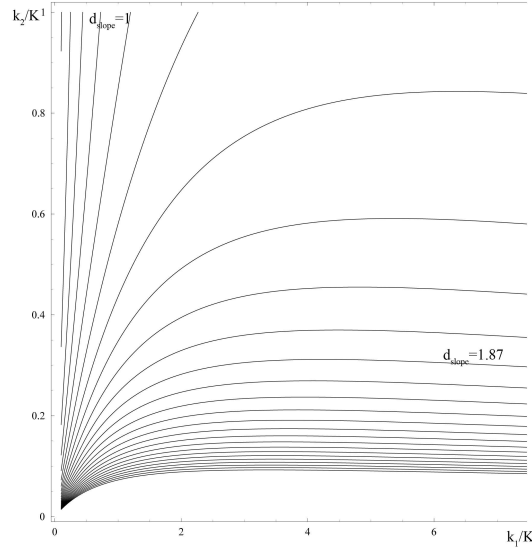


**Figure 2.16:** Contour plot showing the ratio of the slopes (2.53) as a function of the relative curvatures  $k_1/K$  and  $k_2/K$

value of  $d_{slope}$ . Analytically we can write the following relation between  $k_1/K$  and  $k_2/K$  ensuring that the slope ratio is equal to  $d_{slope}$ :

$$\frac{k_1}{K} = [2((k_2/K)^2 - 2(k_2/K)^2 d_{slope} + (k_2/K)^2 d_{slope}^2)]^{-1} [1 + 3k_2/K - 2k_2/K d_{slope} + 2(k_2/K)^2 d_{slope} - 2(k_2/K)^2 d_{slope}^2 \pm \sqrt{\psi(k_2/K)}]. \quad (2.54)$$

Here

$$\begin{aligned} \psi\left(\frac{k_2}{K}\right) &= 1 + 6\frac{k_2}{K} + 9\left(\frac{k_2}{K}\right)^2 + 4\left(\frac{k_2}{K}\right)^3 \\ &\quad - 4\frac{k_2}{K}d_{slope} - 8\left(\frac{k_2}{K}\right)^2 d_{slope} - 4\left(\frac{k_2}{K}\right)^3 d_{slope} \end{aligned} \quad (2.55)$$

One can see that for  $d_{slope} = 1.87$  the value of  $k_1/K$  is real only if  $k_2/K < 0.294$ . In the Huxley and Simmons model the value of  $k_2$  is chosen to be infinite. Following their reasoning, we choose for  $k_2$  the largest possible value compatible with the condition  $d_{slope} = 1.87$ ,  $k_2/K = 0.294$ . This gives  $k_1 = 4.17K$ . We would like to keep the values of  $k_2$  as large as possible to maintain the link with experiment. Indeed, the higher is the compliance and the smaller is the step of the power stroke. Our relatively low value of the  $k_2$ , results from the hypothesis that the filaments are rigid. In fact, one can think that the compliance of the second well also includes this extra-compliance of the filaments. In general with the increase of  $k_1$  the ratio of the slopes first increases up to a maximum, but then it decreases because the



population in the first well becomes lower. The characteristic behavior is shown in Fig. (2.17) for a representative value of  $k_2/K$ .

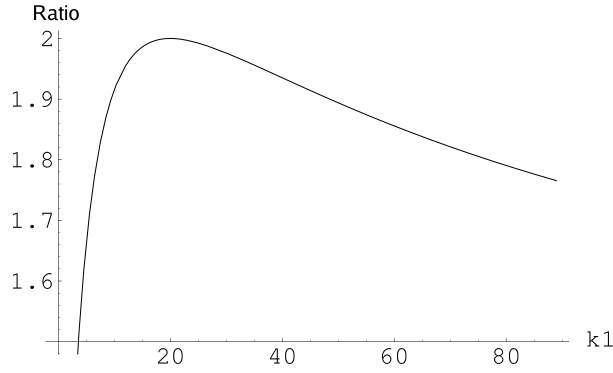


**Figure 2.17:** Ratio of the slopes of  $T_1(\delta)$  and  $T_2(\delta)$  as a function of the parameter  $k_1$ . Abscissa in  $pN/nm$

Now, we can use the expression (2.47), and the approximation (2.52), to match the values of both slopes  $dT_1(\delta)/d\delta$  and  $dT_2^*(\delta)/d\delta$  with those observed experimentally. We can write

$$\frac{d}{d\delta} \left( \frac{T_2(\delta)}{T_0} \right) = \left[ \frac{k_1 \sqrt{(k_2 + K)^3} l_0}{k_2 \sqrt{k_1 + K} (\sqrt{k_2 + K} + \sqrt{k_1 + K})} + \frac{\sqrt{k_1 + K}}{\sqrt{k_2 + K} + \sqrt{k_1 + K}} (l_0 - a) \right]^{-1} = s \quad (2.56)$$

where we have assumed that  $l_0 - a = 10.8 \text{ nm}$ . We can obtain an analytical expression for  $l_0(s)$ :

$$l_0(s) = \frac{\left( \frac{k_1}{K} + 1 \right) \frac{k_2}{K} \left[ 1 + \sqrt{\frac{k_1/K + 1}{k_2/K + 1}} \right] \left[ 1 + \sqrt{\frac{k_2/K + 1}{k_1/K + 1}} - (l_0 - a)s \right]}{\frac{k_1}{K} \left( \frac{k_2}{K} + 1 \right) \left[ 1 + \sqrt{\frac{k_2/K + 1}{k_1/K + 1}} \right] s}. \quad (2.57)$$

In Fig. 2.18 we show how  $l_0$  depends on  $k_2/K$  for the given value  $s = 0.138 \text{ nm}^{-1}$ , and under the assumption that  $k_1/K$  is determined by (2.54). The solution (2.57) exists up to  $k_2/K = 0.294$ , where  $l_0 = 0.05 \text{ nm}$ .

As we have shown above our model is able to reproduce the linear segments of both curves,  $T_1(\delta)$  and  $T_2(\delta)$ . To test the validity of the adopted analytical approximation, (see (2.37)) we can make direct numerical integration in the formulas (2.42), (2.44), (2.43). These formulas represent the exact solution for the tensions after a given incremental step. In Fig. 2.19(a) we show superimposed: the

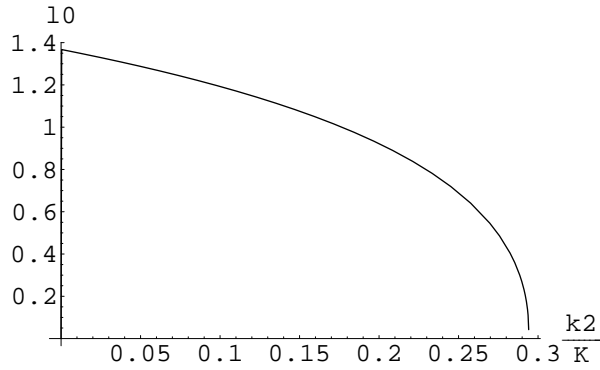


**Figure 2.18:**  $l_0$  (in  $nm$ ) as a function of  $k_2/K$  for  $s = 0.138 \text{ nm}^{-1}$  and  $d_{slope} = 1.85$

experimental data (points), their linear fitting (straight dashed lines), the direct numerical integration of (2.44), (2.43) (continuous lines) and the functions  $T_2(\delta)/T_0$  generated by the approximate model (2.52) (curved dashed line). As we see, our approximation for  $T_2(\delta)$  is very good, especially for large values of  $\delta$ . The slope of the curve  $T_1(\delta)/T_0$  is slightly overestimated. Since also the slope of  $T_2(\delta)/T_0$  ended up slightly overestimated, we used the values of parameters obtained above (see Table 2.1) only as an initial guess and then made a careful fit to the exact experimental data. Regarding the figures shown in this Section, only the ratio  $k_2/K$  had to be changed. Thus from now on we use  $k_2/K = 0.310$  instead of the previous value  $k_2/K = 0.294$ . The new fit of the experimental data is shown in Fig. 2.19(b). The final set of parameters is collected in the column *Analytical values* of Table (2.1).

In Fig. 2.19(b) we can see an important feature of the curve  $T_2(\delta)$  which will be discussed in the next Section: the presence of a region where the slope  $dT_2(\delta)/d\delta$  is negative. This feature has not been observed in direct experiments. The same problem resurfaces in the original Huxley and Simmons model if the realistic values of the coefficient  $K$  is used [48] (see Section 1.3.3).

## 2.7 Negative slope of the $T_2(\delta)$ curve

Our analysis has been so far focussed on the slope of the curve  $T_2(\delta)$  at large negative values of  $\delta$ . Now we concentrate on the behavior of this function near  $\delta = 0$ . As we have seen the value of the parameter  $K$  does not affect the linear behavior of  $T_2(\delta)$  at large  $\delta$ , however it notably affects the slope of the curve  $T_2(\delta)$  at small  $\delta$ . To compute the function  $T_2(\delta)$  when  $n_2^\delta \neq 1$ , the exact values of  $n_1^\delta$  and  $n_2^\delta$  are needed. They can be taken either from the approximate expression (2.52),

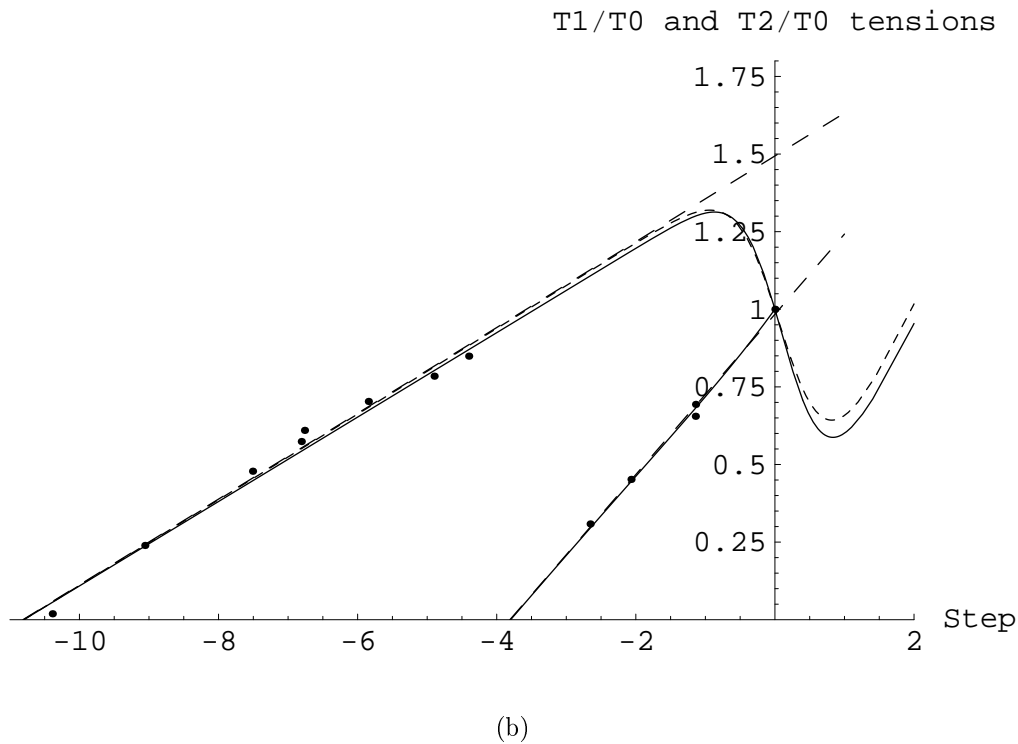
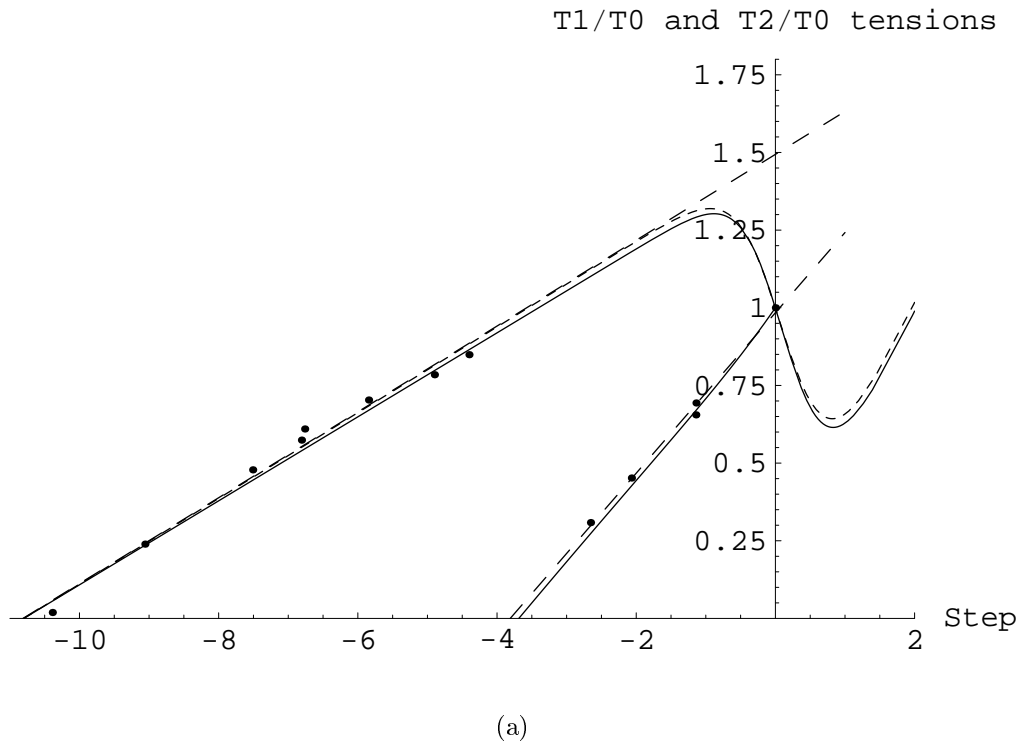


**Figure 2.19:** Fitting of data. Points: experimental data from [43]. Straight dashed lines: linear best fitting of the experimental data. Solid lines: prediction from the model of  $T_2(\delta)/T_0$  and  $T_1(\delta)/T_0$  from direct integration of (2.44), (2.43). Curved dashed line: prediction using the approximations (2.52). (a)  $k_2/K = 0.294$  (b)  $k_2/K = 0.310$ . Abscissa units: nm

or from the direct numerical integration of the formulas (2.36).

We have already seen that  $dT_2(0)/d\delta = -\infty$  if the concentration of Xbs is found from the condition of global minimum of the energy (Fig. 2.14). Let us also recall how the Huxley and Simmons model deals with the problem of the negative slope of the  $T_2(\delta)$  curve at  $\delta \simeq 0$ . Using their notations, and the particular shape of their chemical energy we obtain that the steady state population of Xbs can be computed as  $n_1^\delta = 1 - n_2^\delta$ ,  $n_2^\delta = 1/(1 + k_-/k_+)$ , where  $k_\pm$  are the rate constants that regulate kinetics of the jumps between the energy wells. In the Huxley and Simmons model it is assumed that  $k_+/k_- = e^{-\frac{yKh}{k_BT}}$ , equation (1.14). We recall that their  $y$  and  $h$  are the analogues of our  $\delta$  and  $a$ . In their case, the value of  $n_2^\delta$  is known when one knows the numerical values of the coefficient  $Kh/k_BT$ . In Huxley and Simmons model the value of  $K$  was obtained from an independent set of data on the rate of recovery for the tension. They observed that the value of  $h$  “has to be chosen to give the right shape of the curve of  $T_2$  against  $y$ . [...] lower values give a less inflected curve and higher values give a curve with a region of negative slope”. This behavior is illustrated in Fig. 2.20 where different values of the product  $Kh/k_BT$  have been used. The global minimum behavior mentioned above correspond to the case of either  $K = \infty$  or  $T = 0$ . By tailoring the value of  $Kh/k_BT$  as in Fig. 2.20 Huxley and Simmons avoided the negative slope of the  $T_2(\delta)$  curve; they used  $Kh/k_BT = 5 \text{ nm}$ .

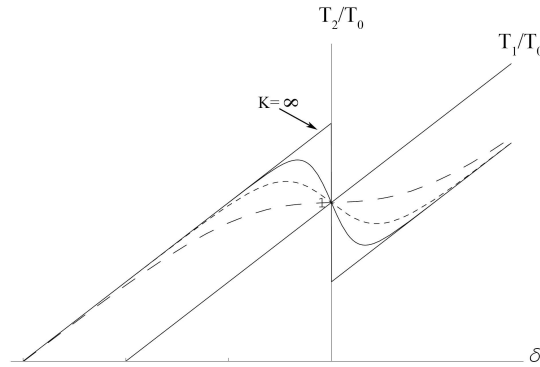


**Figure 2.20:** The curves  $T_2(\delta)/T_0$  and  $T_1(\delta)/T_0$  in the HS71 model computed at different values of  $Kh/k_BT$

The important criticism raised against the Huxley and Simmons 1971 model, was that while  $h = 8 \text{ nm}$  was chosen to be compatible with experiments, the stiffness of the elastic element had to be at the unrealistically low level of  $K = 0.2 \text{ pN/nm}$ . With the realistic value of  $K$ , say  $K = 2 \text{ pN/nm}$ , the curve  $T_2(\delta)$  predicted by the Huxley and Simmons model necessarily shows a negative slope at

$\delta = 0$ .

Below, we show how the assumption of finite elasticity of the wells can decrease the negative slope of the  $T_2(\delta)$  at  $\delta = 0$  even though it can not eliminate this effect completely.

The approximate expression for the function  $T_2(\delta)$ , which describes its behavior at small  $\delta$ , is given by equation (2.43). In this approximation, we have already computed the values of  $n_1^0$  and  $n_2^0$  (equation (2.52)). To compute the function  $T_2(\delta)$ , we need the values of  $n_1^\delta$  and  $n_2^\delta$  when  $\delta \neq 0$ . In this case the exponential terms in the expressions (2.51) and (2.50) will not be equal. For  $n_2^\delta$  we obtain the following expression:

$$n_2^\delta = \left[ 1 + \frac{\sqrt{k_2 + K}}{\sqrt{k_1 + K}} e^{f(\delta)} \right]^{-1} \quad (2.58)$$

where:

$$f(\delta) = -\frac{\delta K[\delta K(k_1 - k_2) + 2a(k_1 + K)k_2 + 2K(k_1 - k_2)l_0]}{2k_B T(k_1 + K)(k_2 + K)}. \quad (2.59)$$

For  $n_1^\delta = 1 - n_2^\delta$  an equivalent expression can be written.

From (2.58) (2.59) it is not straightforward to see how the parameter  $K$  influences the slope of the curve  $T_2(\delta)$ . Let us first concentrate on the exponential term in (2.58): this term's  $\delta$  dependence is the principal cause of the negative slope of the function  $T_2(\delta)$  at  $\delta = 0$ . In what follows we limit our analysis to the negative values of  $\delta$ . We would like to maintain the value of  $n_2^\delta$  as low as possible for small negative  $\delta$ , therefore  $f(\delta)$  should be small. We observe that when  $k_1 = k_2 = k$ ,  $f(\delta) = -(a\delta/k_B T) (Kk/(K + k))$ , so  $n_2^\delta$  will increase faster at larger  $K$ s. The term  $Kk/(K + k)$  is equal to  $K$  when  $k = \infty$ , and decreases if elasticity of the wells is taken into consideration  $k < \infty$ . This also decreases the negative slope of  $T_2(\delta)$ . We emphasize that within our model we essentially redefine the meaning of the elasticity of the Xb. In fact, the Xb is represented as an elastic spring, in series with another elastic bi-stable snap spring, so the stiffness of the Xb is the global stiffness of the system. More precisely we can use the formula for two elastic elements in series,  $K_{effective} = Kk_{1/2}/(K + k_{1/2})$ , where we have to choose  $k_1$  and  $k_2$  for the first and the second well respectively.

Next we observe that, if  $k_1 > k_2$ , as required by the condition on the relative slopes of  $T_2(\delta)$  and  $T_1(\delta)$ , then the higher is the  $k_1$  (or the  $l_0$ ) the smaller is the slope of  $T_2(\delta)$  at  $\delta = 0$ . This fact is illustrated in Fig. 2.21. The value of  $l_0$  can not be too high, because there is no evidence that the Xbs can generate considerable force in both states. As explained in the previous Section, the values of  $k_1$  and

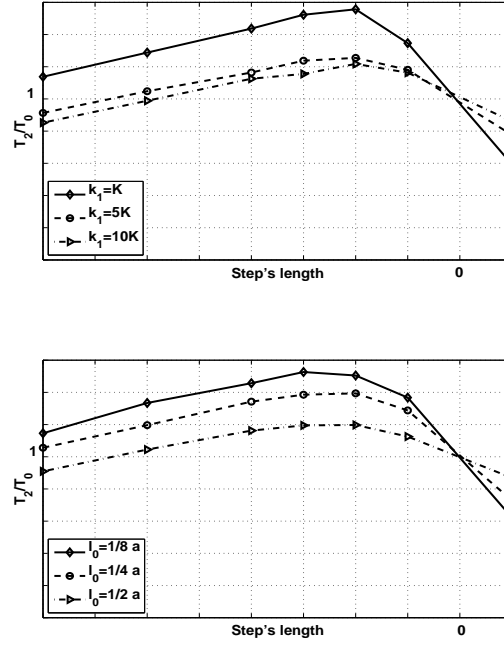


**Figure 2.21:** Effects of  $k_1$  and  $l_0$  on the curve  $T_2(\delta)/T_0$ , when all the Xbs have the same attached sites. a) Effect of  $k_1$ . Increasing the stiffness of the first well, decrease the negative slope of the curve around zero. The decrease is less marked at higher values of  $k_1$ . b) Effect of  $l_0$ . An increase in the value of  $l_0$  have the same effect as the increase of  $k_1$

$l_0$  are tightly linked to the two parameter  $k_2$  and  $K$ , because of a constraint that must be imposed on their relative value. More specifically to reproduce the ratio of the slopes for  $T_2(\delta)$  and  $T_1(\delta)$  curves at large negative  $\delta$ , the value of  $k_2$  must be necessarily lower than a certain value. In addition, we would like to maintain the global stiffness at the same order of magnitude as experimentally observed. We can now identify the global stiffness with  $k_2 K / (k_2 + K)$  if the stiffness of the Xbs is measured in rigor [55], where  $n_2 = 1$ . Since  $k_1 > k_2$  this value represent the lower bound for the global stiffness. We therefore impose that  $k_2 K / (k_2 + K) \geq 1 \text{ pN/nm}$ , which implies  $k_2 \geq K / (K - 1) \text{ pN/nm}$ . The constraint  $k_2 / K \lesssim 0.3$  found in Section 2.6, gives  $K / (K - 1) \leq k_2 \lesssim 0.3K$  so necessarily  $K \gtrsim 4 \text{ pN/nm}$ .

We can now consider the effect of  $K$  on the slope of the curve  $T_2(\delta)$  at  $\delta = 0$  (see Fig. 2.22, where the curves  $T_2(\delta)$  are plotted for increasing value of  $K$ ). We see that, to have a non-negative slope, the value of  $K$  should be lower than  $1 \text{ pN/nm}$ , which is incompatible with our other constraints. From now on, we choose the value for the global stiffness,  $1 \text{ pN/nm}$  which fixes completely all other parameters of the model. From Fig. 2.22 one can see that the slope  $dT_2(0)/d\delta$

remains negative. The resolution of this last incompatibility with the experiment will be our main preoccupation in the rest of the present Section 2.7.

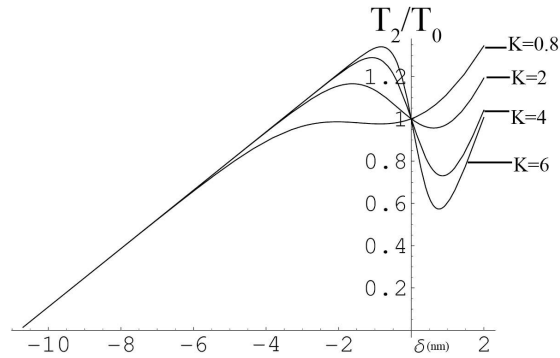


**Figure 2.22:** The effect of the increasing value of the stiffness of the elastic element  $K$  on the negative slope of the curve  $T_2(\delta)$  at  $\delta = 0$ . We change  $K$  from  $0.8 \text{ pN/nm}$  to  $6 \text{ pN/nm}$ . The linear segment of the curve  $T_2(\delta)$  at large negative  $\delta$  is unaffected by  $K$

The problem can be approached in two different ways. One option is to consider a potential inhomogeneity inside the fiber, viewed as a chain of sarcomeres. Another option is to assume a nontrivial distribution of attachment points for different Xbs inside the half sarcomere.

### 2.7.1 Inhomogeneity in a chain of sarcomeres

Suppose now that the behavior of a single half-sarcomere is given by our model describing several identical Xbs that act in parallel. As we have seen, the half-sarcomere acts like a single contractile element with a non monotone tension-deformation curve  $T_2(\delta)$ . The actual experiments are made not on a single half-sarcomere but on myofibril. We may then assume that a chain of our half-sarcomere in series should be used as a model describing the observed behavior of a myofibril during contraction. The negative slope in a response of a single element, should lead to a global inhomogeneity in the system. When a small perturbation is imposed on a system with  $dT_2(0)/d\delta < 0$ , the sarcomere that is shorter than its neighbors, will generate more force. As a consequence, it will shorten further and, since the total length is fixed, its neighbor will be stretched with a subsequent decrease of the force [62], [73], until the rise of the force in the parallel elasticity brings the sarcomere in equilibrium. This process, anyway, leads to development of inhomogeneity that can explain the flattening of the global tension elongation curve.

The mechanical problem for a series of bi-stable elastic springs at temperature  $T = 0$ , was studied in [62], where an analytical solution for the tri-parabolic model was found. This analytical solution is available only for unrealistically simple energies of the elements producing piece-wise linear tension-deformation curves. Below we extend this approach to the case of realistic  $T_2(\delta)$  curves generated by our model of half-sarcomere.

### Series connection of N half sarcomeres

We begin with a review of the results obtained in [62]. Consider first a chain of 2 half sarcomeres, representing the simplest case of the general theory  $N=2$  (Fig. 2.23). Suppose that each half-sarcomere is characterized by a piecewise parabolic

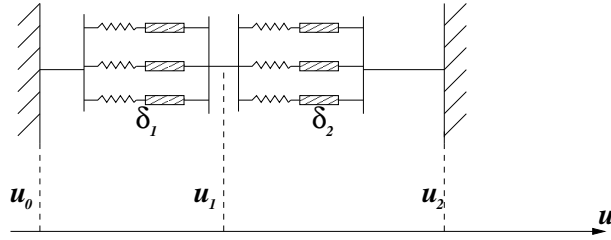


**Figure 2.23:** Model of two half-sarcomeres in series. Each half-sarcomere is formed by  $N_{Xb}$  in parallel

energy

$$w(\delta) = \begin{cases} \frac{1}{2}(\delta + 1)^2 & \delta \leq -t \\ \frac{1}{2}([(1 - t^{-1})\delta^2 + (1 - t)]) & -t \leq \delta \leq t \\ \frac{1}{2}(\delta - 1)^2 & t \leq \delta \end{cases} \quad (2.60)$$

It is a smooth function formed by three parabola, two downward and one upward, as shown in Fig. 2.24(a), where the phases are I and III have positive curvatures, and phase II has negative curvature. The corresponding tension-deformation curve is trilinear as shown in Fig. (2.24(b)). This shape roughly approximates the  $T_2(\delta)$  curve obtained in Section 2.6. The number of elements in each phase can be expressed as a vector  $(k, l, m)$ , where  $k$ ,  $l$  and  $m$  are the numbers of elements in phase I, II and III, respectively. When  $N=2$ , the classes of solutions corresponding to the homogeneous phases I, II and III, are  $(2, 0, 0)$ ,  $(0, 2, 0)$  and  $(0, 0, 2)$ , while solutions  $(1, 1, 0)$ ,  $(1, 0, 1)$  and  $(0, 1, 1)$  corresponds to inhomogeneous microstructures.

The equilibrium problem at  $T = 0$  can be reduced to finding the critical points



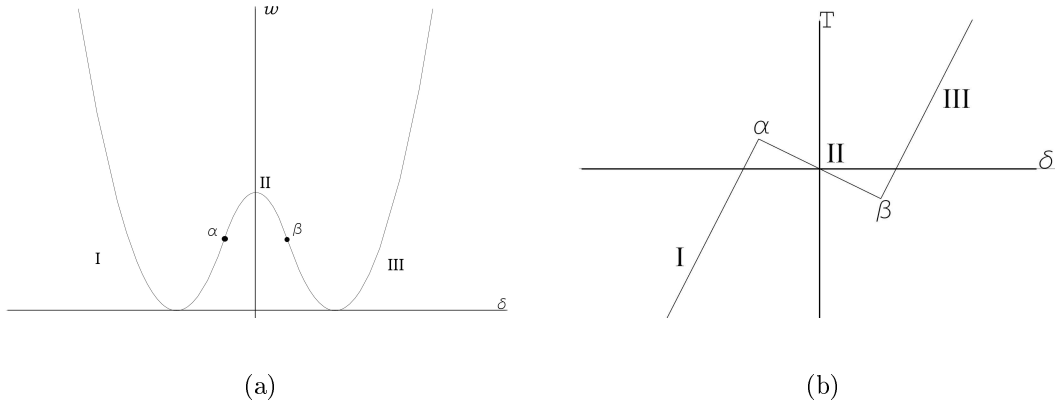


**Figure 2.24:** (a) Energy function for a single element. (b) Tension deformation curve for a single element

of the total energy

$$W(\delta_1, \dots, \delta_N) = \sum_{i=1}^N w(\delta_i) \quad (2.61)$$

where due to the global isometric constrain

$$\sum_{i=1}^N \delta_i = N\bar{\delta} \quad (2.62)$$

The system of equilibrium equations takes the form

$$w'(\delta_i) = \sigma \quad i = 1, \dots, N \quad (2.63)$$

where  $\sigma$  is the tension in the chain, which is equal for all elements.

With the simple  $w(\delta)$  defined in (2.60), it is possible to find the equilibrium strain-force relation explicitly. To this end we need to invert the relation:

$$N\bar{\delta} = k\delta_I(\sigma) + l\delta_{II}(\sigma) + m\delta_{III}(\sigma) \quad (2.64)$$

where  $\delta_I(\sigma)$ ,  $\delta_{II}(\sigma)$  and  $\delta_{III}(\sigma)$  are the linear strain force relations corresponding to phases I, II and III respectively. In this way we obtain the global force-strain relation for the whole cycle, and can also compute analytically the equilibrium energy of the entire chain. Defining the “volume fractions”

$$x = k/N, \quad y = l/N, \quad z = m/N \quad (2.65)$$

where  $x + y + z = 1$ , one can obtain

$$\bar{\sigma}(\bar{\delta}) = E(\bar{\delta} - \delta_0) \quad (2.66)$$

where we have defined the effective elastic modulus along the corresponding branch  $(x, y, z)$  as

$$E = [1 - y(1 - t)^{-1}]^{-1}, \quad (2.67)$$

and the reference strain

$$\delta_0 = z - x. \quad (2.68)$$

Correspondingly, the overall equilibrium energy for the tri-linear chain can be written

$$\bar{w}(\bar{\delta}) \equiv W/(Na) = \frac{1}{2}E(\bar{\delta} - \delta_0)^2 + \frac{1}{2}y(1 - t). \quad (2.69)$$

Here  $a$  is the reference length of each half-sarcomere. The curves  $\bar{w}(\bar{\delta})$  and  $\bar{\sigma}(\bar{\delta})$  are shown in Fig. 2.25 (from [62] where  $\bar{\varepsilon} = \bar{\delta}$ )

The above solution is also suitable for our problem where a myofibril is interpreted as a chain of half-sarcomeres with non-monotone tension-deformation relations. In our case, the explicit expression of the tension-deformation curve of a unit is not as simple as (2.60) even in the approximate version, however some useful insight can be derived by the analyses developed in [62] and [73].

Let us first examine how the curvatures of the wells affect the stability of the inhomogeneous configuration. For instance, in the case  $N=2$ , one can question the stability of the configuration (1,1,0). In the tri-linear case we know that [62] if the absolute value of the (negative) modulus of phase II is greater than the two equal (positive) moduli of phases I and III, so that

$$t^{-1} - 1 > 1 \quad (2.70)$$

where  $t$  is defined by (2.60), then the configuration (1,1,0) is not stable and the configuration (2,0,0) “snaps” at some value of  $\bar{\delta}$  into the configuration (1,0,1). The global tension elongation curve will not show any region with negative slope, but will instead show points of discontinuity (see Fig. 2.25).

We can explain this result graphically by using a realistic  $T_2(\delta)$  curve. We recall that for  $N = 2$  the total deformation constrain can be written as  $\delta_1 + \delta_2 = 2\bar{\delta}$ . We can, therefore, represent at a given  $\bar{\delta}$  the tension-deformation curve for the second half-sarcomeres  $T_2^2(\delta_2)$ , in the form

$$T_2^2(\delta_1) = T_2^2(2\bar{\delta} - \delta_1) \quad (2.71)$$

The relations  $T_2^1(\delta_1)$  and  $T_2^2(\delta_1)$  are plotted in Fig. 2.26 and in Fig. 2.27 for  $T_2(\delta)$  obtained in Section 2.6. The  $T_2^1(\delta_1)$  curve is always centered in the origin, while the

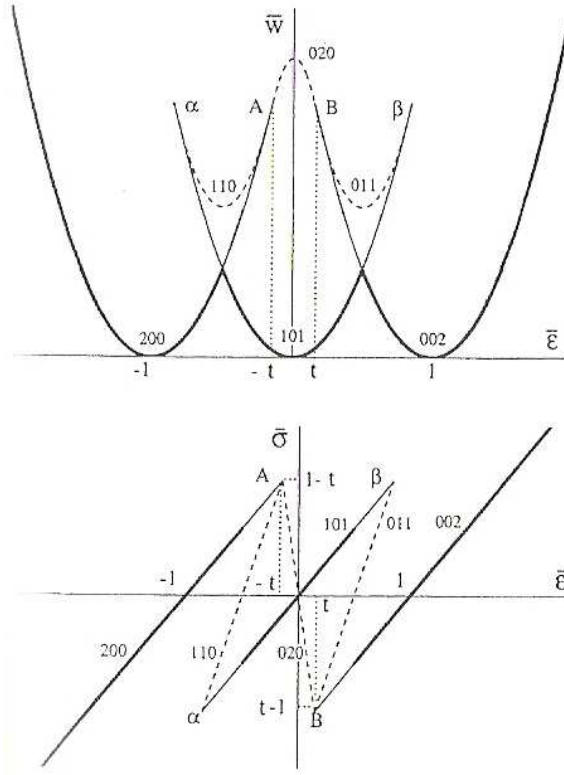


**Figure 2.25:** Overall energy-strain relation and force strain relation for the case  $N=2$  and  $t^{-1} - 1 > 1$ . From [62]

$T_2^2(2\bar{\delta} - \delta_1)$  curve gets shifted to the left for increasing values of  $\bar{\delta}$ . The equilibrium solution corresponds to points where

$$\frac{dW(\delta_1, \bar{\delta})}{d\delta_1} = \frac{d(w_1(\delta_1) + w_2(2\bar{\delta} - \delta_1))}{d\delta_1} = T_2^1(\delta_1) - T_2^2(2\bar{\delta} - \delta_1) = 0, \quad (2.72)$$

meaning again that tensions are the same in both elements. Graphically it is the point of intersection of the curves  $T_2^1(\delta_1)$  and  $T_2^2(\delta_1)$ . A point of equilibrium is stable when

$$\frac{d^2W(\delta_1, \bar{\delta})}{d\delta_1^2} = \frac{dT_2^1(\delta_1)}{d\delta_1} - \frac{dT_2^2(2\bar{\delta} - \delta_1)}{d\delta_1} > 0. \quad (2.73)$$

Graphically this means that the configuration is stable when the  $T_2^1(\delta_1)$  curve crosses the  $T_2^2(2\bar{\delta} - \delta_1)$  curve from below, and is unstable if it crosses from above. One can see that the configuration  $(0,2,0)$  is always unstable. When the maximum of the absolute value of the modulus in phase II is smaller than the moduli in phases I and III as in Fig. 2.26, the two configurations  $(1,1,0)$  and the symmetric  $(0,1,1)$  are stable (shallow spinodal region). When the negative modulus is sufficiently larger, as in Fig. 2.27, the stable configurations are  $(2,0,0)$  and  $(1,0,1)$ , while the

configuration (1,1,0) is unstable. The corresponding equilibrium curve  $\sigma(\bar{\delta})$  for the overall chain is continuous as in Fig. 2.28(a) for the first case. For the second case, shown in Fig. 2.28(b) the tension changes suddenly when one of the half-sarcomeres jumps from one stable configuration to the other. In what follows the

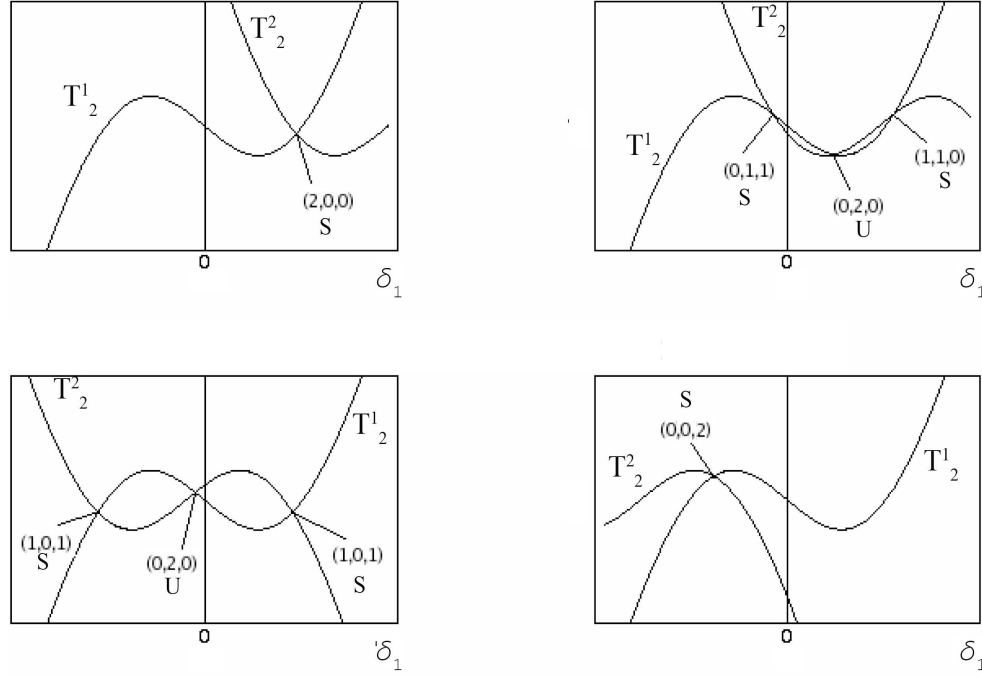


**Figure 2.26:** Tension-deformation curves for the chain with two elements in series. The case of shallow spinodal region ( $t > 1/2$ ), S=stable, U=unstable. The system presents a stable configuration with one element in the spinodal region

absence of the negative slope in the global tension deformation curves will be used to explain the experimentally observed positive slope of the  $T_2(\delta)$  curve. However, to make the resulting pictures more realistic we need to increase the number of element in the chain.

In the case of  $N$  elements one can show that no more than one element in the spinodal region (in phase II) can be present in a stable configuration. Indeed if we rewrite the total energy of the chain with  $N$  elements as a function of  $N-1$  variables:

$$\bar{W}(\delta_1, \dots, \delta_{N-1}) = W \left( \delta_1, \dots, \delta_{N-1}, N\bar{\delta} - \sum_{i=1}^{N-1} \delta_i \right) \quad (2.74)$$

we obtain that the equilibrium configuration  $\delta_i(\bar{\delta})$  is a local minimum of this energy

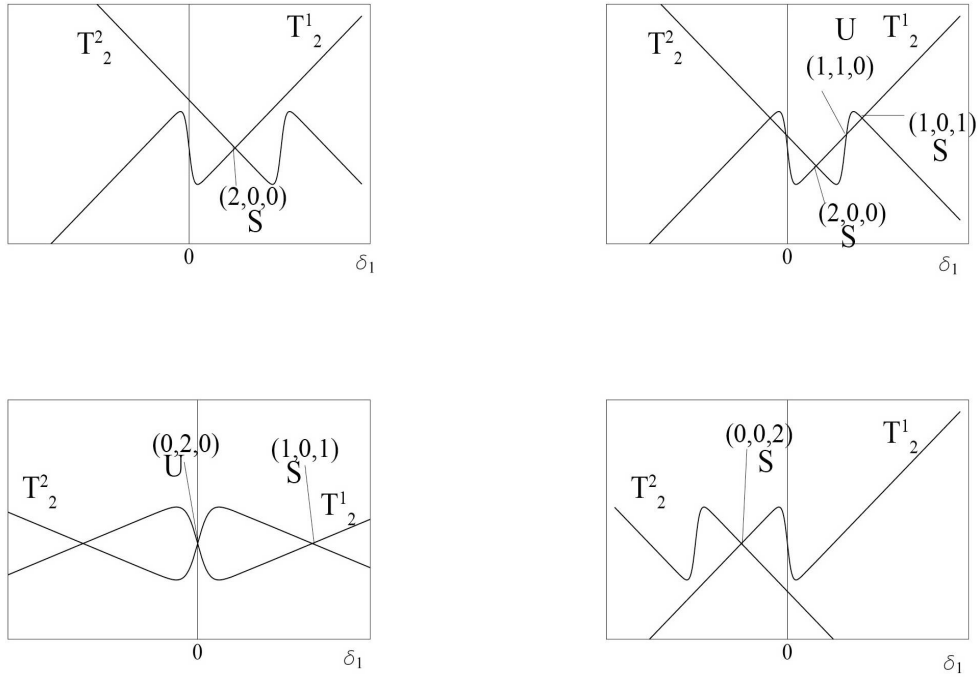


**Figure 2.27:** Tension-deformation curves for the chain with two elements in series. The case of steep spinodal region ( $t < 1/2$ ). The system does not present a stable configuration with one element in the spinodal region

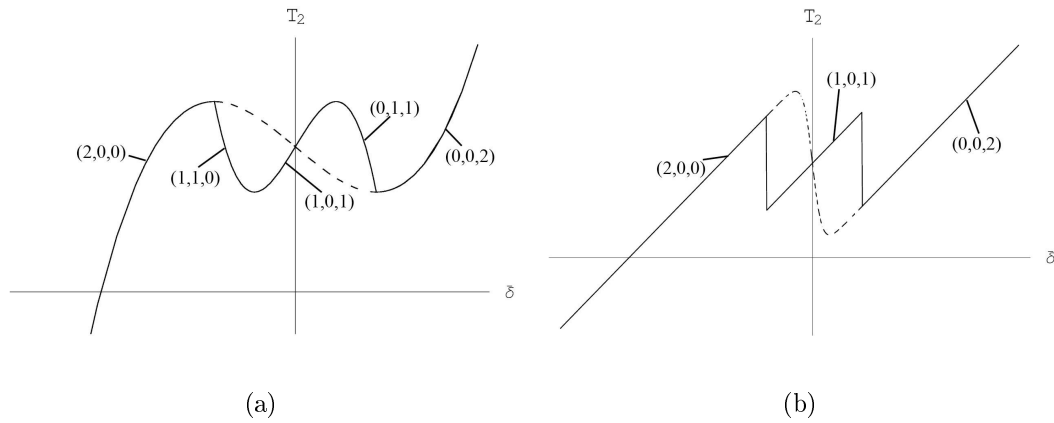


**Figure 2.28:** Overall tension-deformation curve for a chain with two elements superimposed on the  $T_2 - \delta/2$  curves for a single element (dashed). (a) Shallow spinodal region ( $t > 1/2$ ) (b) Steep spinodal region ( $t < 1/2$ )

if the Hessian matrix is positive definite

$$\mathbf{H} = \begin{bmatrix} E_1 + E_N & E_N & \dots & E_N \\ E_N & E_2 + E_N & \dots & E_N \\ \dots & \dots & \dots & \dots \\ E_N & E_N & \dots & E_{N-1} + E_N \end{bmatrix} > 0$$

Here  $E_i = w''(\delta_i)$ , the tangential elastic moduli in the wells. To insure the positive definiteness of this matrix, we must require

$$A_j > 0, \quad j = 1, \dots, N-1 \quad (2.75)$$

where

$$A_j \equiv \left( \prod_{i=1}^j E_i \right) \left( 1 + \sum_{i=1}^j \frac{E_N}{E_i} \right) \quad (2.76)$$

are the principal minors of the Hessian matrix.

With the definition of  $k$ ,  $l$ ,  $m$  given above, we observe that stability depends only on  $l$ , the number of elements in the spinodal region. Thus if  $l = 0$  we have  $E_i > 0$  for all  $i = 1, \dots, N$ , and the matrix  $\mathbf{H}(\bar{\delta})$  is obviously positive definite. In the case  $l \geq 2$ , one can always regroup the elements in such a way that the first and the last elements are in the spinodal region. In this case, we have  $E_1 < 0$  and  $E_N < 0$  and so also  $A_1 < 0$ . Therefore, every configuration with more than one element in the spinodal region is unstable. Now, consider configurations with one element in the spinodal region. Suppose that this element is in the  $N-1$  position. Then  $A_j > 0$  for  $j = 1, \dots, N-2$  and stability depends on the sign of

$$A_{N-1} = \left( \prod_{i=1}^N E_i \right) \left( \sum_{i=1}^N \frac{1}{E_i} \right). \quad (2.77)$$

We can rewrite this expression as:

$$A_{N-1} = (E(\delta_I))^k (E(\delta_{II}))^l (E(\delta_{III}))^m \left( \frac{k}{E(\delta_I)} + \frac{l}{E(\delta_{II})} + \frac{m}{E(\delta_{III})} \right) \quad (2.78)$$

Now, since  $E(\delta_{II}) < 0$ , the necessary and sufficient condition for stability is:

$$\frac{k}{E(\delta_I)} + \frac{1}{E(\delta_{II})} + \frac{m}{E(\delta_{III})} < 0 \quad (2.79)$$

The elements are connected in series, so the effective elastic modulus can be written as:

$$\frac{\partial \bar{\sigma}}{\partial \bar{\delta}} = \left( \frac{1}{N} \sum_{i=1}^N \frac{1}{E_i} \right)^{-1} \quad (2.80)$$

and the stability condition for  $l = 1$  says that the overall modulus of the corresponding equilibrium branch must be negative.

For tri-linear element, the overall tension-deformation curve in the case of  $N$  half-sarcomeres, was obtained analytically in [62]. The stable branch are shown in Fig. 2.29 for the case of sufficiently steep spinodal region. There are two thresholds formulated in terms of overall strain  $\bar{\delta}$  ( $\bar{\varepsilon}$  in figure) outside which the system behaves like a chain of springs with convex energies. Here we have the so-called Cauchy-Born solutions, the homogeneous trivial configurations in which the elements are equally deformed. Inside these thresholds, the overall tension deformation curve does not show any regions with negative slope, however the global minimum solution (Maxwell path, see Fig. 2.29) presents a series of discontinuities in the tension due to the tension jumps as the elements transform from one phase to the other.

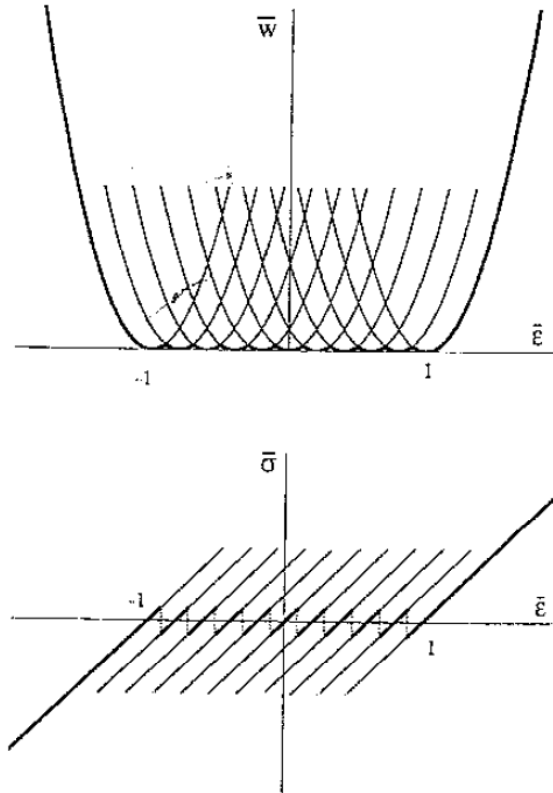


**Figure 2.29:** Absolute minimizer for the chain with ten trilinear springs. Maxwell path: bold line. From [62]

In the above consideration we have made implicitly a hypothesis that the kinetics of the transformation inside individual Xbs is much faster than the rate of the overall deformation. In this case, at each  $\delta$  we can deal only with one value of

tension. Even in this approximation, we have been dealing so far only with global minimum strategy corresponding to the assumption that the temperature  $T = 0$ , but the system can still overcome the barriers between the states with equal energy. In the next section we drop some of those assumptions and present a more realistic approach which takes into consideration a stochastic nature of the problem.

### Stochastic dynamics in a chain of half-sarcomeres

In order to construct a more realistic path for the chain of half-sarcomeres, we can use the stochastic dynamics method proposed in [73]. The method is based on the algorithm generated by Gillespie in the 1977 [15], to simulate efficiently systems of chemical reactions using limited computational power.

Consider a chain of  $N$  half-sarcomeres, each one represented by  $N_{Xb}$  cross-bridges acting in parallel. Each  $Xb$  can be in two configurations, one generating the high force (2.12) and another one generating the low force (2.11). For each  $Xb$  the passage from one configuration to the other is considered a stochastic event.

For simplicity, we shall assume that the change of configuration for each  $Xb$  is described by a jump process [73]. As in the original HS71 model, the rate constants are related through (1.14) and depend on the total length of the half-sarcomere. At every switching event (which represent the power stroke of one  $Xb$ ), the tension generated by the half sarcomere under consideration changes and a new mechanical equilibrium is reached before the next event takes places. The new mechanical equilibrium affects the length of all the half-sarcomeres in the chain. The present mechanical configuration defines the probability of the subsequent switching event (see Section A.9). The resulting system follows a particular set of local minima of the total energy instead of the global minimum.

We did not explore with this method our global model presented in Section 2.3, where both chemical rate constants  $k_+$  and  $k_-$  depend on the stretch of the half sarcomere (see later in Section 2.8). Instead, to roughly capture the elasticity inside the wells, we have made the following choice of the constants:

$$\begin{aligned} k_+ &= k^0 \left( e^{\frac{-Kd\delta/2}{k_B T}} \right) \\ k_- &= k^0 \left( e^{\frac{Kd\delta/2}{k_B T}} \right) \end{aligned} \tag{2.81}$$

where the constant  $k^0 = 1000s^{-1}$ . In this way we guarantee that both rate constants are affected by a change in the length of the half-sarcomere, still assuring that their ratio satisfies equation (1.14). A different choice was made in [73] where



(to mimic the hypothesis made by Huxley and Simmons in [10])  $k_-$  was made to be constant and  $k_+$  was defined by (1.14). However, despite this change, the results are similar.

With the Gillespie method one can create, point by point, the overall  $T_2 - \delta$  curve, imposing a value of the total deformation  $\delta$  and following the time evolution of the tension up to the steady state. In this way we can simulate the “real” stochastic behavior, obtaining a particular sequence of local minima chosen by our dynamics.

In Fig. 2.30 and Fig. 2.31 we show two numerical tests, with four and sixteen half sarcomeres. We can see that the analytical requirement excluding half-sarcomeres in the spinodal region is respected. Overall we obtained jumps and only positive slope of the overall  $T_2(\delta)$  curve. By increasing the number of half sarcomere, we approach a curve with a flat portion in the central region.

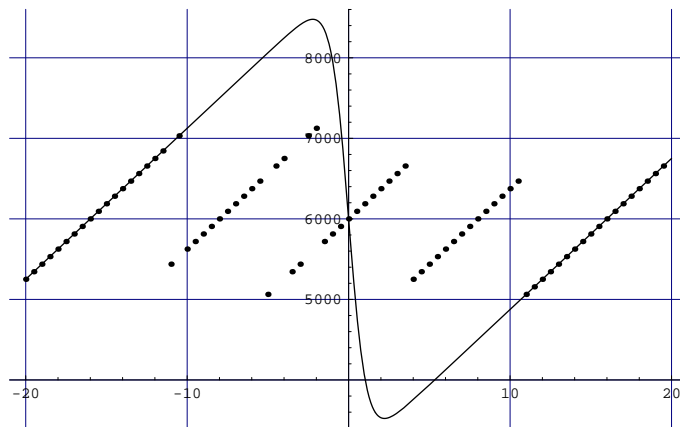


**Figure 2.30:** Tension deformation curve for four half-sarcomeres. Simulation (points) and  $T_2(\delta)$  curve for a single half sarcomere (solid line)

Notice that in real experiments, because of the large number of sarcomeres, it is not possible to see the jumps in the  $T_2(\delta)$  curve associated with the popping of individual half-sarcomeres. However, a non-homogenous distribution of the sarcomere’s lengths should be possible to observe in the myofibril. While some experiments indeed show such an inhomogeneity, at least in some regions of the tension-length curve [24], [89], it is not clear whether this mechanism is really operative in the muscle fibers [90].

To summarize, the method described above can potentially reproduce the flat portion of the  $T_2(\delta)$  curve under the assumption that different half-sarcomeres can be viewed as following different paths. A fully mechanical description of the energy landscape can be obtained only for rather simple shape of the  $T_2(\delta)$  curve

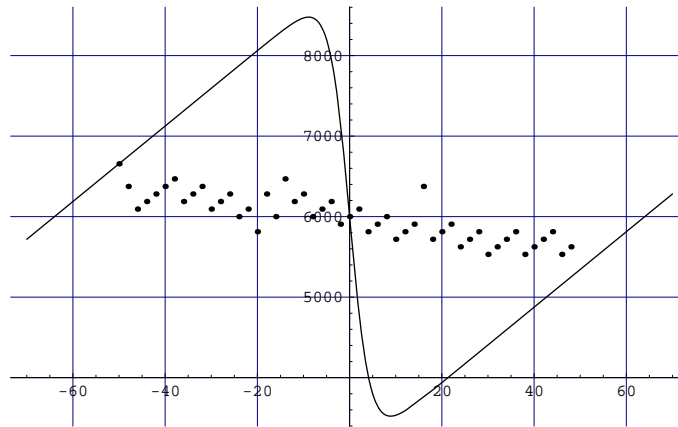


**Figure 2.31:** Tension deformation curve for sixteen half-sarcomeres. Simulation (points) and  $T_2(\delta)$  curve for a single half sarcomere (solid line)

describing individual half-sarcomeres. In order to proceed in the general case when the temperature  $T \neq 0$ , the stochastic dynamics methods appear to be necessary. The Gillespie method requires introduction of a chemical reaction and of the related rate constants. This is, however, against our main idea of staying with a fully mechanical model of muscle contraction. Simulation of a large scale continuous stochastic dynamics for the whole chain does not appear doable at the moment. Therefore, in the next Section, we focus on another way to capture the plateau of the  $T_2(\delta)$  curve.

## 2.7.2 Distribution of the attachment positions

Another way to obtain the flat plateau of the  $T_2(\delta)$  curve is to assure inhomogeneity already at the level of individual Xbs [48]. We recall that the basic element of every model of muscle contraction is the presence of thermal fluctuations. Even if these fluctuations small, compared to the scale of the power stroke, they can influence significantly the level of the stretch of the elastic element in the state of attachment to the actin filament. In the presence of thermal fluctuations we must also consider the possibility that the head attaches to actin site when its elastic element is away from its reference state. This will lead to a situation in which some Xbs have the elastic element stretched more than others, or even compressed. As a result we loose the uniformity of the population of Xbs. As it was observed in [48] where this mechanism has been proposed for the first time, this leads to the averaging of the ordinates of  $T_2(\delta)$  over the distribution of the attachment sites.

Let us first show how the distribution of the attached sites affects the formulas obtained in Section 2.6. The dispersion in the attachment positions can be

mimicked by a nontrivial distribution of the values of  $l_0$ . Assume that for the  $i$ -th Xb:

$$l_0^i = l_0 + \psi^i \quad (2.82)$$

where  $\psi^i$  is a random variable uniformly distributed in the finite interval of possible attachment sites. This range was postulated to be  $\pm 5.5/2 \text{ nm}$  in [48], because  $5.5 \text{ nm}$  is the diameter of the monomer of actin. This will also be the value used in the present work ( $l_0^i \in [l_0 - 2.75 \text{ nm}, l_0 + 2.75 \text{ nm}]$ ). The assumed dispersion affects directly the steady state probability distribution given by equation (2.35). Thus, we can write:

$$p_s^i(x, \delta, \psi^i) = \frac{e^{-E_T(x, \delta, \psi^i)/k_B T}}{\int_{-\infty}^{\infty} e^{-E_T(x, \delta, \psi^i)/k_B T} dx}. \quad (2.83)$$

The total energy depends on  $\psi^i$  only through the elastic energy

$$E_e(x, \delta, \psi^i) = \frac{1}{2} K (x - l_0 - \psi^i - \delta)^2. \quad (2.84)$$

The total tension in the steady state is then given by:

$$T_2(\delta) = \sum_{i=1}^{N_{Xb}} T_2^i(\delta) = \sum_{i=1}^{N_{Xb}} \int_{-\infty}^{\infty} (-K(xp_s(x, \delta, \psi^i) - (l_0 + \psi^i) - \delta)) dx \quad (2.85)$$

At a given  $\delta$  the tension  $T_2^i(\delta)$  for the  $i$ -th Xb is equal to the tension generated by the Xb with  $\psi^i = 0$  additionally stretched (or compressed) by  $\delta^i = \delta + \psi^i$ . The overall relative tension  $T_2(\delta)$  when the imposed increment is  $\delta$  is then the average of the values given by (2.29) over the range  $[\delta - 2.75 \text{ nm}, \delta + 2.75 \text{ nm}]$

$$T_2(\delta) = \sum_{i=1}^{N_{Xb}} T_2(\delta^i) \quad (2.86)$$

Similar formulas can be obtained for  $T_1(\delta)$ .

A nontrivial dispersion, compatible with the assumed distribution has been confirmed by X-ray interference studies in [88]. The authors used a high-resolution small angle X-ray scattering to study X-ray interference effects generated by the arrays of myosin Xbs in contracting muscle to obtain sub-nanometer resolution of the movements of the Xb during contraction. The observations show that in isometric contraction the lever arm angles are dispersed through  $\pm(20^\circ - 25^\circ)$  on either side of the mean orientation [88]. Also, it is shown that, during quick release, the Xbs move towards the new conformation in synchronized fashion, with constant dispersion.

An indirect evidence of the attachment site non-uniformity can be obtained from the multi-exponential fitting of the tension-time curves obtained in the experiments with sudden total length increment (see [49], [14], [86]). To explain this idea it is sufficient to recall that in the Huxley and Simmons 1971 model the rate of tension recovery  $r$  was given by:

$$r(\delta) = k_+ + k_- = k_-(1 + e^{-\frac{yKh}{k_B T}}) \quad (2.87)$$

where, again, their  $y$  is our  $\delta$ . If all Xbs have the same attachment distance  $l_0$ , then the tension vs. time curve for the half-sarcomere is:

$$T(t, \delta) = (T_1(\delta) - T_2(\delta))e^{-r(\delta)t} + T_2(\delta). \quad (2.88)$$

In the case when this assumption is valid, the experimental curve should be described by one exponential function. If we consider two equal populations of Xbs, with two different distances from the attachment site, say  $l_0 + \psi$  and  $l_0 - \psi$ , there appear two different rates  $r(\delta)$  which we shall denote by  $r(\delta + \psi)$  and  $r(\delta - \psi)$ . In this case the tension vs. time curve is given by:

$$T(t, \delta) = \frac{N_{Xb}}{2}[T_2(\delta + \psi) + (T_1(\delta + \psi) - T_2(\delta + \psi))e^{-r(\delta + \psi)t}] + \quad (2.89)$$

$$\frac{N_{Xb}}{2}[T_2(\delta - \psi) + (T_1(\delta - \psi) - T_2(\delta - \psi))e^{-r(\delta - \psi)t}]$$

One can see a sum of two exponential terms instead of one. The steady state value of the total tension is the average of the two values of  $T_2(\delta)$  of the corresponding populations. If more populations are present, a multi-exponential fitting would be needed to represent the resulting tension-time curve. In general, the dispersion implies that each Xb has its own level of pre-stretch and therefore the total energy is different for different elements. The global recovery can then be fit by a sum of exponential terms with different exponents. in the next Section we show that this is exactly what follows from experimental observation.

Therefore we can accept that the attachment sites are dispersed and, by performing a direct integration in the formulas for the tension (see, for instance, equation (2.85)), obtain the curves shown in Fig. 2.32(a). As we see, if one includes the distribution of attachment sites, averaging out the tension in the central region, one obtains a rather realistic behavior of the  $T_2(\delta)$  curve with negative slope flattened around  $\delta \simeq 0$ . The dispersion also affects the slopes of the linear segments of the  $T_2(\delta)$  curve and the  $T_1(\delta)$  curve. For instance, by maintaining the same values of parameters as in Fig. 2.19(b) but adding the dispersion of the attachment sites,

we obtain the curves shown in Fig. 2.32(a), where the curves with no dispersion are also shown for comparison. The remaining quantitative inconsistency leads to the necessity to slightly changing the values of parameters. The  $T_1(\delta)$  and  $T_2(\delta)$  curves obtained by the best fit (values reported in Table 2.1, column *Best fitting*) are shown in Fig. 2.32(b).

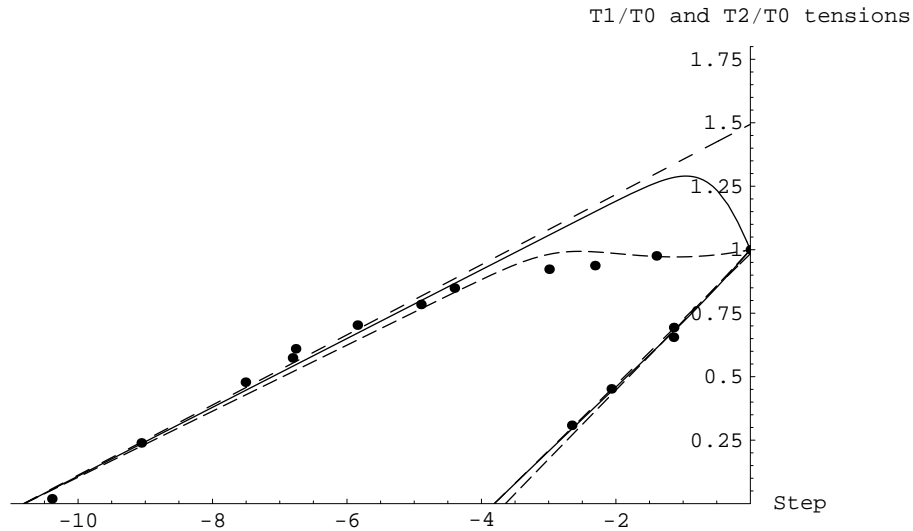
One can see that the predictions of the resulting model are in rather good agreement with experiments. While the optimal fitting should also depend on the elasticity of the filaments, which is not considered here, the basic features of the fast muscle response appear to be captured by the model with only two conformational states. This is most remarkable in view of the fact that we did not impose any phenomenological dependence of the rates of transitions on the length increment  $\delta$ .

**Table 2.1:** Values and meaning of the main parameters used for the numerical simulations and analytical computation for the purely Huxley and Simmons type model

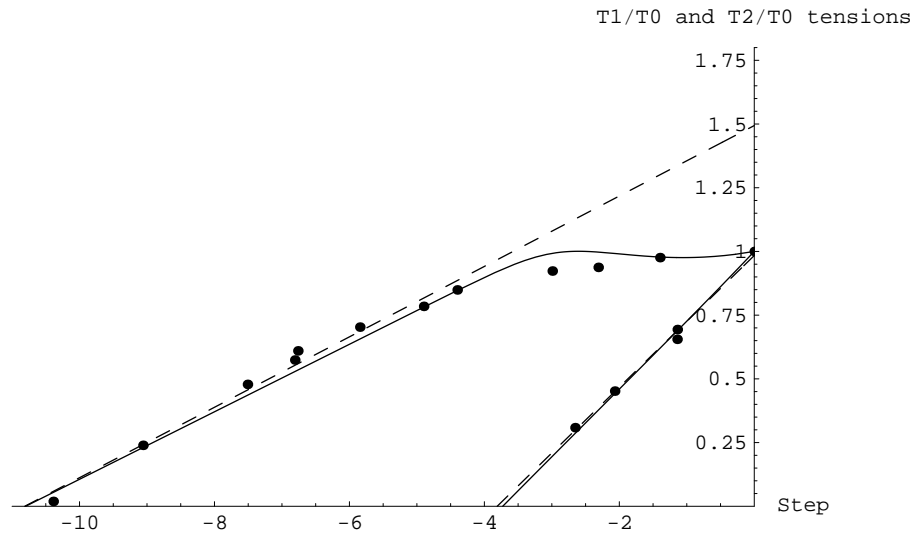
Description	Analytical value	Best fitting value
Intercept of $T_2/T_0$ with the abscissa	$\delta_{(T_2=0)} = 10.8 \text{ nm}$	-
Intercept of $T_1/T_0$ with the abscissa	$\delta_{(T_1=0)} = -3.87 \text{ nm}$	-
Slope of the $T_2/T_0$ vs. $\delta$ curve	$0.138 \text{ nm}^{-1}$	-
Slope of the $T_1/T_0$ vs. $\delta$ curve	$0.258 \text{ nm}^{-1}$	-
Rate of the slopes	1.87	-
Total stiffness $k_2 K / (k_2 + K)$	$1 \text{ pN/nm}$	-
Elasticity of the elastic element $K$	$4.4 \text{ pN/nm}$	$4.03 \text{ pN/nm}$
Elasticity of the low force generating state $k_1$	$18.17 \text{ pN/nm}$	$11.4 \text{ pN/nm}$
Elasticity of the high force generating state $k_2$	$1.29 \text{ pN/nm}$	$1.33 \text{ pN/nm}$
Ratio $k_2/K$	0.294 (0.310)	0.330
Curvature of the maximum $k_3$	$-8 \cdot 10^3 \text{ pN/nm}$	$8 \cdot 10^3 \text{ pN/nm}$
Position of the maximum $b$	-	$a_1(0) - (a_1^0 - a_2^0)/5$
Pre-stretch in low force generation state $l_0$	$0.05 \text{ nm}$	$0.39 \text{ nm}$
Distance between the chemical minima $a$	$10.75 \text{ nm}$	$10.41 \text{ nm}$
Thermal energy $k_B T$	$4.14 \text{ pNnm}$	-
Drag coefficient of the Xb $\eta$	$60 - 90 \text{ pNns/nm}$	-

## 2.8 Rate of fast tension recovery

In the Huxley and Simmons 1971 paper three features of the fast tension recovery were highlighted: the linear decrease in tension  $T_1(\delta)$ , the nonlinearity of the steady state tension  $T_2(\delta)$  and the particular kinetics behind the transition from  $T_1(\delta)$  to  $T_2(\delta)$ . In this Section we consider in more detail this last feature and show how



(a)



(b)

**Figure 2.32:** Fitting of the experimental data in the model with nonuniform distribution of the attachment sites. Points: experimental data. Straight dashed line: Linear best fitting of the experimental data. (a)  $T_1(\delta)/T_0$  and  $T_2(\delta)/T_0$  predicted without dispersion of attachment site (continuous lines) and with dispersion (dashed lines),  $k_2/K = 0.294$  (b)  $T_1(\delta)/T_0$  and  $T_2(\delta)/T_0$  with a dispersion of attachment site,  $k_2/K = 0.310$ . Abscissa units: nm

our modification of the Huxley and Simmons model matches the peculiarities of the kinetics of force recovery.

We recall that after the imposed length step, the tension quickly reaches the value  $T_1(\delta)$  and then follows an almost exponential time trajectory before reaching the final value  $T_2(\delta)$  (see Fig. 1.14(a)). Some authors used a multi exponential fitting to describe this curve and as a result had to deal with several characteristic times [49] [14] [86], while others have simply taken as a characteristic scale the time needed to reach the value  $T_1 + (T_2 - T_1)/2$ . This last approach is equivalent to approximating the tension-time curve with a single exponential function of time:

$$T(t, \delta) \simeq (T_1 - T_2)e^{-rt} + T_2. \quad (2.90)$$

One can then define the resulting parameter  $r$  as the characteristic rate of the process: indeed  $r^{-1}$  is the time needed to reach the  $(1 - 1/e) = 64\%$  of the total recovery.

In experiments it takes several milliseconds to reach the value  $T_2$ . After shortening the final tension  $T_2$  is reached after a shorter time, less than one millisecond for high negative length increment. In general the rate of recovery  $r$  varies with  $\delta$ . Thus we already know that  $r(\delta)$  is low at high stretch step and increases almost exponentially as one passes to higher shortening steps (see Fig. 1.15). Huxley and Simmons fitted the experimental dependence  $r(\delta)$  with the function:

$$r(y) = r_0(1 + e^{-\alpha y})$$

with  $r_0 = 0.2 \text{ ms}^{-1}$  and  $\alpha = 0.5 \text{ nm}^{-1}$ .

The particular shape of the experimentally measured function  $r(\delta)$  affected considerably the structure of the Huxley and Simmons 1971 theory. Thus, the choice of very narrow energy wells in this model was directly linked to the necessity to reproduce the particular slow recovery at large positive stretching steps.

To explain this statement we recall that the Huxley and Simmons 1971 model predicts that  $r(\delta) = k_+ + k_-$ , where the  $k$ 's are the reaction constants controlling the rate of transition from one conformational state to the other. The condition of detailed balance in our notations ( $a$  is negative in our model) requires that  $k_+/k_- = \exp[-\delta K(-a)/k_B T]$ . Given this condition one still has the freedom to modify the constants at different values of  $\delta$  in order to fit the experimental data. In the Huxley and Simmons model this freedom is essentially absent because the energy landscape, even if degenerate, is given. By putting a very narrow well in the post-power stroke state, Huxley and Simmons put the maximum and the

minimum at the same value of  $x$ . In this case every change in the stretch of the elastic element affects both the “well” and the “barrier” in the same way. The condition  $k_- = \text{const}$  is guaranteed by this choice, and consequently  $r$  goes to zero at high positive increments according to

$$r(\delta) = k_+ + k_- = k_-(1 + \exp[-\delta K(-a)/k_B T]). \quad (2.91)$$

Under this assumption the fitting of the experimental rate recovery curve becomes possible and it gives the values of both  $k_-$  and  $Ka$ . We recall that the value of  $Ka$  obtained in this way by Huxley and Simmons turned out to be grossly underestimated.

Before discussing quantitative effects of the elasticity of the wells, we observe that by dropping the hypothesis of infinitely steep wells, we loose the strong asymmetry of the function  $r(\delta)$  for lengthening ( $\delta > 0$ ) and shortening ( $\delta < 0$ ). Indeed, in this case,  $k_-$  is no longer constant and increases with  $\delta$  (this also justifies the assumption (2.81)).

In our general case we can quantify the dependence of the kinetic constants on the structure of the energy landscape by using Kramers’ theory (see Section A.7, we also refer to [74]). The recovery of tension is a non-equilibrium process, and the canonical distribution does not allow one to compute the tension transients. We should instead solve directly the Fokker-Plank equation and obtain the time dependent probability distribution  $p(x, t)$ . We recall that Kramers’ theory (see Section A.7) is based on the hypothesis that, in a double well potential, the time needed to relax inside each of the wells is much shorter than the mean time of the transition between the wells. This is true for the case of muscle with realistic values of parameters and correct geometry of the myosin heads [64]. Thus, if the drag coefficient of the particle is  $60 - 90 \text{ pNns/nm}$ , the characteristic time to relax inside each minima is of the order of  $\tau_1 \eta / K \simeq 0.1 \mu\text{s}$ . The mean exit time should be comparable to the time scale of the recovery process giving  $\tau_2 \simeq 1 \text{ ms}$ . Now, it is easy to check  $\tau_2 \gg \tau_1$  as required, and one can approximate the diffusion process by a jump process. Defining the fraction of Xbs in each well during the transient as:

$$\begin{aligned} \bar{n}_1^\delta(t) &= \int_{a/2}^{\infty} p(x, \delta, t) dx \\ \bar{n}_2^\delta(t) &= \int_{-\infty}^{a/2} p(x, \delta, t) dx, \end{aligned} \quad (2.92)$$

and the corresponding quantities at the steady state (2.36), one can write:

$$\dot{\bar{n}}_1^\delta(t) = -\dot{\bar{n}}_2^\delta(t) = -k_+ \dot{\bar{n}}_1^\delta(t) + k_- \dot{\bar{n}}_1^\delta(t) = k_- - (k_+ + k_-) \bar{n}_1^\delta(t). \quad (2.93)$$



In the Kramers' theory the “chemical” rate constants are fully determined by the shape of the energy landscape. Thus for  $k_-$  we obtain:

$$k_- = (k_B T / \eta) [n_2^\delta \int_{a_2}^{a_1} p_s(x, \delta)^{-1} dx]^{-1} \quad (2.94)$$

which gives for the rate of recovery:

$$r(\delta) = k_+ + k_- = \frac{k_B T / \eta}{n_1^\delta n_2^\delta \int_{a_2}^{a_1} p_s(x, \delta)^{-1} dx}. \quad (2.95)$$

Here  $p_s(x, \delta)$  in (2.94) and (2.95) is a function of the energy landscape which can be found from equation (2.35). Fitting of the experimentally observed rate of recovery  $\delta$  dependence will then pose a constraint. We shall view this constraint as a restriction on the height of the energy barrier between the wells.

Observe that since  $k_2 \neq \infty$  it is no longer true that  $k_- = \text{const}$  as in the Huxley and Simmons case. From equation (2.95) we can see that the leading term is inversely proportional to  $n_1^\delta n_2^\delta$ , and when  $\delta$  is positive and large, we expect that  $n_2^\delta \simeq 0$  and  $n_1^\delta \simeq 1$ . Therefore  $r(\delta)$  must increase for high positive values of  $\delta$  which is in contradiction with observations.

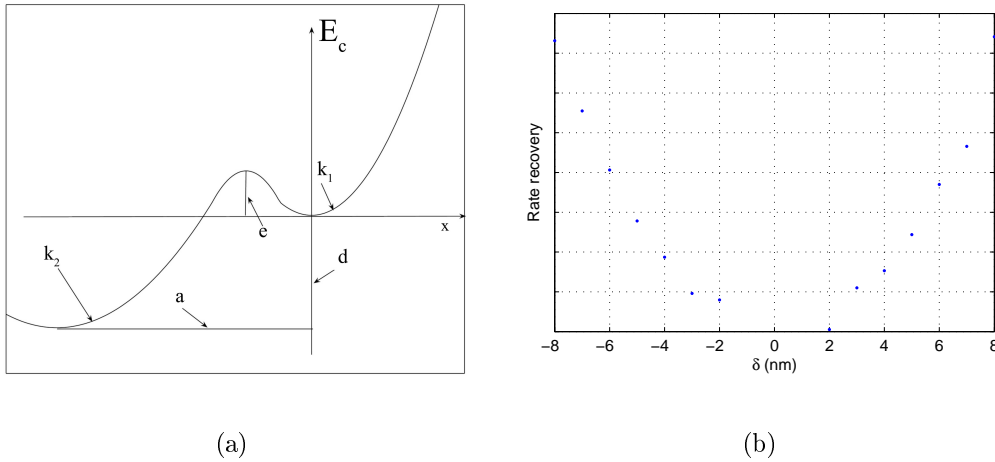


**Figure 2.33:** Increasing rate of recovery for high stretches and related chemical energy. (a) Chemical energy (b) Rate of recovery vs  $\delta$

One way to avoid this behavior at large  $\delta > 0$  is to make the maximum of the energy (the barrier height) dependent on the imposed step. To this end we can consider a piecewise parabolic energy, with the third parabola placed upside down

between the two conventional parabolic wells:

$$E_c(x) = \begin{cases} \frac{1}{2}k_1x^2 & x \geq b_1 \\ \frac{1}{2}k_3(x-b)^2 + e & b_2 \leq x < b_1 \\ \frac{1}{2}k_2(x-a)^2 + d & x < b_2 \end{cases} \quad (2.96)$$

Here, as postulated,  $k_1 > 0$ ,  $k_2 > 0$  and  $k_3 < 0$ . The function (2.96) is shown in Fig. 2.33(a), where the height of the energy is denoted by  $e$ . The parameters can always be chosen in such a way that the total energy is a continuous function of  $x$ , even if its first derivative is not. The smoothness of the energy is not important for computing the integrals in the formula for  $p_s(x, \delta)$ . If the maximum is constant the rate of recovery shown behavior discussed before, as shown with a numerical simulation in Fig. 2.33(b). Suppose now that the local maximum of  $E_c(x)$  representing the barrier is a monotonically increasing function of  $\delta$ ,  $e = e(\delta)$  as in Fig. 2.34(a). In this case we can reduce the rate of recovery in stretching tests, obtaining a realistic behavior as in Fig. 2.34(b). Indeed, with the increase in  $e$  the weight of the integral term in (2.95) also increases which can in principle balance the term  $n_1^\delta n_2^\delta$  and ensure the desired shape of  $r(\delta)$ . This is however not the choice that we

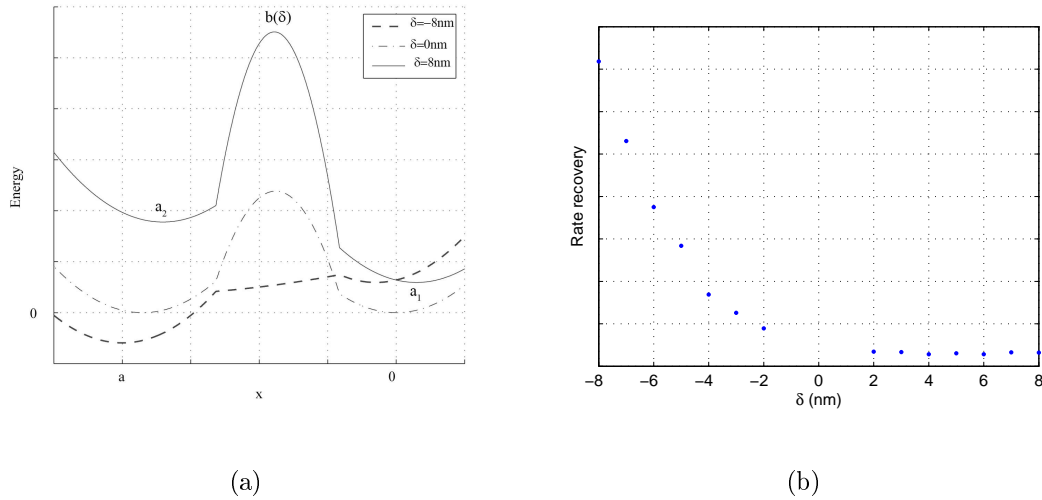


**Figure 2.34:** Variable barrier in the chemical energy. (a) Shape of  $E_t$  for three values of  $\delta$ , the maximum  $e$  is a function of  $\delta$ . (b) Rate of recovery when  $e(\delta)$

make in the rest of the Thesis.

We decided instead to simply omit the stretching part of the curve  $r(\delta)$ , for the following reasons. First, recent studies show that in the stretching experiments

mechanisms other than simple power stroke may be important in generating the tension recovery [91]. Till now we always considered that, even if the skeletal muscle's myosin has two heads, only one head is involved in the power stroke process. If, on the other hand, the steric effect due to the stretch allows the second head to be attached contemporarily, a change in the total number of Xb has to be introduced, probably as a function of the stretch itself. Second, the experimental time scale of tension recovery after stretch is so slow (tens of milliseconds [49]) that the attachment-detachment process may become important. Both mechanisms, getting the second head involved and activating the attachment-detachment mechanism, are neglected in the Huxley and Simmons model. We also omitted them in the present study which only aims at describing the effect of elasticity in the wells. In what follows we shall be mostly preoccupied with the physiological range of behavior of muscles, which means with the shortening range. In this case we can avoid introducing questionable  $e(\delta)$  behavior.

With this limitations in mind, we can still deal quantitatively with the two other defects of the Huxley and Simmons 1971 model. We recall that already in the 1978 [17] it was observed that the hypothesis of narrow potential wells leads to an unrealistic time scale of the transition process. Indeed, the rate of transition is slower at  $\delta = 0$ , where the Xb has to be stretched up to  $a$  in order to jump, than at  $\delta = a$ , where it can jump without being stretched at all. Huxley and Simmons did not know the elastic energy associated with this stretch, because  $K$  was unknown, but they associated the difference in the values of  $E_c(x)$  in the bottoms of the wells with the ATP consumption needed to change the configuration. More specifically, they assumed that the energy needed to stretch a Xb up to  $a$  is  $18k_B T$ , which is the free energy liberated by the ATP as known at that time. Because the rate of recovery is changing exponentially with the  $\Delta E/k_B T$ , they deduced that the ratio of the rates in the cases  $\delta = 0$  and  $\delta = a$  has to be equal to  $e^{-18} = 10^{-8}$ , a value much higher than experimentally observed. Huxley came back to this problem in 1996 [48], showing that indeed at realistic values of  $K$ , the rate of recovery is unrealistically fast (see Fig. 2.5).

Regarding the second problem with the HS71 model, we have to reiterate again that Huxley and Simmons used a jump process to simulate the change in configuration, and that  $k_-$  was used as a free parameter whose value could be imposed to fit the experimental data. In a more realistic model (2.96) the Xb has to stretch the elastic element to overcome the energy barrier  $E_{max} = d$ . In the Langevin equation setting for a single quadratic energy well we can estimate the mean first

passage time (see Section A.6.3), obtaining:

$$t_K = \eta/K \sqrt{\pi/4} \sqrt{k_B T / E_{max}} \exp[E_{max}/k_B T] \simeq 1 \text{ s} \quad (2.97)$$

Here we used  $\eta = 90 \text{ pNns/nm}$ ,  $K = 1 \text{ pN/nm}$ ,  $k_B T = 4.14 \text{ pNnm}^2$  and  $E_{max} = 80\% \Delta G_{ATP} = 20 k_B T$ .

This rough estimate is obviously not compatible with the observed time scale of the process. The non-zero curvatures of the wells help, however, to avoid the problem. The equation (2.97) shows that the time needed to overcome the barrier is related only to its height. With our first double parabolic energy model (2.7) and, with  $l_0 = 0$ , the energy barrier is equal to:

$$\Delta E_T = \frac{1}{2}(k_1 + K) \left[ -\frac{ak_2(K + k_2)^2 - \sqrt{a^2 k_2^2 (K + k_2)^2 (K^2 + 2Kk_1 + k_1 k_2)}}{(k_1 - k_2)(K + k_2)} \right]^2. \quad (2.98)$$

One can see that  $\Delta E_T$  approaches asymptotically the value  $1/2Ka^2$  when  $k_2$  goes to infinity. For finite values of  $k_2$  the barrier is lower than that as shown in Fig. 2.35 for given values of  $K$  and  $k_1$ . In the case of narrower wells the Xb that is in the well on the right does not feel the presence of the second well till it reaches the maximum, which for  $k_2 = \infty$  is in  $x = a$ , therefore this value of  $x$  has to be reached only through thermal diffusion in a quadratic potential with curvature  $K + k_1$ . Within the hypothesis of elastic wells, thermal fluctuations must stretch the elastic element only till an intermediate configuration because afterwards the system will be driven by the drift forces. Mathematically this means that the value of  $t_K$  (2.97) has to be computed with the lower value of  $\Delta E_T$  obtained from equation (2.98).

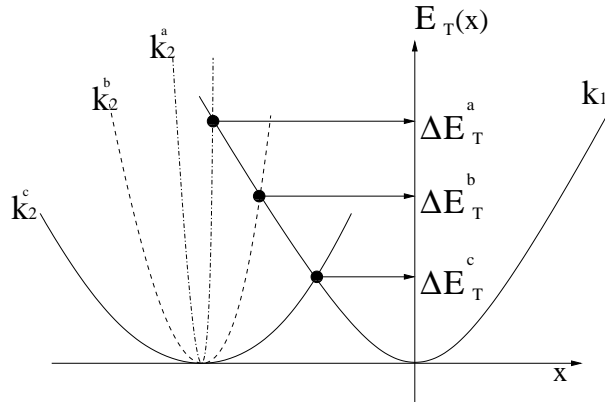


**Figure 2.35:** Effect of the lowering of  $k_2$  on the size of the energetic barrier.  $k_1$  and  $K$  are assumed constant. The figure is a sketch where the third parabola is not considered

To summarize, introduction of the elasticities in the wells affects the first mean passage time and allow the fitting of  $r(0)$ . To reproduce the whole curve  $r(\delta)$  in the shortening regime, we need to consider the third parabola as in (2.96). In order to affect as less as possible the results obtained for the steady state, we choose to make this third parabola as narrow as possible. In this way we can match the continuity condition without affecting the bottom areas of the minima.

The Kramers' theory (see Section A.7) gives an analytical expression for the dependence of the rate of recovery on  $\delta$  (equation (2.95)). It can be simplified further when the asymptotic approximation, described in equations (2.41), is valid. In this case we obtain (see [74] for a formal derivation):

$$r(\delta)^{-1} = \quad (2.99)$$

$$2\pi[n_1 n_2]^{\frac{1}{2}} [|E_T''(b)|^{-\frac{1}{2}} E_T''(a_1)^{-\frac{1}{4}} (E_T''(a_2))^{-\frac{1}{4}}] \exp \left[ \frac{2E_T(b) - E_T(a_1) - E_T(c_2)}{2k_B T} \right].$$

Here we have used the hypothesis concerning the narrow structure of the third parabola, allowing us to approximate the value of the variable  $x = x_{max}$  (where the total energy reaches its maximum) by  $b$ . Indeed, because  $K/k_3 \simeq 0$ ,

$$x_{max} = \frac{K/k_3 \delta + b}{1 + K/k_3} \simeq b. \quad (2.100)$$

Within this approximation, the presence of the third parabola gives rise to a constant multiplier (pre-exponential factor) in (2.99) of the form

$$|E_T''(b)|^{-\frac{1}{2}} \exp \left[ \frac{E_T(b)}{k_B T} \right].$$

This constant value has been used to fit  $r(0)$ .

With all the approximation made, the analytical expressions needed to analyze the influence on  $r(\delta)$  of the parameters of the model are too complex, due to the presence in equation (2.99) of the terms  $n_1$  and  $n_2$ . Therefore, instead of using the analytical solution we can as well turn to direct numerical integration in the formula (2.95). We assume that we are in the framework of the distributed attachment sites model as in Section 2.7.2. Then for each attachment site we obtain its own value of  $r(\delta)$ . To replace them by a single function of  $r(\delta)$  allowing one to make comparison with experiments, we plot the curve

$$f_{exp}(t) = \frac{1}{n_{exp}} \sum_{i=1}^{n_{exp}} e^{-\alpha^i t} \quad (2.101)$$

and then perform one-exponential fitting of this curve. The resulting function  $r(\delta)$  is strongly controlled by the choice of the parameter  $b$  and we used this remaining freedom to fit the experimental curve. In fact, this parameter can be viewed as a kind of opposite to the one used in Huxley and Simmons 1971 to fit the same curve: shifting  $b$  to the left, makes the dependence of  $k_+$  on  $\delta$  weaker, because the local maximum at  $b$  and the local minimum in the first well, become closer.

The overall predictions of the model are compared with experimental data in Fig. 2.36 for the set of parameters reported in Table 2.1, column *Best fitting*. This set of parameters works rather well for both the rate of recovery and the steady state behavior (see Fig. 2.32(b)).

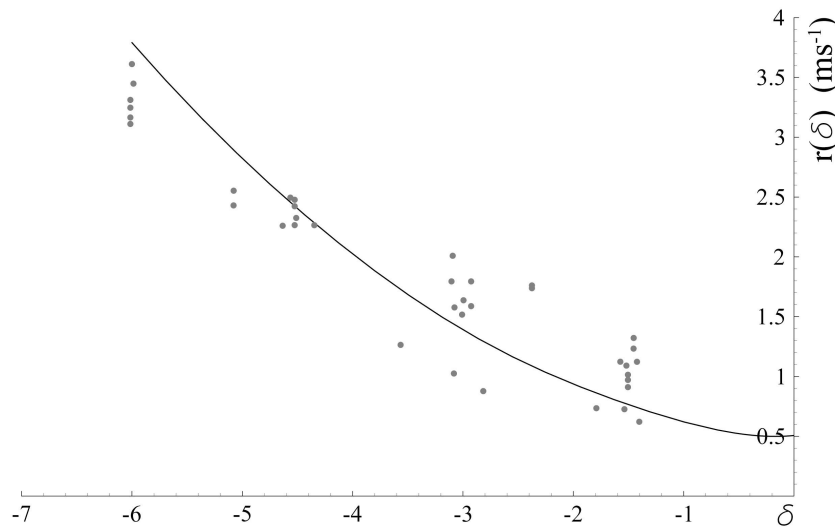


**Figure 2.36:** Rate of the tension recovery at different length steps  $\delta$ . Comparison of the predicted values (solid line) at the values of parameters shown in table (2.1), and the experimental points (from [10], [14], [67], adapted to be consistent)

## 2.9 Discussion

We would like to make some final comments regarding the description of the overall elasticity, since its value have previously generated problems for the Huxley and Simmons 1971 model. The introduction of the elasticities in the wells, makes ambiguous the definition of the *total* stiffness of the Xb. This stiffness is represented by two elastic elements in series and does not depends on  $K$  only. It also depends on the state of the bi-stable element. If the experimental rigidity is measured in rigor, where  $n_2 = 1$  and  $n_1 = 0$ , it should assume the value  $k_2 K / (k_2 + K)$ . We choose the parameters  $k_2$  and  $K$  to ensure that this total stiffness is equal

to  $1pN/nm$ . This value is lower than the values obtained in experiments, but we should remember that the elasticities of the filaments have been neglected in our analysis. The experimentally measured value of total elasticity does not take into account the compliance of the filaments, while the data that we have used are obtained from the whole structure: cross-bridge and filaments. Thus, the value assumed for total elasticity in our model is  $1pN/nm$ , which must be interpreted as the elasticity of the cross-bridge and the filaments connected in series. This makes this “seemingly” low value realistic.

In this Chapter we have obtained a quantitative description of the power stroke in a fully mechanical framework. We model the other part of the Xb cycle, the attachment-detachment process, in the next Chapter.

# Chapter 3

## The attachment-detachment process

### 3.1 Introduction

The physiological shortening of skeletal muscles can vary over a wide range of lengths, reaching up to several centimeters. Since the sarcomeres in the myofibril are distributed in series, such huge contraction is achieved by means of a much smaller shortening of each half-sarcomere. The series structural organization allows each half-sarcomere to maintain its length in the plateau interval of the relation force-length  $F-l$  described in Chapter 1. This helps to stabilize muscle mechanical behavior and optimize the force generated. In the experiments of interest the sarcomere, having a physiological length of  $2.2\ \mu m$ , can shorten in the range of tenths of a micrometer [67]. A single myosin motor produces a force of  $5\ pN$  [92] and due to the parallel distribution of the contractile units inside the sarcomere, the tension generated in each actin filament can be two orders of magnitude larger.

As described in Chapter 2, the typical size of the power stroke is of the order of ten nanometers [84] and the distribution of the Xbs in parallel limits the maximum power-stroke related shortening of a half-sarcomere to this value. The larger global shortening (tenths of a micrometer) is generated by a cyclic interaction of the Xbs with the active sites on the actin filament. During this process a detachment in the post-power stroke configuration of Xb is needed before the next attachment in the pre-power stroke configuration takes place. As explained in Chapter 1, the corresponding cycle was first proposed in 1971 [9], it is now called Lymn-Taylor cycle. The description of this cyclic attachment-detachment process can be found neither in the HS71 model nor in the model described in Chapter 2, because both neglect the attachment-detachment process. In order to have a comprehensive mechanical model of muscle contraction a new component has to be added.



A first model of cyclic interaction between actin and myosin was already presented in Huxley 1957 model [4] described in Chapter 1. Its first essential feature is that each Xb contains an elastic element which allows for Brownian oscillations before the attachment and which generates a force after the attachment. The second essential feature is that the rate constants for the attachment-detachment process depend on the stretching of the elastic element and are asymmetric around the unstressed configuration. As we show, these are the two fundamentals hypotheses behind the so-called *Brownian ratchet* idea which is the main subject of the present Chapter. Recently Brownian ratchets have been used to model the behavior of various molecular motors (see [68] for a comprehensive review), a family of proteins that transform chemical energy into mechanical work.

Skeletal muscle myosin II, the main protein of the contraction mechanism, belongs to the superfamily of a motor proteins found in eukaryotic tissues. Motor proteins generate motion inside the cell which is faster than diffusion: the complex structure and the dimension of the eucaryotic cells make the diffusion process too slow to supply the needed transport velocities of nutrients, waste, protein etc. An increase in the size of the cell by a factor of 10 should be slowing down the diffusional transport by a factor of 100 (see Section A.4 in Appendix). Instead motor proteins can transport cargos at constant speed by walking along either the microfilaments (actin) or microtubules.

The most prominent example of actin motors is myosin II, while kinesin and dyneins are microtubule motors. Two important aspects common to all cytoskeleton filaments have been observed experimentally: first they exhibit periodicity with the period of the order of  $10nm$ ; second they are polar, so it is possible to define a “positive” direction for the motion (see [50] and references therein). Modeling of the motion of actin motors must take into consideration that the acting configurational forces are only few times  $k_B T$ , and therefore the escape times for the energy wells is finite. Therefore molecular motors are microscopic objects that live in Brownian domain. Since they move along one dimensional periodic structures they can be modeled as Brownian ratchets [40], [32], [51].

We start by introducing a simple non Brownian mechanical model of a ratchet which furnishes the desired extension of the model proposed in Chapter 2 but which is not compatible with the idea that the motor is powered by the hydrolysis of ATP. Therefore we reintroduce fluctuations and review the particle motion in a tilted periodic potential subjected to thermal noise. Then we move to Brownian motors, exhibiting the variety of their types and explaining the way in which they are able

to rectify the external noise using an appropriate structure of the potential and a source of colored noise which maintains the system out of equilibrium. In particular we describe in some detail two important types of Brownian ratchets that can be useful in muscle mechanics. Next we modify one of these models and adapt it to the physiology of muscle contraction. We then consider several interacting motors and introduce the system of stochastic differential equations governing their collective dynamics. The analytical treatment of such type of systems does not appear feasible and to analyze different relevant regimes we develop a numerical method allowing one to simulate the behavior of the proposed model. Some qualitative results obtained in the course of our numerical experiments are discussed at the end of the Chapter.

## 3.2 A model of frictional motor

The model of Huxley and Simmons is able to mimic the steady state tension developed by the muscle in the isometric case ( $T_0$ ). This tension however is maintained without consumption of energy, which violates physiological experience. As we have seen in Section 1.3.1, where we described the experiments made by A.V. Hill in 1938, during isometric contraction skeletal muscles constantly produce heat (see the *maintenance heat rate* term in (1.1)). This fact indicates that cyclic actomyosin interaction requiring energy source is present even during macroscopically steady isometric contraction. In Section 3.1, we discussed the need of a new component in the model in order to describe the large observed shortening of muscles. Now we see that such extension of the model is needed even to describe the steady state force generation in the isometric case.

To understand this better we may think in terms of an analogy with a car that is kept steady on an uphill road. We can reach this situation in two ways, either by activating the mechanical breaks, where no energy is required, or by maintaining the engine working and producing a forward force that balances exactly the backward force. Obviously, in the latter situation the clutch is constantly generating heat and therefore the energy has to be constantly consumed. Despite the losses this situation is more flexible allowing the driver to adapt quickly to change in the external conditions (e.g. green light replacing red light).

We can use this intuitive analogy to try to mimic the attachment-detachment cycle responsible for a constant force and a constant heat rate in tetanized muscle. Consider the following mechanical model. Suppose that a body with weight  $P$  is

placed on a belt which is moving with a speed  $v$ . The belt is characterized by a coefficient of dynamic friction  $\mu_d$  and the load is attached to a spring of rigidity  $K$  (see Fig. 3.1(a)). The equation of motion for a continuously sliding body can be written as

$$m\ddot{x}(t) + Kx(t) + \mu_d P = 0. \quad (3.1)$$

The body reaches the steady state  $\ddot{x} = \dot{x} = 0$  at the position  $x$  where  $-Kx = \mu_d P$ . Observe that the constant force that the model produce is exerted on the external wall. In order to produce this constant force, a certain amount of energy must be spent to maintain motion of the belt. If we substitute the elastic element with a constant force  $T$ , the body will moves only when  $T = \mu_d P$ , but at this value the velocity can not be determined by this model (Fig. 3.1(a)) The problem with this

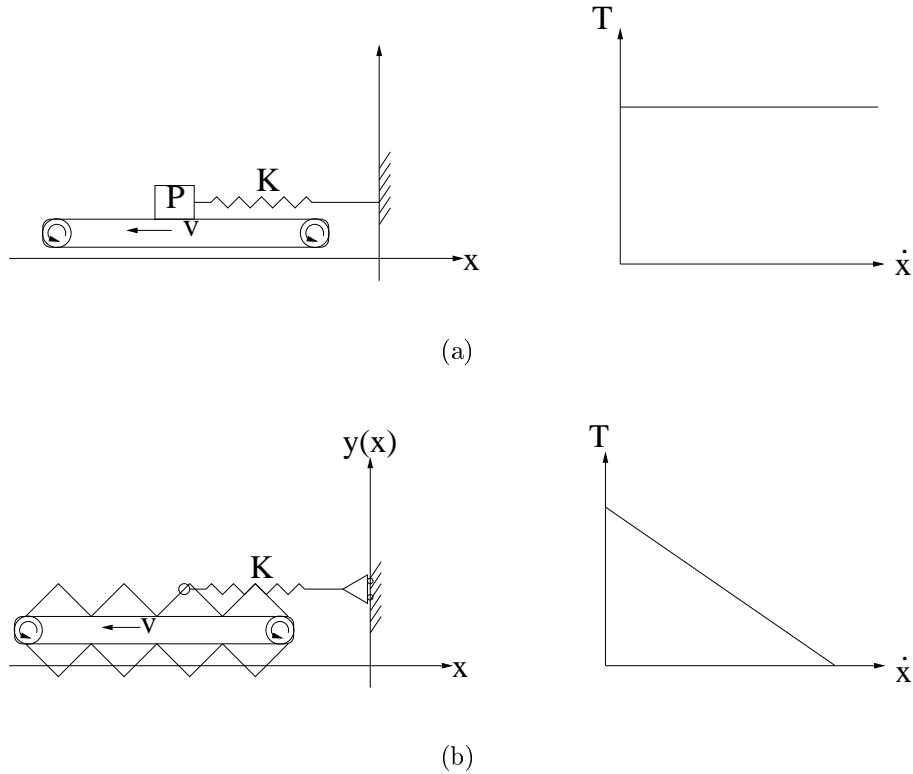


**Figure 3.1:** Mechanical models for a constant heat production. (a) Friction belt. (b) Rugged rail

model is that the force does not depend on the velocity. In order to relate the generated force with the velocity we can replace the frictional belt by a rugged landscape as in Fig. 3.1(b). Using a bit oversimplified approach, we can view the particle  $x$  as moving on a two-dimensional rail  $y(x)$ . Suppose for simplicity that

the rail is piecewise linear:

$$y(x) = \begin{cases} +\tan(\alpha)(x - n/2) & n < x < n + 1/2 \\ -\tan(\alpha)(x - n/2) & n + 1/2 < x < n + 1 \end{cases} \quad |n| = 0, 1, \dots \quad (3.2)$$

Suppose that the rail is moving in the negative direction at a constant speed  $v$  so that  $y(x, t) = y(x + vt)$ . Suppose also that the particle is embedded in a viscous fluid which provide in this model a dissipative mechanism. Finally, we place a spring which links the particle to a fixed position  $x = 0$ . In the overdamped regime, the equation of motion of the particle takes the form

$$[1 + \tan^2(\alpha)]\dot{x}(t) + \frac{K}{\eta}x(t) + v \tan^2(\alpha) = 0. \quad (3.3)$$

The solution can be written as:

$$x(t) = -\frac{v\eta}{K} \tan^2(\alpha) [1 - e^{-\frac{K}{\eta} \cos^2(\alpha)t}] \quad (3.4)$$

It is not difficult to see that the switch from one branch in (3.2) to the other does not change the reaction force acting on the particle due to the rail. The position of the particle reaches the steady state  $x = -(v\eta/K) \tan^2(\alpha)$  exponentially fast. As we see the higher is the velocity of the belt the larger is the force acting on the spring. The motion of the belt here is mimicking the effect of the ATP hydrolysis.

If we switch from the isometric condition to an isotonic one, removing the spring and applying to the particle a constant external force  $F_{ext}$ , we can construct the force velocity curve:

$$\dot{x}(t) = -\cos^2(\alpha) [F_{ext}/\eta + v \tan^2(\alpha)]. \quad (3.5)$$

One can see (Fig. 3.1(b)) that the velocity depends on  $F_{ext}$  linearly. The main problem with this model is however elsewhere. Thus it is clear that the isotonic energy release due to hydrolysis of ATP can not be represented by the unidirectional force generated by the moving belt. The way to overcome this problem is to replace a mechanical ratchet by a Brownian ratchet.

### 3.3 Brownian ratchets

When thermal fluctuation are not negligible, the equation of an overdamped motion of a particle in a potential  $V(x)$  takes the form (Langevin equation, see Section A.3):

$$\eta\dot{x}(t) = -V'(x) + \sqrt{\eta k_B T} \Gamma(t). \quad (3.6)$$

The random term  $\Gamma(t)$  corresponds to white noise and has the following proprieties:

$$\langle \Gamma(t_1) \rangle = \int_{-\infty}^{\infty} x_1 p_{\Gamma}(x_1, t_1) dx_1 = 0, \quad (3.7)$$

where  $p_{\Gamma}(x, t)$  is the probability that  $\Gamma$  assumes the value  $x$  at time  $t$ , and

$$\langle \Gamma(t_1) \Gamma(t_2) \rangle = \int_{-\infty}^{\infty} \int_{-\infty}^{\infty} x_1 x_2 p_{\Gamma}(x_1, t_1; x_2, t_2) dx_1 dx_2 = \delta(t_1 - t_2). \quad (3.8)$$

In what follows for every function  $f(x)$  of a stochastic variable  $x$  whose probability density function is  $p(x)$ , the brackets  $\langle f(x) \rangle$  will stand for its average value computed as:

$$\langle f(x) \rangle = \int_{-\infty}^{\infty} f(x') p(x') dx'. \quad (3.9)$$

Now suppose that  $V(x)$  is a double well potential. Then, as it was explained in Chapter 2, equation (3.6) describes the Huxley and Simmons type model (see equation (2.32)). The corresponding Fokker-Plank equation has the following steady state solution:

$$p_s(x) = N \exp[-V(x)/(k_B T)]. \quad (3.10)$$

The crucial condition for (3.10) to be admissible is that the probability current

$$S = -\frac{V'(x)}{\eta} p - \frac{k_B T}{\eta} \frac{\partial p}{\partial x} = 0. \quad (3.11)$$

We recall that in the steady state we must have  $S(x) = \text{const.}$  When we know additionally that the energy  $V(x)$  goes to infinity at the boundaries, we can conclude that  $S = 0$ .

When we consider a periodic potential  $V(x)$ , the condition  $S(x) = 0$  is no longer true, and the most important part of the analysis is to compute the constant  $S$  for the steady state. The constant  $S$  is a function of the parameters of the potential  $V(x)$ . In Appendix (Section A.8) we show that the constant probability current  $S$  is related to the mean velocity  $v$  (*drift* velocity) of the particle through the following relation:

$$\langle v \rangle = \langle \dot{x}(t) \rangle = 2\pi S \quad (3.12)$$

An important observation concerning the periodic potential  $V(x)$  was obtained by Risken [23]. He showed that in a periodic potential  $V(x)$  of period  $L$  which is tilted by a constant force  $F$ , i.e.  $V(x + L) = V(x) + F$ , the steady state drift velocity is given by:

$$\eta v = \eta \langle \dot{x}(t) \rangle = \frac{2\pi D(1 - e^{-2\pi F/D})}{\int_0^{2\pi} e^{V(x)/D} dx \int_0^{2\pi} e^{-V(x)/D} dx - (1 - e^{-2\pi F/D}) \int_0^{2\pi} e^{-V(x)/D} dx \int_0^x e^{V(x')/D} dx'} \quad (3.13)$$

where  $D = k_B T / \eta$  is the diffusion coefficient. We immediately see that  $\langle \dot{x} \rangle \neq 0$  if and only if  $F \neq 0$  despite an asymmetry of the potential. This excludes the possibility of constructing a motor which is able to extract work from a source of thermal fluctuations. The basic idea behind this result can be traced back to a conference talk by Smoluchowski in Münster 1912 which was elaborated on later in Feynman's Lectures on Physics [6]. Both authors considered a device, shown in Fig. 3.2, which consists of an asymmetric gear known as a ratchet, which rotates freely in one direction but is prevented from rotating in the opposite direction by a pawl. The ratchet is connected by a massless and frictionless rod to a paddle wheel that is immersed in a bath of molecules at a given temperature. Each time a molecule collides with a paddle, it imparts an impulse that exerts a torque on the ratchet (the mechanism is imagined to be small enough that this tiny force could move it). Because the pawl only allows the motion in one direction, the net effect of many such random collisions should allow the ratchet to rotate continuously in that direction. The ratchet's rotation can then be used to do work on other systems, for example for lifting a weight against gravity. The energy necessary to do this work apparently would come from the heat bath, without any heat gradient.

Equation (3.13) is in contradiction with this seemingly intuitive result, because necessarily  $v = 0$  when no external force  $F$  is acting on the system. Actually this intuition is wrong. Indeed, in the Smoluchowski and Feynman's *Gedankenexperimenten* the pawl must be extremely soft to admit a rotation even in the forward direction, and as pointed out already by Smoluchowski, it is also subjected to a non-negligible random thermal fluctuations. The flux in one direction is only possible if the two parts of the system are kept at different temperatures.

Now observe that only when the constant  $S$  in equation (3.12) is different from zero do we have a net flux of particles in the steady state. To have such a flux the system must be either affected by a directional force  $F$  or be maintained by external actions in out of equilibrium state. In the case of muscles, this external action is provided by the ATP splitting, which gives the required energy to bias the motion. the question is how to imitate mechanically the presence of the resulting non-equilibrium noise.

The transport phenomena in spatially periodic systems that are out of thermal equilibrium have been recently reviewed in [68]. In very general terms, thermal ratchet is a mechanical system which is subjected to an asymmetric periodic potential  $V(x, t)$ , is affected by an external force  $F(t)$  with zero average, and is exposed to thermal fluctuations, modeled as a white noise  $\Gamma(t)$ . Under the action of these

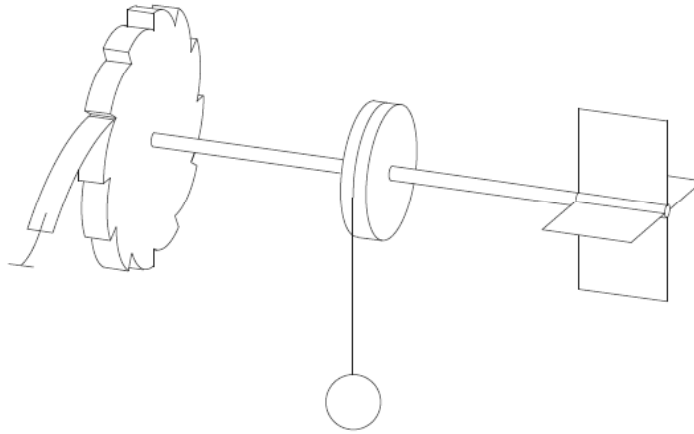


**Figure 3.2:** The ratchet (left) is connected by an axle with the paddles (right) and with a spool (center), which may lift a load. From [68]

forces the probability distribution can reach the steady state  $p_s(x)$  with a non-zero flux.

Thermal ratchets have been used to describe different physical systems. A systematic classification of different ratchet models can be based on the type of external action, [68]. The basic working model in the overdamped situation can be written as:

$$\eta \dot{x}(t) = -V'(x(t), f(t)) + F(t) + \Gamma(t) \quad (3.14)$$

where  $\Gamma(t)$  is the thermal noise, not necessarily white. Another term can be added to account for a passive external force  $F_{ext}(x)$ : if the system is carrying a cargo as in the load clamp device, then  $F_{ext}(x) = const$ , if it is stretching a spring, as in the length clamp device, then  $F_{ext}(x) = Kx$ .

The condition  $F(t) = 0$  distinguishes the class of *pulsating ratchets* whose two important subgroups are the *traveling potential ratchets* with:

$$V(x(t), f(t)) = V(x - f(t)) \quad (3.15)$$

and different assumptions on  $f(t)$ , and the *fluctuating potential ratchets* where:

$$V(x(t), f(t)) = V(x) [1 + f(t)]. \quad (3.16)$$

In this last class, when  $f(t)$  takes only the values 1 or  $-1$ , we have the so-called *on-off ratchet*.

The second main group of Brownian ratchets is called *tilting ratchets*. Then

$f(t) = 0$  and  $F(t)$  is either a periodic function with zero mean:

$$\frac{1}{T} \int_0^T F(t) dt = 0 \quad (3.17)$$

as in *rocking ratchets*, or a unbiased stationary random process, as in *fluctuating force ratchets*. As we have seen in our discussion of purely mechanical ratchets, if  $F(t)$  has a non-zero mean, we can have a non zero flux even if the potential is symmetric. Finally, it is possible to brake thermal equilibrium by considering a space or time dependent temperature distribution (*temperature or Seebeck ratchet*) or a non-trivial viscosity profile (*friction ratchets*).

Two simplest models from this catalogue can be used as the principal basis for the description of contracting muscles. The first one is the model of Magnasco proposed in 1993 [32]. It is the simplest tilting ratchet with a time periodic force (rocking ratchet). The second model was developed by Prost and collaborators around the same time [40] (see also [28]) and is the simplest fluctuating potential ratchet.

### 3.3.1 Magnasco model

Magnasco [32] showed that, if the periodic potential is asymmetric, an external force, which is periodic in time and have zero mean, can generate a net flux in one direction. The magnitude of the flux depends on the shape of the potential. Magnasco considered the following Langevin equation:

$$\dot{x}(t) = -V'(x) + F(t) + \Gamma(t). \quad (3.18)$$

The associated FPE, can be written as:

$$\begin{aligned} \partial_t p + \partial_x J &= 0 \\ J &= -k_B T \partial_x p + (-V'(x) + F(t))p \end{aligned} \quad (3.19)$$

As we have already mentioned, Risken [23] obtained an analytical solution for the flux  $J$  in the case when the force  $F$  is constant (equations (3.12) and (3.13)). Magnasco computed it explicitly in the case of a piecewise linear potential as in Fig. 3.3: here  $\lambda_1$  and  $\lambda_2$  are the fractions of the total period ( $\lambda = \lambda_1 + \lambda_2$ ) where the potential has constant derivatives,  $Q/\lambda_1$  and  $-Q/\lambda_2$ , correspondingly,  $\Delta = \lambda_1 - \lambda_2$ . The analytic form of this potential is the following:

$$V(x) = \begin{cases} \frac{Q}{\lambda_1}(x - n\lambda) & n\lambda < x < n\lambda + \lambda_1 \\ \frac{Q}{\lambda_2} - \frac{Q}{\lambda_2}(x - n\lambda) & n\lambda + \lambda_1 < x < (n+1)\lambda \end{cases} \quad |n| = 0, 1, \dots \quad (3.20)$$



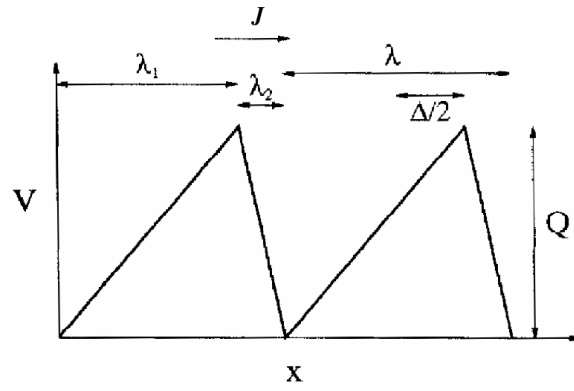


**Figure 3.3:** Piecewise linear potential adapted from [32]. The arrow indicates the direction of the probability current  $J$ . The preferred direction is the one towards lower  $|V'(x)|$

By using (3.20), the probability current  $J$  can be written as:

$$J(F) = \frac{P_2^2 \sinh[\lambda F/2k_B T]}{k_B T \left(\frac{\lambda}{Q}\right)^2 \left\{ \cosh\left[\frac{Q - \Delta F}{k_B T}\right] - \cosh\left[\frac{\lambda F}{2k_B T}\right] \right\} - \frac{\lambda}{Q} P_1 P_2 \sinh\left[\frac{\lambda F}{2k_B T}\right]},$$

$$P_1 = \Delta + \frac{\lambda^2 - \Delta^2}{4} \frac{F}{Q},$$

$$P_2 = \left(1 - \frac{\Delta F}{2Q}\right)^2 - \left(\frac{\lambda F}{2Q}\right)^2.$$
(3.21)

Using this result one can compute the average probability current  $J$  for the case when the fluctuations of the force are slow enough to justify the use of a parameterized steady state solution. Then:

$$J = \frac{1}{p} \int_0^p J(F(t)) dt$$
(3.22)

where  $p$  is the period of oscillations of the force  $F(t)$ . Suppose  $F(t)$  is represented by a square wave of amplitude  $A$ :

$$F(t) = \begin{cases} A & np < t < (n+1)p \\ -A & (n+1)p < t < (n+2)p \end{cases} \quad n = 0, 2, \dots$$
(3.23)

Then one can write:

$$J = \frac{1}{2} [J(A) + J(-A)],$$
(3.24)

where  $J(A)$  is given by equation (3.21). The analytical solution obtained in this way is unaffected by the frequency of oscillations  $1/p$ . This is the consequence of

the hypothesis that the steady state  $J = \text{const}$  is reached immediately after the force changes its sign.

The behavior of the probability current  $J$  as a function of the amplitude  $A$  of the fluctuating force is illustrated in Fig. 3.4 adapted from [32]. We see that while the force  $F(t)$  has zero average the flux is non-zero, due to the asymmetry of the potential. Actually, the flux may be non-zero even without thermal fluctuations: in the zero temperature limit the system works as a mechanical ratchet. The problem is that for the zero-temperature case  $T = 0$  there is a threshold value of  $A$  below which the particle can not overcome the potential barriers. Starting from this value of  $A$  there is an interval of amplitudes in which the particle can climb the potential on one side but not on the other. The flux increases with  $A$  till the second threshold is reached. Afterwards the particle can climb both barriers, but with different rates. Starting from this second critical value of  $A$ , the flux  $J$  starts to decrease and tends asymptotically to zero because the relative importance of the asymmetry of the barriers diminishes as the amplitude of the tilting force  $F$  tends to infinity.

When the temperature is different from zero, the flux  $J \neq 0$  for every value of  $A$  because thermal fluctuations help crossing the barriers. More precisely, an increase in temperature decreases the effective threshold where the flux becomes observable (see Fig. 3.4). Since the motor is able to move in a viscous environment,

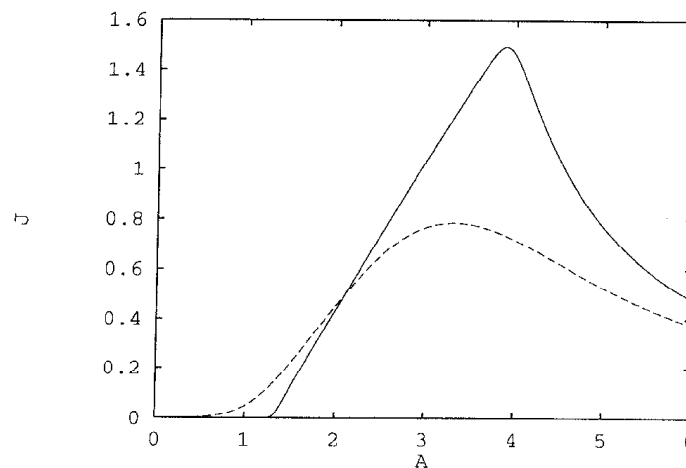


**Figure 3.4:** Plot of  $J$  as a function of the amplitude  $A$  at low (solid line) and high (dashed line) temperature. From [32]

it is also able to generate a force and move a cargo, if an external device is added. In what follows, we shall add to equation (3.18) a term  $F_{ext}(x)$  to mimic the force production in the muscle.

### 3.3.2 Prost et al. model

Another relevant motor model is an *on-off ratchets* proposed by Prost et al. [40]. This type of ratchets appears to be natural choice for modeling of the Xb cycle. Once the Xb reaches the post-power stroke state, it detaches from the actin filament, and then comes back to the pre-power stroke state. In this state it fluctuates until it can attach to another active site and generate another power stroke. Whatever chemical or physical reasons govern the attachment process, the search for the attachment site by the Xb in the attached state can be described as diffusion in a periodic asymmetric potential. In the fully detached state similar motion can be viewed as a diffusion in a flatter potential. In both cases, a parabolic potential may be added to describe the elastic element that links the Xb to the myosin filament, however such elastic spring has not been taken in consideration in the original Prost et al. 1994 paper. In this work equation (3.14) was specialized only for the abstract on-off ratchet.

$$\eta \dot{x}(t) = -V'(x(t), f(t)) + \Gamma(t) \quad (3.25)$$

The authors proposed a model for  $V(x, f) = V(x)f(t)$  assuming that the particle can exist in two states with different potentials  $W_1(x)$  and  $W_2(x)$ , shown in Fig. 3.5. Their analytical descriptions are similar to the one given by equation (3.20). The two potentials have the same periodicity  $p = a + b$ , but different maxima  $\overline{W}_1$  and  $\overline{W}_2$ . The amplitude of the modulation  $f(t)$  is given by a symmetric dichotomous noise, i.e. by a stochastic process that switches back and forth between two values with transition probabilities  $\omega_1(x)$  and  $\omega_2(x)$ .

The coupled master equations for the densities  $P_1(x, t)$  and  $P_2(x, t)$  describing the probability of a particular particle location in each of the potentials have the form:

$$\begin{cases} \partial_t P_1 + \partial_x J_1 = -\omega_1(x)P_1 + \omega_2(x)P_2 \\ \partial_t P_2 + \partial_x J_2 = +\omega_1(x)P_1 - \omega_2(x)P_2. \end{cases} \quad (3.26)$$

Here the fluxes are given by:

$$\begin{cases} J_1 = -D_1 [P_1(x)\partial_x(W_1/k_B T) + \partial_x P_1] \\ J_2 = -D_2 [P_2(x)\partial_x(W_2/k_B T) + \partial_x P_2] \end{cases} \quad (3.27)$$

The diffusion constants  $D_1$  and  $D_2$  can be in general different, for instance due to different temperatures in the two states. The derivation of the two source terms in the right hand side of the two equations in (3.27) is completely analogous to the

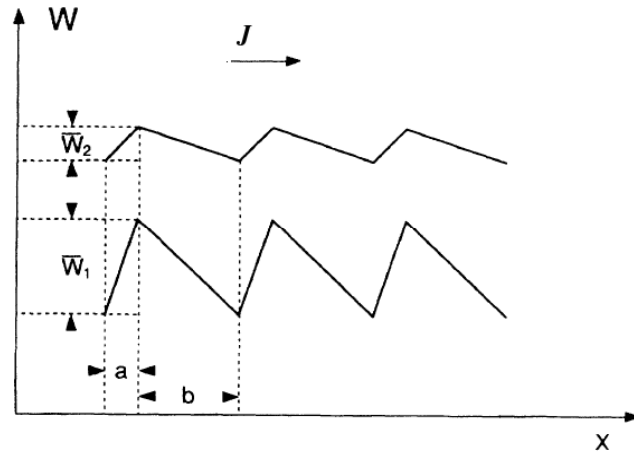


**Figure 3.5:** Three periods of the sawtooth potentials  $W_1(x)$  and  $W_2(x)$ , adapted from [40]. The arrow indicates the direction of the probability current  $J$ . The preferred direction is the one with higher  $|V'(x)|$

derivation of the standard one particle Fokker-Planck equation (see Section A.5). The two source terms in (3.26) are loss and gain contributions due to the switch between the two potential with probability  $\omega_1(x)$  and  $\omega_2(x)$  (see [68]).

By direct substitution in equations (3.27), one can show that Boltzmann distribution (3.10) with  $V(x) = W_1(x)$  and  $V(x) = W_2(x)$  are the solutions of the equation  $J_1 = 0$  and  $J_2 = 0$  respectively. Moreover, if detailed balance is respected and the transition rates satisfy the equilibrium equation:

$$\frac{\omega_1}{\omega_2} = \exp [(W_1(x) - W_2(x)) / k_B T], \quad (3.28)$$

then the Boltzmann distributions (3.10) are the solutions describing the steady state  $\partial_t P_i = 0$  for the entire system and the total particle current becomes  $J = J_1 + J_2 = 0$ .

After observing these facts the authors of [40] explore what happens if an external action drives  $\omega_1/\omega_2$  out of the detailed balance given by (3.28). They conjecture that this effect can represent a compound like ATP, which biases one state over the other. They supposed that  $\omega_2$  has a constant value, and that  $\omega_1$  is given by the relation:

$$\omega_1(x) = \omega_2 \exp [(W_1(x) - W_2(x)) / k_B T] + \Omega(x) \quad (3.29)$$

where  $\Omega(x)$  is the external source of non-equilibrium, which in the first approximation can be taken to be equal to a constant. Now limit the analysis to the steady state situation and define the total density  $P(x) = P_1(x) + P_2(x)$  and the

two functions  $\lambda_1(x)$  and  $\lambda_2(x)$ :

$$\begin{cases} \lambda_1(x) = P(x)/P_1(x) \\ \lambda_2(x) = P(x)/P_2(x). \end{cases} \quad (3.30)$$

Using these representations, it is possible to demonstrate that  $P(x)$  obeys a single Fokker-Plank equation with probability current:

$$J = J_1 + J_2 = -D [P \partial_x (W/k_B T) + \partial_x P] \quad (3.31)$$

where  $D = \lambda_1 D_1 + \lambda_2 D_2$  is the *effective diffusion coefficient* and  $W$  is the *effective potential*:

$$W(x) - W(0) = \int_0^x \frac{D_1 \lambda_1 \partial_x W_1 + D_2 \lambda_2 \partial_x W_2}{D} dx + k_B T [\ln(D)]_0^x \quad (3.32)$$

Since the effective potential  $W$  does not depend on time, the analysis can be reduced to the one done by Risken. The steady state solution is again described by (3.13). The total flux is different from zero if and only if  $W(x+p) \neq W(x)$ , in which case the system acts as if it was subjected to an asymmetric potential tilted in average by a force  $F = -[W(x+p) - W(x)]/p$ . Notice that if the detailed balance condition (3.28) is satisfied, the integrand in (3.32) is the derivative of :

$$-k_B T \ln[D_1 \exp(-W_1/k_B T) + D_2 \exp(-W_2/k_B T)] \quad (3.33)$$

and  $W$  is periodic (not tilted). This shows that deviation from equilibrium is indeed necessary to produce a net flux.

If a non-equilibrium condition of the type (3.29) is satisfied, a non-zero flux appears. Some numerical illustrations originating from direct solution of the Langevin equation associated with (3.26) and (3.27), are presented in [40].

We comment here on two interesting results in order to emphasize the main differences between Prost et al. and Magnasco models. First, the direction of the flux in the Prost et al. model, shown by the arrow in Fig. 3.5, is opposite with respect to the one predicted by the Magnasco model (see Fig. 3.3) given the same asymmetry of the potentials. The reason is that the flux in the Prost et al. model is generated because  $a \neq b$ . Indeed, in the attached state the particle reaches fast the minimum of the well in the potential  $W_1(x)$  (relaxation inside the well). When the potential changes to  $W_2(x)$ , the particle diffuses in a flatter potential from the same point  $x$ . If it moves a distance greater than  $a$ , but smaller than  $b$ , before the potential switches again, there is a larger probability that the particle will be in

the well located to the right than the one located to the left of the original well. This leads to generating a net flux.

Second, the effect of ATP is more explicitly linked to the physics of hydrolysis in the model of Prost et al. than in Magnasco model. Although the Prost et al. model deal with an abstract ratchet, an explicit application of it to the molecular motors and also to muscle mechanics was briefly proposed in [40], in particular the authors observed that “*Although “attached” and “detached” correspond to complex and various underlying behaviors, an essential feature for motion generation is the existence of these two states*”. They also observed how the model allows, for instance, to analyze different effects due to different choices of the function  $\Omega(x)$ . In particular the model predicts saturation of the average velocity  $V$  as a function of the excitation amplitude  $\Omega$ , as shown in Fig. 3.6, where it was assumed that  $\Omega(x) = \Omega\theta(x)$  where  $\theta(x)$  is different from zero only near the wells of  $W_1(x)$ . Such saturation behavior is typical for the motor velocity as a function of ATP concentration across the broad range of motor protein assemblies [34].

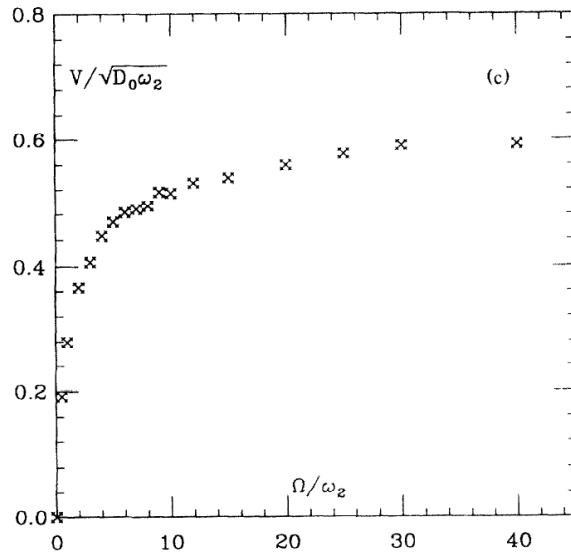


**Figure 3.6:** Average velocity as a function of the external action  $\Omega$  showing saturation (see text). From [40]

### 3.3.3 Cooperative and non-cooperative motors

Both approaches discussed above, the Magnasco ratchet and the Prost et al. ratchet, can explain the motion of a particle in an asymmetric potential when it is subjected to thermal fluctuations. If the system includes a number of particles, as in the case of  $N$  myosin heads on one thick filament, the main conclusions

are still valid given that the particles are not interacting with each other. The mean velocity will then be the average velocity of the population. However, by ignoring cooperativity the resulting models are only marginally related to the mechanics of contraction in skeletal muscles.

In the next Section we show how the interaction between particles can be included and developed the corresponding numerical approach. Before doing this, it is instructive to discuss two examples in which the models of the type described above are quantitatively applied to kinesin and to a single myosin head. In general molecular motors can be divided into two main groups depending on whether they are designed to operate in groups (cooperative) or individually (processive). Kinesin and some myosin proteins, such as myosin V, belong to the processive motor category, while myosin II is a cooperative motor. What differentiates the two types of motors is the living time for the attached state. In processive motors, it is high enough to work with only two heads. Thus when the first head is attached, the second one oscillates around its mean position and due to the asymmetry of the track attaches preferentially along the ‘plus’ direction of the microtubule. At this point, the latter can detach and repeat the same process; with this “step by step” motion, kinesin can make several moves before both heads detach from the microtubule. The living time of the attached state for myosin II is not enough to produce this motion however the link to the thick filament allows for the cooperation effect with others Xbs.

### Kinesin model

A quantitative analysis of a kinesin motion was presented in [45] where two heads were assumed to be linked through a linear “active” spring. This means that the spring can use the ATP splitting energy to change its reference length. The model is described in Fig. 3.7(a). The two particles start from the same well (upper figure). When the reference length of the spring switches from zero to 8 nm, it pushes the two heads in the opposite directions. Because of the asymmetry of the potential, only one head makes a forward step of 8 nm relaxing the spring (middle figure). This unstrained situation is perturbed by a second change in the reference length of the spring that comes back to zero. Now the two heads are pulled together and end up again in the same well because the asymmetry of the potential facilitates the forward step of the second head (bottom figure).

Even if this model predicts an inchworm motion, while a hand over hand motion has been later proven to be the case for the kinesin and myosin V (see for instance

[70]), we describe it here, because it shows, in an instructive way, how the Brownian ratchets theory can be quantitatively applied to the processive motors. The motion of the heads is described by the system of coupled Langevin equations:

$$\begin{cases} \eta \dot{x}_1 = -\partial_x V(x_1) - F_{load} + K[x_2 - x_1 - l(t)] + \sqrt{2k_B T/\eta} \Gamma(t) \\ \eta \dot{x}_2 = -\partial_x V(x_2) - F_{load} + K[x_1 - x_2 - l(t)] + \sqrt{2k_B T/\eta} \Gamma(t) \end{cases} \quad (3.34)$$

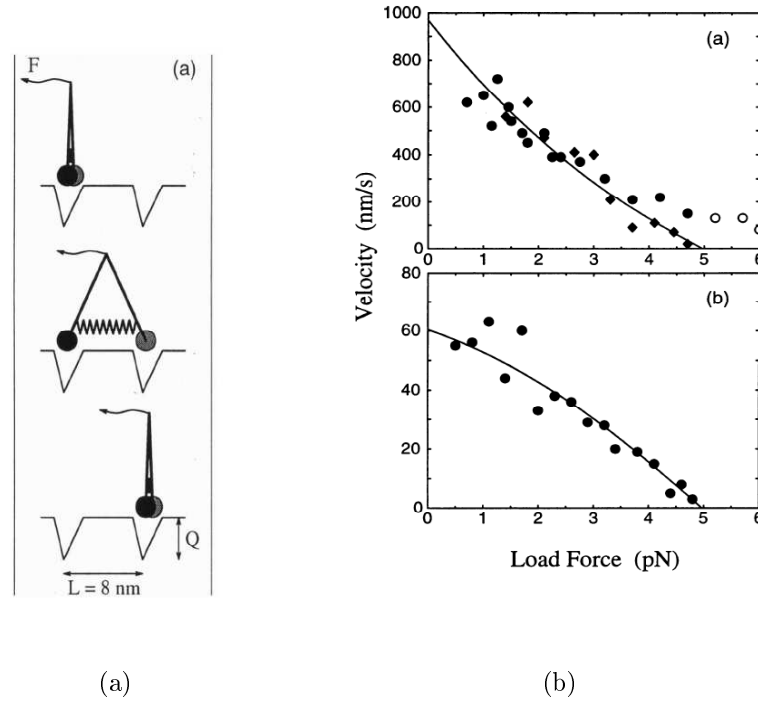


**Figure 3.7:** Kinesin model and numerical results. (a) Schematic picture of the potential and subsequent steps of the heads. (b) Force-velocities curves for individual kinesin molecule at different ATP concentrations (points: experiment, line: prediction of the model). From [45]

One can see that the motor is transporting a load ( $F_{load}$ ). The out of equilibrium condition is imposed through the oscillation of the rest length of the spring  $l(t)$  which changes from zero to  $8 \text{ nm}$  imitating the hydrolysis of one ATP molecule. The system proceeds in a step by step motion in one direction, and shows different velocities at different external loads: the comparison of the model predictions (lines) with experiments (points) is shown in Fig. 3.7(b). One can see that the model shows a rather good agreement with experiments. Kinesin motion is a very active field and Brownian ratchet theory is applied with success (see [68] and references therein).



### Single head model

Now let us turn to the examples where both Magnasco and Prost et al. models were applied to the myosin II directly and where certain agreement with experiments have been reported. This is the situation when the interaction of a single head with an actin substrate could be the subject of study. An experimental trace of the movements of a single myosin head was recorded in [60] by using original manipulation technique having nanometer accuracy. The displacements of the head in time, and the corresponding model predictions are shown in Fig. 3.8 and Fig. 3.9.

In the theoretical analysis, breaking of the detailed balance was simulated in different ways. First a constant load was added to an asymmetric potential creating the tilted ratchet described by Risken (equation (3.13)). Second different types of flashing fluctuations of the potential amplitude were tried, including a square wave (as in the Prost et al. model) and a sinusoid wave.

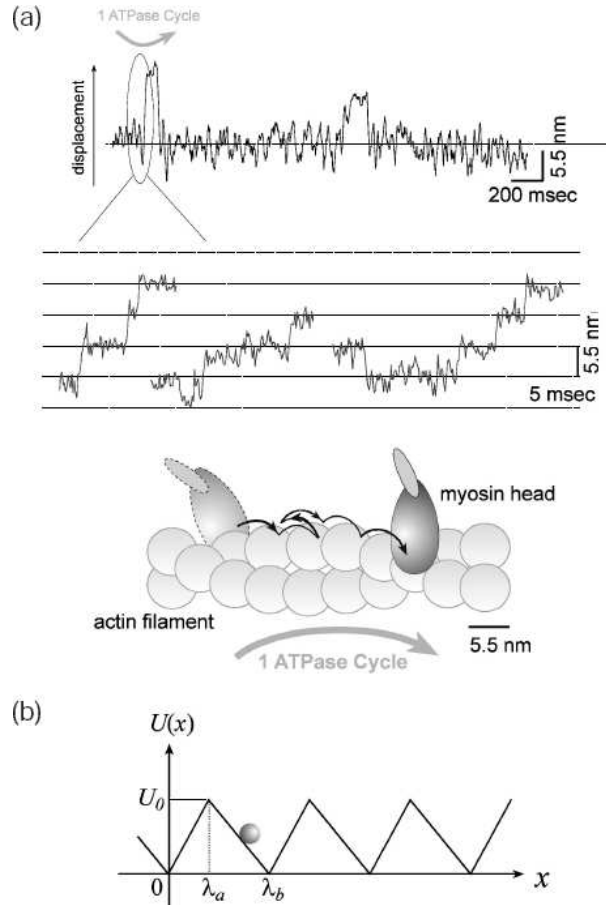


**Figure 3.8:** Stochastic movement of myosin. (a) Experimental traces of the movement and picture of the model. (b) Periodic saw-tooth shaped potential used in [60]. From [71]

The experimental method developed in [60] for measuring the displacement of the myosin head by using a scanning probe allows one to obtain an excellent signal to noise ratio. The myosin head rigidly attached to the relatively large scanning probe could steadily interact with actin without diffusing away from the filament. The basic features of the experiment, summarized in [71], are as follows: i) The size of each step is  $5.5 \text{ nm}$ , similar to the diameter of the actin monomer, ii) Steps occur occasionally in the backward direction even if the motion is preferentially directed towards one ends of the actin filament; iii) On applying a load to the myosin, the number of steps decreased. The movement of myosin was also simulated numerically using the corresponding overdamped Langevin equation:

$$\eta \dot{x} = -V'(x, t) + \sqrt{2k_B T / \eta} \Gamma(t). \quad (3.35)$$

The results for different types of motors are given in Fig. 3.9.

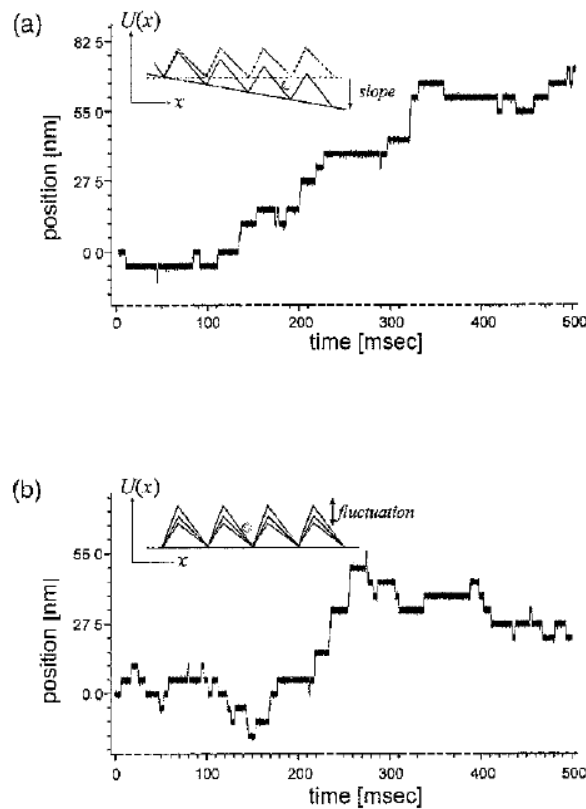


**Figure 3.9:** Simulations of the myosin head: (a) Tilted potential (b) Flashing potential. From [71]

This last example is one of the few cases where application of the theory of Brownian motors to myosin II was attempted. We reiterate however that it was a case of a single attached head. The analysis of the cooperativity effects due to

many heads was initiated in the Jülicher-Prost paper [42] (see also [50] [54] and [65]). The authors consider a rigid backbone with rigidly connected motors (see Fig. 3.10). The resulting system is characterized by only one degree of freedom. The way the motor cooperate is through the total force which is a sum of forces exerted by individual motors. Some interesting effects have been found in this sys-

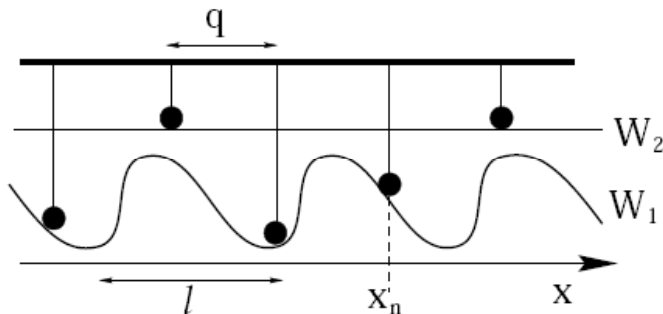


**Figure 3.10:** Representation of two state many-motor system. The particles are rigidly attached to a common backbone and can stay in two different states. The “attached” potential is periodic and asymmetric. From [54]

tem, for instance, a dynamic phase transition leading to spontaneous oscillations. The authors demonstrated the existence of a critical value of the parameter  $\Omega$  in (3.29), above which three velocities correspond to one external force. This leads to situations in which the motors might either go in one direction or in its opposite for the same value of  $F_{ext}$ , which generates the oscillatory behavior. This effect is observed in muscle cells under suitable condition ([50] and references therein). The Jülicher-Prost model has also been modified and applied to study the behavior of other cooperative motors [51], but always under an assumptions of a rigid link between motors and backbone. See also [94] for a recent analysis of the effect of the geometry on the cooperation between myosins in muscle. In this Section we develop a model of elastically cooperative Brownian motors.

To summarize, none of the models presented in literature, which use the Brownian ratchet theory to explain muscle contraction, deal with a detailed description of the Xb cycle. The effect of the ATP hydrolysis is mainly to destroy the detailed balance, while the power stroke is hidden somewhere in the force generated by the periodic potential. Later in this and in the next Chapter we propose some new ideas of how cooperativity can be integrated into the model of Brownian ratchet in an attempt to construct a detailed model of the whole Xb cycle. As a novelty, we consider an elastic link between the backbone and the heads. Only a Magnasco type model for the Brownian ratchet will be used to simulate the attachment-

detachment process. To justify this choice, in view of the fact that the Prost et al. type models are apparently more faithful to the physics of the phenomenon, we recall that our main aim is to give a purely mechanical description of the contraction phenomenon. The fluctuating ratchets of Prost et al. require a definition of the transition rates between states 1 and 2, given by the functions  $\omega_1(x)$  and  $\omega_2(x)$  in equation (3.27). Introducing these functions is similar, in a sense, to imposing particular dependencies of the attachment detachment rates on  $x$  in the Huxley 1957 model. We have shown in Chapter 2 how this arbitrariness can be avoided in the fully mechanical description where the chemical transition rates are not defined but computed as, for instance, in the Huxley and Simmons 1971 model. Now we would like to extend the same approach to a set of interacting Xbs (inside one half-sarcomere), which can attach and detach from an actin filament.

### 3.4 Direct simulation of a set of stochastic equations

We recall that the motion of a single particle in a sawtooth potential  $V(x)$  tilted by an external force,  $F_{ATP}(t)$ , which mimics the effect of the ATP and whose sign changes periodically in time, is described by the associated Langevin equation. In the overdamped case we can write:

$$\eta \dot{x} = -V'(x) + F_{ATP}(t) + \sqrt{\eta k_B T} \Gamma(t) \quad (3.36)$$

where

$$\langle \Gamma(t_1) \rangle = 0 \quad (3.37)$$

and

$$\langle \Gamma(t_1) \Gamma(t_2) \rangle = \delta(t_1 - t_2). \quad (3.38)$$

We have shown that, under certain assumption, the associated steady state Fokker-Plank equation can be solved analytically. The mathematical difficulty that arises when several particles are interacting with each other forces one to turn to a direct numerical simulation of a coupled set of stochastic ODE.

The direct numerical approach reduces to solving the Langevin equations of the motion for a particular realization of the random process. Instead of using the probability distribution given by the associated Fokker-Plank equation, this method consists in generating of a certain number of realizations starting from the same initial conditions. After these individual trajectory are obtained, one can

compute the mean value for the variable of interest. To solve stochastic differential equation, we use the simplest Euler algorithm [74]. In the case of a single particle we first follow the time path  $x(t)$  by solving (3.36), and then repeat the experiment for a population in order to construct the probability distribution of a single Xbs.

The Euler algorithm for the equation (3.36) can be written:

$$x(t + \tau_{step}) = x(t) - \frac{1}{\eta}(V'(x(t)) + F_{ATP}(t))\tau_{step} + \frac{\sqrt{\eta k_B T}}{\eta} \sqrt{\tau_{step}} w(0, 1) \quad (3.39)$$

where  $w(0, 1)$  is a normally distributed random variable with zero mean

$$\langle w \rangle = 0 \quad (3.40)$$

and the variance

$$\langle w_1 w_2 \rangle = \delta_{12}. \quad (3.41)$$

We would like to give an idea why parameter  $\tau_{step}$  appears under the square root in (3.39), a rigorous derivation can be found in [30] and [63]. First of all, we notice that, by neglecting the non-thermal forces in (3.39) (purely diffusion case), we can write:

$$x(t) = x(0) - \sqrt{\frac{k_B T}{\eta}} \int_0^t \Gamma(t') dt'. \quad (3.42)$$

Now from (3.38), we see that  $\Gamma(t)$  has the dimension  $t^{-1/2}$ , so its time integral has the dimension of  $t^{1/2}$ . Therefore,

$$x(t + \tau_{step}) \neq x(t) - \sqrt{\frac{k_B T}{\eta}} \Gamma(t) \tau_{step} \quad (3.43)$$

in contrast to the classical Euler method for the deterministic differential equations. From the properties of  $\Gamma$  detailed in (3.37) and (3.38), we obtain instead that [23] the function

$$w(\tau_{step}) = W(t + \tau_{step}) - W(t) = \int_t^{t+\tau_{step}} \Gamma(t') dt', \quad (3.44)$$

is a random variable which is normally distributed with zero mean and variance  $\tau_{step}$ . Therefore, we can write

$$w(\tau_{step}) \sim \sqrt{\tau_{step}} w(0, 1) \quad (3.45)$$

where  $w(0, 1)$  was defined by (3.40) and (3.41). A general rule is that when a potential is acting on the particle,  $\tau_{step}$  represents the interval of time during which the actual  $V(x, t)$  potential can be substituted by the constant potential  $V(x, \tilde{t})$

frozen at time  $\tilde{t}$  just before the time step. To simulate properly the physics of the phenomenon, the time step has to be much shorter than the typical time scale of the process: normally two orders of magnitude difference is enough. In the case of piecewise linear potential, the typical time scale is:

$$\tau = \frac{\eta L}{|V'_{max}|} \quad (3.46)$$

where  $\eta$  is the drag coefficient,  $L$  the typical length of the potential and  $|V'_{max}|$  the maximum force acting on the particle. We can make an estimate of  $\tau$  by using the values of parameters given in Tab. 2.1 of Chapter 2. The condition  $\tau_{step} \ll \tau$  limits  $\tau_{step}$  to tens of picoseconds and the time scale of the attachment-detachment process is in the range of tenths of seconds. This implies that in order to obtain a quantitative description of the system, the simulations must contain at least  $10^{10}$  time steps for each particle of the analyzed population. Since this type of computations can easily become too heavy, we abandon the idea to obtain quantitative results and from now limit ourselves to only a qualitative analysis. This means that we describe the system by using the values of parameters that are sometimes grossly exaggerated.

### 3.5 Thermal ratchet

Before describing and analyzing in detail our way of modeling the cooperative motors, we can try to use the numerical method introduced in Section 3.4 to describe the behavior of a simplest thermal ratchet which is somewhat similar to the Feynman's ratchet and pawl model. As we have already mentioned, the only way to induce a net flux in one direction is to maintain the ratchet and the pawl at two different temperatures.

The interest in the analysis of such a model is not only historical. Thus, Vale and Oosawa in 1990 [25] proposed a Feynman's type model to explain the directional motion of molecular motors, with explicit reference to myosin II. They argued that the hydrolyzation of the ATP molecule could convert a certain amount of chemical energy into heat, generating locally the temperature anomaly and distorting the equilibrium character of the thermal fluctuations. If this is true, we can have all the ingredients of a temperature ratchet. Despite being very intuitive, this model was later proved to be unrealistic due to quantitative estimates summarized in [26], [37], [47]. According to the authors, the temperature variations, in regard to both amplitude and duration, may not be sufficient to generate quantitatively

measured speed of motion. Magnasco and Stolovitzky came back to the study of the Feynman ratchet in 1998 [56], however, not in the molecular motors framework. Here we would like to show numerically how a simple thermal ratchet can predict a net motion in one direction and generate a position vs. time path similar to the one observed in [71] (see Fig. 3.8).

Consider a system of two particles  $x_1$  and  $x_3$  subjected to two different temperatures  $T_1$  and  $T_2$ . The particle  $x_1$  moves in a periodic asymmetric potential as in (3.20) and its motion is described by the Langevin equation (3.6). The particle  $x_3$  is linked to  $x_1$  through a spring of rigidity  $K$ , but it is otherwise free. The system of equations describing the model is the following

$$\begin{cases} \eta \dot{x}_1 = -V'(x_1) - K(x_1 - x_3) + \sqrt{\eta k_B T_1} \Gamma_1(t) \\ \eta \dot{x}_3 = K(x_1 - x_3) + \sqrt{\eta k_B T_3} \Gamma_3(t). \end{cases} \quad (3.47)$$

The correlations of the functions  $\Gamma_1(t)$  and  $\Gamma_2(t)$  describing thermal fluctuations are given again by (3.37) and (3.38). Both, difference in temperatures and asymmetry of the potential  $V(x)$  are needed in order to make the system move.

Performing the analysis for a large number (100) of systems (3.47) we can show that the mean position of  $x_3$  shifts in time in one preferred direction (see Fig. 3.11). The average motion is a linear function of time. A representative picture of the particle trajectory  $x_1(t)$  is given in Fig. 3.12, where we can see that while the average stochastic motion shifts the particle in one preferential directions, the individual jumps in the opposite direction can also takes place. Adding an external

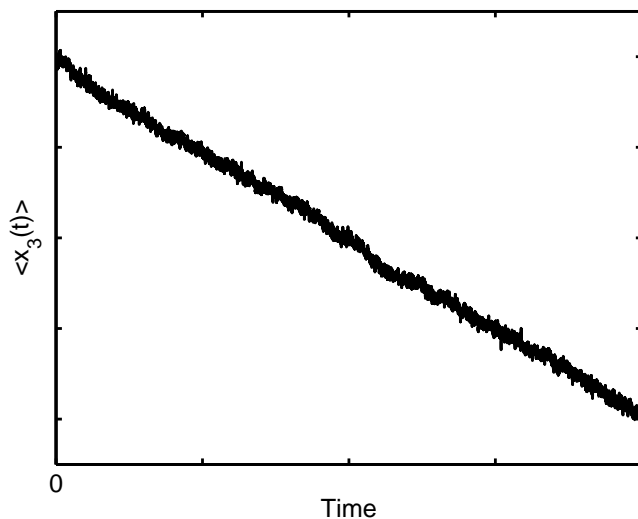


**Figure 3.11:** Mean displacement of the thermal ratchet (3.47)

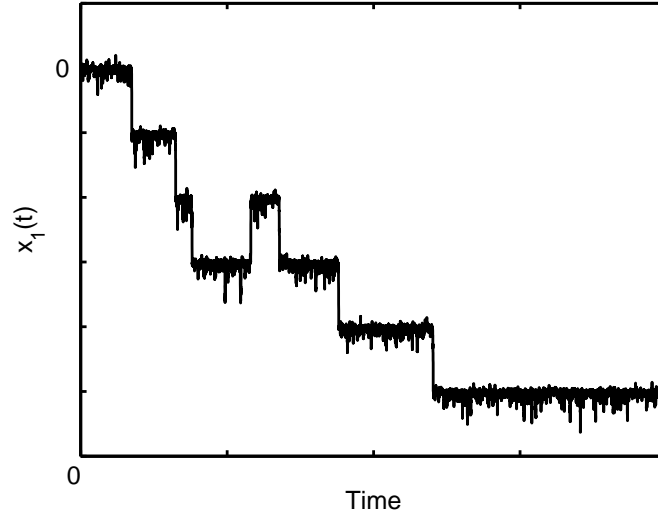


**Figure 3.12:** Sample trajectory  $x_1(t)$  of a thermal ratchet (3.47)

force  $F_{ext}$  acting at the particle  $x_3$  we can slow down and even invert its motion. A force-velocity curve could have been plotted for this “toy” model, however this is not necessary in view of its oversimplified nature. We shall perform this type of analysis only for the system presented in the next Section, which is especially designed to model cooperative motors, responsible for muscle contraction.

## 3.6 Cooperative Magnasco model

### 3.6.1 Governing equations

Here we study the behavior of a set of interacting Magnasco motors. Consider a population containing  $N_{Xb}$  cross-bridges subjected to thermal fluctuations, each moving in a piecewise linear potential  $V(x)$  whose derivative is described by:

$$V'(x) = \begin{cases} V_{max}/(\lambda_1 L) & nL < x < nL + \lambda_1 L \\ -V_{max}/(\lambda_2 L) & nL + \lambda_1 L < x < (n+1)L. \end{cases} \quad (3.48)$$

Here parameters  $\lambda_2$  and  $\lambda_1$  characterize the asymmetry of the potential with period  $L$  and  $V_{max}$  is the maximum value of the potential, see Fig. 3.13. Index  $n$  describes a particular well in which the particle is currently located. We now add a rigid backbone which is coupling individual particles, as in a real half-sarcomere. To simulate the effect of a backbone we introduce another variable,  $x_3$ , which describes its position. The position of each Xb will be given by  $x_1^i$  where  $i = 1, \dots, N_{Xb}$ . The



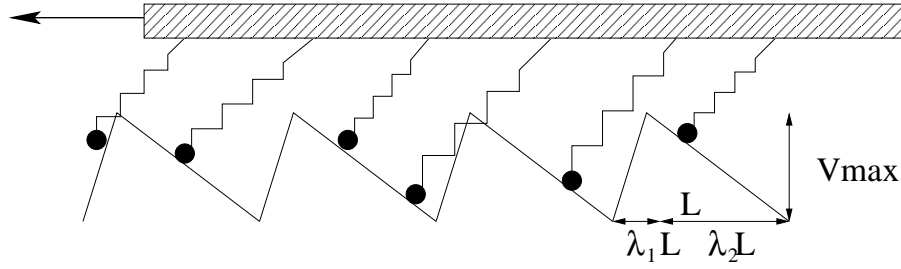


**Figure 3.13:** Model of a family of interacting cooperative motors. The particles move to the left which mimics shortening experiments

system of coupled differential equations for  $x_1^i(t)$  and  $x_3(t)$  can be written as:

$$\begin{cases} \eta_1 \dot{x}_1^i = -V'(x_1^i) + F_{ATP}(t) - K(x_1^i - x_3^i) + \sqrt{\eta_1 k_B T} \Gamma_1(t) & i = 1, \dots, N_{Xb} \\ \eta_3 \dot{x}_3 = F_{ext} + \sum_{i=1}^{N_{Xb}} (K(x_1^i - x_3)) + \sqrt{\eta_3 k_B T} \Gamma_3(t) \end{cases} \quad (3.49)$$

Notice that  $x_3^i = x_3^1 + (i-1)l = x_3 + (i-1)l$  where the variable  $x_3$  describes the position of the backbone and the length  $l$  is the distance between the attachment sites of two successive heads. The position of attachment site on the backbone are  $x_3^i$ , where, again  $i = 1, \dots, N_{Xb}$ . As in the Magnasco model, the ATP related periodic force is given by:

$$F_{ATP}(t) = \begin{cases} +F_{ATP} & m\Delta t_{ATP} < t < (m+1)\Delta t_{ATP} \\ -F_{ATP} & (m+1)\Delta t_{ATP} < t < (m+2)\Delta t_{ATP} \end{cases} \quad m = 0, 1, \dots \quad (3.50)$$

The system (3.49) is able to mimic the force-clamp device if an external force  $F_{ext}$  is applied to the rigid backbone. The same system can also describe the isometric contractions if we substitute the last equation in (3.49) with:

$$x_3(t) = x_3(0). \quad (3.51)$$

By imposing condition (3.51) in (3.49) and averaging the noise term we obtain the expression for the force generated in the system:

$$F_{ext} = -\sum_{i=1}^{N_{Xb}} (K(x_1^i - x_3^i)). \quad (3.52)$$

Now, suppose that  $L = l$ . Then due to periodicity of the potential  $V(x)$ , we can introduce now variables  $x_1^i = x_1^i - (i-1)L$  and absorb the parameter  $L$  into the potential without affecting the behavior of the system. The resulting numerical

algorithm for solving (3.49) is then

$$\begin{cases} x_1^i(t + \tau_{step}) = x_1^i(t) - V'_{eff}(x_1^i(t), x_3(t), t) \frac{\tau_{step}}{\eta_1} + \sqrt{k_B T \frac{\tau_{step}}{\eta_1}} w_1(0, 1) \\ x_3(t + \tau_{step}) = x_3(t) + \left[ F_{ext} + \sum_{i=1}^{N_{Xb}} (K(x_1^i(t) - x_3(t))) \right] \frac{\tau_{step}}{\eta_3} + \sqrt{k_B T \frac{\tau_{step}}{\eta_3}} w_3(0, 1) \end{cases} \quad (3.53)$$

where the effect of the actin potential  $V(x)$ , of the ATP force  $F_{ATP}(t)$  and of the elastic element that links the head to the myosin filament are all combined in the effective potential

$$V'_{eff}(x_1^i(t), x_3(t), F_{ATP}(t)) = V'(x_1^i) - F_{ATP}(t) + K(x_1^i - x_3). \quad (3.54)$$

We recall that  $w(0, 1)$  is a random variable normally distributed with zero mean and unit variance. The larger size of the rigid backbone with respect to the Xb head is represented by a higher value of the corresponding drag coefficient  $\eta_3 \gg \eta_1$ .

### 3.6.2 Benchmark problem: $K = 0$

The numerical computations at  $K = 0$  give the independent path followed by each Xb and given by  $x_1^i(t)$  and the path of the backbone given by  $x_3(t)$ . The typical solution for  $x_1^i(t)$  is shown in Fig. 3.14: the head stays in the well for a finite amount of time, then jumps forward or backward very fast, as predicted by the Kramers' theory discussed in Chapter 2. If the potential contains an asymmetry, then the jumps will take place preferentially in one direction. We recall that as in the original Magnasco model, we use the stepwise periodic ATP force with zero mean (3.23). The value of the period  $p$  is important because there is a threshold for  $p$  below which the particle does not jump during the time of simulation. This threshold value depends on the time scale of the process, and since here our intention is to present only qualitative results, the value of  $p$  was chosen to be sufficiently above the threshold to be able to observe the jumps. This value must be simultaneously small enough to let  $F_{ATP}$  change sign several times between two successive jumps.

Let us first demonstrate the importance of the asymmetry of the potential. Thus, if the potential is symmetric ( $\lambda_1 = \lambda_2$ ) then distribution of particles is expected to evolve in time as a Gaussian distribution with zero mean and with variance which increases linearly with time. When the time scale is such that the period  $L$  is much smaller than the diffusing distance, as in Fig. 3.15(a), then the system does not see the periodicity of the potential and the corresponding

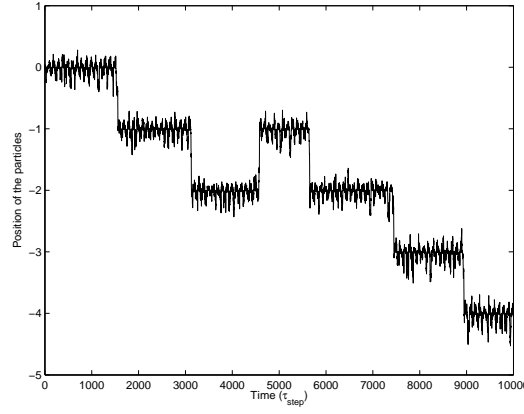


**Figure 3.14:** Typical trajectory of a single head in an asymmetric tilted potential with  $K = 0$ . The trajectory is representative also for  $K \neq 0$

probability density function  $p(x, t)$ , can be approximated by (see (A.35) in Section A.4):

$$N_{Xb}p(x, t) = \frac{N_{Xb}}{\sqrt{4\pi k_B T / \eta t}} e^{-\frac{x^2}{4t k_B T / \eta}} \quad (3.55)$$

In the computation the time is just the number of iterations multiplied by  $\tau_{step}$ . In Fig. 3.15(a) the distribution of  $X_b$ s is shown at three different fractions of the total time,  $t = t_{Tot}/10, t_{Tot}/2, t_{Tot}$  and is superimposed with the distribution given by (3.55). If an asymmetry is added to the potential ( $\lambda_1 \neq \lambda_2$ ) then a net

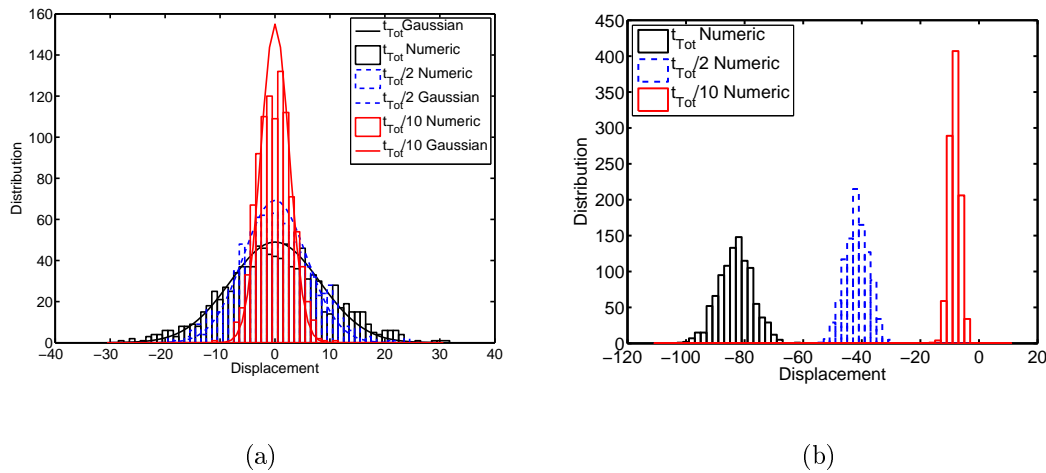


**Figure 3.15:** Distribution of a population of  $N_{Xb} = 800$  cross-bridges, with  $K = 0$  and  $L = 1$ , at different fractions of the final time  $t_{Tot}$ . (a) Symmetric periodic tilting potential (b) Asymmetric periodic tilting potential

flux in one direction will take place. The distribution of particles is again almost

Gaussian with variance that increases linearly with time and with mean that now also varying linearly with time (see Fig. 3.15(b)).

The effect of the level of noise and of the amplitude  $F_{ATP}$  on the steady state flux, obtained in direct numerical simulation, can be compared to the analytical solution of Magnasco. The comparison shows identical behavior of the numerically and analytically obtained functions  $J(F_{ATP})$  (see Fig. 3.16 and Fig. 3.4 taken from [32]).

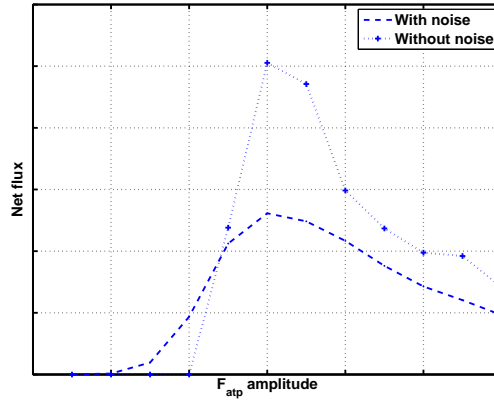


**Figure 3.16:** Steady state probability flux obtained from numerical simulation with and without noise

The system (3.49) can also generate force, which can be measured if a bead is attached to a particle. In this way one can describe the motion of a motor protein transporting a cargo (this problem is analyzed in [85] with a Prost et al. model). By putting a constant external force  $F_{ext}$  instead of the term  $-K(x_1^i - x_3)$  in equation (3.49) we obtain

$$\eta_1 \dot{x}_1 = -V'(x_1) + F_{ATP}(t) - F_{ext} + \sqrt{\eta_1 k_B T} \Gamma_1(t). \quad (3.56)$$

The presence of the external force reduces the mean displacement of the particle. The resulting force velocity curve is shown in Fig. 3.17. Its non-linearity is a somewhat non intuitive result from the point of view of purely mechanical ratchet operating at  $T = 0$ . Indeed suppose that the effect of the motor reduces to generating a mean constant force  $F_{max}$ . Then the total force  $F_T$  acting on the particle can be written as  $F_T = F_{max} - F_{ext}$ . This shows that in a viscous environment the force velocity relation should be linear because  $F_T = \eta v$ . As we have seen from Fig. 3.17 the situation at  $T \neq 0$  is much more complex. Here we do not attempt to make quantitative comparison of computed and experimentally measured force

velocity curves, however it is clear that the qualitative behavior is well captured by the model.

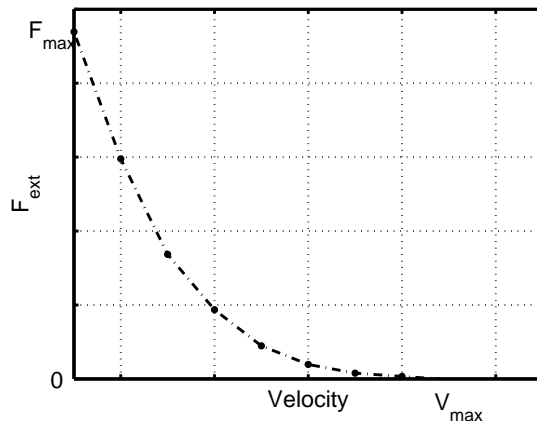


**Figure 3.17:** Force vs. velocity curve for a pure Magnasco model  $K = 0$

It is of interest to compute numerically the *stall force*,  $F_{max}$ , which is a particular value of  $F_{ext}$  that brings the mean displacement to zero. The mean trajectories of particles for different values of  $F_{ext}$  are shown in Fig. 3.18(a). Observe that having a zero mean flux at  $F_{ext} = F_{max}$  does not prevent each particle to move. In fact the stall value of the force creates a situation which is analogous to a case of pure diffusion, when the mean-square displacement increases linearly with time. In our simulations of an isometric contraction we checked that two neighboring particles (at time  $t = 0$ ) can move arbitrary far apart after a certain amount of time (see Fig. 3.18(b)). This behavior is not compatible with what one expects in the case of cooperative motors. Indeed when the isometric conditions are imposed it is known that all the Xbs, attached or detached, remain close to their original positions. This happens because they are linked to a fixed thick filament through elastic elements with  $K \neq 0$ . We therefore conclude that the model with  $K = 0$  has to be discarded.

### 3.6.3 Cooperative Magnasco model with $K \neq 0$

To take the backbone into consideration, we assume that  $K \neq 0$ . Interestingly certain questions become simpler in the case when  $K \neq 0$  than in the case when  $K = 0$ . Thus while in the original Magnasco model we had to change  $F_{ext}$  to find the stall force  $F_{max}$ , now its value is immediately determined imposing the condition (3.51) and waiting until the force (3.52) generated by the tilting reaches its steady value. we now proceed with performing several types of numerical experiments.

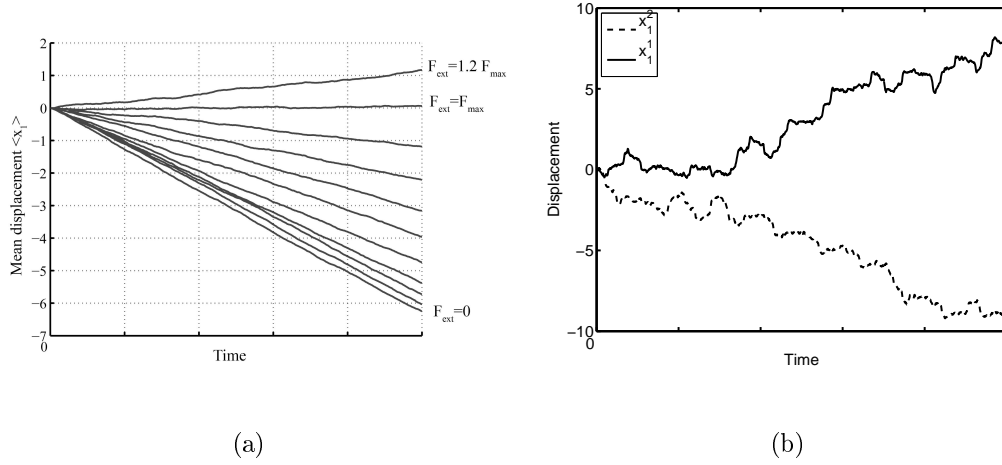


**Figure 3.18:** The behavior of the Magnasco model ( $K = 0$ ): (a) Mean displacement vs. time of a population of particles at different values of external forces between 0 and  $1.2F_{max}$  (see text for the definition of  $F_{max}$ ). (b) Displacement vs. time for two particles at the stall force

### Tetanzation

Starting from a delta function type distribution of particle positions at  $t = 0$ , we can turn on the ratchet and try to reconstruct the tension time curve until the force reaches a constant value. Later we shall be using the limiting distribution of particle positions obtained in this experiment as the initial condition in order to study the behavior of the system in other loading devices.

When the particles are interacting with the backbone, the instant in which  $F_{ATP}(t)$  changes sign becomes important for the global behavior. We observe that if there is a synchronicity among the Xbs, meaning that all particles feel the value  $+F_{ATP}$  or the value  $-F_{ATP}$  at the same time  $t$ , then the tension vs. time curve for isometric tetanization shows oscillatory behavior as in Fig. 3.19(a). Similar oscillatory behavior has been observed in other models [50] and linked to some experimental observations obtained in non-physiological condition [53]. However, in these model the oscillations are generated by different phenomena, while the synchronicity can be viewed as unphysical, because the effect of the ATP on each head should be random and therefore unsynchronized. To simulate this effect, a dispersion has been added to the switch times of the tension:

$$F_{ATP}^i(t) = \begin{cases} +F_{ATP} & m\Delta t_{ATP} < t + \phi^i < (m+1)\Delta t_{ATP} \\ -F_{ATP} & (m+1)\Delta t_{ATP} < t + \phi^i < (m+2)\Delta t_{ATP} \end{cases} \quad m = 0, 2, 4, \dots \quad (3.57)$$

Here  $\phi^i$  is randomly distributed variable between zero and  $\Delta t$ ,  $i = 1, \dots, N_{Xb}$ . In this way, each Xb is affected by the same force  $F_{ATP}$  for a time  $\Delta t$ , but asynchronously for different elements. Under these assumption the tension vs. time curve approaches the steady state without oscillations as shown in Fig. 3.19(b). We observe that the curve in Fig. 3.19(b) looks rather realistic in terms of experiments [52].

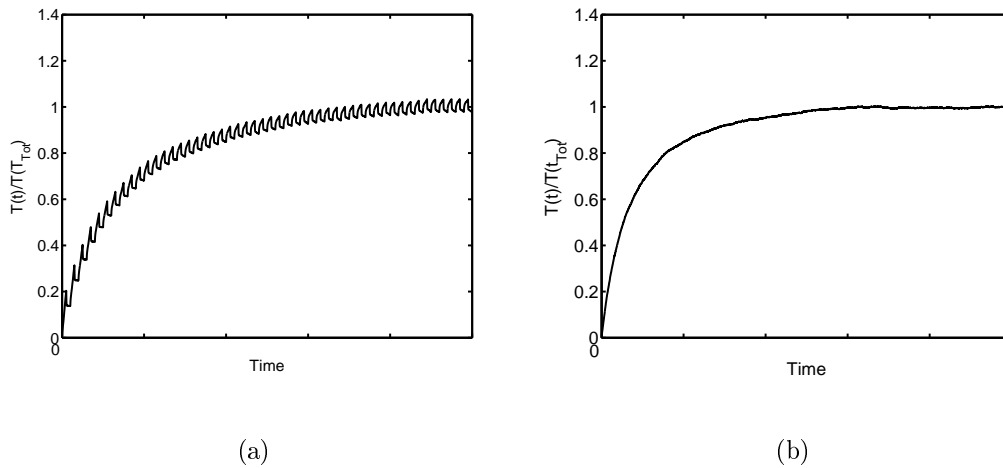


**Figure 3.19:** Tension time curve describing isometric tetanization for a system with a backbone. (a) Normalized tension vs. time in synchronous tilting. (b) Normalized tension vs. time in asynchronous tilting

### Isotonic loading: experiments

As we have already mentioned, the Huxley and Simmons model and its proposed modifications analyzed in Chapter 2, can not deal with the entire Xb cycle shown in Fig. 1.5 of Chapter 1, because they are based on the hypothesis that the population of attached Xb is fixed, meaning that no new Xb can attach and that all the attached Xbs stay attached during the test. Since the model from Chapter 2 has all the same ingredients, it can not show total recovery in isometric experiments and can not generate a constant velocity of shortening when a constant load is applied. The maximum shortening predicted by this model will be limited by the value  $a \simeq 11 \text{ nm}$  (see Table 2.1). On the contrary, the model presented in the present Chapter misses the fast phases of recovery but it is adequate to simulate the protocol that leads to the construction of the force-velocity curve.

Recall that when a muscle fiber with fixed length is stimulated to produce fused tetani (say of 1 s duration as in [67]) it generates an isometric tetanic force

corresponding to the plateau level  $T_0$ . This has been reproduced in the simulations shown in Fig. 3.19(b). After reaching this level of tension, the control can be shifted from fixed-end mode to force clamp mode, first, at the same level of tension  $T_0$ . This will keep the length of the muscle fixed. Suppose now that after 20 *ms* a rapid change in the external force completed in 150  $\mu s$  is imposed, as in experiments [67]. If the applied tension after the change is lower than  $T_0$ , one can recognize four phases of the relaxation process shown in Fig. 3.20. First, half-sarcomeres shorten by few nanometers, coincidentally with the force drop (phase 1). Then there is a phase of slower but still rapid shortening (phase 2). It is then followed by a phase of reduced speed of contraction (phase 3). Finally the phase is reached during which the shortening takes place at a steady velocity  $V$  (phase 4).

There is a clear relation between phase 1 and the undamped relaxation of the elastic element and between phases 2 and 3 and the working of a bi-stable mechanism inside the myosin heads, described in Chapter 2. A strong evidence of such a relation is given in [67] where the shortening just after phases 1 ( $L_1$ ) and 2 ( $L_2$ ), has been studied for various values of the imposed tension. The authors plotted  $L_1$  and  $L_2$  on the tension-length plane and superimposed the experimental results for  $T_1$  and  $T_2$  obtained from the length clamp experiments (see Fig. 2.15). One can see that the resulting points are almost identical. As we have already seen in the isometric contraction, the power strokes takes place asynchronously (at different times) in different Xbs. On the contrary, phases 2 and 3 can be explained by a synchronization of the power strokes generated by the attached Xbs just after the step on the external force. While the phases 2 and 3 are out of reach for the model discussed here, the subsequent process of attachment-detachment, which is responsible for the phase 4 where muscle produces a constant velocity of shortening, will be simulated in the next Section. One would expect that this constant velocity increases when the external force decreases as in the experimentally measured force velocity relation described in Chapter 1.

### Isotonic loading: simulations

Now we show that the model developed in this Chapter (see (3.49), (3.53)) can simulate the relaxational behavior associated to phases 1 and 4. In our numerical experiments we shall follow the time path of  $x_3$  given by (3.53), starting from initial condition  $x_1^i(0) = x_3(0) = 0$ . We start with rising tension in the course of isometric contraction  $x_3(t) = 0$  up to the moment when the force reaches a constant value  $F_{max}$ . Then, at a moment that we call  $t_{jump}$ , we change the external force



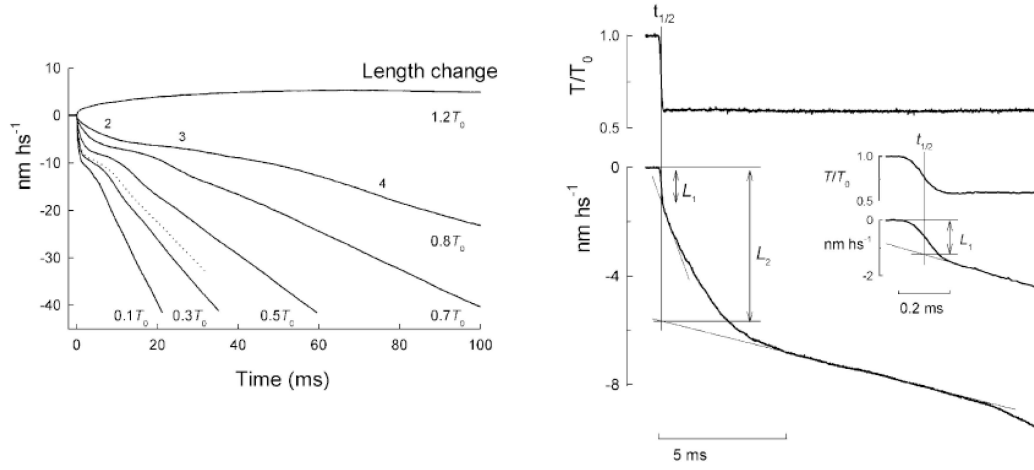


**Figure 3.20:** Experimental traces of a shortening muscle contracting against constant loads. From [67]

in (3.53) to  $F_{ext} = \alpha F_{max}$  with  $0 \leq \alpha \leq 1$ . In Fig. 3.21(a) we show the computed trajectory  $x_3(t)$  at different values of  $\alpha$ . One can see that the experimental behavior is reproduced both in phase 1 and in phase 4. As we have already mentioned, the well reproduced phase 1 is related, but it is not completely defined, by the value of  $K$ , since this fast shortening results from both the shortening of the elastic element and the relaxation of the particles inside each well. One can see that the description of phase 4 also looks rather realistic.

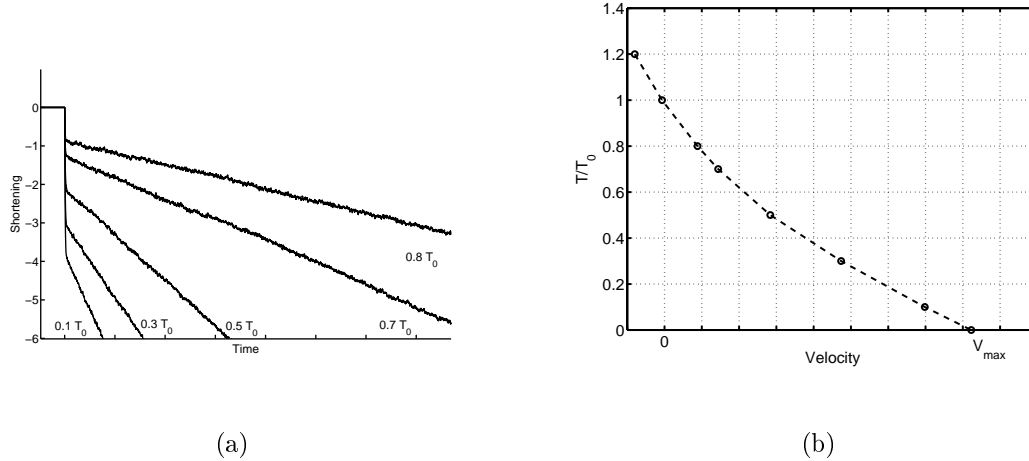


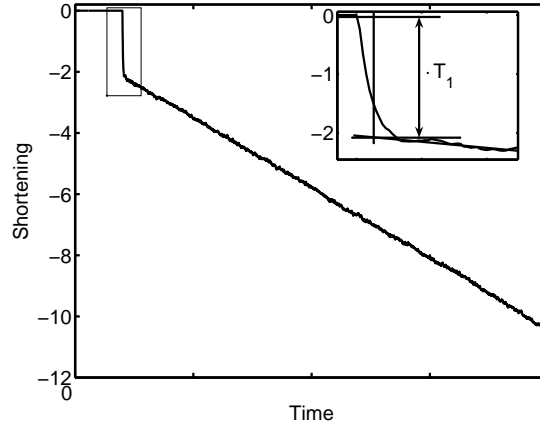
**Figure 3.21:** Simulation results in the case of force clamp simulation. The values of parameters are reported in table 3.1. (a) Simulated traces of a shortening muscle contracting against constant loads. (b) Simulated force vs. velocity curve for  $0 < \alpha < 1.2$

From the analysis of phase 4 at different  $\alpha$  we can construct the force velocity curve (see Fig. 3.21(b)). This curve shows expected non-linear relation between

**Table 3.1:** Values and meaning of the main parameters used for the numerical simulations for the original and cooperative Magnasco type model of (3.49)

Description	Numerical values
Periodicity $L$	1 nm
Asymmetry $\lambda_1$	0.3
Maximum of the potential $V_{max}$	$10k_B T$
ATP force modulus $ F_{ATP} $	$1.2 V_{max}/\lambda_2 L$
Drag coefficient of $x_1, \eta_1$	$10^2 \text{ pNns/nm}$
Drag coefficient of $x_3, \eta_3$	$10^3 \text{ pNns/nm}$
Time between oscillations $t_{ATP}$	$10^3 \tau_{step}$
Asynchronisation $\phi^i$	$i \cdot t_{ATP}/N_{Xb}$ for $i = 1, \dots, N_{Xb}$
Noise term $k_B T$	4.14 pNnm
Elastic constant $K$	0 or 30 pN/nm

the external force and the velocity of isotonic contraction. The model does not predict a change in the slope of the force-velocity curve at the isometric ( $v = 0$ ) point, which is observed experimentally (see Fig. 1.13). The main drawback of the model however is the absence of the phases 2 and 3. This can be seen in a zoom to the first moment after the jump (Fig. 3.22). More precisely, after the fast

**Figure 3.22:** Detailed analysis of the elastic relaxation after the jump in load,  $F_{ext} = 0.5T_0$ . A more detailed behavior in the first phase is shown in the box. The phase 3 is not present

shortening related to phase 1, which looks diffused as in experiments, the backbone starts immediately to shorten with a constant velocity since  $\eta_3 \ll \eta_1$ . The absence of phase 2 and 3 is obviously due to the fact that we dropped the bi-stable elements whose power step can be fostered by the step in  $F_{ext}$ . This observation bring us to the next Chapter, where we try to link the two models, described in Chapter 2 and in Chapter 3, together. These two models have been so far very successful

in describing of two different sets of experimental data. Now we would like to link them together in an unified model in order to describe the full Xb-cycle.

# Chapter 4

## Full cross-bridge cycle

### 4.1 Introduction

The model proposed in Chapter 2 deals only with a swinging lever arm dynamics which is supposed to explain the power stroke in active muscle. The model proposed in Chapter 3 describes the cyclic aspects of isometric contraction. We have seen that the model from Chapter 2 is related to phases 2 and 3 in Fig. 1.5, where the head is attached to the actin filament, while the model from Chapter 3 is related to phases 1 and 4 in the same figure, where the head detaches the filament and then reattaches again. The model from Chapter 3 does not capture fast recovery of tension after a small increment of length, which is related to the power stroke, while the model from Chapter 2 can not describe the steady state shortening of a muscle subjected to a constant load.

In the current literature, the analogues of our two models are viewed more as antagonistic than complementary. Thus Esaki and collaborators [71] say explicitly that there are two major classes of models dealing with conversion by the myosin II motor of the chemical energy into mechanical energy. The lever-arm swinging model belongs to the first class, which they call “deterministic” and “mechanistic”. The Brownian ratchet models belong to the second class, which they call “stochastic”. In this Chapter we attempt a unification of these two types of models. We begin by showing that their differences are more subtle than it can appear at a first glance. This has already been pointed out, for instance, in [68] and [69].

Since the necessity of thermal noise to ensure motion is the main difference between deterministic and stochastic models we shall first discuss the role of temperature in the models described so far in the Thesis. Thus, in the Eisenberg and Hill’s type models [17], [43], the power stroke is linked to the production of force.

The existence of two detached states is needed to have a cyclical path and the jumps between states are only marginally related to the Brownian environment in which the process takes place. Thus, while the chemical reaction that mimics the jumps is indeed frozen at  $T = 0$ , the chemical rate constants are defined phenomenologically with no reference to the actual diffusion process. The thermal noise has an indirect effect on the rate constants, but the mechanical behavior leading to the production of force is basically analogous to what one expects in the deterministic case.

On the other hand, as we have already explained, Magnasco model even at  $T = 0$  acts like a macroscopic mechanical ratchet, generating net flux in one direction in a semi-infinite interval of the fluctuating force amplitudes  $F_{ATP}$ . The thermal fluctuations increase the flux in a section of this range, while reducing it in another section, the one corresponding to higher levels of forces amplitudes (see Fig. 3.4). In this sense we are having an essential *Brownian ratchet* only at certain values of the parameter  $F_{ATP}$ . To emphasize the difference between mechanical ratchet and thermal ratchet, Wang and Oster [69] proposed a flashing ratchet where the periodic potentials  $\phi_1(x)$  and  $\phi_2(x)$  are such that  $\phi_2(x) = \phi_1(x + L/2)$ , where  $L$  is the period for both of them. In this case, the particles can show a net flux even without thermal fluctuations. Its motion is driven only by the periodic chemical cycle and the mechanical relaxation inside each minima is deterministic as it is clear from Fig. 4.1. Despite this, Jülicher and collaborators observed how this type of potential does not generate motion if the transition rates obey detailed balance [50]. In this case, in fact, we are in the same situation described in the Prost et al. model (see Section 3.3). Vale and Oosawa [25] have been the first to pose the crucial question regarding the relative importance of thermal fluctuation  $\Gamma(t)$  versus conformational changes powered by chemical driving forces, including the ones involved in the power stroke (see [68]).

It is perhaps worthwhile to observe that even the Huxley and Simmons 1971 model, which introduced the power stroke in order to explain the fast generation of force, operates with chemical energy landscape that is actually both periodic and tilted by a constant force (see Fig. 1.25). The effect of ATP can be viewed in this model as responsible for this tilt in the potential. Thermal fluctuations then make chemical transitions between the states possible. The tilt acts only in one direction, which allows for a net flux. In this sense the power stroke model and the ratchet model are not so different.

To summarize, the power stroke approach and the Brownian ratchet approach

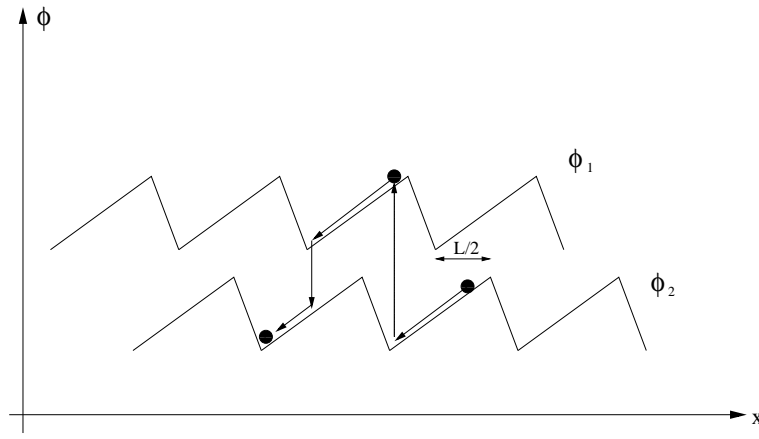


**Figure 4.1:** Fluctuating ratchet that creates a non-zero flux without thermal fluctuation

must be related in order to describe one major process: the muscle contraction. In this last Chapter of the Thesis we make a first attempt to place both models in the same framework allowing one to describe the entire Xb-cycle in a purely mechanical language.

Notice that the new model of power stroke proposed in Chapter 2 is based on the theory of thermal diffusion which is exactly the same setting as the theory of Brownian ratchets described in Chapter 3. This unification was achieved due to abandoning of the jump process approach which is normally assumed for the description of the power stroke. In this common framework a direct link can be built between our power stroke model and the ratchet theory described in Chapter 3. As we show later in this Chapter, building such an unified theory is not a straightforward task. Moreover our analysis shows some serious limitations of this whole approach. However, on a qualitative level we have been successful in providing a consistent mechanical interpretation of the whole body of experimental behavior.

## 4.2 Numerical implementation of the power stroke model

### 4.2.1 Isometric case

We recall that the analytical results presented in Chapter 2 were obtained by using the Kramers' ansatz for the time dependent probability distribution  $p(x, t)$  and from the explicit representation of the steady distribution  $p_s(x)$ . Both results

were obtained from the Fokker-Plank equation which is equivalent to the solution of the stochastic equation of motion (Langevin equation). Thus for each head  $x_2(t)$  we considered the equation:

$$\eta_2 \dot{x}_2(t) = -E'_c(x_2(t)) - K(x_2(t) - x_3(t)) + \sqrt{\eta_2 k_B T} \Gamma(t) \quad (4.1)$$

where we have explicitly written the force contributions from the two terms forming the total energy  $E_T(x)$ : the chemical energy  $E_c(x)$  and the energy of the elastic element. Equation (4.1) also shows the dependence of the elastic force on the position of the backbone  $x_3(t)$  which, in the isometric contraction case is given by:

$$x_3(t) = l_0 + \psi. \quad (4.2)$$

Here  $\psi$  is the distribution of the attachment sites described in Section 2.7.2, which will be used later in the modeling of a population of Xbs.

We begin by reformulating our modified Huxley and Simmons model presented in Chapter 2 in the framework of the Brownian ratchet model described in Chapter 3. We recall that the noise is characterized by the following relations:

$$\langle \Gamma(t_1) \rangle = 0 \quad (4.3)$$

$$\langle \Gamma(t_1) \Gamma(t_2) \rangle = \delta(t_1 - t_2) \quad (4.4)$$

The Euler algorithm for equation (4.1) reads:

$$\begin{aligned} x_2(t + \tau_{step}) = x_2(t) &- \frac{1}{\eta_2} (E'_c(x_2(t)) - K(x_2(t) - x_3(t))) \tau_{step} \\ &+ \frac{\sqrt{\eta_2 k_B T}}{\eta_2} \sqrt{\tau_{step}} w(0, 1). \end{aligned} \quad (4.5)$$

Since equation (4.5) is stochastic, in order to simulate the average of  $x_2(t)$  we have to follow the trajectory of a population of  $N_{Xb}$  particles each corresponding to a different realization of the noise term. Each particle also has a different value of  $\psi$  from (4.2).

A typical behavior generated by the model when the backbone is in its resting position  $x_3(t) = l_0$  (isometric contraction) is shown in Fig. 4.2(a). We see that the head jumps back and forth between the energy wells because the two phases have the same total energy and there is no preferred state. To ensure this, we impose condition (2.10), as in Chapter 2. The fact that in the isometric case the two phases have the same total energy is then strictly true only for the Xb with  $\psi = 0$ .

As we see in Fig. 4.2(a), particles explore all the energy landscape spending in each of the wells a time that is proportional to the corresponding probability. The amplitude of oscillations is inversely proportional to the stiffness of the wells. Thus in the figure the elastic modulus of the well centered near zero is higher than the one for the well describing the “short” phase. The histogram showing the probability distribution of the position  $x_2(t)$  during the total time of the simulation, has locally Gaussian structure around the two minima of the energy, as it has been predicted by the associated FPE. The same is true for the probability distribution of Xbs at a given time, shown in Fig. 4.2(b).

### 4.2.2 Length clamp device

According to (3.52), the tension in the numerical experiment simulating the length clamp can be calculated as:

$$T(t) = \sum_{i=1}^{N_{Xb}} [-K(x_2^i(t) - x_3^i(t))] \quad (4.6)$$

where  $x_3$  are given by:

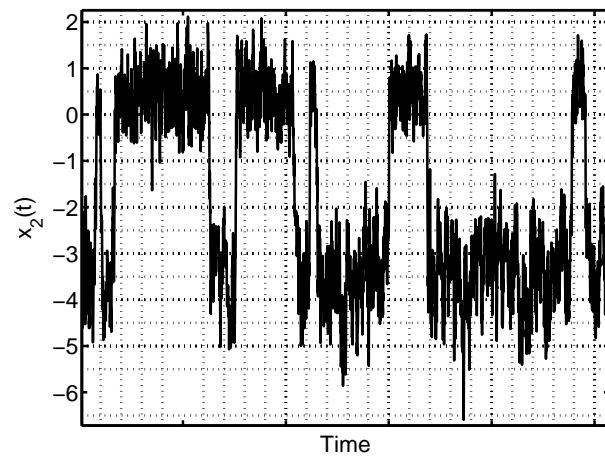
$$x_3^i(t) = \begin{cases} l_0 + \psi^i & t \leq t_{jump} \\ \delta + l_0 + \psi^i & t > t_{jump} \end{cases} \quad (4.7)$$

In Fig. 4.3 we present  $T(t)$  curve for negative values of  $\delta$ . The direct numerical simulation confirm the analytically predicted response of the system and allows one to extract the values  $T_1(\delta)$  and  $T_2(\delta)$  as well as the parameter characterizing the rate of recovery.

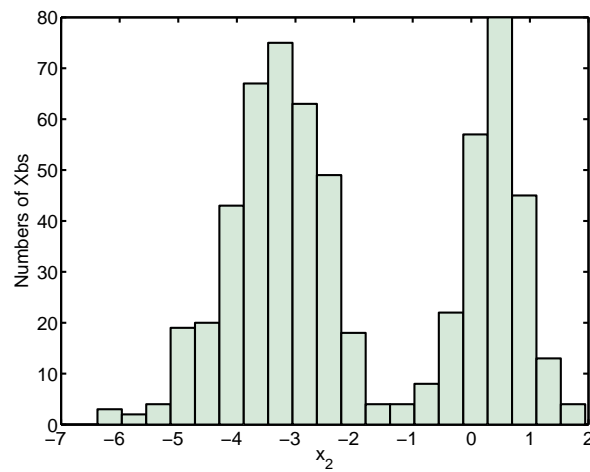
To verify the quantitative accuracy of our numerical scheme and the validity of Kramers’ approximation used in Chapter 2, we can compare the results of the two approaches applied to the length clamp experiment using the set of parameters reported in Tab. 4.1. The kinetics of tension recovery for a particular value of  $\delta$  is illustrated in Fig. 4.4(a). The corresponding multi-exponential curve (see Section 2.8) obtained from the approximate theory, is superimposed. To plot this curve,  $n_{exp}$  ( $= 10$ ) exponential contribution are computed from the Kramers’ theory based on  $n_{exp}$  populations of Xbs with different attachment positions  $\psi$ . The tension  $T_{exp}$  is computed from the formula:

$$T_{exp}(n_{iter}) = \frac{1}{n_{exp}} \sum_{i=1}^{n_{exp}} e^{-\alpha^i n_{iter}} \quad (4.8)$$





(a)



(b)

**Figure 4.2:** Numerical simulation of isometric contraction. (a) Time path of a Xb in a double well potential. (b) Histogram describing the population of Xbs

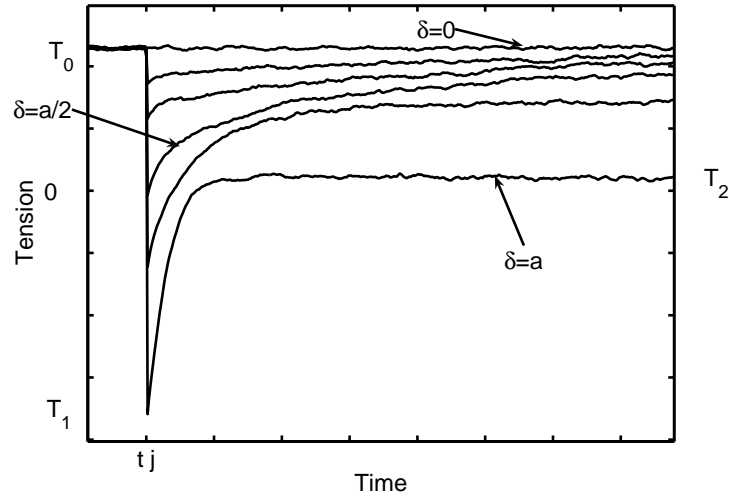


**Figure 4.3:** Simulation of the force vs. time relation at different applied length steps

where  $n_{iter}$  is the number of effective time steps from the time  $t_{jump}/\tau_{step}$  till end of the simulation  $t_{tot}/\tau_{step}$ ,  $\tau_{step}$  is the effective time step,  $t_{jump}$  the value of  $t$  when the increment in length is applied,  $t_{Tot}$  the total time of the simulation,  $\alpha^i$  is the  $i$ -th exponent computed from equation (2.95) with  $\psi = \psi^i$ . The tension is normalized by  $T_1$  and shifted vertically to ensure that  $T_2 = 0$ . One can see that the kinetic curves obtained by the two methods, analytical and numerical, are similar, except for the very fast components. For those the relaxation inside the minima is also important and the Kramers' approximation fails.

**Table 4.1:** Main parameters used in the comparison of the behavior predicted by the Kramers' theory and the numerical simulations based on (4.1) and (4.7)

Description	Numerical values
Distance between the minima $a$	10.8 nm
Elasticity of the elastic element $K$	2 pN/nm
Elasticity of the low force generating state $k_1$	4 K
Elasticity of the high force generating state $k_2$	K
Curvature of the maximum $k_3$	-20 pN/nm
Drag coefficient of $x_2$ , $\eta_2$	60 pNs/nm
Dispersion of the attachment sites $\psi$	$\pm 2.75$ nm
Noise term $k_B T$	4.14 pNnm

As far as the steady state tension  $T_2(\delta)$  is concerned, we remark that in numerical experiments the curve  $T_2(\delta)$  has to be constructed by points, as in real experiments. In Fig. 4.4(b) we superimposed the analytical curve obtained from equation (2.43) and the points obtained from the simulations; the two methods

predicts exactly the same behavior. The numerical code is therefore verified and we can use it in the next Section to simulate the whole Xb cycle.

### 4.3 Whole cycle models

In the previous Sections we reformulated the models for the power stroke and for the attachment-detachment process by using the same framework. This allows us to construct a unified model allowing one to describe the whole Xb cycle and to study its different features. The considerations below will be based on the Magnasco type model proposed in Chapter 3, however similar conclusion can be made if other type of Brownian ratchets are used as building blocks. We begin by describing the behavior of a model of unification which assumes that the chemical energy describing the power stroke is extended periodically.

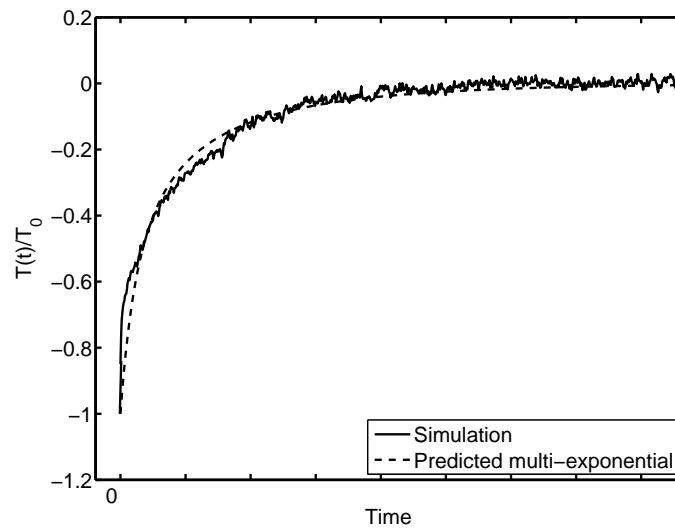
#### 4.3.1 Extended Huxley and Simmons potential

When a small increment of the length is imposed, the HS71 model [10] allows each head to explore only two wells of the chemical energy landscape. However, the idea of the authors was that this chemical energy is periodically extended (see Fig. 1.25). In this case an isotonic experiment should in principle be able to show several jumps of each head. Thus, even in the rapid length increment experiment described in [10], the heads, after a fast recovery of tension  $T_2$ , must evolve towards a new equilibrium state reaching in the long term, again the tension  $T_0$  (Section 1.2). To simulate this behavior we introduce a periodic potential which, as in the HS71 model, is tilted in one direction.

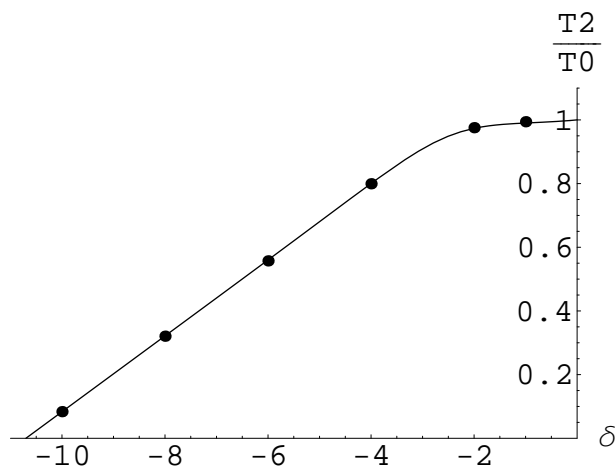
In this new model every well of the resulting ratchet, has two smaller sub-wells, as shown in Fig. 4.5. We suppose that the energy landscape is piecewise linear with a derivative given by:

$$V'(x) = \begin{cases} \frac{h}{\lambda_1^a(\lambda_1^a + \lambda_2^a)L} & nL < x < [n + \lambda_1^a(\lambda_1^a + \lambda_2^a)]L \\ \frac{-(h-d)}{\lambda_2^a(\lambda_1^a + \lambda_2^a)L} & [n + \lambda_1^a(\lambda_1^a + \lambda_2^a)]L < x < n(\lambda_1^a + \lambda_2^a)L \\ \frac{H-d}{\lambda_1^b(\lambda_1^b + \lambda_2^b)L} & [n + (\lambda_1^a + \lambda_2^a)]L < x < [n + (\lambda_1^a + \lambda_2^a) + \lambda_1^b(\lambda_1^b + \lambda_2^b)]L \\ \frac{-H}{\lambda_2^b(\lambda_1^b + \lambda_2^b)L} & [n + (\lambda_1^a + \lambda_2^a) + \lambda_1^b(\lambda_1^b + \lambda_2^b)]L < x < n(L + 1) \end{cases} \quad (4.9)$$

Here index  $n$  describes a particular well. We refer to Fig. 4.5 for the meaning of the parameters.



(a)



(b)

**Figure 4.4:** Length clamp experiment. Analytical results from Kramers' theory compared to numerical simulations. (a) Kinetics of the recovery of tension (rugged line: simulation, dashed line: Kramers' theory). (b)  $T_2(\delta)$  curve (solid line: Kramers' theory, points: simulation)

We observe that the original Huxley and Simmons' model is able to describe constant tension  $T_0$  generated in isometric contraction. When a muscle is isometrically tetanized,  $T_0$  is maintained while each Xb goes through all four phases shown in Fig. 1.5, so that in average the number of heads in each phase remains approximately constant. When  $\delta(t) = 0$ , the HS71 model implicitly assumes that for each Xb that detaches, another replaces it in the same position, which leaves  $T_0$  constant. In the similar way, jumps between larger wells mimic in this model the attachment-detachment process. The implicit assumption is that for each head that detaches from the post-power stroke state, another head immediately attaches in the pre-power stroke state.

We assume that the difference in the energy levels of the two sub-wells is equal to  $K(\lambda_1^a + \lambda_2^a)$ , (see condition (2.10)). The jump between these sub-wells represents the power stroke. After every attachment-detachment process, the particle  $x_1$  is in the pre-power stroke state, and can change the configuration again, switching to the post-power stroke state, in order to pull the myosin backbone. We suppose that all the particles are attached to the backbone through a spring, the jump between the post-power stroke state toward the next pre-power stroke state stretches this elastic element. Formally, this stretch is zero in the Xb cycle, and here can be here reduced assuming  $\lambda_1^b + \lambda_2^b \ll \lambda_1^a + \lambda_2^a$ .

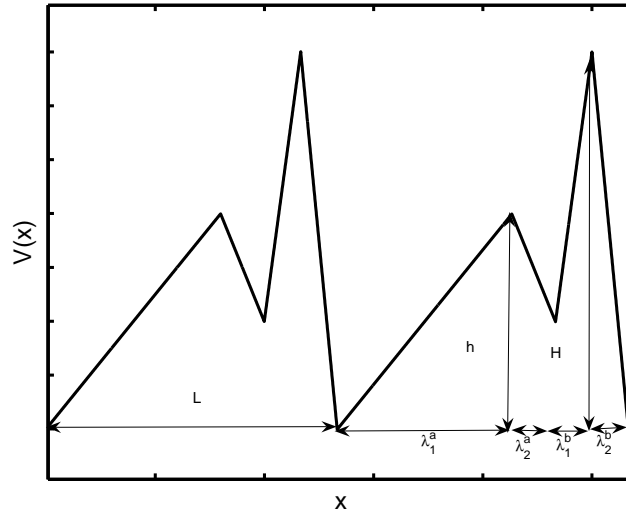


**Figure 4.5:** Potential of the periodically extended HS71 model, where the bi-stable element is incorporated into the ratchet potential

To implement this model numerically we assume that all the Xbs (all the particles) evolve in the piecewise linear potential (4.9). The resulting system of equa-

tions reads: backbone  $x_3$  reads:

$$\begin{cases} \eta_1 \dot{x}_1^i = -V'(x_1^i) + F_{ATP} - K(x_1^i - x_3) + \sqrt{\eta_1 k_B T} \Gamma_1(t) & i = 1, \dots, N_{Xb} \\ \eta_3 \dot{x}_3 = F_{ext} + \sum_{i=1}^{N_{Xb}} (K(x_1^i - x_3)) + \sqrt{\eta_3 k_B T} \Gamma_3(t) \end{cases} \quad (4.10)$$

In order to simulate the constantly tilted potential of Fig. 1.25, we have added to (3.49) a constant force  $F_{ATP}$ . In this way  $\langle F_{ATP}(t) \rangle \neq 0$  and we have an *asymmetrically tilted ratchet* (see also [68]). We shall come back to the meaning of  $F_{ATP}$  later in this Chapter.

A numerical study of this model is rather heavy in terms of the time needed to generate a quantitative response curves. The reason is that in order to provide two different time scales, one for the power stroke and another for the attachment-detachment processes, we need to impose a constraint  $H \gg h$  (separating the scales of the relative height of the barriers, see Fig. (4.9)). We recall that also  $\lambda_1^b + \lambda_2^b$  has to be small; these two requirements together make the ratio  $\eta_1(\lambda_1^b + \lambda_2^b)L/H$  also small which limits the maximum  $\tau_{step}$  as described in Section 3.4.

We turn now to the discussion of the simulated force time curve showing the response to a given length step (Fig. 4.6). One can see that both fast and slow time scales have been resolved. The force tends towards the steady value  $T_0$ . Before that, a rapid increment in the total length ( $\delta < 0$ ) generates a drop in the tension due to the elastic element which links  $x_1$  to the backbone, but then jumps between the sub-wells rise the value of the tension up to  $T_2$ . This last state is no longer a steady state, as in the model of Chapter 2 where the chemical energy was going to infinity at the boundary of the two-well region. In a larger time scale the variable  $x_1$  can overcome the higher barrier and make it into another two-well region. This increases the tension applied to the backbone and bring it back to its original value  $T_0$ .

Despite the fact that this picture looks rather realistic, the model is not satisfactory because we used an explicit tilting force in order to break the detailed balance. In the next section we show how such purely mechanical bias can be avoided and how the Xb cycle can be described by an oscillating Brownian ratchet without permanently tilting forces.

### 4.3.2 Chemical-Spring-Motor model (CSM)

As a first attempt to couple the models presented in Chapters 2 and 3, we consider a system with two particles  $x_1$  and  $x_2$ , moving in the potentials  $V(x_1)$  and

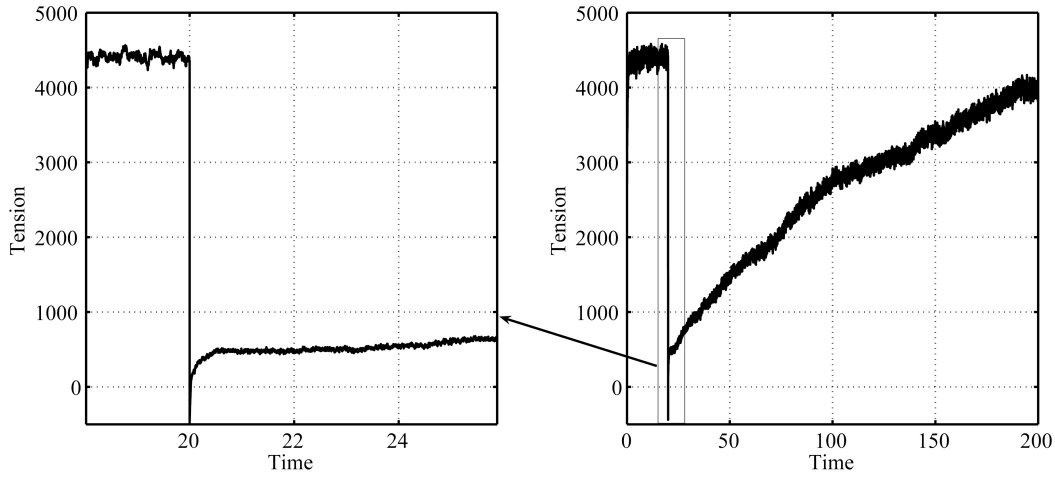


**Figure 4.6:** Tension vs. time curve showing fast and slow time scale for the periodically extended HS71 model. Parameters are taken from Table 4.2. Tension: arbitrary units. Time scales:  $10^3 \tau_{step}$

$E_c(x_2)$  respectively. Here  $V(x)$  is an asymmetric periodic piecewise linear potential described in Chapter 3 (equations (3.48)):

$$V'(x) = \begin{cases} V_{max}/(\lambda_1 L) & nL < x < nL + \lambda_1 L \\ -V_{max}/(\lambda_2 L) & nL + \lambda_1 L < x < (n+1)L \end{cases} \quad (4.11)$$

and  $E_c(x)$  is a piecewise quadratic double well potential described in Chapter 2 (equations (2.96)). Due to the total length constrained, the energy  $E_c(x)$  can be written in terms of the variable  $x_3$ :

$$E_c(x_2, x_3) = \begin{cases} \frac{1}{2}k_1(x_2 - x_3)^2 & x_2 \geq b_1(x_3) \\ \frac{1}{2}k_3(x_2 - x_3 - b)^2 + e & b_2(x_3) \leq x_2 < b_1(x_3) \\ \frac{1}{2}k_2(x_2 - x_3 - a)^2 + d & x_2 < b_2(x_3) \end{cases} \quad (4.12)$$

The two particles  $x_1$  and  $x_2$  are assumed to be linked by a linear elastic element with stiffness  $K$ . The coordinate  $x_3$  can be viewed as the position of a backbone (myosin) attached to the controlling loading device. The coordinate  $x_1$  is then the position of the myosin head along the actin filament. The actin filament is represented by the periodic potential  $V(x_1)$ . The coordinate  $x_2$  describes the swinging lever-arm portion of the head that can be in two configurations described by the energy  $E_c(x_2)$ . These notations will be operative throughout this Chapter. The model is graphically illustrated in Fig. 4.7.

We assume that the particles are embedded in a viscous environment and that their respective drag coefficients  $\eta_i$  are different, reflecting the fact that their geometries are different. Finally, the whole system is subjected to an external random

**Table 4.2:** The main parameters used for the numerical simulations of the periodically extended HS71 model.

Description	Numerical values
Periodicity $\lambda_1^a + \lambda_2^a + \lambda_1^b + \lambda_2^b$	1.1 nm
Width lower peak $\lambda_1^a + \lambda_2^a$	1 nm
Width higher peak $\lambda_1^b + \lambda_2^b$	0.1 nm
Internal asymmetry $\lambda_1^a$	0.8 nm
External asymmetry $\lambda_1^b$	0.05 nm
Noise term $k_B T$	1 pNnm
Drag coefficient of $x_1$ , $\eta_1$	1 pNns/nm
Higher peak potential $H$	$5k_B T$
Lower peak potential $h$	$4k_B T$
ATP force modulus $ F_{ATP} $	$0.8 h / \lambda_1^a L$
Dispersion of the attachment sites $\psi$	$\pm 0.5$ nm

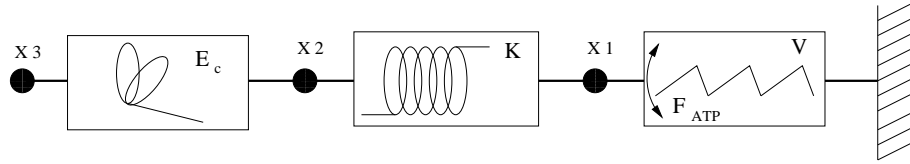


**Figure 4.7:** CSM model for a single Xb: series connection of a bi-phase element, an elastic element and a motor element

force represented by a white noise. To complete the description of a ratchet, a piecewise constant tilting force  $F_{ATP}(t)$  with zero mean  $\langle F_{ATP}(t) \rangle = 0$ , is added to the periodic potential  $V(x)$ :

$$F_{ATP}(t) = \begin{cases} +F_{ATP} & n\Delta t_{ATP} < t < (n+1)\Delta t_{ATP} \\ -F_{ATP} & (n+1)\Delta t_{ATP} < t < (n+2)\Delta t_{ATP}. \end{cases} \quad (4.13)$$

In addition an external force  $F_{ext}$  can be applied to the backbone  $x_3$  (load clamp device) or its position can be prescribed by a length clamp device. In the case of load clamp device the system of stochastic ordinary differential equation for a single Xb can be written as:

$$\begin{cases} \eta_1 \dot{x}_1(t) = -V'(x_1(t)) + K(x_2(t) - x_1(t)) + F_{atp}(t) + \sqrt{\eta_1 k_B T} \Gamma(t) \\ \eta_2 \dot{x}_2(t) = -E'_c(x_2(t) - x_3(t)) - K(x_2(t) - x_1(t)) + \sqrt{\eta_2 k_B T} \Gamma(t) \\ \eta_3 \dot{x}_3(t) = E'_c(x_2(t) - x_3(t)) + F_{ext} + \sqrt{\eta_3 k_B T} \Gamma(t). \end{cases} \quad (4.14)$$

Conditions (4.7) replace the third equation in the case of a length clamp device.



Extensive numerical experiments have been performed for the model (4.14). We have found that the model can reproduce the  $T_2(\delta)$  curve in the fast regime, however it fails to reproduce the peculiarities of kinetics of the process leading to the steady state at high values of  $\delta$ . The fast branch of the typical tension vs. time curve is shown in Fig. 4.8, where we see no elastic response (no  $T_1$  phase) is present. This negative result eliminates the necessity to discuss the slow relaxation predicted by the model.

To explain the result we first observe that since the particles are embedded in a viscous environment only potential  $E_c$  is shifted when a  $\delta$  increment is instantaneously imposed on  $x_3$  in a length clamp device. In the meantime the particle  $x_2$  remains where it had been before the step. If the shift of the potential (i.e. the value of  $\delta$ ) is larger than the distance between the minima, all the particles  $x_1^i$  end up after the step in one well, and the steady state tension is recovered due to fast relaxation within this well. There is no subsequent change of configuration which leads to the absence of the characteristic fast recovery stage.

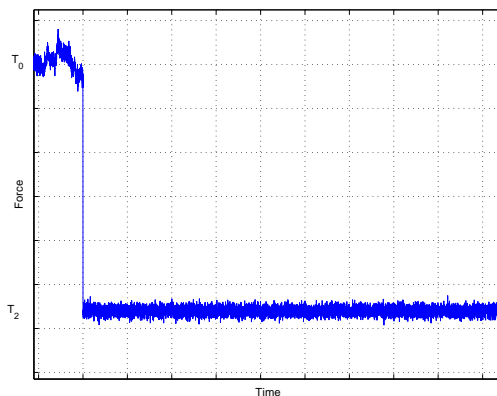


**Figure 4.8:** Tension vs. time curve predicted by the CSM model in a clamp device

This analysis suggests that we must also consider differently designed configurations of the basic elements: a spring, a snap-spring and a motor.

### 4.3.3 Spring-Chemical-Motor model (SCM)

A more detailed look at the cross bridge structure is needed to proceed further. Recent observations (see for instance [72]) have characterized with high precision the structure of the myosin head and of its two sites with the affinity for the actin and for the ATP, respectively. For the purpose of designing only a prototypical model (we refer to [72] and references therein for a complete scheme) it is enough to

assume that the myosin head has three major sub-structures: the first one attaches to actin filament, the second one can rotate with respect to the first one generating the power stroke, and finally the third one couples the second one with the myosin backbone (see Fig. 4.9). Normally, the elastic component is identified with the third structure, however this is not universally accepted.

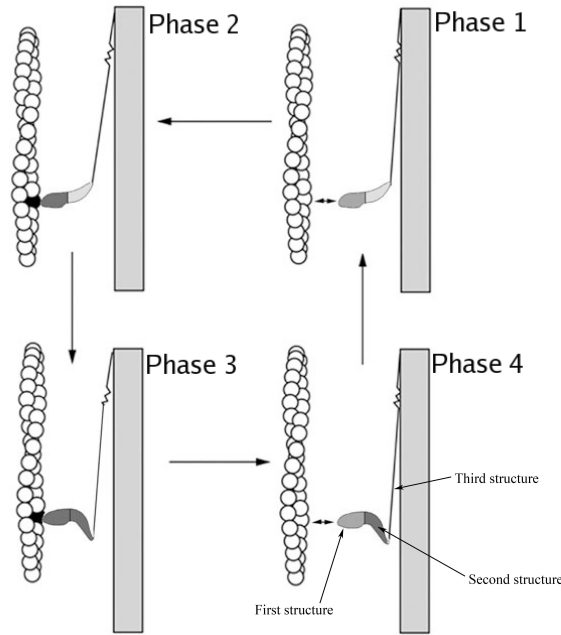


**Figure 4.9:** Cross bridge cycle with emphasized sub-structure of the myosin head. The phases 1 to 4 are added to the original figure to relate it with Fig. 1.5. From [72]

A consideration of the molecular structure of the Xb suggests another way of coupling the elements. Thus we can assume that the lever arm of the Xb, represented by the coordinate  $x_2$ , is linked to the clamp device (ultimately the myosin thick filament, the coordinate  $x_3$ ) through an elastic element of stiffness  $K$ . The lever arm can be in two different states and the corresponding chemical energy  $E_c(x_2, x_1)$  takes the form:

$$E_c(x_2, x_1) = \begin{cases} \frac{1}{2}k_1(x_2 - x_1)^2 & x_2 \geq b_1(x_1) \\ \frac{1}{2}k_3(x_2 - x_1 - b)^2 + e & b_2(x_1) \leq x_2 < b_1(x_1) \\ \frac{1}{2}k_2(x_2 - x_1 - a)^2 + d & x_2 < b_2(x_1) \end{cases} \quad (4.15)$$

This potential is affected by the attachment position of the myosin head (attachment site, coordinate  $x_1$ ) which is moving on the actin filament itself and therefore feels a periodic asymmetric potential  $V(x_1)$ . Regarding the motion of  $x_1(t)$ , we

stress that the time it spends in the bottom of the well of  $V(x_1)$  before the jump into the neighboring well must be much longer than the time needed for the jump itself (see Section A.6.3). The resulting model is schematically depicted in Fig. 4.10.

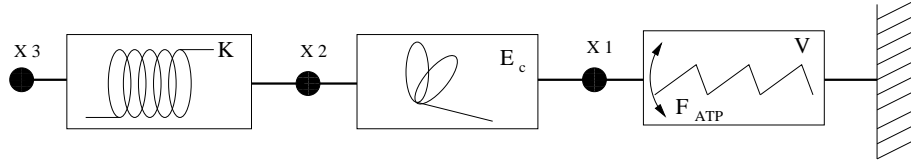


**Figure 4.10:** SCM model for one Xb: series connection of an elastic element, a biphasic chemical element and of a motor element

In this new arrangement of elements changing of the location of the attachment site affects directly the relative conformational state of the chemical energy represented by the variable  $x_2 - x_1$ . The set of stochastic equations for a single head can now be written as:

$$\begin{cases} \eta_1 \dot{x}_1 = [-V'(x_1(t)) + F_{atp}(t) + E'_c(x_2(t) - x_1(t) - \psi)] + \sqrt{\eta_1 k_B T} \Gamma(t) \\ \eta_2 \dot{x}_2 = -E'_c(x_2(t) - x_1(t) - \psi) - K(x_2(t) - x_3(t)) + \sqrt{\eta_2 k_B T} \Gamma(t) \\ \eta_3 \dot{x}_3 = K(x_2(t) - x_3(t)) + F_{ext} + \sqrt{\eta_3 k_B T} \Gamma(t) \end{cases} \quad (4.16)$$

To reproduce the isometric tension experiment we start with the initial condition  $x_1(0) = 0$ ,  $x_2(0) = 0$  and  $x_3(0) = 0$ . As it has been already noted, the reference lengths in the numerical code can be set equal to zero without loss of generality. By imposing the condition  $x_3(t) = 0$ , we let the system (4.16) evolve while we record the tension generated by the system

$$T(t) = -Kx_2(t). \quad (4.17)$$

The probability distribution associated with  $x_1$  in the steady state  $T = T_0$ , which affects the stretch of the elastic element, can no longer be found analytically. As a consequence, we can not compute from equation (2.10) the value of  $d$  in  $E_c$ , which is necessary to assure that the Xbs in the isometric contraction can jump back and forth between the energy wells as in the original HS71 model. To resolve this problem, we associate the steady value  $T_0$  reached by (4.17) with  $F_{motor} = T_0$  and impose a particular pre-stretch on the elastic element  $x_3(0) = l_0$  such that:

$$-\frac{1}{2}K(a_1 - l_0) - \frac{1}{2}K(a_2 - l_0) = F_{motor}. \quad (4.18)$$

In the left hand side of this equation we see the mean tension generated at  $\langle x_1 \rangle = 0$ . This follows from (2.19) under the assumption that the Xb spends half of the analyzed time  $t_{Tot}$  in each well of the chemical energy  $E_C$  ( $a_1$  and  $a_2$  are the two minima given by (2.9)). Substituting (2.9) in (4.18) we obtain

$$l_0 = \left[ 2 \frac{F_{motor}}{K} - \frac{ak_2}{k_2 + K} \right] / \left[ \frac{2K + k_1}{K + k_1} + \frac{K}{k_2 + K} \right] \quad (4.19)$$

where  $a$  is the distance between the minima of  $E_c$ . During the isometric contraction with  $x_3(t) = l_0$ , we now have  $\langle x_1 \rangle = 0$  because the effect of the motor is compensated by the pre-stretch. With the value of  $d$  computed from (2.10), (4.19) we can be sure that the conformational transition is not biased and that Xb oscillates between equivalent states during isometric contraction.

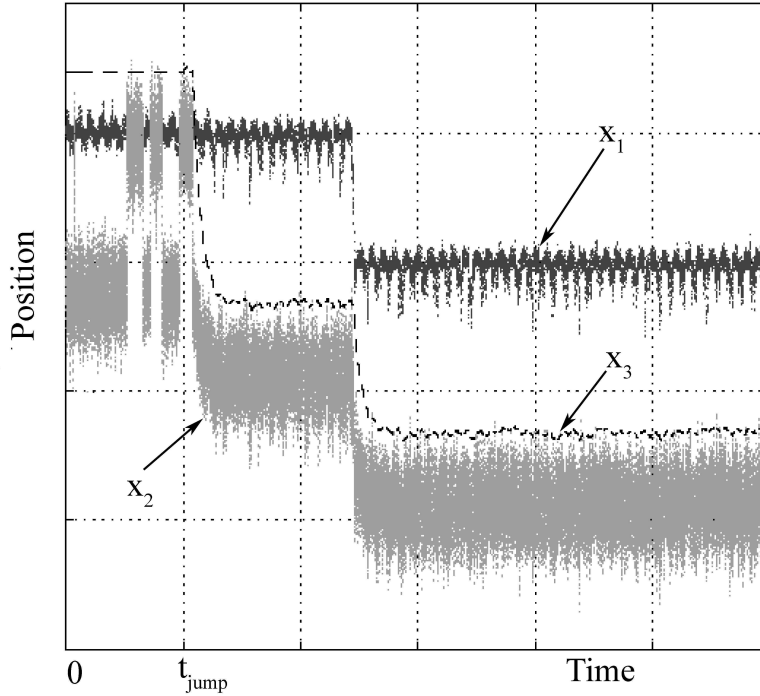


**Figure 4.11:** Position vs. time curves for the particles  $x_1$ ,  $x_2$  and  $x_3$  in a force clamp experiment

In Fig. 4.11 we show the response of the system (4.16) to the sudden switch at the time  $t_{jump}$  from isometric contraction,  $x_3(t) = l_0$ , to isotonic contraction with  $F_{ext} = 0.5T_0$ . In the interval  $0 < t < t_{jump}$  we see that  $x_1(t)$  lies near zero while the bi-stable element, the lever-arm represented by  $x_2(t)$ , oscillates between two states. At  $t > t_{jump}$ , the variable  $x_3$  moves towards negative values which relaxes the elastic element. The smaller elastic force acting on  $x_2$  allows the bi-stable

element to shift toward the high force generation phase, which is now representing the global minimum of the energy (see Chapter 2). This power stroke shifts  $x_3$  in the same direction and after a fast relaxation, the force acting on  $x_1$  starts to oscillate around the imposed value  $F_{ext} = 0.5T_0$ . Since  $T_0 = F_{motor}$  is the force that maintained, in the isometric case, the variable  $x_1$  in the original well of the periodic potential, it now starts moving in the direction imposed by the motor. This motion takes place at a longer time scale than phenomena described above. In Fig. 4.11 we see only one jump of  $x_1$ . This jump mimics the attachment-detachment process of the head. It leads to a shift of  $E_c(x_2, x_1)$  through (4.16) and results in the identical displacement of  $x_2$  and  $x_3$ . In experiments (see Fig. 3.20) the shortening of the muscle, represented here by the time history of  $x_3(t)$ , does not exhibit jumps. Since the model presented here predicts a stepwise motion for  $x_3$  we still need to average the results over the effect of several Xbs acting on the same myosin backbone. This suggests another modification of the model.

#### 4.3.4 Spring-Chemical-Motor model with a backbone (SCM1)

In experiments the total length of the muscle changes in a smooth way because the myosin filament is affected by a population of Xbs which act asynchronously. The effect of each power stroke is averaged out due to the existence of the common backbone. To simulate this effect we consider a model in which the coordinate  $x_3$  is common to the whole population of Xbs which are posed in parallel. The configuration is illustrated in Fig. 4.12.

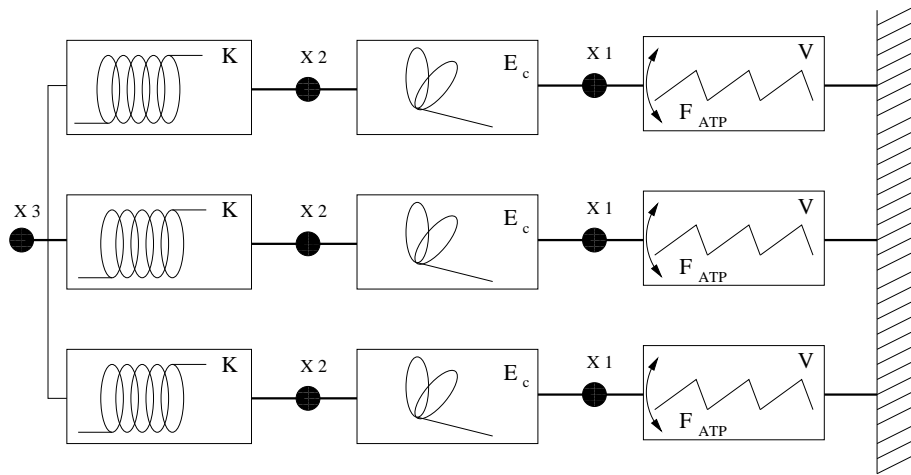


**Figure 4.12:** SCM1 model with a common  $x_3$  for the Xbs

The set of stochastic equations for this model can be written as follows:

$$\begin{cases} \eta_1 \dot{\bar{x}}_1 = [-V'(\bar{x}_1(t)) + F_{atp}(t) + E'_c(\bar{x}_2(t) - \bar{x}_1(t) - \bar{\psi})] + \sqrt{\eta_1 k_B T} \Gamma(t) \\ \eta_2 \dot{\bar{x}}_2 = -E'_c(\bar{x}_2(t) - \bar{x}_1(t) - \bar{\psi}) - K(\bar{x}_2(t) - x_3(t)) + \sqrt{\eta_2 k_B T} \Gamma(t) \\ \eta_3 \dot{x}_3 = \sum_{i=1}^{N_{Xb}} K(x_2^i(t) - x_3(t)) + F_{ext} + \sqrt{\eta_3 k_B T} \Gamma(t) \end{cases} \quad (4.20)$$

where the chemical energy is defined in (4.15), the periodic potential is defined in (4.11) and  $F_{ATP}$  is given by (4.13). The overlined quantities are vectors of length  $N_{Xb}$ , say  $\bar{x} = (x^i) = (x^1, x^2, \dots, x^{N_{Xb}})$ , and the difference between a vector and a scalar is computed as:

$$\bar{x} - x_3 = (x^1 - x_3, x^2 - x_3, \dots, x^{N_{Xb}} - x_3). \quad (4.21)$$

In order to understand this model, we analyze below the response of the system first in a length clamp device and then in a force clamp device. As we are going to see, the predictions for  $x_3(t)$  are in qualitative agreement with experiments. While for a population of Xb, due to averaging over the  $x_3^i(t)$ 's, even the SCM model predicts qualitatively similar smooth curves, the SCM1 model has a clear advantage. In this model the actual position of  $x_3(t)$ , not only the mean value  $\langle x_3(t) \rangle$  as in SCM model, is only weakly sensitive to the positions of the individual  $x_3^i(t)$ . This is important because in the second equation of (4.16) the variables  $x_3^i(t)$  affect the behavior of the corresponding  $x_2^i(t)$  directly.

### Length clamp device

If we prescribe the motion of the backbone  $x_3(t)$  as in equation (4.7) and average out the noise term, the third equation of the system (4.20), becomes:

$$0 = N_{Xb} K(\langle \bar{x}_2(t) - x_3(t) \rangle) + F_{ext}. \quad (4.22)$$

This means that the external force, is proportional to the mean stretch of the elastic element times the number of Xbs connected in parallel. The relation (4.22) will be used in the simulations to compute the force in the length clamp protocol.

In Fig.4.13 we plot the tension  $F_{ext}(t)$  produced by the system in response to a single shortening step. This time we are interested in what happens at both short and long time scales. In Fig. 4.13(b) we see that the rapid tension recovery matches qualitatively well the exponential relaxation characterizing the fast stage up to the plateau. In Fig. 4.13(a) the typical simulation for long times is reported. Here

we see the slower recovery of the force towards the original tension  $T_0$ , exactly as in experiments. The corresponding force velocity curve is also in accordance with experiments: the curve  $F - v$  is qualitatively similar to the one presented in the end of Chapter 3 (see Fig. 3.21(b)).

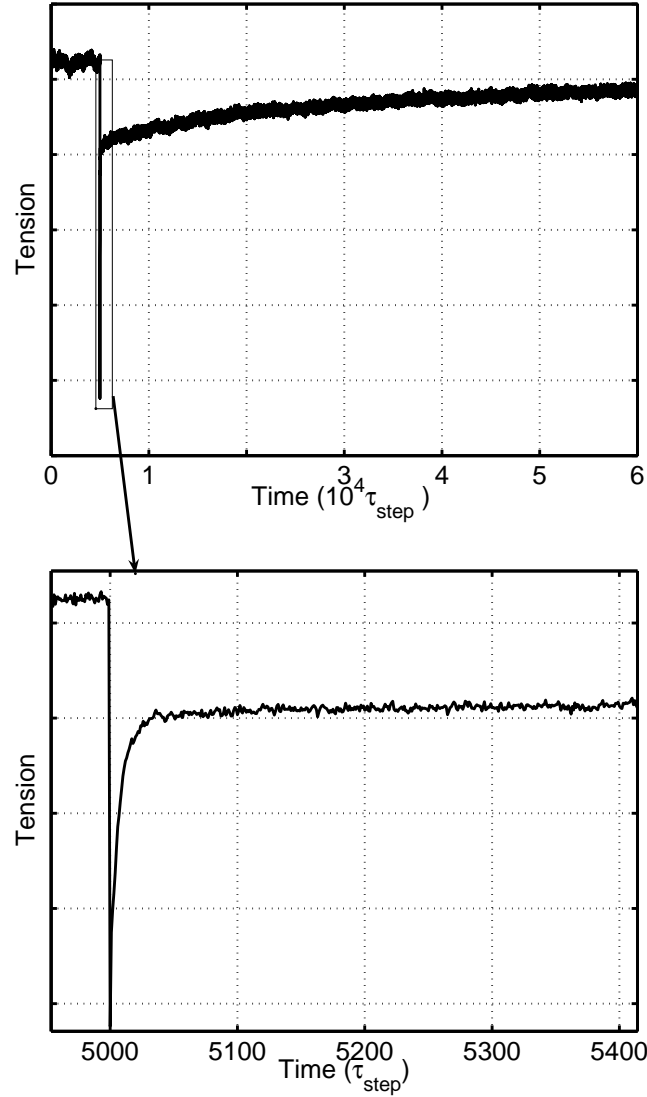


**Figure 4.13:** Long (a) and short (b) time scale behavior of the SCM1 model in response to a shortening step

While the overall behavior very nicely conforms with macroscopic experimental observations. A more detailed analysis of the short time scale response shows some details which also agree with observation. Thus in our numerical experiments, the expected level of tension  $T_2(\delta)$  does not form a perfect horizontal plateau. In experiments the relaxed stredd  $T_2(\delta)$  also does not always appear in the form of a real plateau and represents instead just a region with a low speed of recovery

[43]. Within this indeterminacy in the exact interpretation of the  $T_2(\delta)$  level, the general difference between reaching  $T_2(\delta)$  and the more slow recovery of the isometric tension  $T_0$  due to the attachment-detachment process is well defined in both numerical and physical experiments.

### Force clamp device

To show in more detail the working of the model we return to the load clamp simulations and compare them with the corresponding experiments. To the author's knowledge, the load clamp experiments are made with higher precision than the length clamp experiments [43], [67]. We refer to Fig. 3.20 where 4 distinct phases, already described in Chapter 3, are clearly visible. In particular, even if no plateau is present, the phases 2, 3 and 4 are well defined. Then a period of reduced rate (phase 3) is observed before the beginning of phase 4, when the rate of shortening becomes constant. As we discussed in Section 3.6.3, phases 2 and 3 are believed to be due to synchronization of the power strokes exhibiting by the attached Xbs.

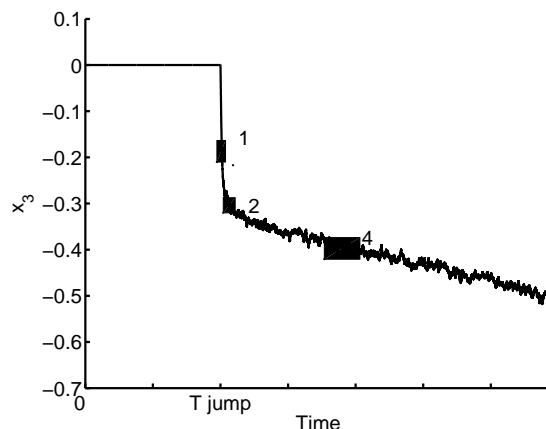


**Figure 4.14:** Load clamp simulation with in the SCM1 model

In all models discussed so far the motor component worked independently of the conformational state of the lever-arm and the associated shortening was always present. Obviously, this shortening is negligible during the relaxation of the elastic element (phase 1) and should not play any role during the rapid shortening due to the power stroke. When these process terminate, it is phase 4 which dominates. In our experiments we have not been able to reproduce the phase with lower rate than phase 4 (the definitive feature of phase 3). This is clearly seen in the simulation of the load clamp device, reported in Fig. 4.14. Such behavior should be common to all models where Brownian motor component works independently of the bi-stable



element. The reason is that the minimal velocity of shortening due to ratchet which is characteristic of phase 4, will be always present even during phase 3. One way to obtain a distinct phase 3 would be to let the motor part know when all the Xbs are in the second well, through a “phenomenological” component in the definition of  $F_{ATP}(t)$ , however we leave this option outside the scope of this Thesis. Instead we would like to maintain our fully mechanical framework for as long as possible without imposing any phenomenological relations between the state of the motor and the chemical driving force determining the power stroke.

As we have seen, the global behavior of the system in the load clamp case, described by the function  $x_3(t)$ , is basically in accord with experiments, but it is also instructive to look at the macroscopically invisible relative displacement  $x_2 - x_1$ . To show the insufficient coordination between the motor part, which simulates the attachment detachment process, and the bi-stable elements, exhibiting the power stroke, we can follow simultaneously the evolution of one of the particles  $x_2$  and the corresponding particle  $x_1$ .

We expect that the jump of the variable  $x_1$  from one well to another on the left side would stimulate the conformational transformation from the “short” phase to the “long” phase of the bi-stable element. In this case a new power stroke can be generated in order to move the backbone continuously. The response of the model is shown in Fig. 4.15, where the relative position of the lever arm in  $E_c$  can be traced from the difference  $x_2 - x_1$  together with the position of the elements  $x_1$  and  $x_3$ . We observe that after the switch from isometric to isotonic contraction at  $t = t_{jump}$ , the fast mechanism indeed generates a power stroke and the variable  $x_2 - x_1$  jumps into the “short” well of the bi-stable potential. In terms of the macroscopic evolution (of  $x_3$ ) this leads to phases 1 and 2. After this, in a longer time scale, the particle  $x_1$  has to move a distance  $L$  to the left to allow for continuous contraction. However, as we see in the figure, after the first jump the variable  $x_2 - x_1$  has no reason to return back to the “long” well. In fact in this test, it remains for the entire period of observations in the “short” well of the bi-stable potential. This well is always energetically preferred because  $x_3$  is continuously moving left relaxing the elastic element. One can see that, in the present form, the model fails to reproduce the entire Xb cycle.

To fix this problem we observe that an important role in the behavior described above was played by the ratio  $L/a$  linking the period of the motor potential  $V(x)$  (4.11) with the distance between the wells in the chemical energy  $E_c$  (4.13). This ratio has been so far chosen to be small ( $L/a = 0.5$  in Table 4.3, i.e. a step of

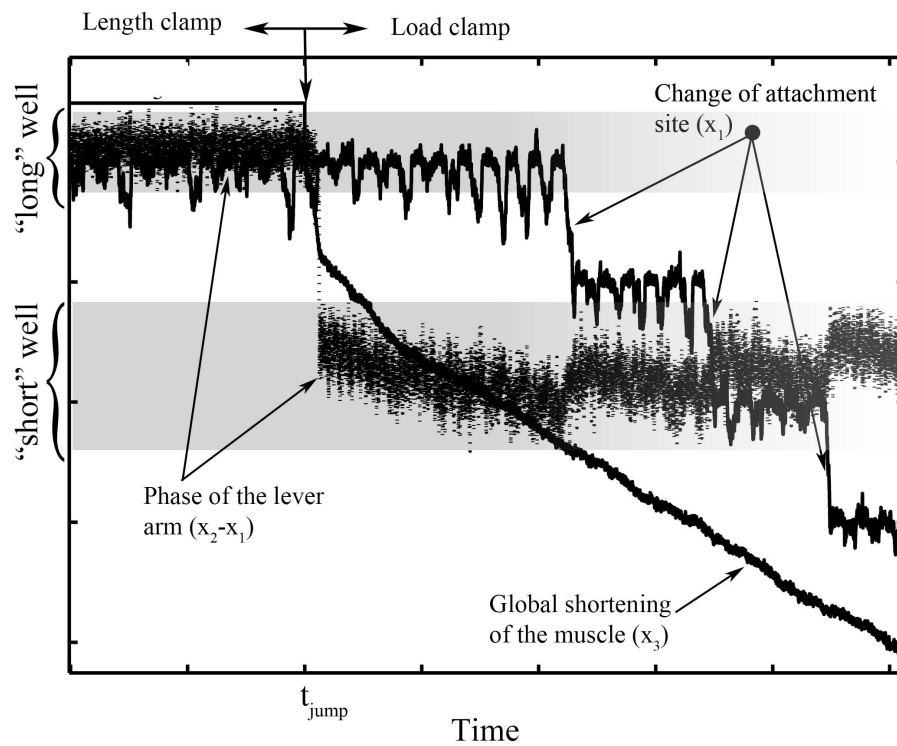


**Figure 4.15:** The graph of position vs. time for a particular  $x_1$  and the associated evolution of the variable  $x_2 - x_1$  and the variable  $x_3$ . Period  $L = 0.5a$ . Only one change of phase of the lever arm  $x_2 - x_1$  is observed while three changes in the attachment position  $x_1$  takes place

**Table 4.3:** The main parameters used for the numerical simulations of the models CSM, SCM-N, and SCM1

Description	Numerical values
Distance between the minima $a$	1 nm
Noise term $k_B T$	1 pN nm
Drag coefficient of $x_2$ , $\eta_2$	1 pN ns/nm
Elasticity of the elastic element $K$	32 pN/nm
Elasticity of the low force generating state $k_1$	5 K
Elasticity of the high force generating state $k_2$	2 K
Curvature of the maximum $k_3$	$-10^2$ pN/nm
Periodicity $L$	0.5 $a$ - 2 $a$
Asymmetry $\lambda_1$	0.3
Maximum of the potential $V_{max}$	15 $k_B T$
ATP force modulus $ F_{ATP} $	1.3 $V_{max}/\lambda_2 L$
Ratio $\eta_2/\eta_1$	0.1
Ratio $\eta_2/\eta_3$	0.01
Time between oscillations $t_{ATP}$	$10^3 \tau_{step}$
Asynchronisation $\phi^i$	$i \cdot t_{ATP}/N_{Xb}$ for $i = 1, \dots, N_{Xb}$
Dispersion of the attachment sites $\psi$	$\pm 2.75$ nm

the motor equals one half of the maximum power stroke). The justification of this value comes from the fact that the actin monomer has a diameter of  $5.5\text{ nm}$ , while the maximum power stroke, observed at low external forces, is about  $11\text{ nm}$  (see Chapter 2). Higher values of the ratio  $L/a$ , could result from taking into consideration the helical twist of the actin filament that allows only particular monomers to serve as active sites for the myosin head.

With this consideration in view we can assume that, for instance,  $L/a = 2$ . Then the model generates similar macroscopic (variable  $x_3$ ) but different microscopic (variables  $x_1$  and  $x_3$ ) behavior. Because the jump of  $x_1$  is now longer, it is sufficient to stretch the elastic element to the degree that makes again the “long” well of the bi-stable element energetically preferable. Then during each attachment-detachment event the variable  $x_2 - x_1$  returns into the pre-power stroke state, as shown in Fig. 4.16. Following the time trajectories of the points we observe two

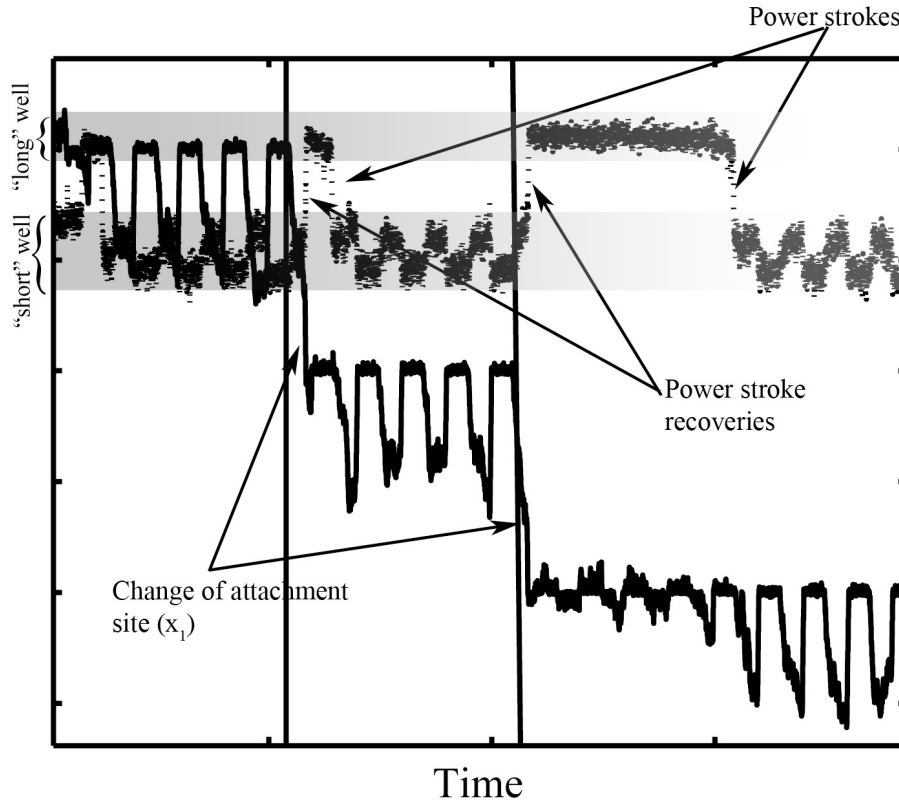


**Figure 4.16:** The graph of position vs. time of a particular variable  $x_1$  and the associated evolution of the variable  $x_2 - x_1$ . Period  $L = 2a$ . When the variable  $x_1$  jumps into the neighboring well, the lever arm  $x_2 - x_1$  comes back to the “long” configuration. After a proper amount of time a new power stroke takes place

jumps of the variable  $x_1$  marked by the two vertical lines. After every jump we see that  $x_2 - x_1$  is shifted back to the “long” well where it can remain for a certain

amount of time before generating a new power stroke.

We conclude that the representation of the whole Xb cycle has been achieved. The variable  $x_2 - x_1$  comes back to the “long” well because of purely mechanical reasons: the elastic element becomes over-stretched after the jump of  $x_1$ . To show this we plot in Fig. 4.17 the configuration of the elastic element  $x_2 - x_3$  together with the evolution of the variable  $x_1$ . The first vertical line shows the moment in which, at a given  $x_1$ , the bi-stable element changes its state and stretches the spring, as in the power stroke of the Xb cycle. The second vertical line shows the moment in which  $x_1$  changes well; it appears that the stretch of the spring increases before the changing of the attachment site of  $x_1$ , and at a certain level of stretch, the spring pulls back the variable  $x_2 - x_1$  into the “long” state. The high

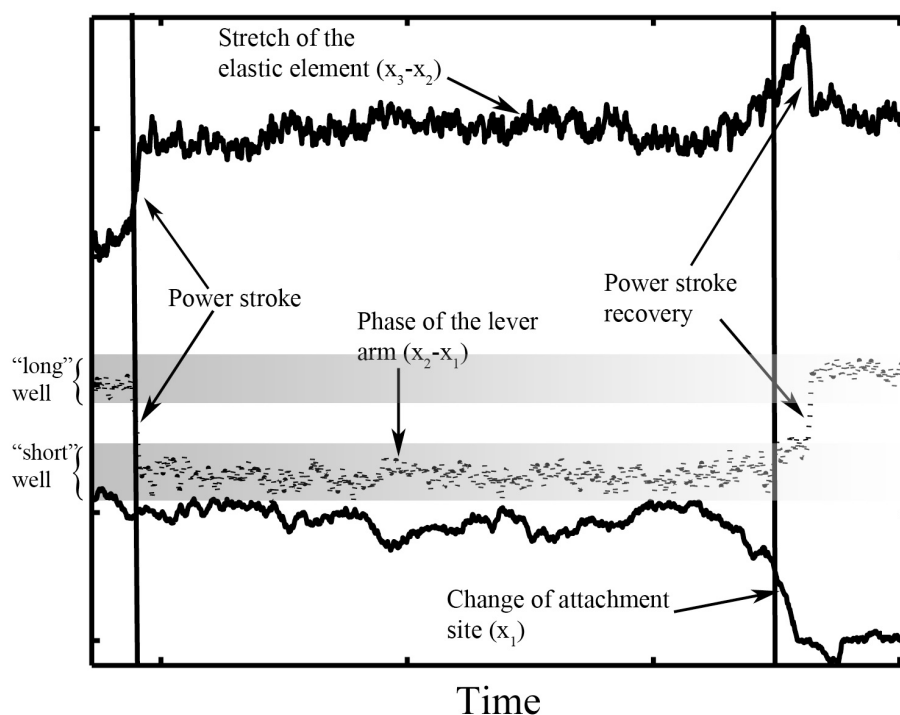


**Figure 4.17:** The graph of position vs. time for a particular variable  $x_1$  and the associated evolution of the variables  $x_2 - x_1$  and the stretch of the spring  $x_3 - x_2$ . Period  $L = 2a$ . The first vertical line shows the moment in which the bi-stable element changes state and the stretch takes place in the spring. The second vertical line shows the moment in which the variable  $x_1$  changes attachment site

tension in the elastic element is relaxed as soon as the bi-stable element assumes its “long” configuration. The macroscopic effect of this little peak on the backbone can be considered negligible. To summarize, we can say that the model is able to

reproduce all the elements of the basic Xb-cycle.

Despite its success, our model, raises again the question regarding the definition of power stroke. Formally we have been defining the power stroke as the change in the configuration of the bi-stable element. Now we see that the attachment-detachment mechanism can also generate force in the muscle, i.e. can stretch the elastic element. We conclude that the change of the attachment site can also be considered as phase of the power stroke. In other words our model contains inside itself two power strokes. This, fundamental observation, has nothing to do with the two power stroke in the attached state proposed by several other authors based on completely different observations (see [10], [43], [96]).

### 4.3.5 Discussion

The problem of two different power stroke shows how different conceptually have been so far the models of Brownian ratchets and of the power stroke. The difference resides principally in the interpretation of the role of ATP. In the Eisenberg and Hill model [17], which is based on the same idea of the Huxley and Simmons' model, there is an explicit link between the change of configuration of the lever arm and the consumption of ATP. This link has been made explicit because the authors associated the difference in the level of the minima of the chemical energy with the free energy liberated by the ATP hydrolysis,  $\Delta G_{ATP}$ . We are not aware of any work questioning this interpretation of the chemical driving force in the power stroke type models. An experimental prove that the conformational change in the myosin head is not simply a mechanical effect and that it actually needs the  $\Delta G_{ATP}$ , is in the different response of the muscles placed in the length clamp device while in rigor and in tetanus [55]. If the ATP is needed only to switch the Xb into the state in which it can perform the power stroke, and if the transition is governed only by mechanical forces, the two experiments should give similar results. Instead the tension recovery  $T_2(\delta)$  in rigor is much smaller than in tetanus [55]. In rigor, the state characterized by the depletion of ATP, all the Xbs are attached to the actin filament and do not have the possibility to detach; moreover the power stroke appears to be almost irreversible. Hence one can conclude that even in the power stroke models, the ATP activity is needed to keep the different level of the minima of the chemical energy  $E_c$ .

In the Brownian ratchets, the role of ATP is different and is mainly to destroy thermal equilibrium. In general we know that the non-equilibrium forcing

together with the asymmetry of the potential, ensures that the particle drifts in one direction. In detail, however the Magnasco type models represent ATP as a force (see  $F_{ATP}$  (4.13)) which acts directly on the particle and allows it to climb preferentially only the smaller slope of the potential  $V(x)$  (see (3.20)). While Prost et al. model represents ATP as breaking the detailed balance in the rates of the attachment-detachment process without seemingly generating a direct force on the particle, its action can also be reduced to the coloring of the external noise. To summarize, ATP appears in two different roles: as a static bias of one of the wells and as a dynamic agent destroying the detailed balance. These two different representations of ATP have been preserved in our models, however, we believe that they have not been fully reconciled.

To match fast and slow time scale events during muscle contraction, a unified interpretation of the physical effect of ATP is necessary. We have made a step in the direction of treating both mechanism from the common point of view, but more work is needed to make them fully coherent. Despite the remaining difficulties in linking the two sides of the contraction phenomenon, the power stroke and the attachment-detachment, the idea of reaching a fully mechanical interpretation of the entire Xb cycle appears now quite feasible. A fully mechanical model, able to reproduce all the features of the muscle's contraction, is of interest first of all in relation to the possibility of artificially creating the devices exhibiting active elasticity.



# Chapter 5

## Conclusions

In this work our goal was to construct a fully mechanical description for the microscopic mechanism of contraction in skeletal muscles. Every mathematical model that aims at describing quantitatively the whole variety of related physical phenomena has to face at least two problems. First, there is a high variability of the experimental results, not only linked to the different muscle types or even animal's species, but also related to a certain number of external factors that are normally easy to control in the classical mechanical tests. Just as an example, frog's muscle experiments show more uniform results between October and March due to seasonal variations in metabolism (G. Piazzesi, personal communication). The second problem is that some physiological and anatomical details of the contraction phenomenon are not even well established in the biological community. Thus, while the main steps of the Xb cycle are widely accepted, some intermediate states exist only as hypotheses that are under debate.

The formulation of a model that describes the contraction of skeletal muscles in a purely mechanical framework is intrinsically affected by these problems. We reviewed previous important contributions aimed at building a comprehensive multi-disciplinary models coupling mechanics with chemistry. A good qualitative agreement with experiments has been reached in these models assuming that some phases of the process can be modeled as purely mechanical while others as non-equilibrium chemical reactions, whose phenomenological description preserve some freedom needed to fit the data. As we have shown, the phenomenological nature of these models limits their predictive power. Even if some chemical stages are likely to be needed as a shortcut for micro-mechanical processes, a description of the entire process should be strongly related to the physics and mechanics of the force producing mechanisms.



We have achieved two main results in this Thesis. First, we have shown that a fully mechanical model with only two configurational states for the Xb can describe the fast recovery of tension quantitatively. Second, we have shown that one can use the Brownian ratchet theory to link qualitatively the main elements of the entire Xb cycle, including both fast and slow stages.

In the first part of the Thesis we concentrated on the analysis of the power stroke mechanism in the attached myosin head. We have shown that the known problems of the classical Huxley and Simmons 1971 formulation can be resolved if the elasticity of the bi-stable configuration is taken into consideration. More recent models have taken the path abandoning the strong physical relation between the rate constants and the stretch of the elastic element. We have improved the Huxley and Simmons model by not only maintaining this relation but even making it stronger through introducing a diffusion process instead of a jump process to model the change in configuration of the myosin head. We have provided a detailed analytical description of the model and demonstrated complete quantitative agreement with experimental measurements.

Two predictions of the model can be directly compared to experiments. First, we have shown that in our model, the plateau in the  $T_2(\delta)$  curve can be obtained with only two stable conformations of the myosin head. In contrast, in other models at least three states have been postulated to achieve this result, see for instance [48]. The existence of a third intermediate state between the pre-power stroke and the post-power stroke states is still under debate. Second, we have constructed a quantitative model of kinetics which predicts realistic rate of recovery  $r(\delta)$ . In a way we managed to circumvent the two main drawbacks of the original Huxley and Simmons model.

The main result of the first part of this Thesis is that the size of the power stroke is not fixed, not even for a single Xb. Our model predicts that, similar to experiments, it changes continuously with varying tension in the elastic element. This understanding can give a new insight concerning the interpretation of the experimental observations obtained with X-ray interference in [84]. These experiments clearly show that the size and the speed of the power stroke depend on the load. Our model predicts that the large power stroke of about 10 *nm* projected from crystallographic studies [61] is actually possible only when the loads acting on the elastic element are sufficiently low, i.e. when the imposed step in length relaxes the elastic element almost completely. This result follows from the fact that in the new model the location of the minima of the total energy depends on the

applied length step. We can therefore confront the claims that the energy required to stretch the elastic element should be larger than the free energy available from the ATP hydrolysis. It is this problem with ATP that has lead some researcher to postulate three or more conformational states for the Xb which are all activated during the power stroke (see for instance [67]).

The idea of considering additional elasticity in each chemical state occupied by a Xb has been previously put forward in [12], [17], [18], and used in several later models. However, in all these models, the elasticity of the Xb has been added at the expense of the elastic element in series. We have shown that in this setting, an independent phenomenological definition of the chemical rate constants associated with the transition from one state to another becomes necessary. Even if the ratio of these constants is well defined by the difference of the free energies of the states, nothing is known about the shape of the energy *between* the states and this information has to be smuggled into the theory implicitly. This is done by exploiting a freedom in choosing the dependence of the rate constants on the imposed step. We have shown that this freedom has often been used to fit the experimental behavior, and that the resulting phenomenological models have no relation to actual microscopic mechanism of the transition between the states. In this sense the model proposed in Chapter 2 is actually closer to the original Huxley and Simmons' model where the step dependence of the chemical constants is uniquely defined by the shape of the energy than most of the recent improvements of this model. Since we managed to preserve a transparent mechanical interpretation of the force producing mechanism, our model opens the way to reproduce the underlying machinery artificially.

In the second part of the Thesis we have made a first attempt to develop a purely mechanical interpretation of the entire Xb-cycle. Since we have first given a mechanical interpretation of the power stroke part of the cycle, allowing one to place it in a diffusion framework, a natural choice to complete the model was to use the ideas of the Brownian ratchet theory which have already been applied to model the diffusion of a particle in an asymmetric periodic potential representing the actin filament.

In Chapter 3 we revisited the theory of Brownian ratchet and applied it directly to muscle contraction. Our choice of using a Magnasco type model to simulate the attachment-detachment process allowed us to maintain the model in a purely mechanical framework, avoiding the use of jump processes. We have adapted this model to our purpose and developed a cooperative version where the particles are

elastically attached to a common backbone simulating the thick filament. We also developed a numerical algorithm to study the behavior of our stochastic system and demonstrate that the resulting model can predict a realistic force velocity curve.

Then we applied these ideas to the modeling of the whole Xb cycle. The resulting approach is original because the description of the power stroke in terms of the diffusion process is new and because we propose a new way of inserting the power stroke into a Brownian ratchet model. By using the new cooperative model we have achieved some encouraging results being able to reproduce the main qualitative features of the whole Xb cycle. In our model the power stroke of the head stretches the elastic element which in turn pulls the myosin backbone and causes contraction. In the meantime a slower process allows the myosin head to come back to the pre-power stroke state to recharge, leaving the tension in elastic element almost constant. Finally, due to the motion of the myosin backbone generated by other heads, the first head generates another power stroke and the cycle repeats itself. one of the main advantages of the ensuing unified model of the power stroke and the attachment-detachment phenomenon is its simplicity and analytical transparency. While we have not made a thorough analysis of the new model, we were able to demonstrate convincingly the main effects.

We discussed limitations of our new interpretation of the Xb cycle and made an important general observation, regarding the need to give a more clear interpretation of the very meaning of the power stroke. In this perspective a much stronger collaboration with biophysicists, biochemists and physiologists becomes crucial.

# Appendix A

## Appendix

### A.1 Brownian motion

Macroscopic movements of the body originate from the microscopic movements of small proteins (myosin) at distances of few nanometers. These movements if properly coordinated result, at a macroscopic scale, in the contraction of the muscles. At the micro-scale thermal fluctuations of the proteins due to interaction with the particles of the surrounding fluids can not be ignored. We review in this Appendix the mathematical description of such fluctuations, starting from the basic concepts of probability needed to introduce the random motion of a free protein in a fluid (Langevin equation). We then recall the link between its mobility and the diffusion coefficient (Einstein's relation). Then, we derive the stochastic differential equation which describes the probability distribution in the case of a system evolving in an external potential (Fokker-Plank equation). We specialize it to the high friction limit which is, of main interest in muscle mechanics. Finally we review the Kramers' theory and the concept of the first passage time adapted to a double well potential. we conclude with the analysis of diffusion of a particle in periodic potential. A more detailed discussion of the related concept can be found in [74] and [23].

### A.2 Probability

For convenience of the reader we begin by mentioning some basic concept of the probability theory. First of all, there are three axioms describing the probability

$P$  of a set of events  $A$ ,  $P(A)$ :

$$P(A) \geq 0 \quad \forall A; \quad (\text{A.1})$$

$$P(\Omega) = 1, \quad (\text{A.2})$$

where  $\Omega$  is the set of all events, and

$$A_i \cap A_j = \emptyset; \forall i \neq j \Rightarrow P(\cup_i A_i) = \sum_i P(A_i). \quad (\text{A.3})$$

Next we need the definition of *conditional probability*. The probability of  $A$  at a given  $B$  is equal to:

$$P(A | B) = P(A \cap B) / P(B). \quad (\text{A.4})$$

If  $B_i$  is a collection of non-overlapping sets whose union is the total space  $\Omega$ , we obtain:

$$\sum_i P(A \cup B_i) = P(A). \quad (\text{A.5})$$

If a random variable  $\xi$  is continuous we can define its probability density  $p(\xi)$ . The probability of  $\xi$  to be between the values  $\xi_0$  and  $\xi_0 + d\xi_0$ , is then  $p(\xi_0)d\xi_0 = P(\xi_0 \leq \xi \leq \xi_0 + d\xi_0)$ . The equation (A.5) can now be rewritten as:

$$p(x) = \int_{-\infty}^{\infty} p(x | y)p(y)dy. \quad (\text{A.6})$$

A physical way to construct  $p_\xi(x)$  (the probability that a stochastic variable  $\xi$  assumes the value between  $x$  and  $x + dx$ ), is to measure a large number of values of  $\xi$  and to define:

$$p_\xi(x) = \lim_{N \rightarrow \infty} \frac{1}{N} \sum_{n=1}^N (\delta(x - \xi_n)). \quad (\text{A.7})$$

The mean value of a function of random variable  $f(\xi)$  will be indicated by the brackets  $< >$  and computed as following:

$$< f(\xi) > = \int f(x)p_\xi(x)dx. \quad (\text{A.8})$$

When  $f(\xi) = \xi^n$ , formula (A.8) generates the *moment* of degree  $n$  of a stochastic variable  $\xi$ .

If we consider two stochastic variables,  $\xi$  and  $\eta$ , the joint probability density is defined by the expression:

$$p_{\xi,\eta}(x,y)dxdy = P_{\xi,\eta}(x \leq \xi \leq x + dx; y \leq \eta \leq y + dy) \quad (\text{A.9})$$

The mean value of  $f(\xi, \eta)$  will then be a double integral:

$$\langle f(\xi, \eta) \rangle = \int \int f(x, y) p_{\xi, \eta}(x; y) dx dy. \quad (\text{A.10})$$

We will also need the *characteristic function* of the stochastic variable  $\xi$ :

$$C_{\xi}(u) = \langle e^{iu\xi} \rangle = \int e^{iu\xi} p_{\xi}(x) dx. \quad (\text{A.11})$$

If  $C_{\xi}(u)$  is known the *moment* of grade  $n$  can be computed by differentiation:

$$M_n = \langle \xi^n \rangle = \frac{1}{i^n} \frac{d^n C_{\xi}(0)}{du^n}. \quad (\text{A.12})$$

Inversely, if all moments are known we can write:

$$C_{\xi}(u) = 1 + \sum_{n=1}^{\infty} (iu)^n M_n / n! \quad (\text{A.13})$$

The last formula will be used in the derivation of the Fokker-Plank equation.

## A.3 The Langevin Equation

At finite temperature, a particle of mass  $m$  embedded in a viscous fluid will be subjected to a series of hits from the much smaller particles of the fluid, that act like a random force reservoir. We call this force  $\Gamma(t)$ . The equation of overdamped motion for the particle in the absence of other external forces can be written as:

$$\dot{v}(t) + \gamma v(t) = \Gamma(t) \quad (\text{A.14})$$

where  $\gamma = \eta/m$  and  $\eta$  is the drag coefficient characterizing the size and the shape of the particle. Equation (A.14) is called the *Langevin Equation*. Here  $\Gamma(t)$  is a stochastic function, which mean that at a given  $\bar{t}$ ,  $\Gamma(\bar{t})$  represents a stochastic variable. The values  $\Gamma(t_1)$  and  $\Gamma(t_2)$  represent two distinct stochastic variables if  $t_1 \neq t_2$ . We shall be considering a one-dimensional problem and impose on  $\Gamma$  two restrictions. First, it must have zero average:

$$\langle \Gamma(t_1) \rangle = \int x_1 p_{\Gamma}(x_1, t_1) dx_1 = 0 \quad (\text{A.15})$$

where  $p_{\Gamma}(x, t)$  is the probability that  $\Gamma$  assumes the value  $x$  at time  $t$ . Second there must be no correlation in time:

$$\langle \Gamma(t_1) \Gamma(t_2) \rangle = \int \int x_1 x_2 p_{\Gamma}(x_1, t_1; x_2, t_2) dx_1 dx_2 = q \delta(t_1 - t_2). \quad (\text{A.16})$$

The Langevin force with correlations described by (A.15) and (A.16), is called a *white* noise. From equation (A.14), we can write:

$$v(t) = v_0 \exp[-\gamma t] + \int_0^t \exp[-\gamma(t-t')] \Gamma(t') dt' \quad (\text{A.17})$$

where  $v_0$  is the value of  $v$  at  $t = 0$ , which we assume to be zero from now on. To determine the value of  $q$ , we can compute:

$$\langle v(t_1)v(t_2) \rangle = \left\langle \int_0^{t_1} \int_0^{t_2} \exp[-\gamma(t_1+t_2-t'_1-t'_2)] \Gamma(t'_1) \Gamma(t'_2) dt'_1 dt'_2 \right\rangle \quad (\text{A.18})$$

which gives:

$$\langle v(t_1)v(t_2) \rangle = \frac{q}{2\gamma} \exp[-\gamma|t_1 - t_2|] - \frac{q}{2\gamma} \exp[-\gamma(t_1 + t_2)]. \quad (\text{A.19})$$

In the long time limit  $\gamma t_1 \gg 1$  and  $\gamma t_2 \gg 1$  only the first term in the right-hand side of equation survives

$$\langle v(t_1)v(t_2) \rangle = \frac{q}{2\gamma} \exp[-\gamma|t_1 - t_2|]. \quad (\text{A.20})$$

Now, recalling that in the state of thermal equilibrium the equipartition law of classical statistical mechanics must be satisfied, we can write:

$$\langle E \rangle = \frac{1}{2} k_B T = \frac{1}{2} m \langle [v(t)]^2 \rangle = \frac{1}{2} m \frac{q}{2\gamma}. \quad (\text{A.21})$$

From (A.21) we obtain for  $q$  the following expression:

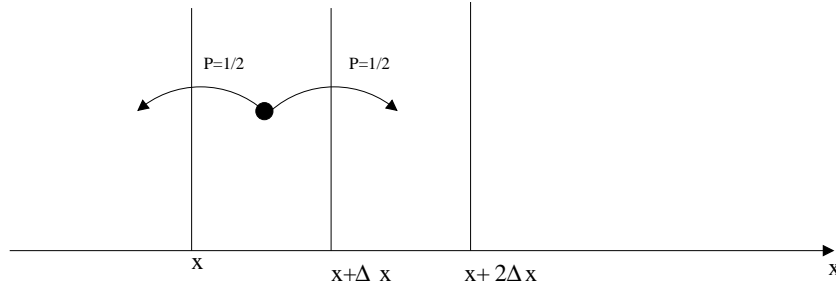
$$q = \frac{2\gamma k_B T}{m}. \quad (\text{A.22})$$

Observe that while we did not give the complete description of the probability distribution for  $\Gamma(t)$ , the linearity of (A.14) allowed us to compute the two-time correlation  $\langle v(t_1)v(t_2) \rangle$  by using only a limited information (A.15) and (A.16). Similarly, we can also compute the mean square displacement  $\langle (x(t))^2 \rangle$  of a position of the particle,

$$\begin{aligned} \langle (x(t))^2 \rangle &= \left\langle \left[ \int_0^t v(t_1) dt_1 \right]^2 \right\rangle = \left\langle \int_0^t v(t_1) dt_1 \int_0^t v(t_2) dt_2 \right\rangle \\ &= \int_0^t \int_0^t \langle v(t_1)v(t_2) \rangle dt_1 dt_2 \end{aligned} \quad (\text{A.23})$$

Now from (A.19):

$$\langle (x(t))^2 \rangle = \int_0^t \int_0^t \frac{q}{2\gamma} \exp[-\gamma|t_1 - t_2|] - \frac{q}{2\gamma} \exp[-\gamma(t_1 + t_2)] dt_1 dt_2 \quad (\text{A.24})$$

**Figure A.1:** Diffusion of a particle

So that:

$$\langle (x(t))^2 \rangle = \frac{q}{\gamma^2}t - \frac{q}{2\gamma} \frac{(1 - \exp[-\gamma t])^2}{\gamma^2} - \frac{q}{\gamma^3}(1 - \exp[-\gamma t])^2. \quad (\text{A.25})$$

Again in a long time limit ( $\gamma t \gg 1$ ) the leading term can be simplified:

$$\langle (x(t))^2 \rangle = 2 \frac{q}{2\gamma^2}t = 2 \frac{k_B T}{m\gamma}t = 2Dt. \quad (\text{A.26})$$

The relation (A.26) is called the Einstein's relation. In order to see why  $D$  is called the diffusion coefficient we need to introduce a continuum description for the movement of a particle in a viscous fluid.

## A.4 Diffusion of a particle in a fluid

The analysis in the previous section allowed us to compare the mean square displacement of a particle with mass  $m$  in a viscous fluid subjected to a random force with zero mean and correlations proportional to a  $\delta$  function. The analysis was made for a single particle and at a microscopic level. Now we would like to describe the evolution of an ensemble of  $N$  particles in a fluid, reasoning in terms of the concentration of the particles and the flux of matter. In this sense the description will be macroscopic.

Without saying anything regarding the physical mechanisms of the motion, we assume that the particle in a position  $x$  can move to positions  $x \pm \Delta x$  during time  $\Delta t$  with equal probabilities as shown in Fig. A.1.

The number of particles that will pass through the section  $x + \Delta x$  in time  $\Delta t$  can be related to the number of particles between  $x$  and  $x + \Delta x$ , which is equal to  $c(x)\Delta x$ , where  $c(x)$  is the concentration. The number of particles between  $x + \Delta x$  and  $x + 2\Delta x$ , is  $c(x + \Delta x)\Delta x$ , therefore

$$\Delta t J(x + \Delta x) = \frac{\frac{1}{2}(c(x) - c(x + \Delta x))}{\Delta x} \Delta x^2 \quad (\text{A.27})$$



where  $J(x)$  the flux of particles through  $x$ . Defining  $D$  as the ratio between  $\frac{1}{2}\Delta x^2$  and  $\Delta t$  (which we suppose to be finite), we obtain:

$$J(x, t) = -D \frac{\partial c(x, t)}{\partial x} \quad (\text{A.28})$$

This formula gives the Fick's law of diffusion.

A non zero gradient in the flux through the area  $A$  will change the local concentration. We can write the following equation of mass balance:

$$\Delta c(x, t) = \frac{A(J(x, t) - J(x + \Delta x, t))\Delta t}{A\Delta x} \Rightarrow \frac{\partial c(x, t)}{\partial t} = -\frac{\partial J(x, t)}{\partial x} \quad (\text{A.29})$$

If we now use the Fick's law, we obtain the following PDE for the concentration:

$$\frac{\partial c(x, t)}{\partial t} = D \frac{\partial^2 c(x, t)}{\partial x^2}. \quad (\text{A.30})$$

For the probability distribution of the position  $x$  for one particle  $p(x, t) = c(x, t)/N$ , we can similarly write:

$$\frac{\partial p(x, t)}{\partial t} = D \frac{\partial^2 p(x, t)}{\partial x^2}. \quad (\text{A.31})$$

To solve equation (A.31), we introduce the Fourier transform of  $p(x, t)$  in  $x$

$$\hat{p}(\omega, t) = \int_{-\infty}^{\infty} e^{(-i\omega x)} p(x, t) dx. \quad (\text{A.32})$$

Computing derivative in time we obtain:

$$\frac{\partial \hat{p}(x, t)}{\partial t} = D \int_{-\infty}^{\infty} e^{(-i\omega x)} \frac{\partial^2 p(x, t)}{\partial x^2} dx \quad (\text{A.33})$$

Finally, integrating by parts and letting the probability  $p(x, t)$  tend to zero as  $x$  goes to infinity, we obtain:

$$\frac{\partial \hat{p}(x, t)}{\partial t} = -D\omega^2 \hat{p}(x, t). \quad (\text{A.34})$$

To illustrate the meaning of coefficients, we can solve this differential equation with an initial condition given by a delta function centered in the origin. Then computing the inverse Fourier transform, we obtain the probability distribution of the position of a particle at time  $t$  in the form:

$$p(x, t) = \frac{1}{\sqrt{4\pi Dt}} e^{-\frac{x^2}{4Dt}}. \quad (\text{A.35})$$

With this expression of  $p(x, t)$ , we can compute the mean value for every function of the stochastic variable  $x$ . In particular, the mean value of  $x^2$  becomes:

$$\langle x^2 \rangle = \int_{-\infty}^{\infty} x^2 \frac{1}{\sqrt{4\pi Dt}} \exp\left[-\frac{x^2}{4Dt}\right] dx = 2Dt. \quad (\text{A.36})$$

We can now identify the coefficient  $D$  in (A.36) with the  $D$  in (A.26). From this considerations one can relate the macroscopic diffusion coefficient to the microscopic information regarding the mechanical motion of a particle. Equation (A.31) is a particular example of a class of equations known as *Fokker-Plank equation*, whose general derivation will be the subject of the next Section.

## A.5 The Fokker-Plank equation

We recall that  $p_\xi(x, t)dx$  is the probability that a random variable  $\xi$  assumes a value between  $x$  and  $x + dx$  at time  $t$ . In the time dependent case, equation (A.6) can be rewritten as:

$$p(x, t + \tau) = \int p(x, t + \tau | x', t) p(x', t) dx'. \quad (\text{A.37})$$

To obtain a differential equation for  $p(x, t)$  we suppose to know all the moments  $M_n$  of  $p(x, t + \tau | x', t)$  with respect to  $x'$ :

$$M_n(x', t, \tau) = \langle (\xi(t + \tau) - x')^n \rangle \quad (\text{A.38})$$

Then, the function  $p(x, t + \tau)$  is equal to the inverse Fourier transform of its characteristic function (see (A.11)). Therefore:

$$p(x, t + \tau) = \frac{1}{2\pi} \sum_{n=0}^{\infty} \left( \int_{-\infty}^{\infty} \exp[-i(x - x')u] \frac{(iu)^n}{n!} du \right) M_n(x', t, \tau). \quad (\text{A.39})$$

By using the identity

$$\frac{1}{2\pi} \int_{-\infty}^{\infty} \exp[-i(x - x')u] (iu)^n du = \left( \frac{\partial}{\partial x} \right)^n \delta(x - x') \quad (\text{A.40})$$

we can write:

$$p(x, t + \tau | x', t) = \left[ 1 + \sum_{n=1}^{\infty} \frac{1}{n!} \left( \frac{\partial}{\partial x} \right)^n M_n(x, t, \tau) \right] \delta(x - x'). \quad (\text{A.41})$$

Inserting the last equation into (A.37) we obtain an expression for the first derivative of the probability distribution  $p(x, t)$ :

$$p(x, t + \tau) - p(x, t) = \frac{\partial p(x, t)}{\partial t} \tau + O(\tau^2) = \sum_{n=1}^{\infty} \left( -\frac{\partial}{\partial x} \right)^n \frac{M_n(x, t, \tau)}{n!} p(x, t) \quad (\text{A.42})$$

Now, expanding  $M_n(x, t, \tau)$  in  $\tau$  and dropping the terms that go to zero with  $\tau$  we obtain:

$$\frac{\partial p(x, t)}{\partial t} = \sum_{n=1}^{\infty} \left( -\frac{\partial}{\partial x} \right)^n D_n(x, t) p(x, t), \quad (\text{A.43})$$

where  $M_n(x, t, 0) = 0$  because no jumps take place, and

$$D_n(x, t) = \frac{1}{n!} \lim_{\tau \rightarrow 0} \frac{M_n(x, t, \tau)}{\tau}. \quad (\text{A.44})$$

By truncating this equation at  $n = 2$ , we obtain the Fokker-Plank equation:

$$\frac{\partial p(x, t)}{\partial t} = -\frac{\partial}{\partial x}(D_1(x, t)p(x, t)) + \frac{\partial^2}{\partial x^2}(D_2(x, t)p(x, t)) \quad (\text{A.45})$$

One can show that if the noise  $\Gamma$  in the Langevin equation (A.14) can be described by a Gaussian distribution, all the moments  $M_n$  with  $n \geq 3$  are equal to zero. In this case, the probability distribution  $p(x, t)$  satisfied the Fokker-Plank equation (A.45) exactly. From (A.14) we can compute:

$$D_1 = \lim_{\tau \rightarrow 0} \frac{\langle v(t + \tau) - v(t) \rangle}{\tau} = \lim_{\tau \rightarrow 0} \frac{1}{\tau} \int_t^{t+\tau} \langle -\gamma v(t') + \Gamma(t') \rangle dt' = -\gamma v(t) \quad (\text{A.46})$$

and in a similar way:

$$\begin{aligned} D_2 &= \frac{1}{2} \lim_{\tau \rightarrow 0} \frac{\langle (v(t + \tau) - v(t))^2 \rangle}{\tau} = \\ &= \frac{1}{2} \lim_{\tau \rightarrow 0} \frac{1}{\tau} \left\langle \int_t^{t+\tau} -\gamma v(t') + \Gamma(t') dt' \int_t^{t+\tau} -\gamma v(t'') + \Gamma(t'') dt'' \right\rangle = \\ &= \frac{1}{2} \lim_{\tau \rightarrow 0} \frac{1}{\tau} \int_t^{t+\tau} \int_t^{t+\tau} \langle \gamma^2 v(t') v(t'') \rangle \\ &\quad + \langle -\gamma v(t') \Gamma(t'') - \gamma v(t'') \Gamma(t') \rangle + \langle \Gamma(t'') \Gamma(t') \rangle dt' dt'' \end{aligned} \quad (\text{A.47})$$

With  $\tau \rightarrow 0$  the first term in the integral above goes to zero as  $\tau^2$  and the second term has a zero average. Therefore we can write:

$$D_2 = \frac{q}{2} \quad (\text{A.48})$$

where  $q$  was defined in (A.22). To summarize, for the process described in (A.14), the probability distribution for velocity, satisfies the following partial differential equation:

$$\frac{\partial p(v, t)}{\partial t} = \gamma v \frac{\partial p(v, t)}{\partial v} + \frac{q}{2} \frac{\partial^2 p(v, t)}{\partial v^2} \quad (\text{A.49})$$

This equation can also be written as:

$$\frac{\partial p}{\partial t} + \frac{\partial S}{\partial v} = 0 \quad (\text{A.50})$$

where we defined the *probability flux*  $S$

$$S = \left[ -\gamma v - \frac{q}{2} \frac{\partial}{\partial v} \right] p. \quad (\text{A.51})$$

From this expression for the flux we can immediately obtain the steady state distribution. Indeed the boundary condition  $S(\pm\infty) = 0$  ensures that  $S = 0$ . Therefore:

$$p(v) = \sqrt{\frac{m}{2\pi k_B T}} \exp\left[-\frac{mv^2}{2k_B T}\right]. \quad (\text{A.52})$$

which is known as the Maxwell distribution.

## A.6 High friction limit

If we couple the Langevin equation (A.14) with the equation for the particle position:

$$\frac{\partial x}{\partial t} = v(t) \quad (\text{A.53})$$

It leads to a Fokker-Plank equation for two variables: position and velocity. We then write:

$$D_x = \lim_{\tau \rightarrow 0} \frac{\langle x(t+\tau) - x(t) \rangle}{\tau} = \lim_{\tau \rightarrow 0} \frac{1}{\tau} \int_t^{t+\tau} \langle v(t') \rangle dt' = v(t) \quad (\text{A.54})$$

and:

$$D_{xx} = D_{xv} = D_{vx} = 0 \quad (\text{A.55})$$

We therefore obtain:

$$\frac{\partial p(x, v, t)}{\partial t} = \left[ -\frac{\partial v}{\partial x} - \frac{\partial}{\partial v}(-\gamma v) + \frac{\partial^2}{\partial v^2} \left( \frac{\gamma k_B T}{m} \right) \right] p(x, v, t) \quad (\text{A.56})$$

Now, we can expect that solving equation (A.56) for  $p(x, v, t)$  and integrating it in  $v$  we obtain the distribution of the particle position  $p(x, t)$ . equation (A.56) contains a full description of the inertial effects due to finite mass  $m$ . As we have already seen the inertial effects can be neglected if  $t$  is sufficiently large. In the opposite limit, when  $t$  is small viscosity is not important and the particle moves at a constant velocity. Using realistic values of constants, one can conclude that the inertial description is relevant only for times of the order of  $t = 10^{-13}s$  and for the displacements of the order of  $0.01nm$ , less than the diameter of the water molecule that hits the particle. For these reasons in what follows we limit our attention to the high friction limit, in which the mass of the particle has a negligible effect.

### A.6.1 The Fokker-Plank equation in the high-friction limit

Neglecting the effect of mass, we shall instead focus on the effect of an external force, described by a potential  $U(x)$ . In this case, we obtain a Langevin Equation

of the type:

$$\eta \dot{x}(t) + U'(x) = \Gamma(t). \quad (\text{A.57})$$

To respect the dimensionality the  $\Gamma(t)$  in (A.57), must be equivalent to the  $\Gamma(t)$  used in (A.14) time the mass. Therefore we can write:

$$\langle \Gamma(t_1) \rangle = 0 \quad (\text{A.58})$$

and:

$$\langle \Gamma(t_1)\Gamma(t_2) \rangle = qm^2\delta(t_1 - t_2) = 2\frac{\eta k_B T}{m^2}m^2\delta(t_1 - t_2) = 2\eta k_B T\delta(t_1 - t_2) \quad (\text{A.59})$$

Following the derivation of the Fokker-Plank equation in the general case (equations (A.46))-(A.47)), and using (A.59) we obtain:

$$D_1(t) = -\frac{U'(x(t))}{\eta}. \quad (\text{A.60})$$

From (A.59) we also obtain that:

$$D_2(t) = \frac{\eta k_B T}{\eta^2} = \frac{k_B T}{\eta}. \quad (\text{A.61})$$

Unifying all these ingredients we finally obtain the Fokker-Plank equation related to equation (A.57) in the form:

$$\frac{\partial p(x, t)}{\partial t} = \frac{1}{\eta} \frac{\partial}{\partial x} \left( U'(x)p(x, t) + k_B T \frac{\partial p(x, t)}{\partial x} \right). \quad (\text{A.62})$$

We can also rewrite equation (A.62) in the form:

$$\frac{\partial p}{\partial t} + \frac{\partial S}{\partial x} = 0. \quad (\text{A.63})$$

where:

$$S = \left[ D_1 - \frac{\partial}{\partial x} D_2 \right] p = -\frac{U'(x)}{\eta} p - \frac{k_B T}{\eta} \frac{\partial p}{\partial x} \quad (\text{A.64})$$

is the flux of probability. In the stationary state  $\frac{\partial p}{\partial t} = 0$  is constant and  $S = \text{const}$ .

The value of  $S$  in the stationary state is given by the boundary conditions. In the case of a *reflecting* barrier, a particle reaching the boundary is reflected back and the net flux  $S$  is zero. Since the flux is constant in the stationary state,  $S = 0$  means automatically that both boundaries must be reflecting. Another type of boundary is the *absorbing* boundary. In this case the particle reaching the boundary disappears (and is eventually brought to the other boundary to preserve the normalization condition). The probability to find a particle on the absorbing boundary is equal to zero.

In the stationary state, with reflecting boundaries, we can solve (A.64) and obtain:

$$p_s(x) = \mathcal{N} \exp \left[ \frac{-U(x)}{k_B T} \right] \quad (\text{A.65})$$

Here  $\mathcal{N}$  is determined by the normalization condition  $\int p_s(x) = 1$ .

### A.6.2 Canonical distribution

Equation (A.65) known as Canonical distribution and is derived directly in equilibrium statistical mechanics. The fundamental postulate of statistical mechanics asserts that, in equilibrium the system  $A$  is likely to be found in any one of the states accessible to it, for instance the probability  $P$  to find the system between the energy  $E$  and  $E + \delta E$  is proportional to the number of states  $\Omega(E)$  with energy  $E$

$$p(E) = C \Omega(E) \quad (\text{A.66})$$

The constant  $C$ , independent of  $E$ , is given by the normalization condition  $C^{-1} = \sum_E \Omega(E)$ . We can define the temperature by

$$1/k_B T = \partial \ln \Omega(E) / \partial E$$

where  $k_B = 1.381 \cdot 10^{-23} J/K$  is the Boltzmann constant. The distribution (A.66) is called microcanonical. When two systems,  $A$  and  $A'$ , are in equilibrium, the total probability  $p_{tot}(E)$  that the system  $A$  has the energy  $E$  is given by the product  $C \Omega(E) \Omega'(E') = C \Omega(E) \Omega'(E^0 - E)$  where  $E^0$  is the total energy and  $E'$  the energy of the second system. We can write the equilibrium condition in the form:

$$\frac{\partial \ln p_{tot}(E)}{\partial E} = 0 \quad (\text{A.67})$$

which gives  $T(E) = T'(E')$ , so the temperatures of the two system must be equal.

Now, if we consider a single Xb in equilibrium with a *heat reservoir*. The probability that the Xb has the energy  $E_r$ , is equal to the probability that the *heat reservoir* has the energy  $E^0 - E_r$ :  $p_s = C' \Omega'(E^0 - E_r)$ . Because  $E_r \ll E^0$  it is possible to expand the logarithm of  $\Omega'$  as:

$$\ln \Omega'(E^0 - E_r) = \ln \Omega'(E^0) - \left[ \frac{\partial \ln \Omega'}{\partial E'} \right]_0 E_r \quad (\text{A.68})$$

Then

$$\Omega'(E^0 - E_r) = \Omega'(E^0) e^{-E_r/k_B T} \quad (\text{A.69})$$

and therefore:

$$p_s = \frac{e^{-E_r/k_B T}}{\sum_r e^{-E_r/k_B T}}. \quad (\text{A.70})$$

where the constant  $C'$  has been again defined by the normalization. The subscript  $s$  indicates equilibrium or steady state. This distribution (A.70) is called canonical. Knowledge of this distribution is sufficient to derive the condition of detailed balance imposed by Huxley and Simmons on the ratio of the kinetic constants,  $k_+/k_-$  (equation (1.14)).

### A.6.3 The First passage time

In the high friction limit one can compute the time needed for a particle to exit from a region bound by certain potential barriers. We can start with the simplest case of a Langevin equation (A.14), when there is no external potential term and  $D_1$  is zero.

Consider a region with a reflecting boundary on the left and an absorbing boundary on the right. As we have already mentioned, one should remove the particles on the right and put them back on the left, in order to have a steady state and to maintain the normalization of the  $p_s(x)$ . In this case we have a constant flux equal to the number of particles per unit of time that intersects a given cross section. The mean first passage time is defined as the inverse of this flux because it is the time needed for a particle starting from the left boundary to reach the right boundary. The Fokker-Plank equation reduces to:

$$\frac{\partial p}{\partial x} = \text{const.} \quad (\text{A.71})$$

This equation must be supplemented by the boundary condition:

$$p(x_0) = 0 \quad (\text{A.72})$$

and the normalization condition:

$$\int_0^{x_0} p(x) dx = 1. \quad (\text{A.73})$$

We obtain:

$$p_s(x) = \frac{-2x}{x_0} + \frac{2}{x_0} \Rightarrow J(x_0) = -D \frac{dp}{dx} = \frac{2D}{x_0^2} \quad (\text{A.74})$$

and therefore, the mean first passage time is:

$$t_k = \frac{x_0^2}{2D}. \quad (\text{A.75})$$

Not surprisingly, this is the same result which we obtained (A.36) when we considered the average distance traveled by a particle in a given time.

More interesting is the case of a particle subjected to a force which is derived from a potential. Suppose  $J_0$  is the constant value of the flux. We can multiply (A.64) by  $\exp[-U(x_0)/k_B T]$  and integrate between  $x$  and  $x_0$  (where  $p(x_0) = 0$ ), obtaining:

$$p(x) = \frac{J_0}{k_B T / \eta} \exp[-U(x)/k_B T] \int_x^{x_0} \exp[U(x)/k_B T] dx. \quad (\text{A.76})$$

Integrating again between 0 and  $x_0$ , an interval over which the total probability must be equal to one, we can represent the inverse of the flux as:

$$t_k = \frac{\eta}{k_B T} \int_0^{x_0} \left( \exp[-U(x')/k_B T] \int_{x'}^{x_0} \exp[U(x'')/k_B T] dx'' \right) dx'. \quad (\text{A.77})$$

This integral can be computed explicitly when the external force is constant and  $U(x) = -Fx$ . We obtain:

$$t_k = 2(\eta x_0^2 / 2k_B T)(k_B T / F x_0)^2 [\exp(-F x_0 / k_B T) - 1 + F x_0 / k_B T]. \quad (\text{A.78})$$

In the harmonic case  $U(x) = \frac{Kx^2}{2}$ , an approximate analytical solution can be obtained in the approximation  $U(x_0) \gg k_B T$  [64]:

$$t_k = \frac{\eta}{K} \frac{\pi}{4} \frac{k_B T}{U(x_0)} \exp\left[\frac{U(x_0)}{k_B T}\right]. \quad (\text{A.79})$$

Equation (A.79) gives the mean time needed for a particle to exit a parabolic well.

## A.7 Kramers' approximation

In 1940, Kramers considered the problem of an escape from a well in relations to kinetics of molecular transformations. He introduced an ansatz which is now called the Kramers' approximation and solved the problem with a double well potential (see Fig. A.2). By using this approximation one can show the relation between the kinetic equation (1.15) used by Huxley and Simmons and the original Fokker-Plank equation associated with a general double well potential with minima in  $x = a$  and  $x = c$  and the maximum (the energetic barrier) in  $x = b$ .

We begin by defining:

$$\begin{aligned} M(x, t) &= \int_{-\infty}^x p(x', t) dx' \\ N_a(t) &= 1 - N_c(t) = M(b, t) \\ N_0(t) &= (c - a)p(x_0, t). \end{aligned} \quad (\text{A.80})$$



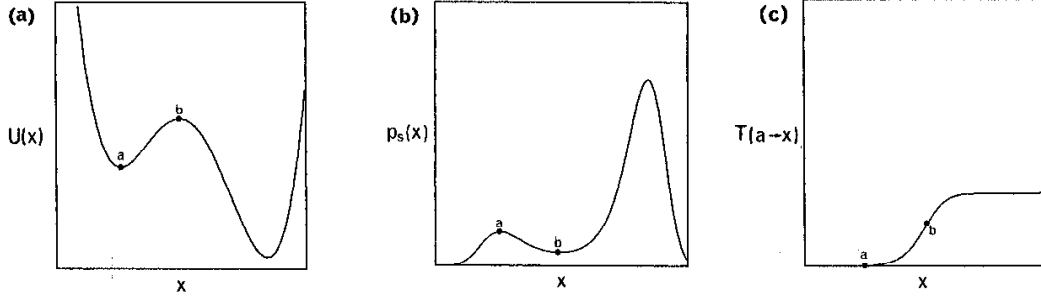


**Figure A.2:** a) Double wellled potential  $U(x)$  b) Stationary distribution  $p_s(x)$  c) Mean first passage time. From [74]

Here  $x_0$  is a generic point between  $a$  and  $c$ . The corresponding stationary quantities are:

$$\begin{aligned} n_a &= 1 - n_c = \int_{-\infty}^b p_s(x') dx' \\ n_0 &= (c - a)p_s(x_0) \end{aligned} \quad (\text{A.81})$$

From the FPE (A.62) we obtain:

$$\frac{\partial}{\partial t} \int_a^{x_0} \frac{M(x, t)}{p_s(x)} dx = D \left[ \frac{p(x_0, t)}{p_s(x_0)} - \frac{p(a, t)}{p_s(a)} \right] \quad (\text{A.82})$$

where  $D$  is defined in (A.61).

The Kramers' approximation assumes rapid relaxation within each well compared to the time scale of a well to well transition. Therefore one can assume that in each well the distribution  $p(x, t)$  is well approximated by the stationary distribution  $p_s(x)$  corrected by the corresponding weights. More precisely, the function  $p(x, t)$  is approximated by:

$$p(x, t) = \begin{cases} p_s(x) \frac{N_a(t)}{n_a} & x < b \\ p_s(x) \frac{N_c(t)}{n_c} & x > b \end{cases} \quad (\text{A.83})$$

Now we can write, from (A.82):

$$\begin{cases} \kappa(x_0) \dot{N}_a(t) = D \left[ \frac{N_0(t)}{n_0} - \frac{N_a(t)}{n_a} \right] \\ \mu(x_0) \dot{N}_c(t) = D \left[ \frac{N_0(t)}{n_0} - \frac{N_c(t)}{n_c} \right], \end{cases} \quad (\text{A.84})$$

Here

$$\kappa(x_0) \simeq \int_a^{x_0} p_s(x)^{-1} dx, \quad (\text{A.85})$$

and

$$\mu(x_0) \simeq \int_{x_0}^c p_s(x)^{-1} dx. \quad (\text{A.86})$$

Since  $-\dot{N}_a(t) = \dot{N}_c(t)$  we can sum both equations (A.84), and write:

$$\dot{N}_a(t) = -\dot{N}_c(t) = -r_a N_a(t) + r_c N_c(t) = r_c - (r_a + r_c) N_a(t). \quad (\text{A.87})$$

Here:

$$r_a = D \left[ n_a \int_a^c p_s(x)^{-1} dx \right]^{-1} \quad (\text{A.88})$$

$$r_c = D \left[ n_c \int_a^c p_s(x)^{-1} dx \right]^{-1} \quad (\text{A.89})$$

Equation (A.87), is the so called master equation describing the process in which the particles can jump between the two wells with rate constants  $r_a$  and  $r_c$ . Solving for  $N_a(t)$ , we obtain an exponential solution describing relaxation to the steady state. The relaxation time is given by:

$$\tau_r^{-1} = r_a + r_c = \frac{(n_a + n_c)D}{(n_a n_c) \int_a^c p_s(x)^{-1} dx}. \quad (\text{A.90})$$

Equation (A.87), is equivalent to equation (1.15) used by Huxley and Simmons. In general, it is possible to show that a FPE can always be approximated by a jump process (master equation)<sup>1</sup> but not vice-versa. Notice that in the Kramers' approximation the rate constants are not phenomenological and have a precise mechanical origin.

## A.8 Brownian motion in a periodic potential

Until now, we have been considering potentials in which the particles were constrained in a finite region. In this case, the flux in the stationary state was equal to zero. This condition allowed us to obtain the explicit expression for the stationary distribution  $p_s(x)$  (see (A.65)).

Another type of stationary solution, when the total probability flux is not zero, can be found in the case when a particle is moving in a periodic potential [23]. The corresponding equation of motion can be written in the form:

$$\gamma \dot{x} = F - f'(x) + \Gamma(t) \quad (\text{A.91})$$

---

<sup>1</sup>The general linear master equation for the probability density is

$$\frac{\partial p_n}{\partial t} = \sum_m [p(m \rightarrow n)p(m) - p(n \rightarrow m)p(n)]$$

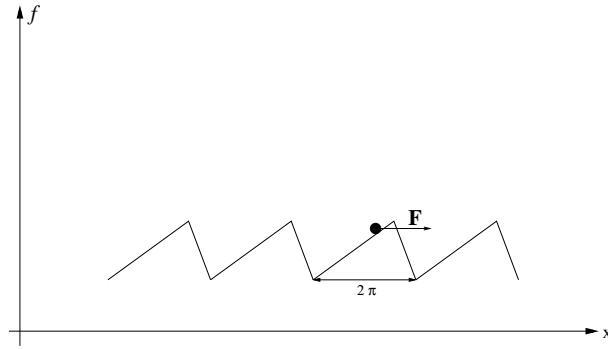


**Figure A.3:** Periodic energy landscape

where  $f$  is the periodic potential,  $F$  is a constant force and  $\Gamma(t)$  is a white noise imitating thermal fluctuations. The corresponding FPE is

$$\frac{\partial p}{\partial t} = \frac{1}{\gamma} \frac{\partial}{\partial x} \left[ f' - F + D \frac{\partial}{\partial x} \right] p = -\frac{\partial S}{\partial x} \quad (\text{A.92})$$

In the steady state, the probability current  $S$  is constant, so:

$$\gamma S = (F - f')p - D \frac{\partial p}{\partial x} \quad (\text{A.93})$$

The solution of this equation can be written as:

$$p(x) = \exp[-V(x)/D] \left( N - \gamma \frac{S}{D} \int_0^x \exp[V(x')/D] dx' \right) \quad (\text{A.94})$$

with the effective potential  $V(x)$  defined by:

$$V(x) = f(x) - Fx \quad (\text{A.95})$$

(see Fig. A.3). To fully define the steady state solution, we need to obtain the values of  $S$  and  $N$ , from the boundary condition and the normalization condition. To apply the boundary condition in the special case of a periodic potential, we can first write (assuming  $0 \leq x < 2\pi$ ):

$$\int_0^{2\pi n+x} e^{V(x')/D} dx' = \int_0^{2\pi} e^{V(x')/D} dx' + \dots + \int_{2\pi(n-1)}^{2\pi n} e^{V(x')/D} dx' + \int_{2\pi n}^{2\pi n+x} e^{V(x')/D} dx' \quad (\text{A.96})$$

Recalling that  $V(x + 2\pi n) = V(x) - 2\pi nF$ , and defining:

$$I = \int_0^{2\pi} e^{V(x')/D} dx' \quad (\text{A.97})$$

we can shift the integration variables in equation (A.97) to obtain

$$\int_0^{2\pi n+x} e^{V(x')/D} dx' = I + Ie^{-2\pi F/D} + \dots + Ie^{-2\pi(n-1)F/D} + \int_0^x e^{V(x')/D} dx' e^{-2\pi n F/D} \quad (\text{A.98})$$

$$= I \frac{1 - e^{-2\pi n F/D}}{1 - e^{-2\pi F/D}} + e^{-2\pi n F/D} \int_0^x e^{V(x')/D} dx'.$$

Introducing this result in (A.94), we obtain:

$$\begin{aligned} p(x + 2\pi n) &= e^{-V(x)/D} \left[ N - \frac{\gamma SI}{D(1 - e^{-2\pi F/D})} \right] e^{2\pi n F/D} \\ &+ e^{-V(x)/D} \left[ \frac{\gamma SI}{D(1 - e^{-2\pi F/D})} - \gamma \frac{S}{D} \int_0^x e^{V(x')/D} dx' \right] \end{aligned} \quad (\text{A.99})$$

We can now require that  $p(x)$  is bounded for large  $x$  (our boundary condition in the case of periodic potential). Then the first bracket on the right hand side of (A.99) must vanish at  $n \rightarrow +\infty$  for  $F > 0$  (or at  $n \rightarrow -\infty$  for  $F < 0$ ). Hence we obtain the first condition between  $N$  and  $S$ :

$$\gamma SI = DN(1 - e^{-2\pi F/D}). \quad (\text{A.100})$$

Next we recall that in the steady state:

$$p(x + 2\pi) = p(x) \quad (\text{A.101})$$

meaning that the probability distribution is periodic. Because of the periodicity, it is possible to normalize the distribution in only one interval. In this case we obtain the second condition on  $N$ :

$$\int_0^{2\pi} p(x) dx = 1. \quad (\text{A.102})$$

We remark that in the problem on the entire real axis with localized initial data, the probability  $p(x, t)$  never reaches a steady state (see [68]), instead  $p(x, \infty) \rightarrow 0$ . It is, however, possible to define a *reduced probability density*  $\hat{p}(x, t)$  as:

$$\hat{p}(x, t) = \sum_{n=-\infty}^{+\infty} p(x + 2n\pi, t) \quad (\text{A.103})$$

$$\int_0^{2\pi} \hat{p}(x, t) dx = 1 \quad (\text{A.104})$$

and the corresponding probability flux:

$$\widehat{S}(x, t) = \sum_{n=-\infty}^{+\infty} S(x + 2n\pi, t). \quad (\text{A.105})$$

Then, due to the linearity of the FPE, it can be rewritten in “reduced” variable as

$$\frac{\partial \widehat{p}}{\partial t} = -\frac{\partial \widehat{S}}{\partial x}. \quad (\text{A.106})$$

The advantage of this rewriting is that now the reduced probability density  $\widehat{p}(x, t)$  subjected to the periodic boundary conditions indeed tends toward a meaningful time independent limit.

With the two conditions (A.100) and (A.102), we can obtain the relation between the mean velocity of the particle and the applied force  $F$  in the form:

$$\begin{aligned} \langle v \rangle &= \langle \dot{x} \rangle = \gamma^{-1} \langle F - f'(x) + \Gamma(t) \rangle \\ &= \gamma^{-1} \langle F - f'(x) \rangle = \gamma^{-1} \int_0^{2\pi} (F - f'(x)) p(x) dx \\ &= \gamma^{-1} \int_0^{2\pi} (\gamma S + D \partial p / \partial x) dx = 2\pi S \end{aligned} \quad (\text{A.107})$$

The drift velocity is then given by the formula which we used in the body of the Thesis

$$\gamma \langle v \rangle = \frac{2\pi D(1 - e^{-2\pi F/D})}{\int_0^{2\pi} e^{V(x)/D} dx \int_0^{2\pi} e^{-V(x)/D} dx - (1 - e^{-2\pi F/D}) \int_0^{2\pi} e^{-V(x)/D} dx \int_0^x e^{V(x')/D} dx'} \quad (\text{A.108})$$

## A.9 Gillespie method

The *Gillespie method* was developed in 1977 [15]. Mathematically it belongs to the category Kinetics Monte Carlo methods, and can simulate the behavior of a system with known rate constants. The method is used in Section 2.7.1 to predict which Xb change configuration at every instant of time in a chain of half-sarcomeres each formed by  $N_{Xb}$  Xbs. The length of each half-sarcomeres affects the rate constants of the change of configuration as in the HS71 model. The main features of the algorithm are:

0. Set the time  $t = 0$
1. Form a list of all possible rates in the system  $k_i(\delta_i)$ , that in our case are a function of the length of the half-sarcomere  $\delta_i$ , given in the first step as initial conditions.

2. Calculate the cumulative function for

$$R_i = \sum_{j=1}^i k_j(\delta_j) \quad (\text{A.109})$$

for  $i = 1, \dots, N$  where  $N$  is the total number of transitions. Denote  $R = R_N$ .

3. Get a uniform random number  $u \in [0, 1]$ .
4. Find the event to carry out  $i$  by finding the  $i$  for which  $R_{i-1} < uR \leq R_i$ .
5. Carry out event  $i$  and update the new values of  $\delta_i$ .
6. Recalculate all rates  $k_i(\delta_i)$  which may have changed due to the transition.

Update  $N$  and the list of events accordingly.

7. Get a new uniform random number  $u \in [0, 1]$ .
8. Update the time with  $t = t + \Delta t$  where  $\Delta t = -\log u / R$ .
9. Return to step 2.

For a more detailed description of the model see [15].



# Bibliography

- [1] Hill A-V (1938) The heat of shortening and the dynamic constants of muscle. *Proc. R. Soc. London B* 126:136-195.
- [2] Hunson J, Huxley H-E (1954) Changes in the cross striation of muscle during contraction and stretch and their structural interpretation. *Nature* 173:973.
- [3] Huxley A-F, Niedergerke R-M (1954) Structural changes in muscle during contraction. Interference microscopy of living muscle fibers. *Nature* 173:971-973.
- [4] Huxley A-F (1957) Muscle structure and theories of contraction. *Prog. Biophys. Biophys. Chem.* 7:255-318.
- [5] Jewell B-R, Wilkie D-R (1958) An analysis of the mechanical components in frog's striated muscle. *J. Physiol.* 143(3):515-40.
- [6] Feynman R-P, Leighton R-B, Sands M (1963) The Feynman Lectures on Physics. *Addison-Wesley, Reading, MA* Vol.1 Chapt. 46.
- [7] Gordon A-M, Huxley A-F, Julian F-J (1966) The variation in isometric tension with sarcomere length in vertebrate muscle fibres. *J Physiol.* 184:170-192.
- [8] Pauling L (1970) General chemistry. *Freeman and Company* San Francisco, CA.
- [9] Lymn R-W, Taylor E-W (1971) Mechanism of adenosine triphosphate hydrolysis by actomyosin. *Biochemistry* 10:4617-4624.
- [10] Huxley A-F, Simmons R-M (1971) Proposed mechanism of force generation in striated muscle. *Nature* 233:533-538.
- [11] Ericksen J-L (1975) Equilibrium of bars. *J. Elast.* 5:191-201.



- [12] Hill T-L, Eisenberg E (1976) Reaction free energy surfaces in myosin-actin-ATP system. *Biochemistry* 15:1629-1634.
- [13] Inbar, Adam (1976) Estimation of muscle active state. *Biol. Cybern.* 23:61-72.
- [14] Ford L-E, Huxley A-F, Simmons R-M (1977) Tension response to sudden length change in stimulated frog muscle fibres near slack length. *J. Physiol.* 269:441-515.
- [15] Gillespie T (1977) Exact Stochastic Simulation of Coupled Chemical Reactions. *The Journal of Physical Chemistry* 81:2340-2361.
- [16] Muller I, Villaggio P (1977) A model for an elastic-plastic body. *Arch. Rat. Mech. Anal.* 65:25-46.
- [17] Eisenberg E, Hill T-L (1978) A cross-bridge model of muscle contraction. *Prog. Biophys. Molec. Biol.* 33:55-82.
- [18] Eisenberg E, Hill T-L, Chen Y (1980) Cross-bridge model of muscle contraction. *Biophys. J.* 29:195-227.
- [19] McMahon T-A (1984) Muscles, Reflexes, and Locomotion *Princeton University Press*
- [20] Ford L-E, Huxley A-F, and Simmons R-M (1985) Tension transients during the rise of tetanic tension in frog muscle fibers. *J. Physiol.* 361:131-150.
- [21] Smith D-A, Sicilia S (1987) The theory of sliding filament models for muscle contraction. I. The two-state model, *J. Theor. Biol* 127:1-30.
- [22] Pate E, Cooke R (1989) A model of crossbridge action: the effects of ATP, ADP and Pi. *J. Muscle Res. Cell Motil.* 10:181-196.
- [23] Risken H (1989) The Fokker-Plank Equation, methods of solution and application. *Berlin Springer-Verlag, 1989, 2nd ed.* Chapt. 11.
- [24] Morgan D-L (1990) New insights into the behavior of muscle during active lengthening. *Biophys. J.* 57:209-221.
- [25] Vale R-D, Oosawa F (1990) Protein motor and Maxwell's demons: does mechanochemical transduction involve a thermal ratchet? *Adv. Biophys.* 26:97-134.

- [26] Leibler S, Huse D-A (1991) A physical model for motor proteins. *C. R. Acad. Sci. Paris* 313:27-35.
- [27] Pate E, Cooke R Simulation of stochastic processes in motile crossbridge systems. *J. Muscle Res. Cell Motil.* 12:376-393.
- [28] Ajdari A (1992) Ph.D. Thesis. *Université Paris 6* Chap. 7.
- [29] Fedelich B, Zanzotto G (1992) Hysteresis in discrete system of possibly interacting elements with a double well energy. *J. Nonlin. Sci.* 2:319-342.
- [30] Kloeden P-E, Platen E (1992) Numerical solution of stochastic differential equations. *Springer-Verlag NY*
- [31] Berg H-C (1993) Random walks in Biology. *Princeton University* Princeton, NJ.
- [32] Magnasco O-M (1993) Forced thermal ratchets. *Phys. Rev. Lett.* 71:1477-1481.
- [33] Rayment I, Rypniewski W-R, Schmidt-Böhl K, Smith R, Tomchick D-R, Benning M-M, Winkelmann D-A, Wesenberg G, Holden H-M (1993) Three-dimensional structure of myosin subfragment-1: a molecular motor. *Science*, 261:50-58.
- [34] Walker R-A, Sheetz M-P (1993) Cytoplasmic microtubule-associated motors. *Ann. Rev. Biochem.* 62:429-451.
- [35] Wakabayashi K, Sugimoto Y, Tanaka H, Ueno Y, Takezawa Y, Amemiya Y (1994) X-ray diffraction evidence for the extensibility of actin and myosin filaments during muscle contraction. *Biophys. J.* 68:1196-1197.
- [36] Goldman Y-E, Huxley A-F (1994) Actin compliance: are you pulling my chain? *Bioph. J.* 67:2131-2136.
- [37] Hunt A-J, Gittes F, Howard J (1994) The force exerted by a single kinesin molecule against a viscous load. *Biophys. J.* 67:766-781.
- [38] Huxley H-E, Stewart A, Sosa H, Irving T (1994) X-ray diffraction measurements of the extensibility of actin and myosin filaments in contracting muscle. *Biophys. J.* 67:2411-2421.

- [39] Slawnych M-P, Seow C-Y, Huxley A-F, Ford L (1994) A program for developing a comprehensive mathematical description of the cross-bridge cycle of muscle. *Biophys. J.* 67:1669-1677.
- [40] Prost J, Chauwin J-F, Peliti L, Ajdari A (1994) Asymmetric pumping of particles. *Phys. Rev. Lett.* 72:2652-2655.
- [41] Brenner B, Chalovich J-M, Yu L-C (1995) Distinct molecular processes associated with isometric force generation and rapid tension recovery after quick release. *Biophys. J.* 68:106s-111s.
- [42] Jülicher F, Prost J (1995) Cooperative molecular motors. *Phys. Rev. Lett.* 75:2618.
- [43] Piazzesi G, Lombardi V (1995) A cross-bridge model that is able to explain mechanical and energetic properties of shortening muscle. *Biophys. J.* 68:1966-1979.
- [44] Stuart Ira Fox (1995) Human physiology *Times Mirror Higher Ed. Group, Iowa* 5th ed.
- [45] Derényi I, Vicsek T, (1996) The kinesin walk: a dynamic model with elastically coupled heads. *Proc. Natl. Acad. Sci.* 93:6775-6779.
- [46] Fung Y-C (1996) Biomechanics. *Springer; 2nd edition* Chapter 9.
- [47] Howard J, (1996) The movement of kinesin along microtubules. *Annu. Rev. Physiol.* 58:703-729.
- [48] Huxley A-F, Tideswell S (1996) Filament compliance and tension transient in muscle. *Journal of Muscle Research and Cell Motility* 17:507-511.
- [49] Piazzesi G, Linari M, Reconditi M, Vanzi F, Lombardi V (1997) Cross-bridge detachment and attachment following a step stretch imposed on active single frog muscle fibres. *J. Physiol.* 498:3-15.
- [50] Jülicher F, Ajdari A, Prost J (1997) Modeling molecular motors. *Rew. Mod. Phys.* 69:1269-1281.
- [51] Derenyi I, Tegzes P, Vicsek T (1998) Collective transport in locally asymmetric periodic structures. *Chaos* 8:657-664.

- [52] Epstein M, Herzog W (1998) Theoretical Models of Skeletal Muscle: Biological and Mathematical Considerations *John Wiley and Sons; 1st edition*
- [53] Fujita H, Ishiwata S. (1998) Spontaneous oscillatory contraction without regulatory proteins in actin filament-reconstituted fibres. *Biophys. J.* 75:1439.
- [54] Jülicher F, Prost J (1998) Molecular motors: from individual to collective behavior. *Prog. Theor. Phys. Supplement* 130:9.
- [55] Linari M, Dobbie I, Reconditi M, Koubassova N, Irving M, Piazzesi G, Lombardi V (1998) The stiffness of skeletal muscle in isometric contraction and rigor: the fraction of myosin heads bound to actin. *Biophys. J.* 74:2459-2473.
- [56] Magnasco M-O, stolorovitzky G, (1998) Feynman's ratchet and pawl. *J. Stat. Phys.* 93:615-632
- [57] Vilfan A, Frey E, Schwabl F (1998) Elastically coupled molecular motors. *Eur. Phys J. B* 3:535-546.
- [58] Barclay C-J (1999) A weakly coupled version of the Huxley crossbridge model can simulate energetics of amphibian and mammalian skeletal muscle *J. Muscle. Res. Cell M.* 20:163-176.
- [59] Duke T-A-J (1999) Molecular model of muscle contraction. *Proc Natl Acad Sci USA* 96:2770-2775.
- [60] Kitamura K, Tokunaga M, Iwane A-H, Yanagida T (1999) A single myosin head moves along an actin filament with regular steps of 5.3 nanometres. *Nature* 397:129-134.
- [61] Holmes K-C, Geeves M-A (2000) The structural basis of muscle contraction. *Philos. Trans. R. Soc. Lond. B Biol. Sci.* 355:419-431.
- [62] Puglisi G, Truskinovsky L (2000) Mechanics of a discrete chain with bi-stable elements *J. Mech. Phys. Sol.* 48:1-27.
- [63] Higham D-J (2001) An algorithmic introduction to numerical simulation of stochastic differential equations. *SIAM rev.* 43:525-546.
- [64] Howard J., (2001) in Mechanics of motor protein and the cytoskeleton, *Sindauer (Sunderland, Ma)*

- [65] Badoual M, Jülicher F, Prost J (2002) Bidirectional Cooperative Motion of Molecular Motors. *Proc. Natl. Acad. Sci.* 99:6696-6701.
- [66] Piazzesi G, Reconditi M, Linari M, Lucii L, Sun Y-B, Narayanan T, Boesecke P, Lombardi V, Irving M (2002) Mechanism of force generation by myosin heads in skeletal muscle. *Nature* 415:659-662.
- [67] Piazzesi G, Lucii L, Lombardi V (2002) The size and the speed of the working stroke of muscle myosin and its dependence on the force. *J. Physiol.* 545:145-151.
- [68] Reimann P, (2002) Brownian motors, noisy transport far from equilibrium. *Physics Reports* 361:57-265.
- [69] Wang H, Oster G (2002) Ratchets, power strokes and molecular motors. *Appl. Phys. A* 75:315-323.
- [70] Asbury C-L, Fehr A-N, Block S-M (2003) Kinesin moves by an asymmetric hand-over-hand mechanism. *Science* 302:2130-2134
- [71] Esaki S, Ishii Y, Yanagida T (2003) Model describing the biased Brownian movement of myosin. *Proc. Japan Acad* 79:9-14.
- [72] Holmes K-C, Angert I, Kull F-J, Jahn W, Schröder R-R (2003) Electron cryo-microscopy shows how strong binding of myosin to actin releases nucleotide. *Nature* 425:423-427.
- [73] Vilfan A, Duke T (2003) Instabilities in the transient response of muscle. *Biophys. J.* 85:818-827
- [74] Gardiner C-W (2004) Handbook of Stochastic Methods: for Physics, Chemistry and the Natural Sciences (Springer Series in Synergetics) pp 342-372.
- [75] Cooke R (2004) The sliding filament model: 1972-2004. *J. Gen. Physiol.* 123:643-656.
- [76] Holmes K-C (2004) Introduction. *Philos Trans R Soc Lond B Biol Sci.* 359:1813-1818.
- [77] Reconditi M, Linari M, Lucii L, Stewart A, Sun Y-B, Boesecke P, Narayanan T, Fischetti R-F, Irving T, Piazzesi G, Irving M, Lombardi V (2004) The myosin motor in muscle generates a smaller and slower working stroke at higher load. *Nature* 428:578-581.

- [78] Szent-Gyorgyi A-G (2004) the early history of the biochemistry of muscle contraction. *J. Gen. Physiol.* 123:631-641.
- [79] Smith D-A, Sleep J (2004) Mechanokinetics of rapid tension recovery in muscle: the myosin working stroke is followed by a slower release of phosphate. *Biophys. J.* 87:442-456.
- [80] Decostre V, Bianco P, Lombardi V, Piazzesi G (2005) Effect of temperature on the working stroke of muscle myosin. *Proc Natl Acad Sci USA* 102:13927-13932.
- [81] Efendiev Y-C, Truskinovsky L (2005) Rversible and irreversible self-heating in one-dimensional chain with buckling elements. *in press*.
- [82] Lan G, Sun S-X, (2005) Dynamics of Myosin-V Processivity. *Byoph. J.* 88:999-1008
- [83] Prylutsky Y-I, Shut A-M, Miroshnychenko M-S, Suprun A-D (2005)
- [84] Reconditi M, Linari M, Lucii L, Stewart A, Sun Y-B, Narayanan T, Irving T, Piazzesi G, Irving M, Lombardi V (2005) Structure-function relation of the myosin motor in striated muscle. *Ann. N.Y. Acad. Sci.* 1047:232-247.
- [85] Zeldovich K-B, Joanny J-F, Prost J (2005) Motor proteins transporting cargos. *Eur. Phys. J. E* 17:155-163.
- [86] Burton K, Simmons R-M, Sleep J Kinetics of force recovery following length changes in active skinned single fibers from rabbit psoas muscle. *J. Physiol.* 573.2:305-328.
- [87] Cooper M-G, Hausman R-E (2006) The Cell: A Molecular Approach. *Sinauer Associates, Inc.; 4 edition* Ch.12.
- [88] Huxley H, Reconditi M, Stewart A, Irving T (2006) X-ray interference studies of crossbridge action in muscle contraction: evidence from quick release. *J. Mol. Biol.* 363:743-761.
- [89] Morgan D-L, Proske U (2006) Sarcomere popping requires stretch over a range where total tension decrease with length. *J. Physiol.* 574(2):629-630.
- [90] Telley I-A, Stehle R, Ranatunga K-W, Pfitzer G, Stssi E, Denoth J. (2006) Dynamic behavior of half-sarcomeres during and after stretch in activated

- rabbit psoas myofibrils: sarcomere asymmetry but no “sarcomere popping”. *J. Physiol.* 573(1):173-185.
- [91] Brunello E, Reconditi M, Elangovan R, Linari M, Sun Y-B, Narayanan T, Panine P, Piazzesi G, Irving M, Lombardi V. (2007) Skeletal muscle resists stretch by rapid binding of the second motor domain of myosin to actin. *Proc Natl Acad Sci USA* 104:20114-20119.
- [92] Piazzesi G, Reconditi M, Linari M, Lucii L, Bianco P, Brunello E, Decostre V, Stewart A, Gore D-B, Irving T-C, Irving M, Lombardi V. (2007) Skeletal muscle performance determined by modulation of number of myosin motors rather than motor force or stroke size. *Cell* 131:784-795.
- [93] Roots H, Offer G-W, Ranatunga K-W (2007) Comparison of the tension responses to ramp shortening and lengthening in intact mammalian muscle fibres: crossbridge and non-crossbridge contributions. *J. Muscle Res. Cell. Motil.* 28:123-139.
- [94] Tanner B-C-W, Daniel T-L, Regnier M (2007) Sarcomere lattice geometry influences cooperative myosin binding in muscle. *PLoS Comput Biol* 3:e115
- [95] Keener J, Sneyd J (2008) Mathematical Physiology: II:Systems Physiology. *Springer 2nd edition* Chapter 18.
- [96] Smith D-A, Geeves M-A, Sleep J, Mijailovich S-M (2008) Towards a Unified Theory of Muscle Contraction. I: Foundations. *Ann. Biomed. Eng.* 36:1624-1640.
- [97] Wikipedia
- [98] <http://www.mrothery.co.uk/muscles/MusclesNotes.htm>
- [99] [web.mit.edu/16.423/www/MuscleSumm.html](http://web.mit.edu/16.423/www/MuscleSumm.html)
- [100] [http://www.unm.edu/~jimmy/muscle2\\_notes.htm](http://www.unm.edu/~jimmy/muscle2_notes.htm)